NIFS-PROC-97

Proceeding of A3 Foresight Program Seminar on Critical Physics Issues Specific to Steady State Sustainment of High-Performance Plasmas, 23-26 June, 2014, Kagoshima, Japan

(Eds.) S. Morita, L. Hu and Y.-K. Oh

Oct. 30, 2014

Proceeding of A3 Foresight Program Seminar on Critical Physics Issues Specific to Steady State Sustainment of High-Performance Plasmas

23-26 June, 2014, Kagoshima, Japan

Edited by

Shigeru MORITA, Liqun HU and Yeong-Kook OH

Abstract

The A3 Foresight Program titled by "Critical Physics Issues Specific to Steady State Sustainment of High-Performance Plasmas", based on the scientific collaboration among China, Japan and Korea in the field of plasma physics, has been started from August 2012 under the auspice of the Japan Society for the Promotion of Science (JSPS, Japan), the National Research Foundation of Korea (NRF, Korea) and the National Natural Science Foundation of China (NSFC, China). The main purpose of this project is to enhance joint experiments on three Asian advanced fully superconducting fusion devices (EAST in China, LHD in Japan and KSTAR in Korea) and other magnetic confinement devices to solve several key physics issues on steady state sustainment of high-performance plasmas. The fourth seminar on the A3 collaboration, as the fifth meeting of A3 program, took place in Kagoshima, Japan, 23-26 June 2014, which was hosted by National Institute for Fusion Science, to discuss achievement during past two years and to summarize intermediate report. New collaborative research was also encouraged as well as participation of young scientists. The topics include steady state sustainment of magnetic configurations, edge and divertor plasma control and confinement of alpha particles.

Key words: superconducting fusion device, magnetic confinement, toroidal plasmas, high-performance plasmas, steady state sustainment, edge plasma, divertor plasma, edge stability, high-energy particle, alpha particle and fusion plasma simulation.

Organization Committee

Shigeru MORITA (National Institute for Fusion Science, Japan)
Liqun HU (Institute of Plasma Physics, Chinese Academy of Sciences, China)
Yeong-Kook OH (National Fusion Research Institute, Korea)

Program Committee

Shigeru MORITA (National Institute for Fusion Science, Japan)
Liqun HU (Institute of Plasma Physics, Chinese Academy of Sciences, China)
Yeong-Kook OH (National Fusion Research Institute, Korea)
Mitsutaka ISOBE (National Institute for Fusion Science, Japan)
Satoshi OHDACHI (National Institute for Fusion Science, Japan)
Satoru SAKAKIBARA (National Institute for Fusion Science, Japan)
Yasushi TODO (National Institute for Fusion Science, Japan)

Conference Secretariats

Masanori KAKIAGE (National Institute for Fusion Science, Japan)
Satsuki MATSUI (National Institute for Fusion Science, Japan)
Shaohua DONG (Institute of Plasma Physics, Chinese Academy of Sciences, China)
Noh-Yeong OH (National Fusion Research Institute, Korea)

Preface

The first meeting of A3 foresight program on Plasma Physics hosted by NFRI (Korea) was held in Jeju Island, Korea on 22nd August, 2012 as coordinator meeting to initiate the A3 program. The first seminar hosted by NIFS (Japan) and the second seminar hosted by ASIPP (China) were held in Kushiro, Japan during 22-25 January, 2013 and in Beijing, China during 20-23 May, 2013, respectively. Concrete planning of collaborative research was made and possible scientific progresses done in steady state sustainment of high-performance plasmas were also discussed in two seminars. Many young scientists were joined in these seminars. The third seminar hosted by NFRI was held in Gyeongju, Korea during 3-4 November, 2013 before 9th Asia Plasma and Fusion Association Conference (APFA 2013) to report the progress and achievement in on-going A3 collaboration.

The fourth seminar of A3 foresight program, as the fifth meeting of A3 program, hosted by NIFS was held in Kagoshima, Japan during 23-26 June, 2014. Results of on-going A3 collaboration were presented to discuss achievement during past two years and to summarize intermediate report. The presentations in the seminar are made at each category; I. Steady state sustainment of magnetic configurations, II. Edge and divertor plasma control (IIa. Transport of edge and divertor plasmas and IIb. Stability of edge plasma), III. Confinement of alpha particles and IV. Theory and simulation.

In total 46 participants attended this seminar (18 from Japan, 16 from Korea and 12 from China) and 41 reports were presented. As a special topics in this seminar, a session on tungsten study including spectroscopy and atomic physics and a session on scientific study by Ph.D. students learning in graduate school were set up to step up the A3 activities.

The seminar was closed with great success, clarifying remarkable progress in researches along A3 program physics subjects and also contributing to the fostering of younger scientists. The organizing and program committees are deeply grateful to all participants and to strong and continuous support from foundation of three countries (NSFC in China, JSPS in Japan and NRF in Korea), with whose support and corporation the seminar was smoothly and successfully concluded.

Shigeru MORITA, Liqun HU and Yeong-Kook OH

Chairpersons of the Organizing Committee


The 5th A3 Foresight Program Workshop
June 23rd -26th, 2014 Kagoshima, Japan
Sponsored by Japan Society for the Promotion of Science, National Natural Science Foundation of China and National Research Foundation of Korea
日中韓フォーサイト事業
A3 Foresight Program
独立行政法人
日本学術振興会
Japan Society for the Promotion of Science

Contents

◆**Session 11**

EAST Next Five-year Plan

J. Li[1], L.Q.Hu, B.J.Xiao, N.Xiang, J.L.Chen, S.H.Dong,
X.J.Zhang, Y.Liu and EAST team

Institute of Plasma Physics, Chinese Academy of Sciences
PO Box 1126, Hefei, Anhui, China 230031
j_li@ipp.ac.cn

1. Introduction:

Experimental Advanced Superconducting Tokamak (EAST) as shown in figure 1 is the first fully superconducting tokamak which was approved by Chinese government in July 1998. Its mission is to conduct fundamental physics and engineering researches of advanced tokamak fusion reactors with a steady, safe and high performance, to provide a scientific base for experimental reactor design and construction. EAST construction started in October, 2000. The assembly was finished at the end of 2005 and the commissioning was completed in March 2006[1]. Progress has been made in plasma operation during past few years [2-3]. During the next 10 years for ITER construction, together with LHD, KSTAR, JT-60SA and WEST tokamaks, EAST will be an important experimental test bench for conducting ITER related steady-state advanced plasma science and technology research.

Fig.1 Experimental Advanced Superconducting Tokamak (EAST)

2. Present State of EAST

Since 2010, significant progress has been made on EAST on both physics and technology fronts towards the long-pulse operation of high-confinement plasma regimes. Over 400s divertor L-mode plasma discharges and long pulse H-modes with duration over several tens of the current diffusion time have been achieved on EAST by the combination of lower hybrid current drive (LHCD) and RF heating. Remarkable efforts have also been made in mitigating type-I ELMs in stationary state H-mode plasma with multi-pulses of supersonic molecular beam injection (SMBI), LHCD, lithium granule and deuterium pellet injection. Over 30s long-pulse H-mode discharges with $H_{(98,y2)} \sim 1$ have been obtained either with ELM mitigation or in a small ELMy regime accompanied by a new electrostatic edge coherent mode. The peak heat load on the divertor, which is over 10 MW/m^2 during type I ELMs, is reduced down to 2 MW/m^2 either by SMBI or LHCD [4-5].

Tremendous efforts have been made during past two years to enhance the EAST capabilities; nearly every sub-system except superconducting magnets has been upgraded or

modified to enable higher performance and truly steady state operation. The major upgrades include:

- H&CD systems have been upgraded around 30MW, namely 4 MW CW 2.45GHz and 6MW 4.6GHz LHCD systems, 12MW CW ICRF system with wide band frequency of 25-70MHz, 4MW 50-80keV NBI system. The 2nd4MW NBI and 2MW ECRH of 140GHz could be ready in October.
- 78 different diagnostics are installed, and all key profiles of plasma parameters will be provided during the coming experiments.
- Upper divertor has been changed into ITER-like W monoblock configuration with up to 10MW/m^2 heat removing capacity as shown in Fig. 2.
- Top and bottom internal crypumps have been installed with a 160M^3/s pumping speed together with enhancement of external pumps.
- 16 ITER-like RMPs coils together with several other new ELM mitigation methods, such as supersonic beam injection, CW Li&D_2 pellet injectors, gas puffing from different target places, up to 1kHz power modulation of H&CD systems(LHCD, ICRF, NBI,ECRH), have been implemented.
- Two pairs of ITER-like VS coils have been installed to better control plasma vertical displacements. Fast control power supply and plasma control system have been upgraded to facilitate the control of high plasma performance discharges.
- Other systems, such as PF&TF power suppliers, cryogenic system, cryogenic transmission line, HTc superconducting current leads and fueling systems have also been upgraded towards more reliable operation condition.

2014 EAST second experiment campaign is planned to start from late October when the second NBI and ECRH are ready, and last till the end of January 2015. Challenges on plasma control, effective H&CD, plasma-wall interactions under long pulse, high heat flux (over 10MW/m2) and high-Z metal wall conditions will be tremendous.

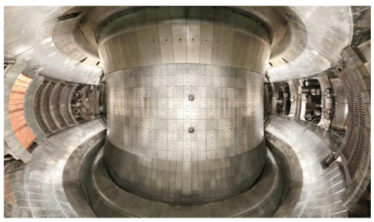

Fig.2 EAST internal plasma phase component structure

3. Next Five Year Plan

Next five year is a very important period of time to explore most of key issues for ITER under steady-state operation condition on EAST. Major efforts will focus on capacity improvement and high performance plasma discharges.

Further increase of H&CD power and diagnostics under CW condition will be one of most important efforts. Since LHCD&ICRF are in very good condition, the establishment of 10MW CW ECRH and optimization of long pulse NBI system will be the most challenging

tasks. Fig.3 shows the future arrangements of major hardwares on EAST during next 5 years.

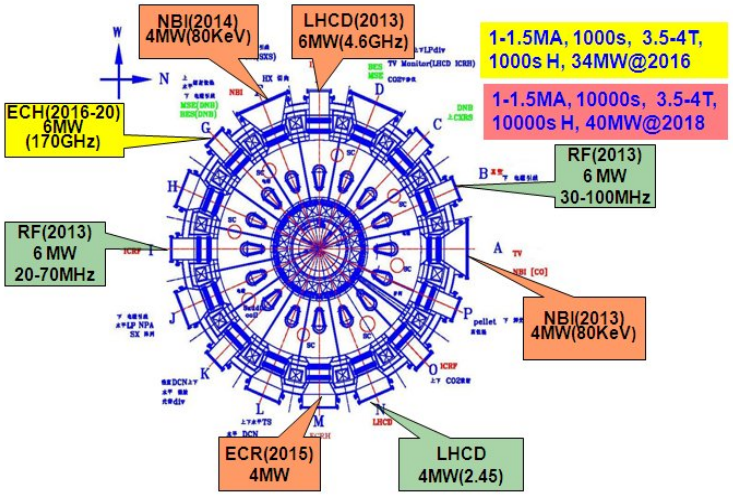

Fig.3 Arrangements of EAST major hardwares for next 5 years

With over 30 MW long pulse H&CD and 80 different advanced diagnostics, EAST will have unique capabilities to address many of the critical physics and technology issues that ITER will encounter. EAST is capable of pulse durations beyond 400 seconds (similar to ITER) with high power electron heating (as in ITER) to challenge power and particle handling at high normalized levels (10MW/m^{-2}) comparable to ITER. EAST also aims to explore steady state operation with advanced tokamak characteristics which would be of great value to ITER but also could lead to an attractive fusion power plant. The table 1 shows the expected plasma performance up to 2018 before ITER construction.

Table 1 Plasma parameters during next 5 years

Parameters \ Year		2014	2015	2016	2017	2018
Ip(MA)		1.0	1.0	1.0	1.5	1.5
LHCD (MW, CW)	2.45GHz	4.0	4.0	4.0	4.0	4.0
	4.6GHz	6.0	6.0	6.0	6.0	6.0
ICRF(MW,CW) 25-70MHz		12	12	12	12	12
NBI(80keV)		8.0	8.0	8.0	8.0	8.0
ECRH		1.0	2.0	4.0	6.0	10
Diagnostics		70	80	80	80	80
Duration(s)		400	1000	1000	1000	1000
t-Hmode(s)		100	400	400	1000	1000
Beta N		2	2-3	2-3	2-3.5	2-3.5

The overall focus of the EAST program in the next 5 years is to develop the scientific and technical basis for high-performance, steady-state operation in ITER and future tokamak reactors. The EAST team has established as a long-term target of very long pulse (400 s)

plasma operation with a plasma current I_P = 1 MA, normalized beta $\beta_N \geq 3$, bootstrap fraction $f_{BS} > 0.5$, and line-averaged density > 0.6 times of the Greenwald limit. With the power available from 2014, steady state scenarios at I_P = 0.5 MA scenario are within reach and will start soon, which will be an exciting and important step toward EAST's long term goals.

To achieve these overall goals requires advances in both technical performance and physics understanding in several areas. Efforts will be made on the following key issues:

•High-power heating and current drive at high density. The EAST facility will start operation in 2014 with 22 MW of RF H&CD source power. Physics issues associated with high-power heating, such as coupling and power deposition at high density, control of power levels and wave phasing, and energetic particle effects, will also need to be further explored.

•Power and particle exhaust in steady-state (400 s) and high power density (~10MW/m^2). Heat and particle removal, compatible with high plasma performance, is essential for successfully making use of EAST's high-power heating capabilities. The EAST team has already made a strong effort in edge physics, and this emphasis will continue as the program moves toward higher power input and longer pulses. On the technical side, operation with new equipment (e.g., ITER like tungsten divertor, internal cry pump) and higher heat loads will increase risks associated with, e.g., component over-heating, deleterious plasma-launcher interactions, and coolant leaks. Attention will be given to mitigating these risks. On physics side, impurity radiation feedback control in both core and DSOL will be continue, together with newly developed snowflake configuration towards long pulse operation.

•Plasma measurements. The EAST facility has, and is still expanding an extensive set of diagnostics making plasma measurements needed for equipment protection and for control, characterization, and understanding of high-performance steady-state plasmas. Future efforts will focus on attaining a high level of availability and reliability in these diagnostics so that they can successfully fulfill these roles. The transition to operation with several-minutes-long pulses will require an evolution toward more efficient steady-state data acquisition strategies, e.g. event-triggering or real-time data reduction.

•Theory-experiment coupling. The theory team has developed simulation capabilities that start to be used to identify steady-state operating scenarios. Going forward, strong theory-experiment collaboration will be essential for the EAST experiment to use these capabilities to maximum advantage in designing and interpreting experiments. More data including detailed plasma measurements will be needed to make comparisons between simulation and experiments. The efforts will focus on subjecting codes to experimental validation as well as understanding the experiment.

•Plasma control. The EAST facility is equipped with an impressive array of plasma control tools, including new three-dimensional control coils, and benefits strongly from international collaboration in the plasma control area. Steady state tokamak operation will require excellent plasma control, including, e.g. control of edge-localized modes (ELMs) and other instabilities, avoidance and mitigation of disruptions, density control, and pressure and current profile control at high density. Using its available tools, and guided by physics measurements and simulations, the EAST control team will work to establish and over time, systematically expand, the operating space for steady-state plasmas.

•ELM mitigation and control. The giant Type-I ELM is unfavorable and must be mitigated in ITER operation due to very strong interaction with plasma facing material which could be easily damaged during long pulse ELM plasma discharge. A few ways for ELM

mitigation have been successfully tested on EAST, such as D_2& Li pellets, supersonic beam injection, and modulated LH wave. 16 ITER like RMP coils have been installed on EAST which could provide different RMP fields of m/n numbers to mitigate ELM. Newly installed ICRF, NBI and ECRH can be operated in a power modulation level up 1 kHz frequency. By using the newly developed methods, together with previous ELM mitigation methods, EAST will establish a few simple and robust ELM mitigation methods towards the application in ITER and future reactor.

4. Summary

The new developed capabilities (over 30 MW long pulse H&CD, actively cooled ITER-like W divertor, 80 diagnostics) will advance EAST to the fore-front of international magnetic fusion facilities which makes it possible in the next five years to be capable of long pulse (400s) high performance discharges. Meanwhile the challenges facing the EAST team in bringing all these new systems into routine operation will also be huge and the risks are high. EAST team together with its international cooperators looks forward to embracing these challenges and significant scientific output which will benefit ITER and the wide international fusion science and technology community.

Acknowledgements:

This work was partly supported by the JSPS-NRF-NSFC A3 Foresight Program in the field of Plasma Physics (NSFC: No.11261140328, NRF : No. 2012K2A2A6000443).

Reference:

[1] Wan Yuanxi, Li Jiangang, Weng Peide, EAST team, First Engineering Commissioning of EAST Tokamak, *Plasma Sci. Technol.* ***8*** *253*

[2] Jiangang Li and Baonian Wan for the EAST Team and International Collaborators, Recent progress in RF heating and long-pulse experiments on EAST, Nucl. Fusion 51 (2011) 094007

[3] G.S. Xu, B.N. Wan，J.G. Li, X.Z. Gong J.S. Hu, J.F. Shan, H. Li, D.K. Mansfield, D.A. Humphreys, V. Naulin for EAST team and international collaborators, Study on H-mode access at low density with lower hybrid current drive and lithium-wall coatings on the EAST superconducting tokamak, Nuclear Fusion, Vol.51, 2011, p072001

[4] J. Li, H.Y. Guo, B.N. Wan, et al., “A long-pulse high-confinement plasma regime in the Experimental Advanced Superconducting Tokamak”, Nature Phys. 9, 817 (2013).

[5] H.Y. Guo, J. Li, X.Z. Gong, B.N. Wan, et. al, “Approaches towards long-pulse divertor operations on EAST by active control of plasma–wall interactions”, Nuclear Fusion, Vol.54, 2014: p.013002-1—013002-9

Operation and engineering research plan in KSTAR

Yeong-Kook Oh, K. R. Park, H. L. Yang, H. K. Kim, D. S. Park, J. H. Choi, J. S. Hong, Y. Chu, J. D. Kong, S. T. Kim, and J. G. Kwak

National Fusion Research Institute, Daejeon, Korea

E-mail : ykoh@nfri.re.kr

1. Introduction

Most of researches in the fusion devices have been concentrated to solve the physics and engineering issues at the high performance steady-state operation which are essential in the operation of ITER and in designing the future power plants. In preparing the ITER initial operation, present key issues are to achieve H-mode under the limited heating power, to suppress or mitigate type-I ELMs, to prevent disruptions, and to stabilize the MHD instabilities such as neo-classical transport mode (NTM) instability. In addition, the validation of the self-regulating high beta operation, fully-non inductive current drive under high density, and control of high heat flux at divertor are important technologies need to be solved in preparing the advanced type DEMO reactor.

Campaign	Highlights and contributions	Key parameters
2008	• First plasma at the first trial • Successful X2 ECH pre-ionization • Contribution to ITER startup	• Ip (1st plasma) > 100 kA • ECH pre-ionization (X2 84 GHz at B_T ~1.5 T)
2010	• Successful H-mode in SC tokamak • Start of proposal-based joint experiments	• Ip (H-mode) ~0.6 MA, P_{NBI}~1 MW
2011	• Successful ELM suppression at low n. • Contribution to ITER ELM control issue	• ELM suppression at n=1, 2 MP
2012	• Stationary H-mode over 16 s • Surpassing n=1 ideal no-wall limit • Showing the potential of advanced plasma research	• t (H-mode) > 16s @ 0.6 MA • β_N ~ 2.9, β_N/ li ~ 4.1
2013	• Demonstration of very low intrinsic error field and TF ripple • Uniqueness of KSTAR device	• $\delta B/B \sim 10^{-5}$

Fig. 1. The brief history of the KSTAR operation and contribution to the fusion community since the first plasma in 2008.

KSTAR project aims to explore the key physics and technologies of the high performance steady-state operation that are essential for ITER and fusion reactor utilizing the advanced superconducting tokamak device [1]. Since the first plasma in 2008 [2], KSTAR device has been operated as an international joint research device and has produced some experimental outcomes which could be contributed to the ITER initial operation. The brief history of the KSTAR operation and contribution is summarized in figure 1. KSTAR showed the successful ECH pre-ionization under the 2nd harmonic condition (f_{ECH} = 84 GHz, at B_T = 1.5 T) during the initial operation in 2008. H-mode discharges under the limited heating power (P_{NBI} ~ 1 MW) was achieved in 2010 according to the plasma shape control and wall conditioning

using glow discharge and boronization [3]. In 2011, KSTAR showed a successful suppression of edge localized mode (ELM) by applying non-axisymmetric magnetic perturbation with low toroidal mode number, n=1 [4]. In the following campaigns, H-mode plasma operation range was extended up to 0.9 MA in current level and 20 s in the flattop duration and higher betaN operation up to 2.9. It showed the reliable operation surpassing the n=1 no-wall limit with betaN/li ~ 4.1. The scanning of the error field revealed a very low intrinsic error field in KSTAR compared to error field in other tokamak devices [5]. The operation results of six campaigns showed that KSTAR has lots of unique features which enable the advanced target operation and physics research such as strong shaping capability, a very low intrinsic error field, small TF ripple, and complex in-vessel control coils.

2. Highlights of the KSTAR 2013 experiments

Despite of the early termination of the 2013 experimental campaign due to an arc in the slow discharge resister (SDR) stack of toroidal field system, KSTAR was able to complete about 85 % of the scheduled experimental proposals. Due to the hardware failure, the planned H-mode discharge at 1 MA and the commissioning of newly installed motor generator system could not be conducted.

The research highlights of the KSTAR 2013 campaign could be listed as follows; (i) The improvement of plasma shaping and achieving early H-mode enabled the achievement of 20s duration H-mode as shown in figure 2. (ii) Low-n intrinsic error field is quite low (δB/B possibly as low as ~10^{-5}) that is likely the result of good coil engineering and alignment. The calculated TF ripple is also small. (iii) The successful achievement of ELM suppression at n=1 and n=2 modes. The control of rotation and neoclassical toroidal viscosity (NTV) were conducted effectively. Those unique features of ELM control at low n-mode seem to be related to the combination of low intrinsic error field and small TF ripple. (iv) Preliminary experiments on the MHD control were conducted such as sawtooth locking experiments using EC modulation, and preliminary NTM control. The passive stabilizer showed the mechanical weakness under the large number of VDE and requires structural reinforcement to reach larger plasma current over 1 MA.

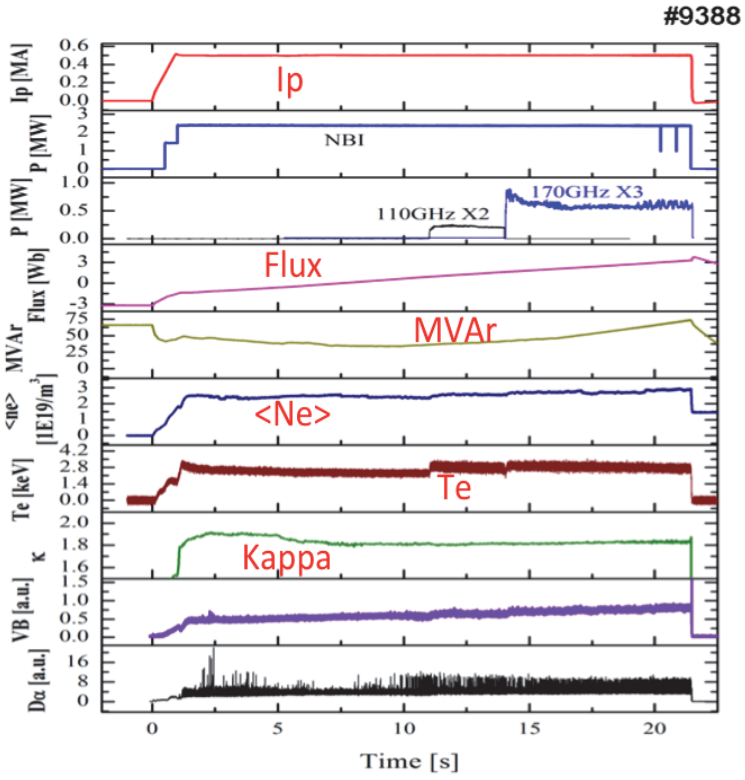

Fig. 2. H-mode discharge with 20s duration. .

3. Status of KSTAR machine upgrade

After the 2013 campaign, the device has been upgraded to enable the KSTAR operation at higher performance. The device upgrade planned to be in two steps. In the first step until 2017, hardware upgrade to support the physics research under the low density and intermediate heating power environment. The passive stabilizers has been upgraded with installing the additional vertical supporters on the lower passive stabilizer to have an mechanical rigidity against VDE and halo current occurrence as shown in figure 3. Newly installed motor generator system (200 MVA, 2 GJ) has been commissioned individually [6] and is ready for the integrated commissioning in connection with PF coils. Several sets of broadband AC power supplies are under procurement for the in-vessel control coils to give more flexibility in the ELM control, rotation control, and dynamic error field control. It could be available from 2015 campaign. NBI-1 system equipped three ion sources are under conditioning. And the control room space will be extended to absorb more participants in the KSTAR experiments. The planned heating power is about 13 MW until 2017.

After validation of the physic research under low density and intermediated power, the system will be upgraded for the experiments under the ITER or DEMO operation range. The long-term plan of hardware upgrade and research is shown in figure 4.

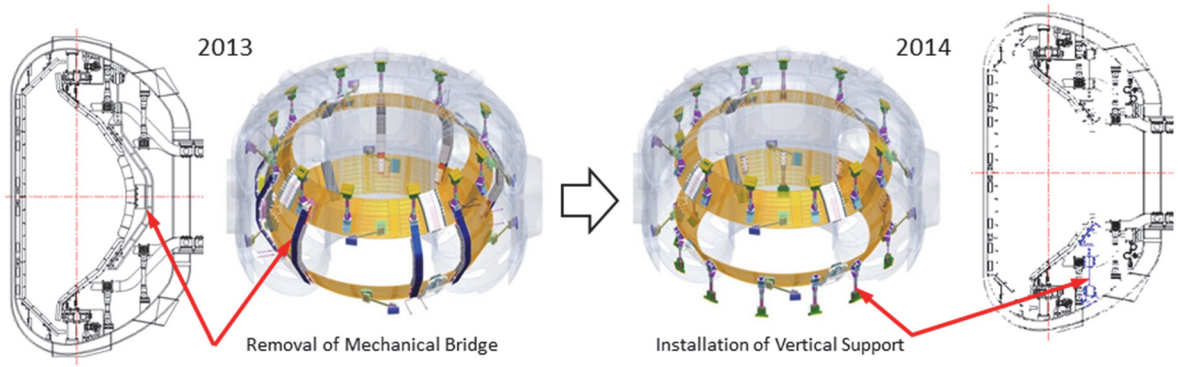

Fig. 3. The installation of the vertical supporters on the passive stabilizer.

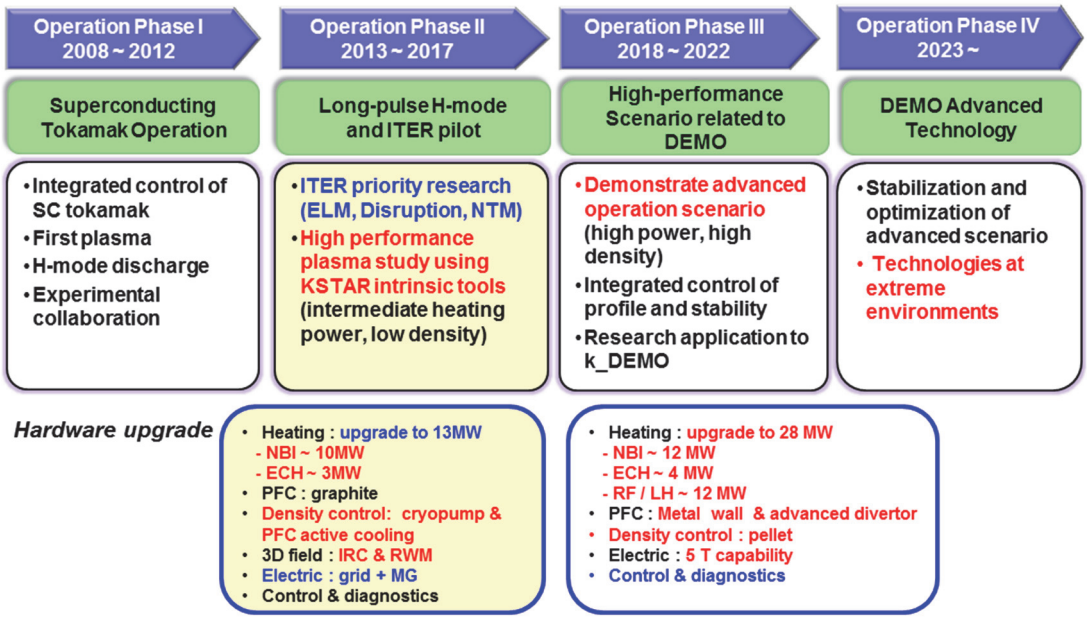

Fig. 4. The long-term research plan and expected hardware upgrade plan.

4. KSTAR operation and research plan

The 2014 campaign will be stared from the end of June and be closed at the end of December, and the plasma experiments could be available from the middle of September until the end of November as shown in figure 5. The available heating power is about 6 MW (5 MW NBI and 1 MW ECCD). Key operation targets in 2014 are (i) H-mode discharge for 30s at 0.5 MA and for about 10 s at 1 MA in plasma current, (ii) sustaining ELM suppression phase up to 10s, (iii) control of β_N using $P_{NBI} \sim 5$ MW and $P_{ECCD} \sim 1$ MW, (iv) routine measurement of profiles and fluctuations at pedestal and (iii) integrated commissioning of motor generator system.

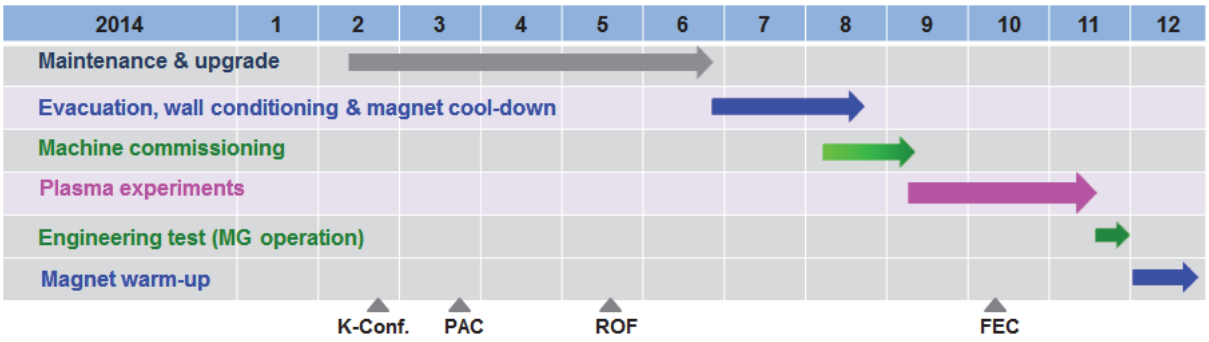

Fig. 5. The operation schedule of the KSTAR 2014 campaign.

KSTAR program has objectives to be a first mover at world fusion research solving the scientific and technical issues of fusion in demonstrating the advanced operation related to ITER and DEMO for the fusion energy commercialization. The hardware upgrade and experiments in phase II until 2017 will be will be concentrated to contribute to ITER and DEMO in several areas including the fundamental physics and innovative control techniques of the ELMs in ITER, innovative physics of L-H transition, impurity control, plasma rotation and momentum transport, understanding the influence of 3-D fields on plasma confinement and stability, and integrated operation scenarios, and runaway electron dissipation [7].

Acknowledgement

This research was supported by Ministry of Science, ICT, and Future Planning under KSTAR project and was partly supported by the JSPS-NRF-NSFC A3 Foresight Program (NSFC: No.11261140328, NRF No. 2012K2A2A6000443). The authors appreciate the efforts of all the staffs in Fusion Engineering Research Center and in KSTAR Science Center in NFRI and the strong participation and contribution from the domestic and international collaborators.

References

[1] M.Kwon et al., Nuclear Fusion, 51, 094006 (2011).
[2] Y.K. Oh et al., Fusion Engineering and Design, 84, 344 (2009).
[3] S.W. Yoon et al., Nuclear Fusion 51, 113009 (2011).
[4] Y.M. Jeon et al., Physics Review Letter, 109, 035004 (2012)
[5] Y. In et al., A3 workshop, June 23-26, Kagoshima, Japan (2014).
[6] C.H. Kim et al., A3 workshop, June 23-26, Kagoshima, Japan (2014).
[7] A. Becoulet et al., 2014 KSTAR Program Advisory Committee Report (2014. 04, NFRI)

Recent Progress on the J-TEXT Tokamak

G.Zhuang[1], K.W.Gentle[2], X.W.Hu[1], Z.Y.Chen[1], Y.H.Ding[1], M.Zhang[1], Z.P.Chen[1], B.Rao[1], J.Chen[1], Q.M.Hu[1], Z.J.Wang[1(*)], L.Gao[1], X.Q.Zhang[1], Z.F.Cheng[1], Y.Pan[1], K.X.Yu[1], H. Huang[2], the J-TEXT team[1]

[1]*State Key Laboratory of Advanced Electromagnetic Engineering and Technology, School of Electrical and Electronic Engineering, Huazhong University of Science and Technology, Wuhan 430074, P.R. China*

[2]*Institute for Fusion Studies, University of Texas at Austin, Austin, 78712, USA*

E-mail contact of main author: wangzj@mail.hust.edu.cn

Abstract. The recent experimental progress on the J-TEXT tokamak is introduced. The interaction between rotating resonant magnetic perturbations (RRMPs) and tearing mode have been carried out on the J-TEXT tokamak and the results show that the magnetic island can be accelerated and fixed to the frequency of the rotating 2/1 RMP, while locked mode can also be unlocked by external RRMPs. A fast frame camera diagnostics has been developed to study the penetration of impurities gas jet and the propagation of cold front induced by the gas jet is observed to be stopped near q=2 surface. To observe the current profile, a high resolution three-wave far infrared polarimeter-interferometer is set up and the first results indicate it works well.

1. Introduction

The J-TEXT tokamak is a circular medium size tokamak reconstructed from TEXT-U[1,2]. It discharges in ohmic mode with limiter configuration. It's main purpose is to train young students and research some special physics topics, such as MHD activity and disruption, edge physics, confinement and transport etc., with modulation tools such as resonant magnetic perturbations (RMPs), super-sonic molecule beam injector (SMBI), massive gas injector (MGI) and biasing electrode system. The routine operation parameters of J-TEXT is described as: the major radius R = 105 cm, the minor radius r = 25-27 cm with a movable titanium-carbide coated graphite limiter, the maximum central-line toroidal field B_T = 2.2 T, the maximum plasma current Ip = 240 kA lasting for 400 ms, plasma densities n_e = 1-8×10^{19} m^{-3}, and electron temperature Te~1 keV. The main work on the J-TEXT tokamak in the recent campaign is focused on the influence of RMPs on plasma and the mitigation of disruptions. Besides some advanced diagnostic tools such as three-wave far infrared laser polarimeter-interferometer is improved simultaneously for further observation of some fine structures.

2. Influence of Rotating Resonant Magnetic Perturbations on tearing modes

2.1. Experimental Setup

In recent years, RMPs are widely studied or used on ELM control[3], RWM control[4], error field correction[5] and control of some other MHD instabilities, such as tearing mode and Kink mode. A thorough understanding of the interactions

between external RMP and plasma is very important. Basing on this, J-TEXT reconstructed the static RMP coils of TEXT-U, which is now named as SRMP. It is installed outside the vacuum vessel wall. On the other hand, to produce a rotating RMP to enlarge our research area, we constructed a rotating RMP system, named as DRMP[6]. DRMP consists of 12 saddle coils, which distributed at four toroidal locations. Because it is installed inside the vacuum vessel, it can produce a fast rotating RMP with the frequency between 800 Hz to 6 kHz. Besides, DRMP can also operate in DC mode to produce static RMPs. With two AC power supplies basing on resonant inverter with a typical phase shift of 90 or -90 degrees, DRMP can produce a rotating 2/1 RMP in co-Ip or counter-Ip direction. The typical mode spectrum of the rotating DRMP field is shown in figure 1. The components m/n = 2/1, 2/3, 2/5 and 2/9 are relatively large, however, for J-TEXT plasmas, the normal safety factor is between 0.9 and 3.5, so it is difficult for these components except for 2/1 to be resonant with the plasma. The eddy current near the coil will lead to a decay of the DRMP field. When the frequency is larger than 1 kHz, the rotating 2/1 perturbation will reduce to about 0.45 Gs/kA. Although it has a large decay, the field strength is enough in most cases.

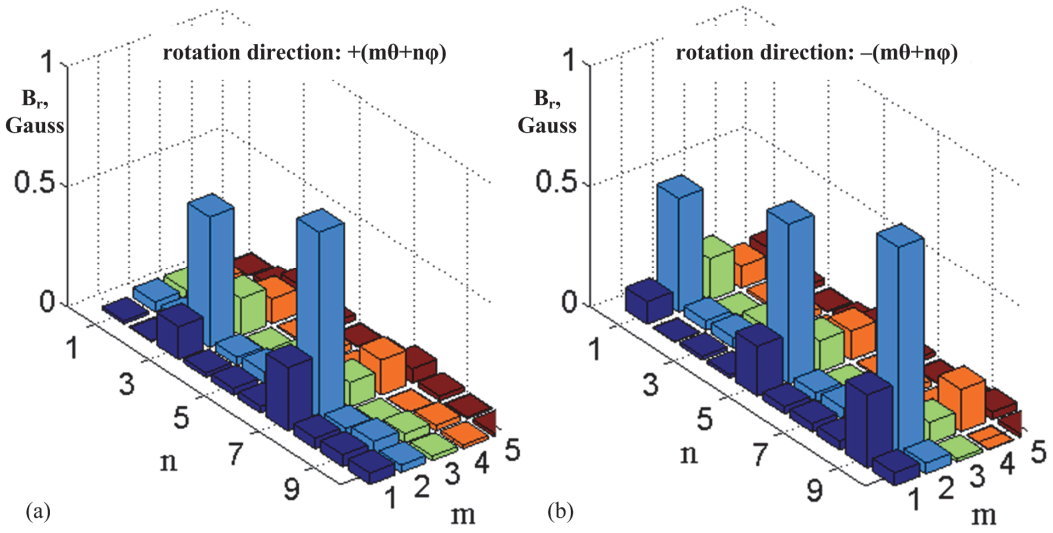

Figure 1. Amplitude distribution of DRMP field components with mn>0. (a) shows the components rotating in +(mθ+nφ) direction and (b) shows ones in -(mθ+nφ).

2.2. Acceleration of magnetic island

By using the rotating 2/1 RMP produced by DRMP system, the rotation acceleration of the magnetic island has been observed on the J-TEXT tokamak[7], as shown in figure 2. After the rotating RMP is applied, the mode frequency began to increase. When the current of DRMP reaches approximately 0.6 kA, the mode frequency jumps abruptly from 4.5 kHz to 5 kHz, which is the rotation frequency of the externally exerted RMP. Then the mode frequency remains at 5 kHz until the DRMP current drops to a small level, at which point the island is unlocked from the rotating RMP. Meanwhile, the edge plasma rotation measured by the Doppler shift of the spectrum of C-V radiation, changes toward the counter-I_p direction. The edge

rotation recovers again after the island is unlocked. Similar results are also obtained in the numerical simulation, as given in figure 3. After the external RMP is turned on, the rotating velocity of the island will experience an oscillation, meanwhile, a decrease of the island width can be found. When the mode is locked, the mode frequency keeps the same with RMP, while the island width increases to a larger level.

As the external RMP has a strong suppression effect on the island width during the locking procedure, it provides a possible control method of tearing mode if the RMP frequency can be kept to be larger than that of the magnetic island. More detailed research will be undertaken in the succeeding works.

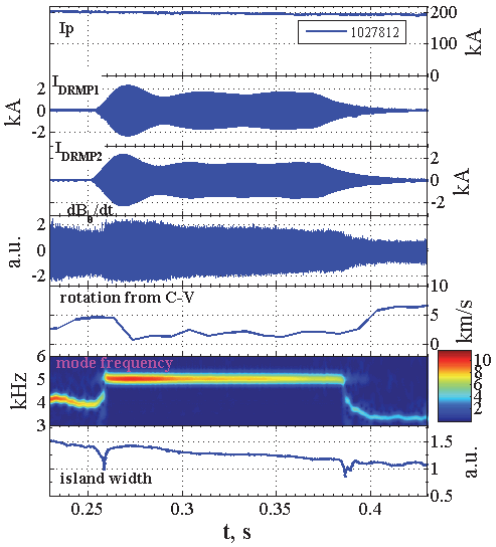

Figure 2. Experimental observation of the acceleration of tearing mode and plasma rotation caused by rotating RMP.

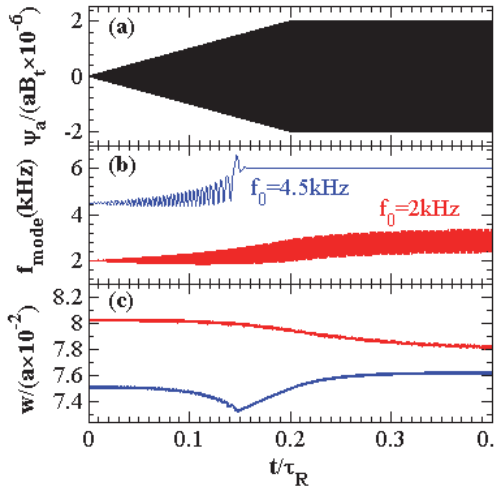

Figure 3. Tearing mode acceleration for both low frequency and high frequency modes in numerical modeling.

2.3 Unlocking of the locked island by rotating RMP

Inspired by the island acceleration results shown in figure 2, it is reasonable to expect that the rotating RMP can unlock the locked mode, and hence avoid locked mode disruption. In order to provide a repeatable locked mode for research, the SRMP coils are used to lock the initial tearing mode for about 200ms, as shown in figure 4. Then SRMP current reduces to a lower amplitude to avoid disruption which may be caused by too large island. A rotating RMP, with 4 kHz in frequency and 4.4 kA in maximum amplitude, was applied during the steady state of locked mode. The island is observed to unlock from the SRMP, and to rotate together with the 4kHz rotating RMP. Further experiments show that, the larger the frequency difference between the (static) island and the rotating RMP, the field strength needed to unlock the island is larger. Therefore, to unlock an error field locked island, the better way is to apply a low frequency rotating RMP, and when the island is locked, increase the frequency gradually to a high level.

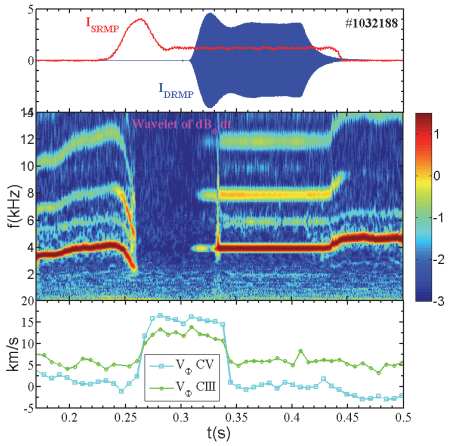

Figure 4. Unlock of the locked mode by rotating RMP with a frequency of 4kHz.

3. Observation of the Penetration of Massive Gas

The major disruption causes damages to the tokamak device by the heat loads, electric magnetic force and hitting of runaway electrons [8,9]. Prevention and mitigation of disruptions are necessary to reliable operation of ITER due to the high thermal and poloidal magnetic energy content of the plasma [10]. It has been proved that the magnitude of these negative effects can be significantly reduced by massive gas injection (MGI) and the understanding of gas jet penetration process is important to improve the gas injection efficiency.

On J-TEXT, a fast frame camera (Phantom V710) was installed at the middle plane of chamber to view the penetration process tangentially. And figure 5 shows a typical fast shutdown discharge by 10 bar Ar MGI. The MGI valve was fired at 0.4s during flattop phase and the plasma disrupted in 3 ms. With the fast frame camera the penetration process of gas jet and the interaction of gas jet with plasma can be obtained, as shown in figure 6. According to the formation time of cold front, it is found that the flight time in the vacuum is about 2ms. When the gas jet went into the plasma interior, a cold front was induced. The cold front penetrates into the plasma interior with a speed in the order of 200m/s. When the cold front penetrate into 0.7 a, strong MHD activities (2/1 mode) were induced which results in loss of confinement and major disruption. The stop of the cold front near the q=2 surface also has been observed on Tore Supra [11].

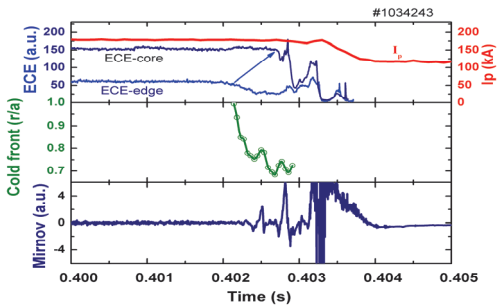

Figure 5. Waveforms of plasma fast shutdown by Ar MGI.

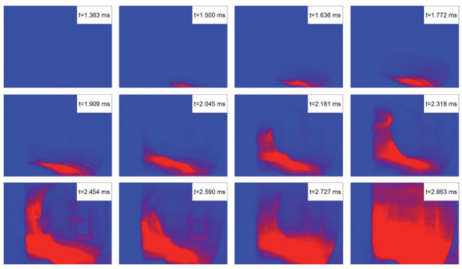

Figure 6. Photographs of gas jet by fast frame camera with filter. The time interval between two adjacent images is 0.136 ms.

4. Upgrade of J-TEXT polarimeter-interferometer system

The J-TEXT polarimeter-interferometer system is developed for plasma equilibrium and stability study in recent years[12,13]. Based on three-wave technique, the system is capable to achieve simultaneous Faraday angle and integrated density measurement with high time response and phase resolution; in addition, the system uses slab probe beam which covers the whole plasma cross section for the measurement, providing excellent spatial coverage and resolution. Recently it is upgraded to 14 chords, with impact parameters from -0.85a to 0.9a (a=25.5 cm) and chord spacing ~35mm. The typical measurement results of multi-chord Faraday angle and integrated density data are shown in figure 7. In sequence the time trace of plasma current, 14 chords Faraday angle and 14 chords integrated density are plotted. It should be noted that the Faraday angle is associated with the projection of magnetic field on the laser probe beam path, therefore the chords passing through plasma at low field side has different sign comparing to those at high field side. With these spatial profiles of Faraday angle and integrated density, safety factor profile, current density profile and electron density profile can be obtained from equilibrium reconstruction. Furthermore, as shown by figure 7, the polarimeter-interferometer is capable to observe the perturbation associated with tearing mode (from ~0.07s to ~0.13s in figure 1) and sawtooth activity (after ~0.2s) on both Faraday angle and integrated density. For different chords the perturbation has different amplitude and phase, which provides information of the spatial structure of magnetic perturbation and density perturbation. Further research is underway.

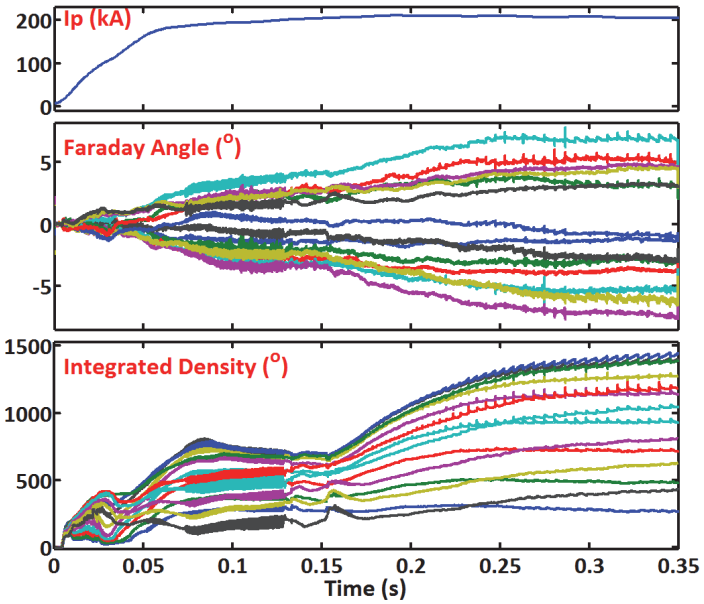

Figure 7. The time trace of typical measurement results of multi-chord Faraday angle and integrated density data.

4. Summary

The recent research work on the J-TEXT tokamak emphasizes on the interaction between RRMPS and tearing modes and disruption mitigation research. The

experiments indicates external RRMPs can accelerate or decelerate the magnetic island and make the mode frequency keep the same with RRMPs which is consistent with the simulation. Especially for the locked mode, the RRMPs can unlock it and to avoid the disruption. The penetration process of MGI is watched by fast frame camera and cold front is analyzed which stops near the q=2 surface. Besides, the polarimeter/interferometer is upgraded to 14 chords with 3.5cm spatial resolution and cover 90% of cross section of J-TEXT. The fine structures of sawtooth and tearing mode can be explored and the relevant work is being carried out.

Acknowledgement We are grateful for the help from the Southwestern Institute of Physics and the Institute of Plasma Physics, Chinese Academy of Science. This work is partly supported by the JSPS-NRF-NSFC A3 Foresight Program in the field of Plasma Physics (NSFC No.11261140328).

References

[1] G. ZHUANG, et al., “The reconstruction and research progress of the TEXT-U tokamak in China”, Nucl. Fusion 51 (2011) 094020.
[2] G. Zhuang, et al., “Recent research work on the J-TEXT tokamak”, Nucl. Fusion 53 (2013)104014.
[3] Y. Liang, et al., “Active control of type-I edge localized modes with n = 1 and n = 2 fields on JET”, Nucl. Fusion 50 (2010) 025013.
[4] M Okabayashi, et al., “Stabilization of the resistive wall mode in DIII–D by plasma rotation and magnetic feedback”, Plasma Phys. Control. Fusion 44 (2002) B339–B355.
[5] Jong-Kyu Park, et al., “Error field correction in ITER”, Nucl. Fusion 48 (2008) 045006.
[6] B. Rao, et al., “Introduction to Resonant Magnetic Perturbation Coils of the J-TEXT Tokamak”, Fusion Engineering and Design 89 (2014) 378–384.
[7] B. Rao, et al., “First observation of rotation acceleration of magnetic island by using rotating resonant magnetic perturbation on the J-TEXT tokamak”, Plasma Phys. Control. Fusion 55 (2013) 122001.
[8] Riccardo V. and JET EFDA contributors, “Disruptions and disruption mitigation”, 2003 Plasma Phys. Control. Fusion 45(2003) A269.
[9] Sebiiller F.C., “Disruptions in tokamaks”, Plasma Phys. Control. Fusion 31(1995) A135.
[10] Commaux N. et al., “Demonstration of rapid shutdown using large shattered deuterium pellet injection in DIII-D ”, Nucl. Fusion 50(2010) 112001.
[11] Reux C. et al., “Experimental study of disruption mitigation using massive injection of noble gases on Tore Supra”, Nucl. Fusion 50(2010) 095006.
[12] CHEN, J., et al., “Design of far-infrared three-wave polarimeter-interferometer system for the J-TEXT tokamak”, Rev. Sci. Instrum. 81 (2010) 10D502.
[13] CHEN, J., et al., “First results from the J-TEXT high-resolution three-wave polarimeter-interferometer”, Rev. Sci. Instrum. 83 (2012) 10E306.

Setup and Commissioning of New Diagnostics on the EAST Device

*Liqun Hu, on behalf of EAST diagnostic team and collabrators**
Institute of Plasma Physics, Chinese Academy of Science, P.O. Box 1126, 230031, China
Email of the responsible person: lqhu@ipp.ac.cn

1. Introduction

EAST (Experimental Advanced Superconducting Tokamak) device is aimed to achieve steady-state (SS) high-performance plasma sustained by intensive use of radio frequency heating and current drive, and to study fusion reactor-relevant physics and technology [1-6]. In the last 7th experimental campaign in 2012, significant progress had been got. 400s long pulse plasma discharge (0.28MA, ne~1.2, Te~1.8keV, P_{LHCD}~1.2MW, Bt~2.5T), stationary H-modes with durations of 35 s (0.28MA, ne~2.2, P_{LHCD}~1.8MW, P_{RF}~1.2MW, Bt~1.9T, H98(y,2)~0.8) and 32s (0.4MA, LSN, P_{LH} ~1.2MW, P_{RF}~1.6MW, f=27MHz, Bt~1.9T), H-mode only by ICRH with a duration of 3.45s and effective ICRF heating (0.5MA, ne~2.0, Bt~1.9T, ΔW~30KJ) have been achieved [7-8]. To approach steady-state (SS) operation of high-performance plasmas and address key physics on fusion reactor-relevant subjects, tremendous and comprehensive upgrade of the EAST machine have been implemented exclusive of outer vacuum chamber after 7th campaign. Capability of the auxiliary heating and current drive on the EAST are doubled with total injection power over 25MW, including new methodology of 4MW@NBI (Neutral Beam Injector), 6MW@4.6GHz LHCD (Low Hybrid Current Driving) and 2MW@140GHz ECRH (Electron Cyclotron Resonant Heating). New ITER-like upper mock-up divertor with W/Cu monoblock structure and enhanced active cooling, additional upper internal cryo-pump, new RMP (Resonant Magnetic Perturbation) and IC (internal coil) Coils for plasma shape and position control, wall conditioning technique (Li oven/granule drop/pellet) and fuelling method (GP, SMBI, Pellet), have been developed and employed.

Diagnostic requirements of the EAST are determined by demands of measurement and physics study to characterize the plasma behavior over the full range of conventional plasma parameters. Following the revolutionary upgrade of the EAST device this time, more horizontal ports are assigned to new systems for plasma heating and current driving, and many new advanced diagnostics especially neutral-beam related diagnostics must be developed and given the port space. Therefore, all diagnostics are rebuilt based on the principle of more compact integration due to limited port window and space available with emphasis on distinguished ability to provide all parameters' profile including the current density profile, global rotation and turbulence, and characteristics of the pedestal region in H-mode plasma, to study and understand critical issues specific to SS high performance plasma.

2. Setup of new EAST diagnostics

EAST diagnostic technique involves electromagnetism, spectroscopy, microwave, laser assistance, particle diagnostics and fusion products, etc. According to application and research objectives, it can be divided into four categories: plant operation and protection, plasma equilibrium and control, research of plasma behavior and performance, and physical understanding of plasma for acquisition of high-performance steady-state plasma.

1) Plant operation and protection

EAST diagnostic systems deploy necessary measurement and feedback signals required by plant operation and protection which are used to measure the basic physical parameters within the range of all EAST operation parameters. For instance, electron temperature and density in plasma core, plasma position and shape, plasma current and loop voltage, vacuum vessel current, HALO current, main impurities, effective charge number and radiation power of plasma, etc. Meanwhile, monitoring of all kinds of engineering and technical parameters which is required by the operation and protection of systems, equipments, components and personnel security, should be realized. The monitoring includes temperature rise and electromagnetic force of important components inside vacuum vessel (divertor plate, limiter, etc.), pressure in vacuum branch, cooling water flow rate and pressure, all kinds of valve operation and emergency protection, as well as real-time monitoring of ionizing radiation and dose rate inside and outside the machine hall, et al.

2) Plasma equilibrium and control

EAST diagnostic systems are asked to provide basic signals based on electromagnetic measurement, such as flux loop, magnetic probe and pick-up coil, in order to achieve plasma equilibrium reconstruction which are critical for active palsma feedback control on stability, soft ramp-up and landing, avoidance of hazards, various configuration formation for realization of different important scenarios. Combining the signals of density from far-infrared interferometer, MHD instability, visible video camera and radiation power, etc., optimization of the EAST plasma performance can be achieved through detailed study of plasma confinement, wave-plasma coupling, interaction between wave and plasma, and divertor plasma performance, particle exhaustion and heat removal.

3) Study of plasma behavior and performance

EAST diagnostic systems provide the spatial distribution of basic plasma parameters from the core to the boundary, including electron temperature and density, ion temperature and density, major impurities and their concentration, radiation power and energy spectrum, effective charge number, speed of runaway electrons and superthermal electrons, edge plasma structure, etc. Interaction between divertor and wall materials with plasma is

monitored in order to provide the information of plasma up-down asymmetry, ablation of wall materials, and divertor plate and limiter temperature for possible erosion state, etc. The production and control of instability is studied to ensure plasma physics experiment on the rails. Currently, EAST diagnostic system upgraded comprehensively with the above capacity has been in commissioning to exhibit their function. It is expected that in one or two years, the usability and reliability of the diagnostic system, data validity and accuracy can be improved greatly. With the technique development of effective in-vessel calibration and collimation, rapid data processing methods, data fitting and interpretation together with model simulation, it will accommodate EAST requirements on various physics study.

4) Plasma physics understanding for acquisition of high-performance steady-state plasma

EAST diagnostic systems provide the spatial distribution of major plasma parameters from the core to the boundary, through projecting measurement data into magnetic surfaces using plasma magnetic surface reconstruction, acquiring plasma transport coefficient using a variety of programs and developing advanced and special diagnostic techniques especially closely related physical diagnostics which help to deepen the understanding of plasma stability, transport and energetic particles, to ensure active control of key parameters' profile. The ability of physical understanding of data is enhanced to furthest guarantee the needs of physical researches on high-performance and steady-state plasma, highly confined operation mode, advanced tokamak operation scenario, energy and particle transport, optimized divertor's ability to expel particles and heat load under near-reactor-core condition, and burn plasma study, etc.

3. Commissioning of EAST diagnostics

Integration of EAST diagnostics can been seen in Fig.1 in which downview of the diagnostics distribution, high integration with compact design and tight neighbouring interval between systems are illustrated. Too much energy has been spent during negotiation and design to accommodate more systems with reasonable viewing sights, interfaces both inside and outside, safety interval among outside subsystems. Even those, many issues are out of careful consideration. For example, movement and sealing of different shutters in periscope systems,

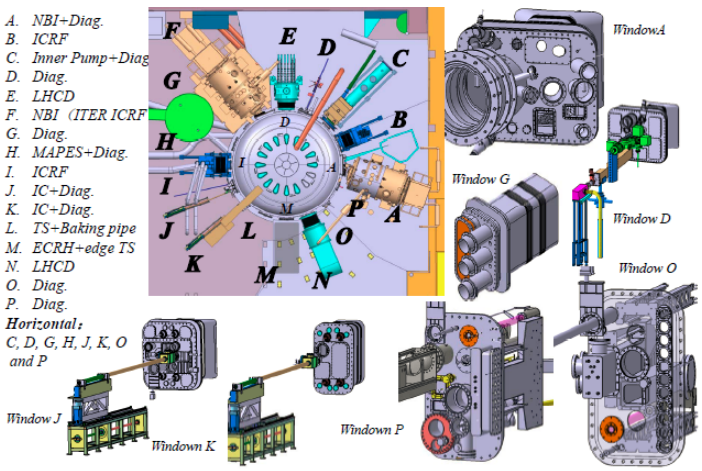

Fig.1 integration and arrangement of EAST diagnostics

electrical shield in neighbourhood and grounding connection bring troubles occasionally. Therefore, further optimization before next campaign for those issues is necessary.

Totally there are eighty diagnostics constructed. Many of them are advanced diagnostics for physics study and understanding as listed in Table 1. They are expected to provide measurement for current density, plasma rotation, lost particles, density and temperature fluctuation, impurity, MHD instability, runway electrons, fusion product, et al so as to find control way for those parameters. The letters "P", "B" and "S" in Table 1 indicate diagnostic roles "Primary", "Basic" and "Supplementary", respectively.

Function	Plasma specification
Plasma rotation profile	Core: XCS (solid D), CXRS Edge: Hot-He beam (5mm, 50kHz,Ti>20eV, >1km/s); ERD(P&T), Edge-CXRS reciprocating probe
q profile/ j relaxation	P: 3 beam Polarimetry-Interferometry System (9ch. H); MSE (2014) B: SXR+EFIT reconstruction
Fusion product Neutron flux spectrum	3He + BF3, Fission chamber BC501 array (3ch)+
Lost ions	sFLIP, H-NPA, FIDA (active and passive, S&f,4cm)
Fluctuation (Te & Ne, V)	Core: CO2 laser scattering (CTS), ECEI (Te, 16ch×26ch, 2.5-2.8T) Polarimetry-interferometry (Ne), Poloidal and radial correlation reflectormeter Edge: Li-BES (Ne/r2cm,p1cm); DBS reflectormeter(Ne/V_E); GPI (Ne, 2mm,400k); Hot He –beam (100K); Fast CCD; MW reflectormeter; ME-SXR (Te, slow); Reciprocating probe+HFS probe
MHD instability Lock mode (MHD)	ECEI (16ch×16ch, 2.5-2.8T), 2D T-SXR camera, Mirnov coil SXR camera, Tang. SXR, Saddle coil
Runaway behaviors	Midplane: BGO + NaI (Forward+backward), IR camera NaI array (5ch) + CdTe + BGO array (4ch)
Edge plasma parameters	Reciprocating probe, Bolometer, Tri-probe, Mach probe, Ha/Da, GPI
RF sheath behavior	Katusmata probe, Microwave reflectometre

Table1 Diagnostics for plasma physics understanding

Some of new diagnostics address to burning plasma study. During development of advanced diagnostics, comprehensive international collaborations have been carried out in different way. Young scientists and talent are educated and become source that plays continuous role in diagnostic technical development and relative physics research. Mutual collaboration will help EAST data configuration construction in wide international frame for sharing and analysis. It is believed that rebuilt EAST diagnostics and efforts involved will enhance EAST device in coming years to find ways for extension of operation regimes with high performance SS plasma in scenarios of longer H-mode, ITB, high β etc., and to seek for answers of new physics and existing observations which have not be fully understood.

With the dramatic increase of the EAST heating power and coming unignored radioactivation and radiocontamination, for the first time, distribution of the ionizing radiation and dose rate of the EAST, mainly on local radiation of neutron and gamma, are measured intensively and formally as shown in Fig.2 to give reasonable estimation of environmental radioactivity to give safe protection for

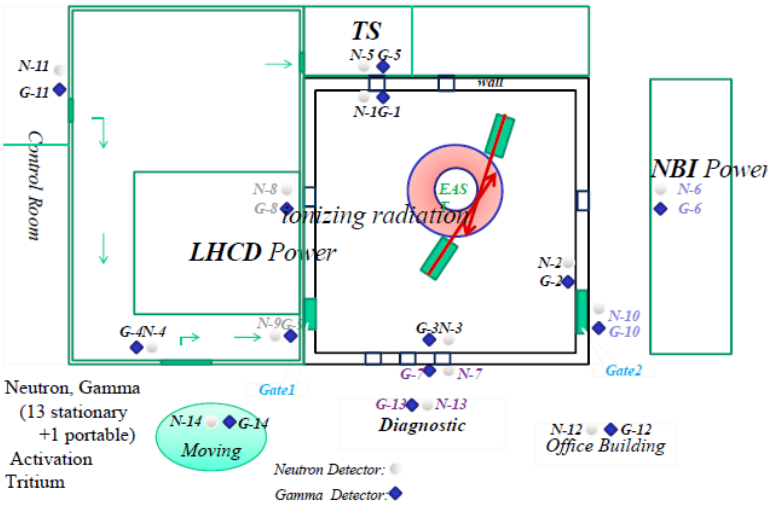

Fig.2 Measurement distribution of ionizing radiation and dose rate

local workers and environment.

4. Summary

Rebuilt EAST diagnostics with more advanced and specific diagnostics will provide more usable and valid data to allow good start for deep physics study and understanding. Data structure construction, data processing and effective interpretation combing with integrated modelling are needed with big efforts to push diagnostics work more reliably and effectively to accommodate EAST requirements on various physics study.

Acknowledgments

The author would like to thanks all members of EAST diagnostic team and all participants from domestic and international facilities for their contributions to EAST project. This work is undertaken partially under the support of the JSPS-NRF-NSFC A3 Foresight Program in the field of Plasma Physics (NSFC No.11261140328 and NRF No. 2012K2A2A6000443).

References:

[1] Baonian Wan, The EAST team and Interational Collaborators, “Physical engineering test and first divertor plasma configuration in EAST”, Plasma Science and Technology, Vol.9, No.2, 2007

[2] Baonian Wan for the EAST and HT-7 teams and collaborator, “Recent experiments in the EAST and HT-7 superconducting tokamaks” (Overview talk), 22nd IAEA Fusion Energy Conference, OV3-4, October 13-18, 2008, Switzerland; Nuclear Fusion, Volume 49, Number 10, 2009

[3] J G Li, Y P Zhao, J S Hu, X Z Gong, Review, R-3, 19th PSI Conference, San Diego, May 24-28, 2010

[4] H.Y. Guo, X. Gao, J. Li, G.-N. Luo, S. Zhu, J.F.Chang, Y.P.Zhao, W.Gao, X.Z.Gong, Q.S.Hu, Q.Li, S.C.Liu,T.F.Ming,J.Qu, Y.J.Shi, B.N.Wan, D.S.Wang, H.Q.Wang,J.Wang, Z.W.Wu, B.J.Xiao, Q.Xu, L.Zhang, W.Zhang, “Recent progress on divertor operations in EAST”, Journal of Nuclear Material, Vol.415, 2011: p.369-374

[5] Jiangang Li and Baonian Wan for the EAST Team and International Collaborators, “Recent progress in RF heating and long-pulse experiments on EAST”, Nuclear Fusion, Volume 51, Number 9, 2011

[6] B. N. Wan, et al., “Progress of Long Pulse and H-mode Experiments on EAST” (OV/2-5), 24th IAEA Fusion Energy Conference, October 8-13, 2012, San Diego, USA

[7] Liqun Hu, on behalf of EAST diagnostic team and collaborators, “Present Status of the EAST Diagnostics”, Plasma Science Technology, Vol.13, No.1, 2011, p.125-128.

*Domestic and international collaborators for the EAST: USTC, SWIP, HUST, Peking University, Donghua University, Tsinghua University, DLUT, HUT, etc. NIFS and JAEA in Japan; NFRI and KBSI in Korea; GA, PPPL, UC Davis, UCLA, UCSD, MIT, Tri Alpha Energy, FRC Austin, ORNL in USA; CEA in France, IPP Germany, etc.

Recent Progress with ICRF Heating on EAST

Xinjun Zhang[1], Y.P. Zhao[1], Y.Z. Mao[1], J.G. Li[1], B.N. Wan[1], L. Hu[1], X.Z. Gong[1], Y.T. Song[1],
Y. Lin[2], G.Taylor[3], J.M. Noterdaeme[4,5], F.Braun[4], S. Wukitch[2], R. Magne[6],
X. Litaudon[6], R. Kumazawa[7], H. Kasahara[7] and EAST Team
[1]Institute of Plasma Physics, Chinese Academy of Sciences, Hefei 230031, China
[2]MIT Plasma Science and Fu sion Center, Cambridge, MA 02139, USA
[3]Princeton Plasma Physics Laboratory,USA
[4]Max-Planck Institute for Plasma Physics, D-85748, Garching, Germany
[5]University of Gent, Belgium
[6] CEA, IRFM, F-13108 Saint-Paul Lez Durance, France
[7] National Institute for Fusion Science, Toki, Japan
Email：xjzhang@ipp.ac.cn

Radio Frequency (RF) power in the ion cyclotron range of frequencies (ICRF) is one of the primary auxiliary heating techniques for Experimental Advanced Superconducting Tokamak (EAST). The ICRF system for the EAST has been developed to support long-pulse, high-β, advanced tokamak fusion physics experiments. The ICRF system can deliver 12 MW of RF power to the plasma for 1000 seconds through two antennas located in B- and I-ports. Each ICRF transmitter with high power up to 1.5MW has been successfully tested on a dummy load. The main technical features of the ICRF system is described.
Two simulation codes, TORIC (a full wave solver) and SSFPQL (the quasilinear Fokker-Planck solver), are combined to simulate the ICRF heating in the EAST 2D magnetic configuration. The fast wave propagation and absorption characteristics, power partitions among the plasma species and the RF driven energetic tails have been analyzed.

1. Introduction

EAST is a fully superconducting tokamak (R = 1.75m, a = 0.4m, Bt = 3.5T, pulse length <= 1000 sec) being commissioned at ASIPP. Since the first plasma in 2006, much significant progress has been achieved [1-3]. Radio frequency (RF) power in the ion cyclotron range of frequencies will be one of the primary auxiliary heating techniques for EAST. With the frequency range of 25 to 70 MHz, it provides heating for the plasmas, centrally peaked current drive, and off-axis current drive using mode-conversion for various operating scenarios over a range of magnetic fields. Two different antenna designs have been produced and fabricated for the ICRF heating experiments. The main technical feature of this RF system is described in the Section 2. The optimization of the ICRF heating at 2.3T is considered by changing the resonance locations in the section 3.

2. The main technical feature of ICRF Systems on EAST

In order to satisfy the requirements of heating in EAST, A 12.0MW ICRF system with long pulse operation at megawatt levels in a frequency range of 25 to 70 MHz has been designed. The RF transmitters were tested in a matched dummy load where a RF output power of 1.5 MW was achieved. The design features for ICRF heating system is shown in table 1.

Table 1 the design feature of ICRH system

RF output power	12.0 MW
Frequency range	25-70MHz
Operation mode	Continue Wave
Transmission line	9 inch coaxial transmission line
Matching system	triple liquid stub tuners
Antenna	A two-straps antenna and a four straps antenna

The ICRF heating system is including RF transmitter [4-6], transmission line, matching system [7], feed through [8], antenna [9-11], antenna loading measurement unit, and data acquisition unit, high voltage power supply system, phase shifter, and DC breaker. Each unit is designed for continue wave (CW) operation. Fig. 1 is shows the view of the 12.0MW ICRF heating system.

Figure 1 View of 12.0 ICRH system In EAST ICRF hall

2.1 RF Power Amplifier

There are eight RF transmitter in the ICRF system. A block diagram of ICRF system with four RF transmitter is shown in Fig. 2. The RF transmitter units are shown in the section enclosed by the dotted black line. A transmitter setup includes the amplitude and frequency control and monitor unit, a RF power amplifier chain, direct current (DC) high voltage power supply (HVPS) [12-13] and cooling system. All the stages of ICRF heating system have intense cooling and can be running in continue wave (CW) mode.

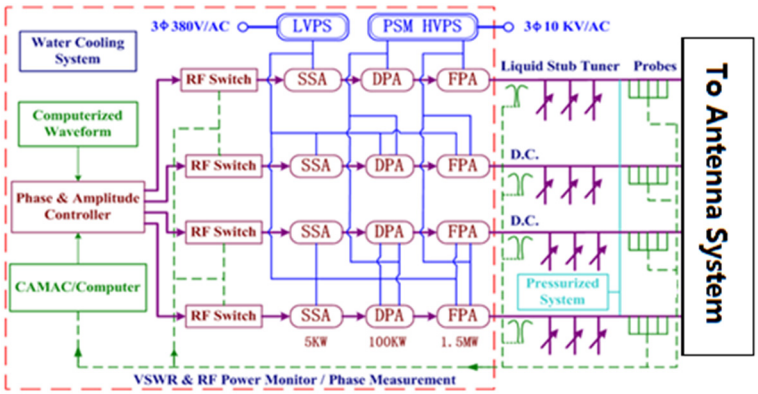

Figure 2. Block diagram of the ICRF system on EAST

Each RF power amplifier chain consists of low power stage and high power stage. The high power part includes a three-stage RF power amplifier chain, i.e. 5 kW-stage broadband solid state amplifier (SSA), 100 kW-stage tetrode drive power amplifier (DPA) and 1.5 MW-stage tetrode final power amplifier (FPA), tunable from 25 MHz to 70 MHz. The powerful tetrodes (TH535, TH525) are used for DPA and FPA.

Transmitter tests were conducted with a matched dummy load over a frequency range from 24 MHz to 70 MHz in steps of 1 MHz. Fig. 3 shows the test results of three transmitters. An averaged maximum RF output power of 1.5 MW was achieved in a frequency range of 25 MHz - 65 MHz with an efficiency varying from 60 to 70 percent.

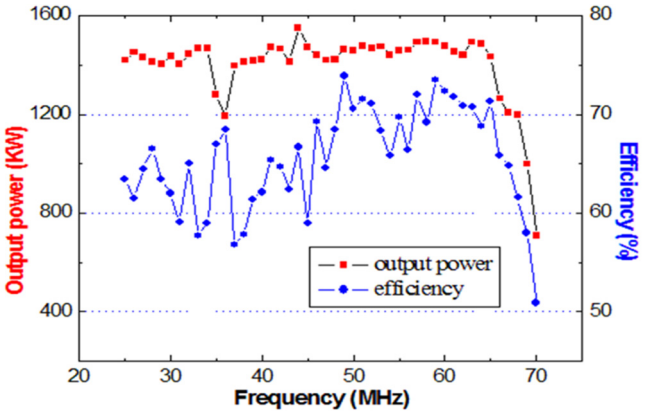

Figure. 3 High power tests of the RF transmitter over the frequency range from 24 MHz to 70 MHz. The averaged RF output power of 1.5 MW was achieved with an efficiency of about 60~70 percent in the frequency range of 25~65 MHz

2.2 The transmission line and RF matching system

To satisfy high power transfer from the transmitter to the antenna, the transmission line size is 9 inch, as shown in Fig 4. Its outer conductor diameter is 230 mm, and inner conductor diameter is 100 mm. The characteristic impedance is 50Ω. Between inner and outer conductor, the dry nitrogen gas is filled at the pressure of 3 atm. To satisfy the CW operation, the inner and the outer conductor must be cooled by the pure water. A DC breaker [14] has been used to isolate the grounds between RF transmitter and the antenna.

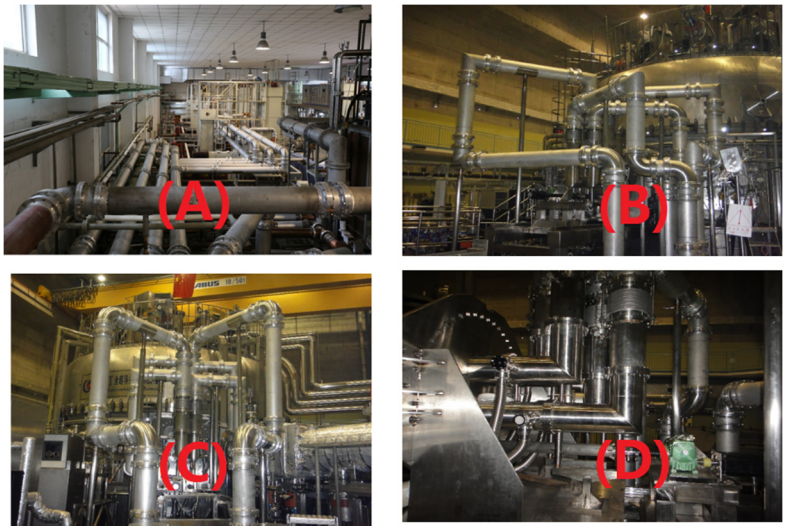

Figure 4 View of the transmission lines: (A) in the ICRH Hall; (B-D) in the EAST Hall

There are eight set of triple liquid stub tuners for EAST 12.0MW ICRF heating system. The stub tuner

is a short-circuited coaxial transmission line with a changeable length. Because the metal contact finger of conventional stub tuner is seriously damaged sometimes, we develop a liquid stub tuner for EAST [7]. It utilizes the difference of radio frequency wavelengths in gas and in liquid due to the different relative dielectric constants. The liquid (i.e. oil silicon) is filled between inner conductor and outer conductor. By using a pump to control the liquid level, the parameters of this matching system can be changed. Since there is no mechanically moving parts, it works more reliable.

2.3 ICRF Antenna systems

There are two ports for ICRF in EAST, as shown in figure 8. Phase between the straps is controlled in the low power parts of the RF system. For long pulse operation, the antennas have many cooling channels inside the current strap, cavity wall, the faraday screen and vacuum transmission line. In order to adjust the coupling of the antenna to plasma, the antenna can be moved a little in radial direction. The current straps located 10mm from the back surface of the Faraday screen. The front surface of the faraday screen is located 5mm from the limiter. The material of the strap is stainless steel 316L. Their edge is rounded to reduce the electric field strength around the current strap. The faraday screen is designed as water cooled and single layered tube. The material of the tube is also stainless steel 316L. The faraday screen of the antenna has be coated by B4C to reduce the impurity radiation during the high power ICRF heating.

The ICRF antenna at B port is grounded at the center and have a coaxial feed line connected to each end of the current strap, as shown in Fig.5 (right). The ICRF antenna at I-port have four current straps. The antenna are folded, end grounded with a central current feed, as shown in Fig.5 (left). Four 1.5MW RF transmitter is attached to each antenna. Phase between the straps is controlled in the low power parts of the RF system.

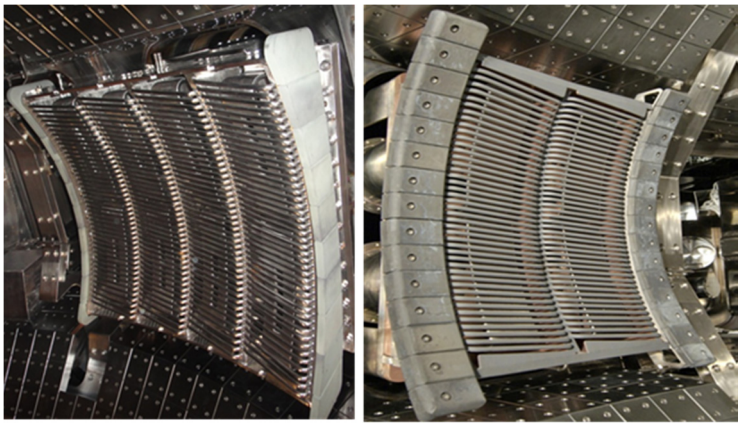

Figure 5 The ICRF antenna systems: Four-strap antenna at I-port(left), Two-strap antenna at B-port(right).

3. Optimization study of ICRF Hydrogen minority heating in a Deuterium plasma

Two simulation codes, TORIC (a full wave solver) [15] and SSFPQL (the quasilinear Fokker-Planck solver) [16], are combined to simulate the ICRF heating in the EAST 2D magnetic configuration. The combined code is applied to the ICRF minority heating of hydrogen in a deuterium plasma with the minority concentration of X[H] up to 10%. The fast wave propagation and absorption characteristics, power partitions among the plasma species and the RF driven energetic tails have been analyzed. ICRH minority heating of hydrogen in a deuterium plasma are evaluated with the combined code and optimized for reaching the enhanced minority ion absorption, which could be used to achieve dominant electrons heating in EAST D

plasmas. Our results confirms that D (H) minority heating could be effective for such high H minority concentrations as~10% being beneficial for lowering the minority tail energy and increasing thermal ions heating. Quasi-linear calculation shows that H minority tails mainly heat bulk electrons. Meanwhile, the power transferred to bulk electrons decreases while increasing the H concentration. Contrarily, increasing the coupling power increases the power partition among bulk electrons.

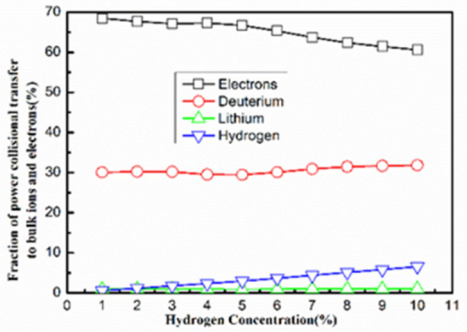

Figure 6. The effect of the hydrogen concentration: The energy of minority tails is mainly transferred collisional to bulk electrons

4. Summary

In conclusion, a 12.0MW ICRF heating system at 25–70 MHz has been successfully commissioned at full power on water dummy load. An averaged maximum RF output power of 1.5 MW was achieved in a frequency range of 25 MHz - 65 MHz with an efficiency varying from 60 to 70 percent. The ICRF system will deliver more than 10.0 MW of RF power to the plasma for long pulse length up to 1000 sec. Detailed simulations have been performed in order to assess the validity of the hydrogen Minority heating scheme (D(H)) to heat EAST plasmas at central magnetic field B_0~2.3T. As expected, the simulations results shows that the H minority heating scenario should give rise to significantly better electron heating.

Acknowledgments

The authors would like to acknowledge the support of the EAST operation and diagnostics group. This work was supported partly by National Magnetic confinement Fusion Science Programme (grant no. 2010GB110000). This work was also supported partly by the National Natural Science Foundation of China under grant no.11105179, and 11175208. This work was partly supported by the JSPS-NRF-NSFC A3 Foresight Program in the field of Plasma Physics (NSFC: No.11261140328, NRF : No. 2012K2A2A6000443)

References

[1] Wan B.N. et al., Fusion Eng. Des. 85(2010) 1048.
[2] Wan B.N. and International Collaborators Nucl. Fusion 49(2009) 104011.
[3] Jiangang Li et al., Nucl. Fusion 51 (2011) 094007
[4] H.L. Zhao et al. Nuclear Electronics& Detection Technology 2010 30 239
[5] G.Chen et al Nuclear Fusion and Plasma Physics 2010 30 67
[6] Y.Z.Mao et al Plasma Science and Technology, 15. 2013 261
[7] P.Wang et al Nuclear Fusion and Plasma Physics 2005 25 278
[8] Q.X.Yang et al Plasma Science and Technology 2011 13 252
[9] Q.X.Yang et al Atomic Energy Science and Technology 2011 45 711
[10] Q.X.Yang et al Nuclear Fusion and Plasma Physics 2011 31 46
[11] C.H.Wang et al Nuclear Fusion and Plasma Physics 2010 30 250
[12] S.Yuan et al Power Supply Technology 2010 32 82

[13] L.Wang et al Atomic Energy Science and Technology 2009 43 935
[14] J.K. Xu et al Nuclear Electronics& Detection Technology 2012 32 489
[15] Brambilla M. 1999 Plasma Phys. Control. Fusion 41 1
[16] Brambilla M. 1994 Nucl. Fusion 34 1121

Ionic Plasmas in Caesium Seeded Negative Ion Source for NBI

K. Tsumori, H. Nakano, M. Kisaki, K. Ikeda, K. Nagaoka, M. Osakabe, Y. Takeiri, O. Kaneko, M. Shibuya, T. Kondo, M. Sato, H. Sekiguchi and S. Komada

National Institute for Fusion Science, 322-6 Oroshi Toki city Gifu 509-5292, Japan

e-mail: tsumori@nifs.ac.jp

ABSTRACT

Characteristics of ionic plasmas produced in beam extraction region of a R&D negative ion source for with the size of NBI are reported. A multi-diagnostic system consisting of a Langmuir probe, cavity ring-down, millimeter-wave interferometer, optical emission spectroscopy and Hα CCD spectroscopy is applied for the investigation of the particle dynamics in the ionic plasmas. The ionic plasmas are produced by seeding caesium (Cs) in the plasma generator of the source without beam extraction, and electrons compensate the lack of the extracted hydrogen negative ions to conserve the charge neutrality during beam extraction. The influence of the applied extraction field affects deeply into the plasma at extraction region.

Introduction

Large-scaled hydrogen negative ion (H^-) sources have been adopted for NBIs to obtain higher neutralization efficiency in the beam energies more than 100 keV [1]. To achieve the negative-ion-based NBIs, high performance negative ion sources have been developed and applied for actual beam injections in NIFS and JAEA [2-4], and RF-driven source is developed for ITER injectors [5, 6]. In order to enhance H^- ions, small amount of Cs vapor is seeded in the hydrogen plasmas generated in the ion sources. Seeded Cs absorbs on the inner metallic wall of source-plasma generator and reduces the workfunction. The H^- ions produced on so-called plasma grid, which separates the source-plasma generator and beam accelerator, are extracted effectively. The surface-produced H^- ions orient to the opposite direction of the beam direction. The first question is what kind of the mechanism takes place to turn the direction of H^- ions. Seeded Cs also reduces a current ratio of extracted electron to H^- ion in the factor of ~10. The current ratio is ~25 % in optimal Cs seeding, and this indicates a density ratio of electron to H^- ion in the beam extraction region is ~0.6 %! The second question is why the electron is reduced the density in the extraction region. Understanding those mechanisms has a possibility to increase the H- current as well as to reduce the electron current more effectively. In order to investigate the mechanisms, we have started an experiment using multi-diagnostic system, which consists of a Langmuir probe, cavity ring-down method, millimeter wave interferometer, optical emission spectroscopy (OES) and Hα CCD measurement, to

measure the dynamics of charged particles in the extraction region. In the article, we report our experimental results.

Experimental Setup

A R&D negative ion source installed at NIFS NBI teststand has been applied in this experiment. The inner volume of the plasma generator is the half value of the LHD-NBI source. The H^- beams ate formed with two segmented accelerator modules, which is two fifth area of the LHD-NBI source. The diagnostic system is lifted on the high voltage stage and the measurement is available during beam extraction.

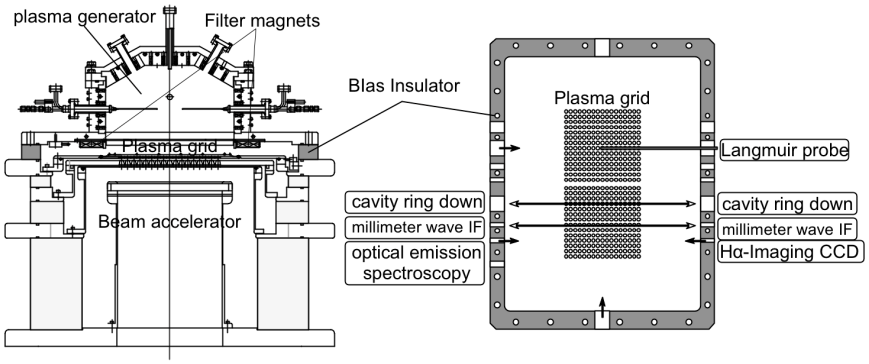

Figure 1. Schematic view of NIFS R&D negative ion source (left hand side) and the plane view of the ion beam extraction region (right hand side)

Schematic view of the R&D ion source and a plane view from the source back plate are shown in Fig. 1. Plasma at extraction region between a pair of filter magnets and plasma grid affects beam characteristics, and diagnostic devices are installed at the sidewalls of the bias insulator. Input arc power is fixed at 50 kW in this experiment.

Experimental Result

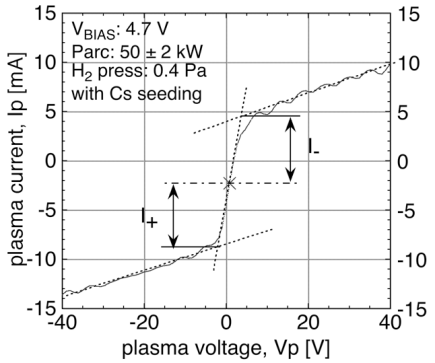

Figure 2. Hydrogen ionic plasma obtained in the Cs seeded negative ion source. The positive and negative currents are indicated as I_+ and I_-, respectively.

By seeding Cs vapor in the plasma generator, H^- current increases and electron current is reduced simultaneously. Electron saturation current measured with Langmuir probe decrease monotonously after starting the Cs seeding, and V-I curve of the probe becomes very symmetric as shown in Fig. 2. The asymptotic lines in the both limit of positive and negative probe voltage are parallel, and this shows quite low electron density is included in the plasma; the ionic plasma is produced in the extraction region. The ionic plasma is reproduced every time with Cs seeding. Although the bias voltage and H_2 gas pressure, which are positively applied to the plasma grid against the arc chamber, are slightly higher than that of the LHD ion source, reduction of the electron current can be explained with this result. In the ionic plasma,

electron density is lower than negative ion current, and here the saturation current measured from the inflection point in Fig. 2 is defined as "negative saturation current" at applying positive probe voltage.

Beam extraction voltage is not applied in that experiment, and difference of the characteristic of the plasma at extraction region is measured with and without applying beam extraction voltage. The changes with and without beam extraction are shown in Fig. 3. In this figure, the H_2 gas pressure is decreased from left to right graphs. Waveforms of negative and positive saturation currents measured with Langmuir probe in upper graphs and the H^- density by means of cavity ring-down (CRD) method [7] is indicated lower ones. The extraction voltage is applied from the time of 0 sec to 1 sec. The negative saturation current increases and the H^- density decreases during beam extraction. The differences are increase by decreasing the H_2 gas pressure. Electron density and energy in the extraction region become lower as increasing the gas pressure, and the result is consistent to the change of negative saturation current with respect to the gas pressure. The density of positive ions is considered not to change during beam extraction, and electrons diffuse on the filament side to compensate the charge density of extracted H^- ions [8, 9].

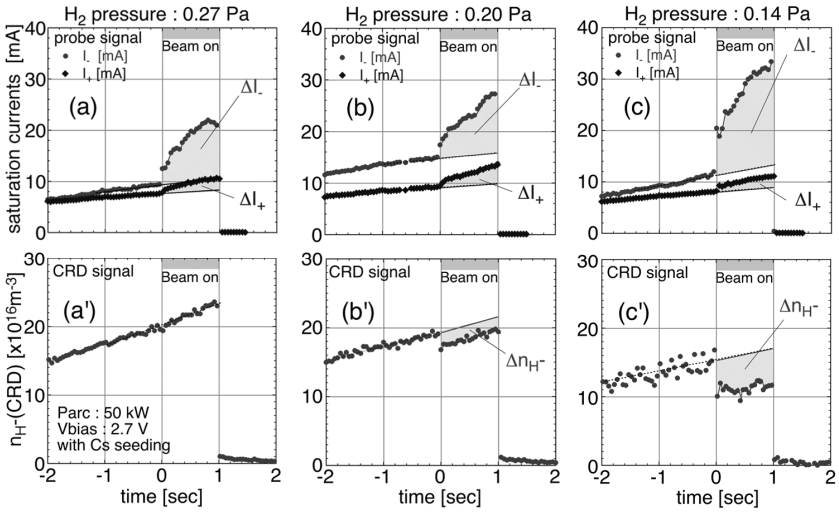

Figure 3. Waveforms of negative and positive saturation currents are shown in the upper row and the H^- densities measured by means of the CRD system are indicated in lower row. The H_2 pressures are 0.27 Pa, (a) and (a'), 0.20 Pa, (b) and (b'), and 0.14 Pa, (c) and (c'). The H^- beam is

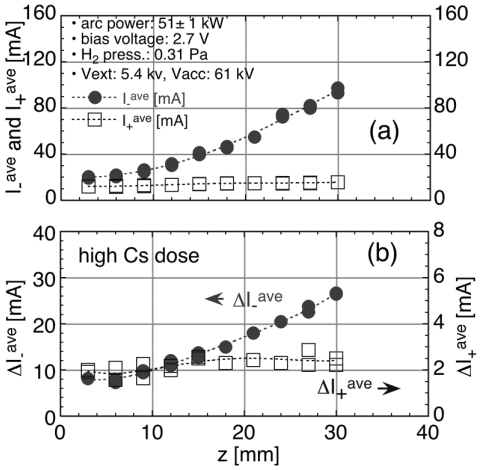

Figure 4. Spatial distribution of the positive and negative saturation currents (I_+^{ave} and I_-^{ave}, respectively) in the direction normal to the PG surface, and (b) current increments during beam extraction (ΔI_+^{ave} and ΔI_-^{ave}, respectively).

Spatial distribution of the positive and negative saturation currents are shown in Fig. 4 with the increments of those currents during beam extraction. The graphs in Fig. 4 (a) indicates ionic plasma is localize near plasma grid with the distance of ~10 mm apart from plasma grid and the electrons increase as increasing the distance. In this case, bias voltage and H_2 gas pressure are not sufficiently optimized for production of ionic plasma but for actual beam injection. Increments of both saturation currents show the similar tendency to the Fig. 4 (a), and this suggests the beam extraction field has the influence in the large distance of the extraction region. In other words, H- ions are extracted

from wide distance in the extraction region. Measurement by means of Hα CCD spectroscopy shows the 2-dimensional distribution of the extracted H^- density and, is consistent to the result obtained with Langmuir probe [8, 10]. In the RF-negative ion source, the H^- ions are considered originated from the direct reflection of the parent particles of H^- ions, proton and H^o, on the conical part of the plasma grid. In this case, the influence of the extraction field should be limited at very vicinity of the plasma grid. Our result suggests the plasma characteristics and mechanism of H^- productions in the filament-arc and RF ion sources are different.

Conclusion

In the Cs-seeded negative ion source for NBI, the electron density is expected ~0.6 % of H^- density from the estimation of extracted currents. The measurement combining a Langmuir probe and CRD method shows the generation of ionic plasma and the result is consistent with the extremely low electron density obtained from the estimation. A Langmuir probe and Hα CCD spectroscopy are applied to measure the distribution of extracted H- ions. From the results obtained by means of those measurements, we can conclude the H^- ions extracted widely from the extraction region, though the mechanism of H- ions to turn the initial direction.

Acknowledgement

The authors would like to acknowledge the continuous encouragement of Prof. Dr. A. Komori, Director General of NIFS. One of the authors (KT) would like to express the appreciations to Prof. Dr. A. Hatayama of Keio University, A. Ando of Tohoku University, Prof. Dr. Wada of Doshisha Univ, Dr. W. Oohara of Yamaguchi Univ, Dr. A. Kojima and Dr. M. Hanada of JAEA for their fruitful discussions.
This work was partly supported by the JSPS-NRF-NSFC A3 Foresight Program in the field of Plasma Physics (NSFC: No.11261140328, NRF: No. 2012K2A2A6000443) and also supported by JSPS KAKENHI Grant Number 25249134 and the budget for the NIFS No.ULRR702 and No. ULRR009.

References

[1] K. H. Berkner, R. V. Pyle and J. W. Stearns, *Nucl. Fusion*, **15**, p. 249 (1975).

[2] Y. Okumura, M. Hanada, T. Inoue, H. Kojima, Y. Matsuda, Y. Ohara, Y. Oohara, M. Seki, Y. Suzuki and K.Watanabe, *Proc. 16th Symp. Fusion Tech*. London UK, Sept. 3-7, 1990, **2**, 1026 – 1030 (1990).

[3] O. Kaneko, Y. Takeiri, K. Tsumori, Y. Oka, M. Osakabe, R. Akiyama, T. Kawamoto, and E. Asano, *Proceedings of the 16th IAEA Fusion Energy Conference*, Montreal, Canada, 7–11 October, **3**, p. 539, (1996).

[4] Y. Takeiri, O. Kaneko, K. Tsumori, Y. Oka, M. Osakabe, K. Ikeda, E. Asano, T. Kawamoto, and R. Akiyama, *Rev. Sci. Instrum*, **71**, 1225– 1230 (2000).

[5] P. Franzen, H.D. Falter, U. Fantz, W. Kraus, M. Berger, S. Christ-Koch, M. Fröschle, R. Gutser, B. Heinemann, S. Hilbert, S.

Leyer, C. Martens, P. McNeely, R. Riedl, E. Speth and D. Wünderlich, *Nucl. Fusion*, **47**, 264–270 (2007).

[6] R. Hemsworth, H. Decamps, J. Graceffa, B. Schunke, M. Tanaka, M. Dremel, A. Tanga, H.P.L. De Esch, F. Geli, J. Milnes, T. Inoue, D. Marcuzzi, P. Sonato and P. Zaccaria, *Nucl. Fusion,* **49**, 1-15 (2009).

[7] H. Nakano, K. Tsumori, K. Nagaoka, M. Shibuya, U. Fantz, M. Kisaki, K. Ikeda, M. Osakabe, O. Kaneko, E. Asano, T. Kondo, M. Sato, S. Komada, H. Sekiguchi and Y. Takeiri, *Proceedings of 2nd International Symposium on Negative Ions, Beams and Sources*, Takayama Japan, *AIP Conf. Proc.* **1390**, pp. 359-366 (2010).

[8] K. Tsumori, H. Nakano, M. Kisaki, K. Ikeda, K. Nagaoka, M. Osakabe, Y. Takeiri, O. Kaneko, M. Shibuya, E. Asano, T. Kondo, M. Sato, S. Komada, H. Sekiguchi, N. Kameyama, T. Fukuyama, S. Wada, and A. Hatayama, *Rev. Sci. Instrum*. **83**, 02B116 (2012).

[9] K. Tsumori, O. Kaneko, Y. Takeiri, M. Osakabe, K. Ikeda, K. Nagaoka, H. Nakano, M. Shibuya, E. Asano, T. Kondo, M. Sato, S. Komada and H. Sekiguchi, *Proceedings of 3rd international symposium on Negative Ion, Beams and Sources,* September 3-7, 2012 Jyvaskyla, Finland, *AIP conference proceedings*, 1515 (2012) pp.149-156.

[10] K. Ikeda, H. Nakano, K. Tsumori, M. Kisaki, K. Nagaoka, M. Osakabe, Y. Takeiri, and O. Kaneko, *Rev. Sci. Instrum*. **85**, 02A724 (2014).

Status and plan of KSTAR plasma control system for steady-state operations

Sang-hee Hahn
National Fusion Research Institute, Daejeon, Korea
Email: hahn76@nfri.re.kr

1. Introduction

Concept of steady-state tokamak discharge [1] has been introduced many years before: The steady-state discharge should have a pulse length that is long enough not only to satisfy demand of daily power productions, but also to sustain steady fusion performance which could reduce thermal/mechanical stress expected to the device. Even the concept was apparent, practical transition to a short pulse to a steady-state one was not achieved until a few tokamaks were equipped by full superconducting (SC) magnets, which led to great reduction of electric power requirement for the required toroidal field (TF) sustainment. In 2013 experiment, KSTAR successfully demonstrated an Ip=0.5 MA, H-mode plasma discharge over 20 seconds using SC magnet system and conventional magnetic controls existing at KSTAR. In order to sustain the plasma in better performance regime, however, development on the real-time kinetic performance control is required. Key themes for the KSTAR include a direct kinetic output control on plasma energy, a real-time Te profile feedback and an integrated MHD controller using Electron Cyclotron Heating/Current Drive.

2. Status of long-pulse capable magnetic control system upgrade

In principle, Feedback control usually enables control unlimited in timescales: limitation of operating time for a feedback computer usually comes from limitation of memory, and data acquisition. For mid-size tokamaks, the required sampling on dealing with MHD-related events (VS, TM, Sawtooth, et cetera…) is more than 10 kHz, which is not a small amount of data, but downsampling is not a practical solution for post-experiment analysis for the feedback control. KSTAR plasma control system hardware uses a Linux kernel hack as the Operating system (OS) for synchronizing the system with the externally provided clock (1Mhz): the technique enabled an extendable cluster system capable of 50 kHz control cycle, but isolation from the data acquisition network during the shot inhibits extension of the maximum pulse length. Efforts of migrating the real-time OS into ITER-compatible standard

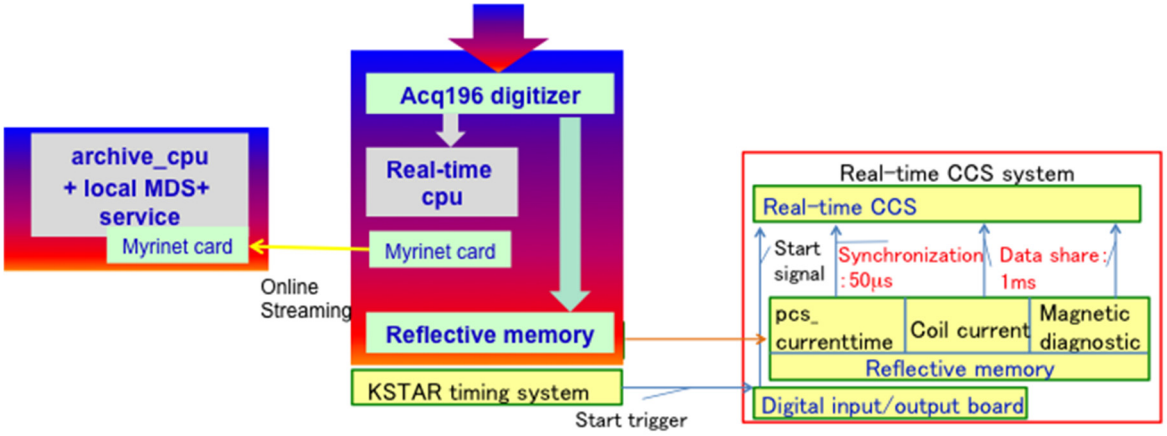

Figure 1. long-puse related system development: A dedicated MDS+ data stream archiving by Myrinet card network / an independent real-time magnetic reconstruction system using real-time data share by Reflective memory net.

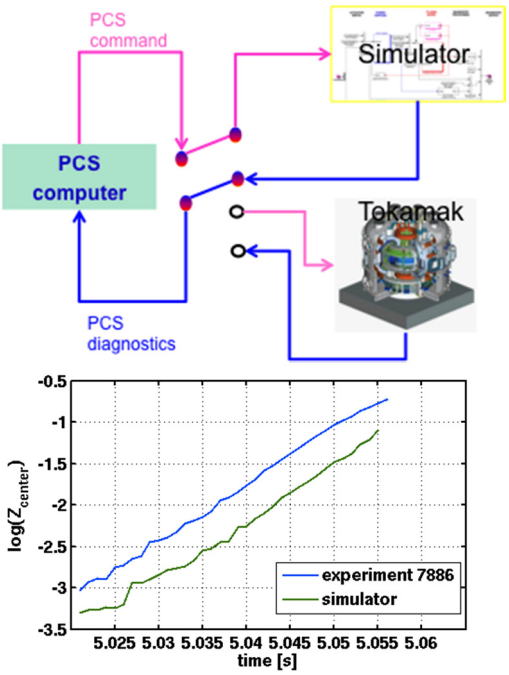

Figure 2. Closed-loop magnetic control simulator environment and its validations: KSTAR simulator provides the same virtual interface for control diagnostics as the real hardware provides (top). Comparison of open-loop vertical growth on experiment in 2012 and the simulator output (bottom).

operating system (MRG-realtime, developed by RedHat and the accelerator community) are ongoing project until 2015. Dedicated performance test showed that a real-time CPU can deal with up to 100 kHz cycle in Feb 2014 [2].

Enabling an online MDS+ data streaming via dedicated real-time network (Myrinet in Figure 1) is introduced also as an alternative way to archive data in unlimited pulse length. KSTAR hardware was confirmed to use 5 kHz to store up to +3000 MDS+ samples for ~80 seconds without missing a time stamp.

Real-time data sharing in KSTAR is achieved by customized Reflective memory (RFM) [3] network. The RFM provides a very fast, and deterministic data sharing up to 256 systems. For sharing magnetic diagnostics measurements for independent system, we implemented a direct PCI bus streaming from 2x96-channel acq196 [4] digitizers to an RFM card. The system provides 192 Channels x 4 kHz simultaneous streaming of raw digitized data to independent system hardware, and was used for implementing the real-time Cauchy Condition Surface (CCS) reconstruction system as collaboration topics with JT-60SA plasma control group [5].

Based on the analysis done in 2012, the effective plasma resistance (Rp) eventually increases as the shot extends. The Rp increase would require more loop voltage, The preprogrammed coil trajectory usually assumes constant Vloop, hence the designed gain set on Ip & shape in the earlier part of discharge may not be suitable if the deviation becomes too big.

In order to incorporate with time-varying plasma resistances for longer pulses, a PCS algorithm has been implemented in order to identify best PF currents for the Rp and the desired shape [6]. The algorithm decomposes the PF current into ohmic and shape vectors. Based on automatically calculated plasma resistance, the PCS computes best FF current values per each coil every 100 milliseconds. The logic has been confirmed by the existing magnetic control simulator, and hardware simulation tests were done under KSTAR hardware during the visit of related GA scientists. The experimental application will commence in the 2014 campaign.

Development of simulation technique and environment is especially necessary, because the tokamaks with superconducting magnets have longer preparation time, mainly due to magnet cool-down conditioning [7], and the between-shot interval cost for longer pulses that are generated by accumulation of the superconducting coil AC losses. In order to design better pulse design, a closed-loop magnetic control simulator [8] has been implemented in 2012 that can simulate virtual interface for magnetic control diagnostics. A measurement on open-loop vertical growth rate provides minimum validation on the conductor model in the simulator. As shown in Figure 2, 2012 experiment showed a very good match with the simulation result for vertical position growth rate (slope of the curve). The closed-loop PCS magnetic control simulator was updated to reflect this open-loop vertical growth rate obtained

by dedicated experiments.

3. Status and plan on kinetic/profile controls

Kinetic performance can be mainly controlled by plasma heating. Until 2013, PCS did not have any control to any heating devices available at KSTAR. With dedicated organization for PCS, integration of heating power control has been initiated with the NBI and ECH for multiple purposes: the beta feedback control has been addressed as the main purpose of NBI integration into PCS in order to maintain plasma energy and to achieve reactor-relevant higher performances easier. The algorithm is a simple PID using an online plasma β_p estimator using dedicated magnetic diagnostics: The PID output gives total power required to NBI, and is divided to the individual ion source as a form of pulse width modulation (PWM) target. The first commissioning of each NB power control algorithm was done in June 2014, and the use of β_p feedback is planned in the same year.

A first attempt of radial Te profile control is done in 2013 by collaboration with Seoul National University (SNU). Based on a simplified transport model in [4], a feedback system using real-time ECE data streaming and 110GHz ECH was constructed. Since KSTAR does not have any q-profile diagnostics, the feedback target was set to only ECE Te profiles at rho_pol = 0.1, 0.2, 0.3, 0.4 and 0.5. Schematic for the real-time system is shown in Figure 3, using EPICS CA for ECE streaming and real-time EFIT flux labels at midplane through the KSTAR RFM network. The control cycle was set to 0.5 seconds, and sent the EC power demand to ECH every cycle. The controller has been commissioned successfully in 2013. Result of this feedback control is shown in Figure 3 for an L-mode plasma #9386, at Ip = 0.6 MA, BT = 2.0 Tesla, PNB = 1.0 MW, Te baseline ~ 1.9 keV. In L-mode discharge, it has been verified that the controller does not have hardware problems and the Te profile seems to slowly approach to its desired target, but the available power of the actuator (EC 110 GHz) is rather limited (<150 kW) to see faster responses.

There is an ongoing activity for implementing integrated controller of MHD using ECH/CD as main actuators. Since the tearing modes (TM) and neoclassical tearing (NTM) will become a candidate of obstacles for both the high performances and the long pulses, a large plan for making active suppressions to this specific exception is ongoing at KSTAR aiming at 2015-16, as shown in Figure 4, which targets suppression of the NTM and sawtooth period controls.

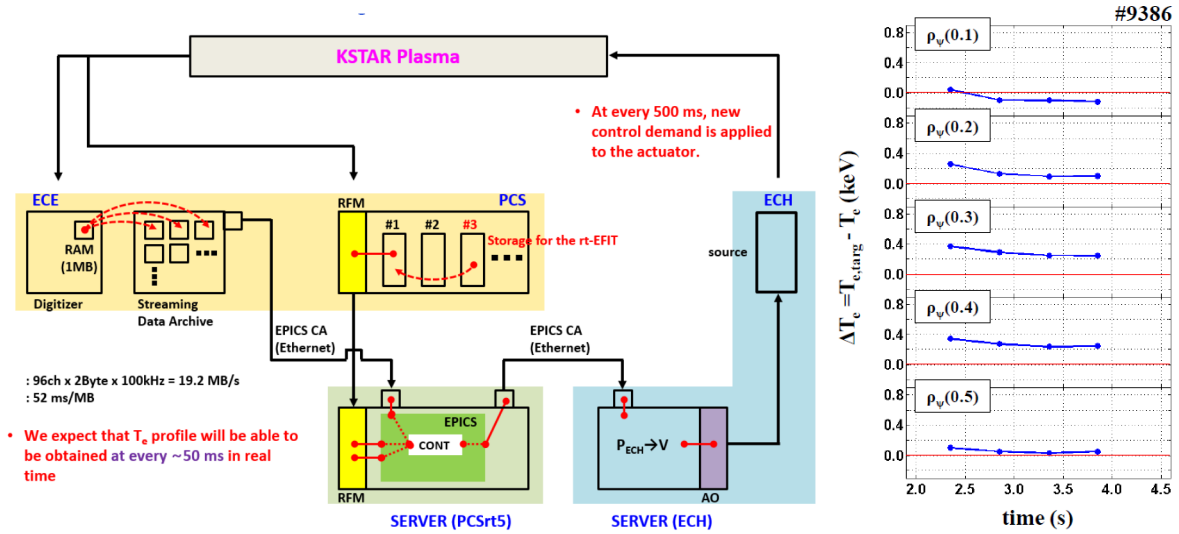

Figure 3. (left) Schematic diagram for SNU-implementation of real-time Te profile control + EC 110 GHz in 2013. (right) Time evolution of Te errors by ~100 kW EC110 at t=3.0s.

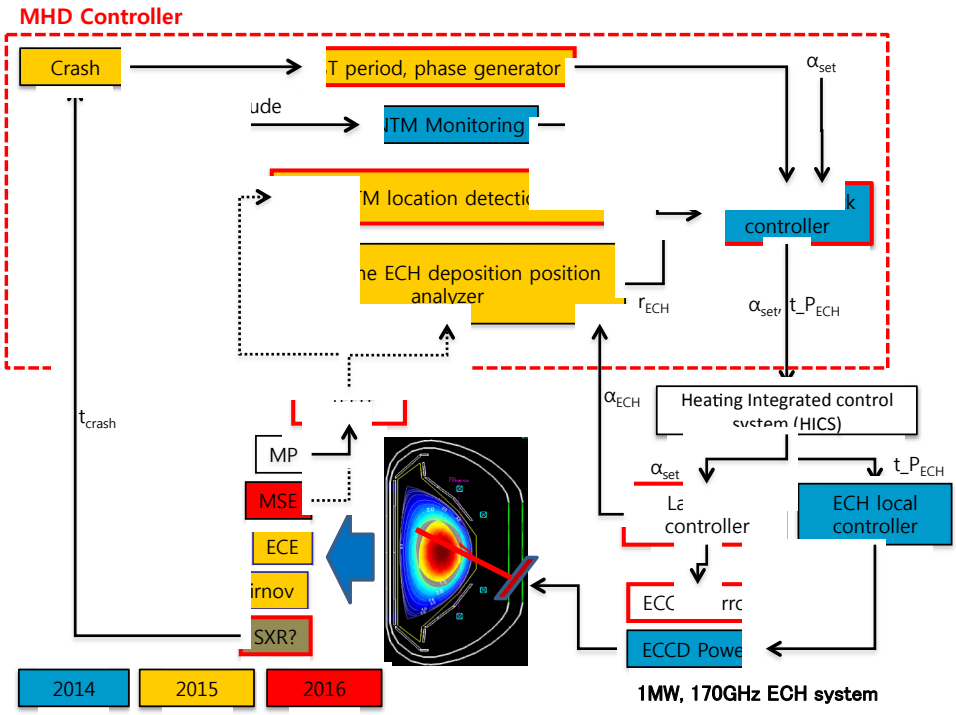

Figure 4. A 3-year plan for the real-time MHD controller featuring TM/NTM suppressions and sawtooth period-locking.

Without any real-time detection of the mode location, the first experiment was executed by a preprogrammed angle scan in 2013. Although the old PLC-based control system had big time delays (~100 ms), a partial suppression of the MHD mode is found using 0.8 MW of EC 170 GHz power at #9133 [10]. The experiment indicates that the Mirnov coil mode amplitude (dB/dt divided by frequency spectrum maxima) can be used as a primary MHD mode detection method. The speed upgrade of the motor controller system into FPGA-based one is done with the time delay ~20 ms.

In September 2014, power on/off control to the gyrotron and real-time feedback on poloidal mirror angle of EC170 GHz has been verified during the plasma commissioning. Before the package is fully implemented, a preliminary feedback system using only a single channel of the Mirnov coil is planned in 2014: The Mirnov and its mode amplitude gives a criterion of starting the suppression logic by turning on the EC power. Since we do not know the exact location, the PCS will move the mirror back and forth around a predetermined position (Z0) to search the best position where the mode amplitude starts decreasing.

A dedicated SW development contract with General Atomics is made in order to add Neoclassical Tearing Mode (NTM) control algorithm until mid 2015. The package will include a feedback algorithm that operates on mode amplitude and plasma density signals to produce on/off commands to gyrotrons and commands to mirrors that define mirror angles, active tracking logic using feedback regulation to maintain a specified alignment based on real-time (RT) q-profile estimates generated by RT EFIT, and a search-based alignment algorithm enabling automatic identification of adequate alignment in absence of direct measurement of island or q- profile.

Acknowledgement

This research was supported by Ministry of Science, ICT, and Future Planning under KSTAR project and was partly supported by the JSPS-NRF-NSFC A3 Foresight Program (NRF No. 2012K2A2A6000443).

References

[1] Lister, J.B. et al., Nucl. Fusion, 40(6), pp.1167–1181 (2000).
[2] Y.J. Kim et al., "*Performance test of new real time plasma control system (PCS) server environment based on MRG-R*", poster presentation in 2014 KSTAR conference (2014).
[3] A product of GE Fanuc.com. For performance details, see table 2 at S. Hahn et al., Fus. Eng. Des., 84, 867-874 (2009).
[4] A product of D-TACQ co. Ltd, http://d-tacq.com
[5] Miyata, Y. et al., Physics of Plasmas, 21(3), p.032502 (2014).
[6] Walker, M.L. et al., "*On-line calculation of feedforward trajectories for tokamak plasma shape control*", In 44th IEEE Conference on Decision and Control, pp. 8233–8239 (2005).
[7] Y.-K. Oh et al., Fusion Engineering and Design, 84(2-6), pp.344–350 (2009).
[8] Sang-hee Hahn et al., Fusion Engineering and Design, 89, 542-547 (2014).
[9] S.H. Kim et al., Nucl. Fusion 52 074002 (2012).
[10] M. Jeong et al., "*Research Activity on Real-Time NTM Control in KSTAR*", presentation of the 4th A3 foresight program workshop, Nov 2013.

Status of the MG installation and the result of the dummy load commissioning

Chang-Hwan Kim, Dae-Young Eom, Seong-lok Hong, Nam-Yong Joung, Jong-Dae Kong

National Fusion Research Institute, Daejeon, Korea

Email : kch2004@nfri.re.kr

1. Introduction

The Korea Superconducting Tokamak Advanced Research (KSTAR) Motor Generator (MG) system has been installation. It is a device which supplies large amount power to the Poloidal Field Magnet Power Supply (PF MPS) for maximum 300 seconds. In the 300 seconds operation scenario in every one hour, the peak reactive power is reached 160 MVA. But the available grid power is only 100MVA at the National Fusion Research Institute (NFRI) site. Also flicker phenomenon may be occurred because PF MPS uses large power for a short time. MG was considered, designed and installed as a method of resolving such problems. Therefore if the MG is operated with a Reactive Power Compensation (RPC) system which is currently used, it will be possible to supply power more stably. Figure 1 shows the entire power system for the KSTAR including the MG power system and RPC system [1].

The components of the MG system are the generator, Variable Voltage Variable Frequency (VVVF) and Excitation system. After installing the MG, individual and linkage commissioning were conducted to determine the stability and performance of the MG system before the superconducting coil commissioning. The main purpose of the superconducting coil commissioning is to check a stable supply of required power by the operation of MPS in the superconducting state. Therefore this test will be performed in the last section of 2014 KSTAR campaign.

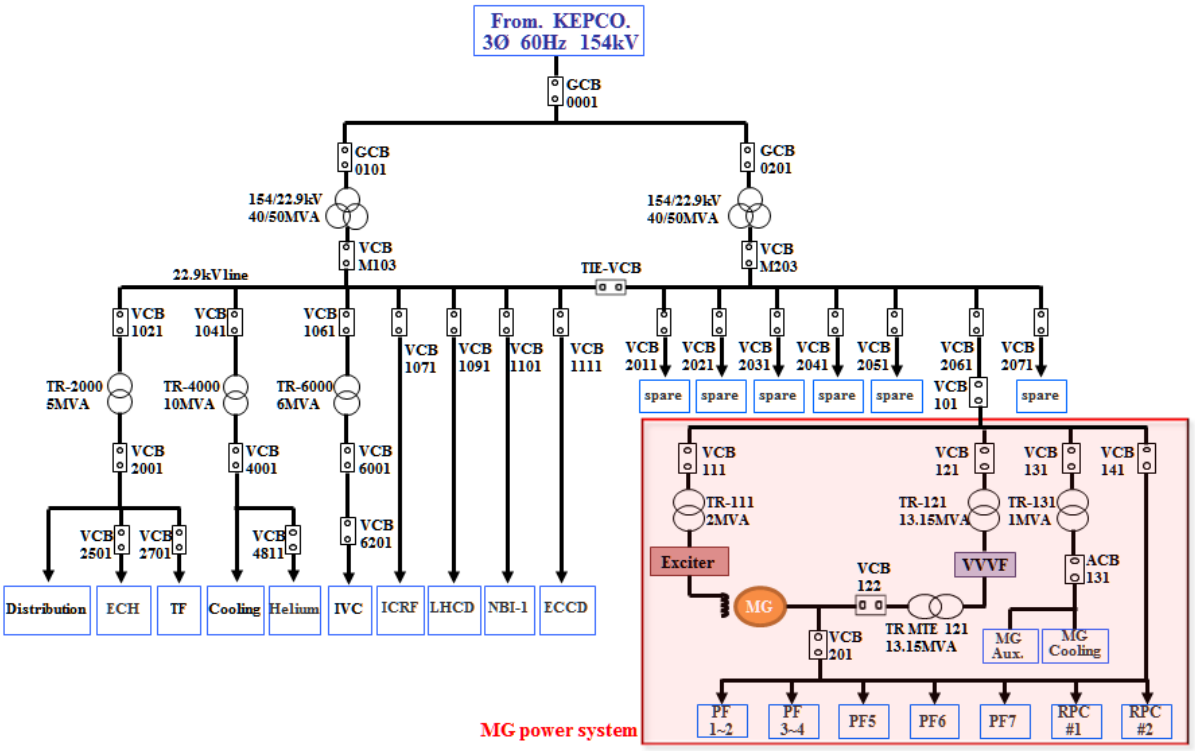

Figure 1. The KSTAR power system

2. Installation of the MG system

The functions of the individual components are VVVF to the MG speed and frequency, excitation system to regulate the voltage, RPC & HF system to remove the harmonics, and cooling facilities to supply cooling water to each device. The nominal operating power of the MG system is about 17.7 MVA from the 154 kV systems. The MG system could deliver power and energy of 200 MVA, 1.6 GJ required by the PF MPS to operate at full rating. [1] The specifications of KSTAR MG system is shown as Table 1.

Table 1. The specifications of MG system

Generator		**VVVF**	
Type	Vertical type	Capacity	12 MVA
Pole	14 pole, Salient pole	Rated Output Voltage	3.3 kVac
Capacity	200 MVA	Rated Output Current	2,100 A
Rated speed	480 ~ 548.5 RPM	Control Method	Inverter, PWM
Winding	3 Phase, Y Connected	Output Frequency	0~64 Hz
Rated Voltage	22.9 kVac	**Excitation system**	
Rated Current	5,042 A	Rated Output Capacity	954 kW
Weight	563 ton	Rated Output Voltage	580 Vdc
Stored energy	2,193 MJ(at 548.5 RPM)	Rated Output Current	1,645 A
Inertia. WR^2	$1.33X10^9$ kgm^2	Control Method	Converter, 6 pulse

The generator is consists of three parts (stator, rotor, and bearing). The generator is a capacity of 200 MVA, a vertical type, has 14 poles and the total weight is 563 ton. The VVVF is an inverter which has a capacity of 12 MVA, and control the frequency within 0~64 Hz range. The excitation system is a 6 pulse converter of 2 MVA capacities. The generator assembly states of each part are shown in figure 2. Especially, the KSTAR MG system does not have pony motors used to accelerate the generator. The motoring and generating is carried out by controlling the VVVF and excitation system. The VVVF supplies active power to the MG during the motoring and rotational speed is controlled. The rated voltage (22.9 kV) is maintained by synchronous operation of the VVVF and stator output.

MG control system consists of the main control system, power analysis system and cooling water control system. The collected information from the VVVF controller, exciter controller, temperature sensors and vibration sensors are transferred to the main control system through the interface controller. The control system of the MG set communicates in Modbus Transmission Control Protocol/Internet Protocol (TCP/IP) method with controller of each device. The configuration of KSTAR MG control system is shown in Figure 3 [2].

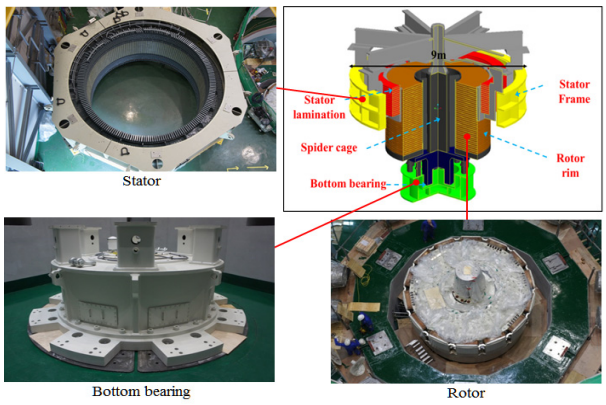

Figure 2. Each parts of the generator

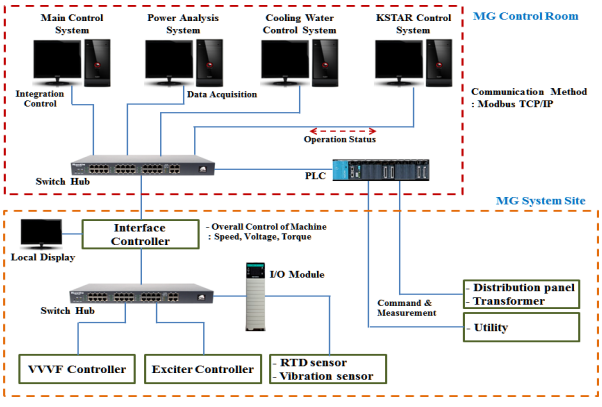

Figure 3. KSTAR MG Control system

To achieve effective MG operation, it is therefore necessary to install a cooling water system to remove the heat load of 3.926 MW generated from the rotor, stator, bearing and VVVF of the MG. During MG operation, even if blackouts or incorrect operations occur, the MG cannot be stopped because it continues to rotate by inertia. To stop the rotating MG, heat energy must be completely discharged [2]. Therefore the cooling system has been installed to allow removing the created heat from the MG system under all circumstances.

3. Result of the commissioning

The commissioning of the MG system is divided into two steps (individual and linkage commissioning). The individual commissioning was conducted in order to verify the performance of each device before the linkage commissioning. The measurement and inspection of each device (generator, VVVF, exciter, as well as power and cooling equipment) for individual test were conducted. Also these tests were passed for the each criterion. The commissioning items are shown in Table 2.

Table 2. The KSTAR MG commissioning items

Division		Test items	
Individual commissioning	Mechanical assembly test	-Stator winding electrical test	-Rotor electrical test
	Static test	-Radial air gap measurement -Mechanical brake system check -Bearing insulation inspection -Grounding test -Top bearing inspection	-H.P jacking oil system driving -Stator winding cold resistance -Speed encoder inspection -Stator winding Capacitance -Bottom thrust bearing inspection
	Rotational test	-Rotor alignment & shaft run-out -Initial rotation and direction check -Vibration measurement -Dynamic braking test -Over speed test -Open & short circuit characteristic -Shaft voltage measurement	-Rotational air gap measurement -Balancing inspection -Mechanical braking test -Maximum rated speed operation -Voltage balancing test -Noise measurement -Deceleration test
Linkage commissioning	No-load test	-Interlock test(Alarm, Trip check) -MG + RPC operation test	-Logic performance check -MG+RPC+PF MPS operation test
	Dummy load test	-Capacity operation (34, 38MVA) -Frequency operation (60, 61Hz)	-With / without RPC test

The linkage commissioning is divided into no-load and dummy load test. Through the no-load test, the MG system's performance and the correlation among the MG, RPC system and PF MPS were verified. The interlock levels of MG system are composed of 4 steps. The actual test of each level has been conducted and confirmed that were normal. The RPC system injection test and PF MPS transformer power input test both have been completed successfully. Based on the results of these tests we have known that the RPC system is possible to inject at any speed or voltage, and it is more stable to turn on the PF MPS after injection of the RPC system at idle mode.

For the dummy load test, several scenarios were prepared by changing the operation capacity, di/dt, duration time, with-without RPC, MG speed, etc. The typical scenario and result of the dummy load test are shown in Figure 4. (Capacity: 33.9MVA, di/dt: 4kA, Duration: 100sec, MG speed/voltage: 514.3 rpm/22.9kV) The PF MPS is operated using the KSTAR main control system during the dummy load test.

According to the results of dummy load test, the MG speed fluctuation range is increased proportionally against the operation capacity and di/dt of the PF MPS. However there was no change by whether injecting the RPC system or not. In both situations the speed and frequency of the MG have almost the same

changing rate. But in case of the Voltage, it was more stable to inject the RPC system than without the RPC system. 36.09 Mvar reactive power is measured and after insert 33 Mvar of the RPC system about 5 Mvar leading reactive power is created.

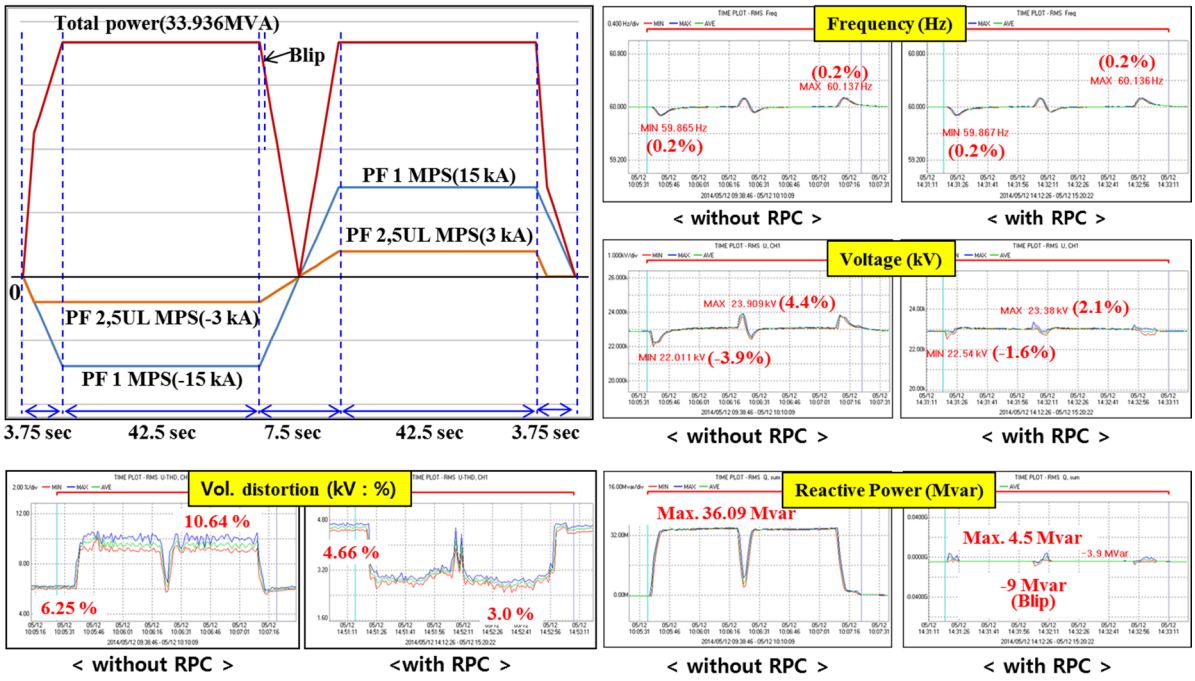

Figure 4. The typical scenario and results of the dummy load test

4. Plan for the superconducting commissioning of the MG system

The external heat exchanger has been installing to manage more stable for the bottom bearing oil temperature. Once this installation is completed, the bottom bearing heat run test is expected. The superconducting commissioning of the MG system will be started in November. The test capacity is up to 130 MVA and will be performed gradually increasing the operation capacity. In addition, the Identification tests of the reasonable capacity of the RPC system will be conducted.

Acknowledgement

This work was partly supported by the JSPS-NRF-NSFC A3 Foresight Program in the field of Plasma Physics (NSFC: No.11261140328, NRF No. 2012K2A2A6000443).

References

[1] C.H. Kim, et al., “Conceptual design of the KSTAR Motor Generator”, Fusion Engineering and Design, 87(2012) 1576-1582

[2] C.H. Kim, et al., ″Completed installations and the individual commissioning of the KSTAR MG system” Fusion Engineering and Design Volume 89, Issue4, April 2014, Page 302-311

[3] N.Y.Joung “Technical report of the MG set cooling system” NFRI technical document, 2012

Investigation of hydrogen isotope removals on deposition layers using ion cyclotron wall conditionings in EAST

N. Ashikawa[1], Y.W. Yu[2], Suk-Ho Hong[3], K. Katayama[4], Y. Torikai[5], F. Ding[2], J.S.Hu[2]

[1] National Institute for Fusion Science, Gifu 509-5292, Japan

[2] Institute of Plasma Physics Chinese Academy of Sciences, Hefei, 230031, China

[3] National Fusion Research Institute, Daejeon 305-333, Korea

[4] Kyushu University, Kasuga, 816-8580 Japan

[5] Toyama University, Toyama 930-8555, Japan

Abstract: Bulk W samples with and without W deposition layers were exposed to deuterium plasma in EAST. Deuterium retentions of W deposition layer were analyzed by TDS. From comparison with deuterium retention on W targets with W deposition layer and without deposition layer, higher deuterium retention in W target with W deposition layer is observed. Oxide layer at the surface of W deposition layer was removed during deuterium plasmas exposures in EAST. Influence of oxide layer in W deposition layer for D trapping is negligible. Reasons of higher hydrogen isotope retentions in metal deposition layer are not clear. This result is one of a good suggestion to understand the hydrogen isotope trappings in metal deposition layer

1. Introduction

Investigations of hydrogen retention and hydrogen isotope-exchange reactions in deposition layer and bulk target of plasma facing materials are one of important issues in magnetic confinement fusion reactors. These plasma wall interactions relate to wall recycling, a dilution of fueling gasses and tritium inventories in vacuum vessel on plasma facing materials.

In ITER and DEMO, controls of fuel recycling under strong magnetic field up to 10 T are required. The ion cyclotron wall conditioning (ICWC) is one of the useful tools for wall conditionings in ITER and DEMO. ICWC has been operated as general operations of wall conditionings in EAST [1] and investigated in fusion devices such as LHD, TEXTOR, JET, and Tore Supra. But ICWC experiments using material probes are not sufficient yet.

Two kinds of material probe analysis for ICWC experiments were done in TEXTOR and LHD. Higher erosion rates (0.4 nm/min) of ICWC were measured at surfaces perpendicular to the magnetic field lines, than at those parallel to it (0.25 nm/min), which of the same order than those of continuous H2-GDC on TEXTOR [2]. In LHD, thin stainless steel, SUS316, samples were exposed to ICWC plasma using the movable material probe system. A holder had three kinds of faces, such as a plasma facing side, a perpendicular side to it, and in a narrow gap mimicking castellations. They were then exposed to He-ICWC discharges only with a cumulated duration of 4000 seconds throughout the experimental campaign. Helium bubble formations were measured by Transmission Electron Microscope (TEM) with F Focused Ion Beam (FIB) milling to observe the cross-sections of target materials. And it was attributed to bombardment by charge exchange neutrals measured by Natural Diamond Detector, and is observed only on the side facing directly the plasma,

indicating that shadowed surfaces not directly exposed to plasma were not accessed by He-ICWC [3].

New experimental proposal for ICWC are planned to investigate effects of energetic particles produced by ICWC and hydrogen isotope exchanges on the surface of target materials in EAST. For two issues for the next ICWC experiment, analyses of impurities and fueling gasses with depth profiles are important.

2. Experimental setup

Before ICWC experiment in EAST, pre-experiments using material probes exposed to plasmas were done in EAST. Samples exposed to deuterium plasmas using the Material and Plasma Evaluation System (MAPES) in 2012. Sample holders were set on cupper cooling plate of MAPES in EAST as shown in Fig.1. 6 samples of 10 mm x 10 mm x 1 mm are installed in a holder on MAPES.

Tungsten deposited layers were produced on tungsten substrate (W bulk) in hydrogen plasma by using the capacitively coupled RF plasma sputtering in Kyushu Univ.[4]. The sputtering device is a parallel plate type generally used. A tungsten plate (99.95% in purity) was mounted on a cathode electrode as sputtering target material. Tungsten substrates were mounted on an anode electrode. When an RF power of 13.56MHz is supplied to the cathode electrode, plasma discharge begins between the cathode electrode and the anode electrode. The tungsten plate on the cathode electrode is sputtered by ion incidents from plasma and emitted tungsten atoms are deposited on the substrates. The thickness of the deposited layer will be about 1 μm.

For target samples and holders, thermocouples are needed with their time evaluation. Langmuir probes are set on Cu cooling plate to measure parameters of edge plasma.

Chemical states of the impurity in the tungsten samples were analyzed by X-ray photoelectron spectroscope (XPS). Deuterium retention and desorption characteristics are measured by thermal desorption spectroscopy (TDS). Trap energies for deuterium in the tungsten samples are analyzed by simulation of thermal desorption based on the results of post mortem surface analysis. In this experiment, we focus on an isotope exchange in the deposited layer. After the deposition layers are exposed to deuterium plasma discharges, TDS analysis will be carried out. From the change of the amount of hydrogen isotopes (H and D) in the deposited layer, we can evaluate an effect of charge exchange particles produced by main

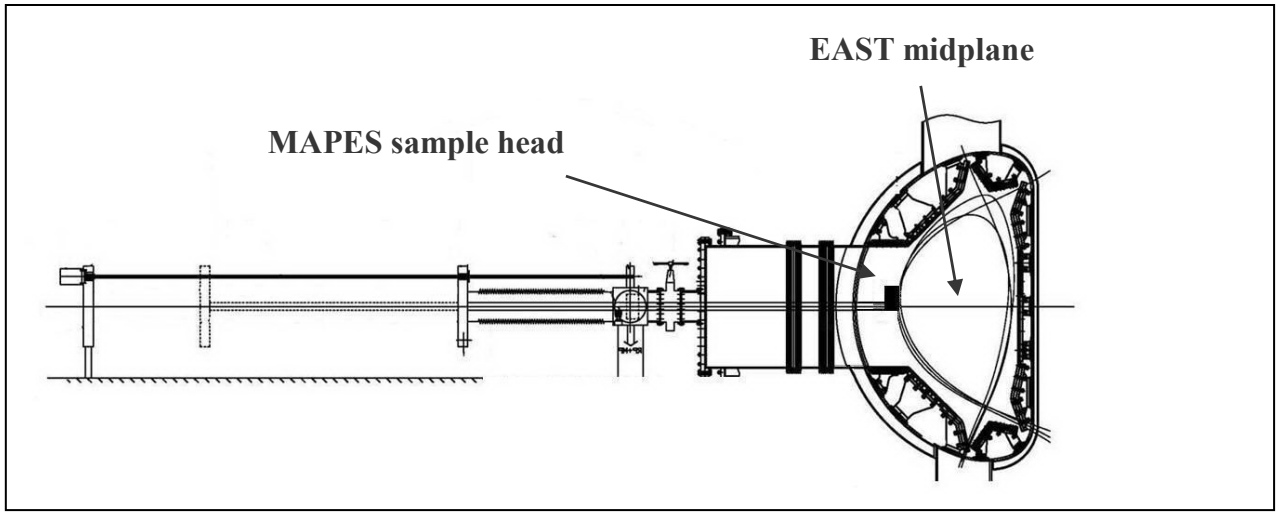

Fig.1 MAPES setup in EAST

plasma discharges. Further, we can discuss the mechanism of hydrogen-isotope exchange in porous tungsten materials. SEM-EDX observation will be done before TDS analysis in order to investigate crack, flaking, deposition of sample targets.

3. Results

Bulk W samples with and without W deposition layers were exposed to deuterium plasma in EAST. Initial amounts of hydrogen were implanted by working gassed during sputtering to make deposition layer and this ratio between tungsten and hydrogen, H/W, is 0.032. This amount of W/H to compare with before and after plasma exposures are the same.

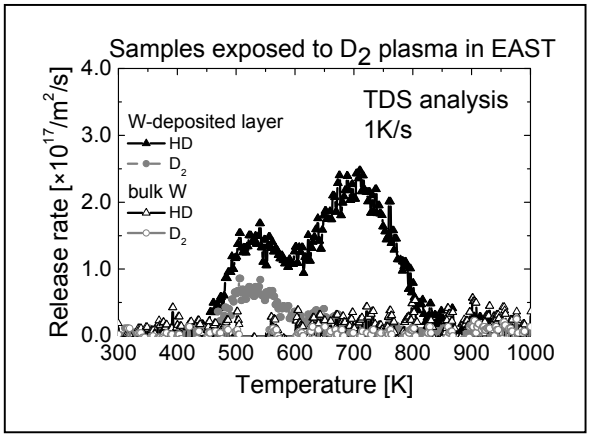

Fig.2. DH and D_2 thermal desorption spectra from W-deposited layer and W bulk targets exposed to EAST D_2 plasmas.

Retained deuterium after plasma exposure was implanted by deuterium plasma in EAST and the ratio between tungsten and deuterium, D/W, is 0.002. The retained deuterium in W deposited layer is more by at least an order of magnitude than that in bulk W. Using X-day photoelectron spectroscopy (XPS), depth profiles of atomic concentrations and chemical bindings are analyzed as shown in Fig.3. An Mg X-ray source of 400 W and a spot size of 800 μm were used. An argon ion gun was used to etch the target samples and analyses their depth profiles. The erosion depths were measured using a contact-probe profilometer and used to calculate the sputtering rate. Major impurity contaminations on the surface of deposition layer are oxygen and carbon due to air contaminations. Lithium coatings as wall conditionings are not observed and then influences of Li re-deposition are negligible.

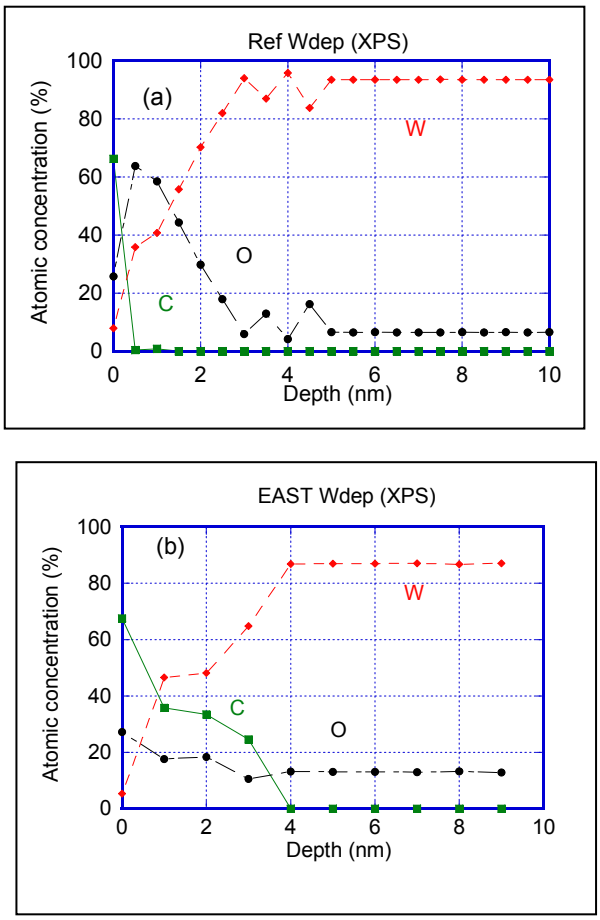

Fig.3 Atomic concentrations of W deposition layer measured by XPS. (a) before and (b) after plasma exposures in EAST.

From a comparison with depth profiles of atomic concentrations as shown in Figs.3, thicker air contaminations on the surface of a target material before plasma exposure were observed. Tungsten oxides were observed using narrow analysis of XPS and this concentration at the depth of 1-2nm on the top surface of W deposition layer is higher than that without W deposition layer. Therefore oxide layers at the top of W deposition layer were removed during

deuterium plasmas exposures in EAST.

In general, metal oxide layers on metal targets are regarded as one of trapping sites for hydrogen isotopes. In this experiment, initial oxide layers produced by air contaminations were removed during plasma exposures and influences of oxide layers for deuterium trappings are low. As other possibility of trapping sites for deuterium isotopes, a grain boundary is considered in W.

4. Summary

It was shown that hydrogen retention by deuterium plasmas in W deposition layer ahead of future ICWC experiment in EAST.

Deuterium retentions of W deposition layer were analyzed by TDS. From comparison with deuterium retention on W targets with W deposition layer and without deposition layer, higher deuterium retention in W target with W deposition layer is observed. Oxide layer at the surface of W deposition layer was removed during deuterium plasmas exposures in EAST. Influence of oxide layer in W deposition layer for D trapping is negligible.

Reasons of higher hydrogen isotope retentions in metal deposition layer are not clear. This result is one of a good suggestion to understand the hydrogen isotope trappings in metal deposition layer

5. Future subject

Improvements of experimental setup at next campaign in MAPES/EAST are discussed. Total amounts of retained deuterium and these depth profiles on W deposition layers are measured. Influences of energetic particles produced by ICWC are also analyzed.

6. Acknowledgement

This work was partly supported by the JSPS-NRF-NSFC A3 Foresight Program in the field of Plasma Physics (NSFC: No.11261140328) and NIFS budget KUHR010 and ULFF004.

[1] J.S.Hu et al., Fusion Engineering and Design, 84(2009) 2167.

[2] T. Wauters at al., 39th EPS Conference on Plasma Phys., Stockholm, July 2-6, 2012.

[3] N. Ashikawa et al.,Plasma and Fusion Research, 6, (2011) 2402138.

[4] S. Ishikawa, K. Katayama, et al.,, Fusion Eng. Des. 87 (2012) 1390.

A3 collaboration activity on PSI, Div/SOL research in KSTAR

Suk-Ho Hong on be half of KSTAR team and collaborators

National Fusion Research Institute, Daejeon, Korea

Email: sukhhong@nfri.re.kr

Research activities on plasma-surface interaction with carbon and metal PFCs for future fusion reactors among A3 countries are introduced. International collaboration with LHD in Japan and EAST in China makes synergistic effect for three machines and get experimental results in much wider parameter windows. Furthermore, different main chamber wall materials, i.e. tungsten environment in EAST and carbon environment in KSTAR and LHS will make cross-fertilization for scientists in A3 institutes.

1. Introduction

In-vessel components are exposed to severe environments, namely to high energy particle and heat flux, and radiation. The components inside the vacuum vessel on which those particle, heat flux and radiation reach, are called plasma facing components (PFCs). The study of interaction between plasma and the surface of PFCs is called “plasma-surface interaction” (PSI). Especially, PSI at limiter and divertor are of interests. Limiter is an in-vessel component which limits the expansion of plasmas, in order to avoid direct contact with vacuum vessel. Divertor is a specially designed in-vessel components which removes impurity particles and heat from the plasmas. PFCs are exposed to harsh environments which lead to the erosion, redeposition, and fuel retention, etc. Therefore, PSI is one of critical parts which has to to be controlled for the successful operation of fusion reactor as a power plant.

Generally, low Z materials such as carbon or beryllium were commonly used [1, 2, 3, 4]. However, ITER will have a metal wall configuration consisting of Beryllium and Tungsten. JET and ASDEX Upgrade (AUG) have employed these beryllium and full tungsten first walls for ITER-relevant experiments (ITER-Like Wall) [1, 2]. Recently, Tore Supra has started the "WEST" project, the abbreviation of "W Environment in Steady-state Tokamak", which includes the change of major machine configuration into a tungsten (W) divertor machine [3]. EAST has manufactured ITER type tungsten divertor structures, successfully tested, and installed for PSI study in 2014 [4]. JET experiments with these ILW configuration shows a remarkable step towards the success of fusion reactor such as 1) a better wall condition for start up and the low impurity levels, 2) the decrease of fuel retention by a factor of 10, 3) reduction of carbon impurity by a factor of 20 while maintaining good confinement [5].

In order to realize thermonuclear energy beyond ITER, international collaboration on PSI, especially on metal wall is not an option, but an obligation. In this paper, we describe selected topics of international collaboration activity on PSI, Div/SOL among A3 countries.

2. Selected topics for A3 collaboration

2.1. Tungsten Material test

The main aim of this topic is to test various bulk and coated materials including tungsten and molybdenum. Several different grades of materials will be used for the experiments. The

experiments will be divided into two categories: long term test and short term test. The long term test is a test for a whole campaign which is equivalent to several thousand seconds of plasma on time. The short term test is a test for a day or a week which is equivalent to several hundred seconds of plasma on time, to check the time evolution of the sample material.

Long term and short term material test will give valuable information on the bulk and coated material property and their performance under high particle and heat flux. Nevertheless, the long term sample is a tile of bulk material made of tungsten or molybdenum, that cannot be exchanged during the campaign. Once it is installed at a fixed location, it will experience entire campaign including baking, initial wall conditioning, etc. Therefore, the result from long term samples Short term samples can be exchanged easily in a day, but their exposure location inside the vacuum vessel is also fixed: the toroidal and poloidal location of the sample cannot be changed, but distance from the last closed flux surface (LCFS) can be varied.

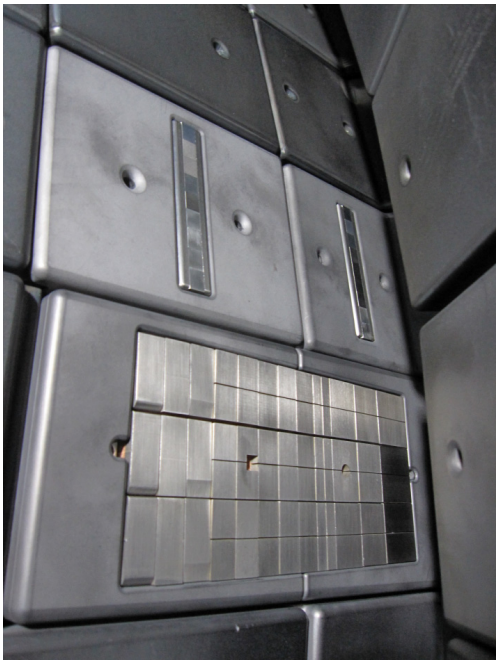

Figure 1. Long term samples installed at KSTAR.

In order to reduce the experimental cost, space, and time, and to be more effective, marker tiles can be placed at several different locations inside the vacuum vessel, and used as short term samples: A marker tile is a tile consisting of several different sets of materials. It can save cost, space, and time for testing several materials with almost the same plasma parameters, particle and heat flux. Nevertheless, it is very important to have as many samples as possible to identify poloidal and toroidal homogeneity of the plasma-surface interaction, which is "assumed" in the first place, because the observation from IR cameras indicates that edge localized modes (ELMs) are not poloidally and toroidally homogeneous [6]. For this, marker tiles with different sets of materials are installed at the central divertor of KSTAR as shown in Fig. 1.

2.2. Castellation structure development and test

Future fusion devices will have higher particle and heat flux than conventional tokamaks, which lead to a higher heat load. PFCs have to be designed to sustain such high heat load and active cooling should be considered seriously, and one of techniques to reduce the particle flux from the plasma is the optimized design of castellated structure: the shape and the angle of the castellation structure can reduce significant amount of heat load on the tile. As a result, a new shape of castellation is proposed [7]. The thermal response of the new castellation structure has been analyzed by using the ANSYS code which shows that the new shape allows operation of even misaligned shaped castellation at 20 MW/m^2 of steady-state thermal load. The PIC code SPICE2 [8] predicts full ion flux suppression in the gaps of shaped castellation, and Monte-Carlo 3D-Gaps code modeling [9] results at least a 20-fold decrease of beryllium content in the gaps.

Several machines are participating on the development and test of new castellation structure. The aim of this study is to test various different castellation structures made of various

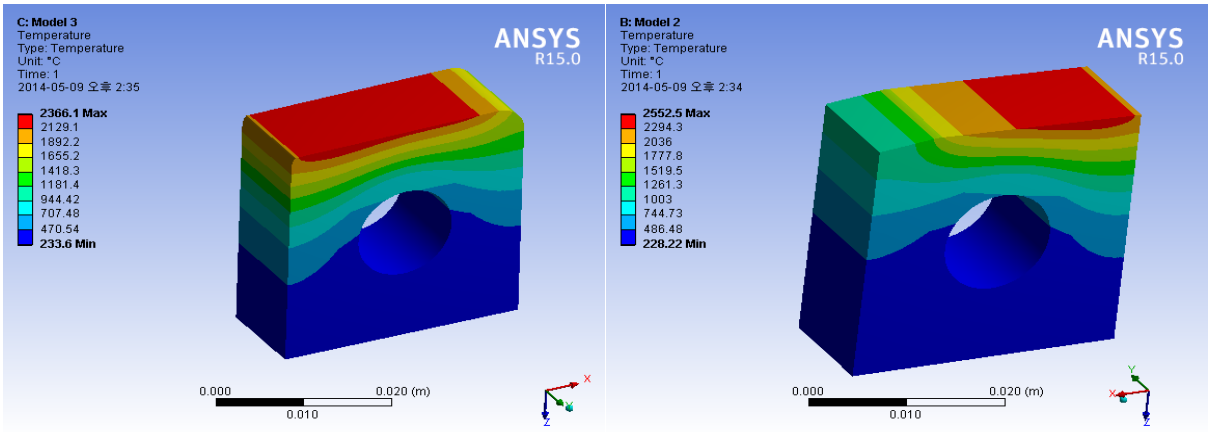

Figure 2. ANSYS simulation on different castellation structures at 20 MW/m^2 heat flux.

materials, and to find the most optimized design for the future fusion reactor. Not only experiments but also modeling and calculations will be performed.

2.3. Surface morphology change.

The surface of a PFC will be damaged by direct exposure to the plasma. Especially, tungsten tiles exposed to D_2 and He plasma shows various phenomena such as blister formation and cracking. Blister formation occurs when D atoms penetrate into the surface of the bulk tungsten and diffused into the grain boundary and retained there. Such blister formation causes damage on the surface of the tungsten PFCs and reduces the lifetime of the PFCs significantly. Furthermore, melting occurs at the damaged surface which creates metal droplets during ELMs and disruptions. Blister formation on tungsten at room temperature occurs at a fluence as low as 10^{23} D^+/m^2 for 1 keV D^+. Size of the blisters increases with increasing flux, but no blister formation on tungsten was observed at a target temperature ≥ 600 °C (1 keV, flux 10^{25} D^+/m^2s). However, blister formation is observed at ion energies as low as 100 eV at room temperature and at a fluence of 10^{25} D^+/m^2. The size of the blister increases with increasing ion energy.

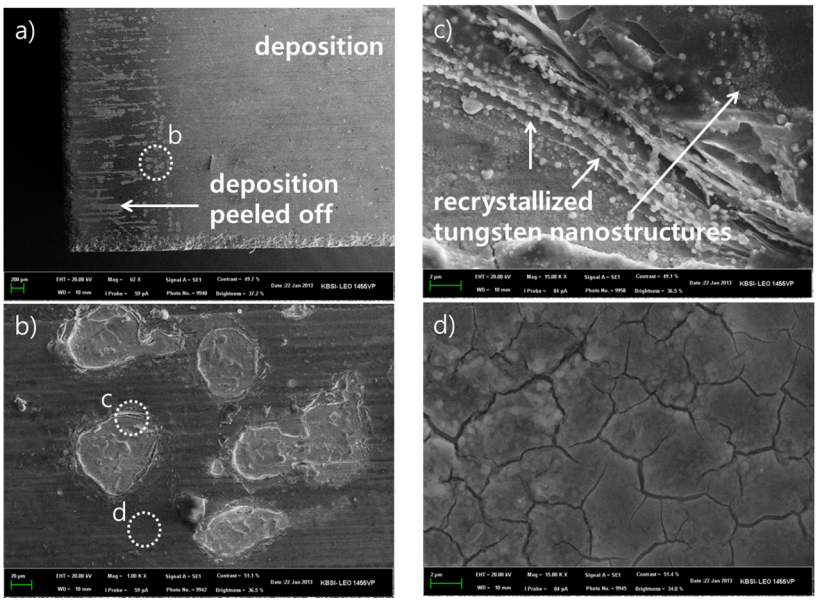

Figure 3. a) SEM image of the surface of the conventional castellation A. Circle and the label b indicate the location of Fig 3b), b) zoom-in SEM image of scars. Circles and labels c and d indicate the locations of Fig. 3c and Fig. 3d, c) zoom-in image of a scar, d) zoom-in image of cracks.

The aim of this study is to understand the change of surface due to plasma-surface interaction

on metal PFCs. In the case of tungsten PFCs, the blister formation and the surface damage by the blisters are of concern. This is very important for future generation of tokamaks with tungsten wall environments. Moreover, the topic is very interesting since it is strongly related to several issues together such as plasma-metal interaction, fuel retention, and diffusion of D atoms into tungsten bulk.

2.4. Heat load analysis for carbon and metal tiles

Control of heat load on PFCs is one of critical issues to be solved for a fusion reactor. Once the heat load exceeds the maximum tolerable value of PFCs, the PFCs will be severely damaged. Such high heat load leads to the melting and metal droplet formation in the case of metal PFCs, sublimation and brittle destruction in the case of carbon PFCs. Consequently, the plasma operation will be affected by the damaged PFCs and a lot of in-vessel dust will be produced. Therefore, the heat load on the PFCs has to be analyzed as accurate as possible.

The aim of this study to develop, quantify, and model the heat load on the PFCs, and compare the differences between carbon and tungsten environments. To do the task, it is necessary to develop/improve techniques in both modeling and measurements: Heat load analysis is usually accompanied by modeling and measurements by IR cameras and thermocouples. By comparing the results from modeling and measurements, more accurate heat load on the PFCs will be given.

2.5. Fuel retention inside the gap and its removal by ICWC

During the plasma operation, ions and charge exchange neutrals bombard PFCs. In the case of carbon based PFCs, carbon and hydrocarbon species are released depending on the energy of impinging particles and the temperature of the PFCs [10, 11]. For instance, for substrate temperature around 750 °K, higher hydrocarbon species such as C_2H_x or C_3H_x are released from the carbon PFCs with low energy (< 50 eV) H+ ion bombardment, while CH_x are dominant with high energy (>50 eV) [10, 11]. Co-deposition of hydrocarbon species causes two issues: 1) fuel retention inside the layer [12], 2) the delamination of deposited layers which causes creation of mobilized dusts [13, 14]. Recent post-mortem analysis from Tore Supra after DITS (Deuterium Inventory in Tore Supra) campaign in 2008 shows that the deuterium inventory was dominated by co-deposition, especially at tile gaps [15]. Thus, fuel retention on tile gaps of PFCs is one of critical issues to be solved for successful ITER operation in D-T phase [16, 17]. For instance, assuming equal mixture rate of deuterium and tritium with a fuel injection rate of 200 Pa m^3 s^{-1} and tritium retention rate of 5 %, in-vessel tritium limit would be reached less than 100-200 of shots (400 sec) [16]. Therefore, the amount of fuel retention has to be monitored as exact as possible, and co-deposit should be removed if it is necessary: Various removal techniques are proposed and tested [18].

The aim of this study to quantify, and model the co-deposition inside the gap structures and to develop/optimize removal techniques such as Ion Cyclotron Wall Conditioning (ICWC). To do the task, it is necessary to make samples in a dedicated way during a plasma session and the samples will be analyzed by various diagnostics.

2.6. Transport of high Z impurities into core plasma

For the use of tungsten as a PFC material leads to a negative effect on the plasma operation: Tungsten is a high Z material which causes radiation loss of core plasma energy.

Therefore, it is necessary to quantify the core accumulation rate and to develop tungsten removal technique from the core, and to understand its transport inside the plasma. As AUG has reported, the use of metal PFCs has reduced the operation window for the plasma experiments. This reveals that the change of wall materials, i.e. the wall condition has direct influence on the plasma start up and plasma operation at flat top. Therefore, the quantification of the tungsten impurity accumulation rate has to be measured and removal technique of impurity from the core by ECRH injection should be developed.

The aim of this study to develop, quantify, and model the tungsten impurity transport. To do the task, it is necessary to improve techniques in both modeling and measurements: Dedicated experiment and modeling by code will bring the knowledge on the impurity accumulation in the core and the consequence of the impurity accumulation.

3. Summary

The results from the topics will bring new information on the PSI under extreme environments such as high particle and heat flux, strong permanent magnetic field, under high vacuum. The scientific results obtained from the project will be presented in conferences and published in peer-reviewed SCI journals.

Acknowledgement

This research was supported by Ministry of Science, ICT, and Future Planning under KSTAR project and was partly supported by the JSPS-NRF-NSFC A3 Foresight Program in the field of Plasma Physics (NSFC: No.11261140328, NRF : No. 2012K2A2A6000443).

References

[1] G. F. Matthews et al., Phys. Scr. T128 (2007) 137
[2] O. Gruber et al., Nucl. Fusion 49 (2009) 115014
[3] E. Tsitrone, Private communication
[4] G. Luo, A3 Foresight Program Seminar, 23 Jan. 2013, Akanko, Hokkaido, Japan
[5] F. Romanelli, "Overview of the JET Results with the ITER-like Wall", 24th Fusion Energy Conference, 8-13 October 2012, San Diego, USA
[6] T. Eich et al., private communication
[7] A. Litnovsky et al., ITPA Div/SOL Meeting in Juelich, Jan., 2012
[8] M. Komm et al., PPCF 53 (2011) 115004
[9] D. Matveev et al., PPCF 52 (2010) 075007
[10] J. Roth, Phys. Scr. T124 (2006) 37
[11] E. Vietzke and A. Haasz, 1996 Chemical erosion Physical Processes of the Interaction of Fusion Plasmas with Solids ed. W. Hofer and J. Roth (New York: Academic) p 135
[12] T. Loarer et al., Nucl. Fusion 47 (2007) 1112
[13] J. Winter, Plasma Phys. Control. Fusion 40 (1998) 1201
[14] S. H. Hong et al., Nucl. Fusion 50 (2010) 035002.
[15] E. Tsitrone et al., Nucl. Fusion 49 (2009) 075011
[16] T. Loarer et al., J. Nucl. Mater. 337-339 (2005) 624
[17] T. Tanabe et al., J. Nucl. Mater. 313-316 (2003) 478
[18] G. Counsell et al., Plasma Phys. Control. Fusion 48 (2006) B189

PWI and edge plasma physics study on EAST

J.L. Chen*, R. Ding, H. Xie

Institute of Plasma Physics, Chinese Academy of Sciences, Hefei 230031, P.R.China

The interaction of plasma with the walls has long been recognized as one of the critical issues in the development of fusion energy research [1]. Because the lifetime of the wall components can be seriously reduced by the substantial particle and heat fluxes, and the impurities eroded from the wall can be transported to the plasma and badly influence the plasma performance. Therefore, studying the physics of plasma wall interaction (PWI) as well as the edge plasma behavior is quite necessary. The Experimental Advanced Superconducting Tokamak (EAST) was built to achieve long pulse and high performance plasma to study the physics and engineering issues relevant to the next-step long pulse fusion devices such as ITER [2]. Much research progress has been obtained on EAST in which the PWI and edge plasma physics is included. In the past two years, most of the components in EAST have been upgraded and at the same time many new features have been implemented for the sake of studying ITER-relevant physics. In the following, the main progresses related to the plasma boundary as well as some new research plans will be introduced. The introduction will be divided into these parts: the plasma facing components (PFCs) in EAST, PWI experiments and modelling, and active control of divertor heat flux.

There are many new features have been equipped in EAST such as the 4MW neutral beam injection (NBI) system, 16 resonant magnetic perturbation (RMP) coils and tungsten-monoblock divertor. Long pulse steady-state and high performance plasma operations are expected to study ITER-relevant physics [3]. The plasma facing materials (PFM) have been changed many times since the first operation for EAST. The initial phase of PFM was full stainless steel material and the first phase was replaced by full SiC coated graphite, then in the second phase the first wall was equipped to Titanium Zirconium Molybdenum (TZM) alloy. In order to study the ITER relevant physics, the upper divertor PFCs have been upgraded in the past 2 years. After the upgrade, the divertor targets are ITER-like W monoblocks and the divertor dome and baffles are flat type W/Cu PFCs, hence the maximum heat flux can be withstood by the divertor targets and dome/baffles are $10MW/m^2$ and $5MW/m^2$ respectively. Therefore at present the PFM is W for upper divertor, Mo for first wall and SiC for lower divertor. In the future the PFM will be replaced by full W materials. The upgrade this time is not only focus on material types but the structure and designing. A better shape of the dome is designed which can satisfy the magnetic field lines in case of incidents such as vertical displacement events (VDE). The new divertor designed as ITER-like cassette body structure. By using this structure the divertor is easy to be installed and replaced. There are totally 80 cassette body structures equipped in EAST, while the number in ITER is 54. What's more, actively water cooling system for the divertor is designed. During the cassette assembly of the prototype set, the tolerance of plasma facing surface is 2mm at toroidal direction and 0.5mm for neighbor of the sets.

Now that the upper divertor PFM has been replaced by the W material, dedicate experiments of operations with W divertor will be done in the coming run campaign. At first along with the upper single null W divertor discharge we can check the operation in L-mode, access to H-mode and operation in H-mode, respectively. After that, these operations can compare with the lower single null C divertor discharge to investigate the patterns such as plasma operation, plasma confinement quality and fuel retention for the different kind of divertors operations. Therefore more experience of operation with W divertor will be accumulated which is very important and useful for ITER. Tungsten is used as the plasma

facing material because it has the advantage of the high melt point, no chemical sputtering and low physical sputtering yield. However, there are still many challenges for the W plasma facing components. Tungsten is a kind of high Z material, so the tolerable W impurity level is pretty low, i. e. the plasma confinement and performance would be badly influenced with even a bit of W impurities. Also, with the totally new W component, it is necessary to achieve reliable tokamak operation scenarios. Furthermore, compatibility with H-mode scenarios and heating methods like ICRF is also needed to study. Research of the tungsten PFC can be taken by the processes of W production, transport and accumulation. All of these processes should be better understood, controlled, and the W impurities need to be mitigated. The W impurities mainly produced by physical sputtering and melting due to the particle and heat flux driven by hot plasma or the transients such as ELMs and disruptions. With respect to the control of W transport, taking advantage of the experiences from AUG [4], JET [5], CMOD [6] is essential. In the very center of plasma, gaining central power by such as NBI, ECRH and ICRH can suppress the neo-classical accumulation of impurities. Gas puffing and ELM control is useful in controlling the W-influx go through the H-mode edge transport barrier. While in the confinement region the impurity gradients are weak due to the turbulent transport. To investigate the W transport in the plasma some detection equipment has been installed in EAST. There are several chords of W spectroscopy diagnostics to measure the W sputtering flux at the local region of the upper divertor. The sputtering flux of W at the divertor region is detected by WI line at 400.9nm. The central W density measurements can be taken by XEUV and SXR spectroscopy systems. Besides, the power handling for the divertor is very important for the divertor target since there are large heat fluxes there. According to the ANSYS simulations for the castellation units, after both sides being shaped the maximum temperature is around 2100 degrees Celsius even with 1mm misalignment, which is sustainable for the upper W divertor target. There are infrared red (IR) cameras have been installed to observe the temperature ranges for the upper and lower divertors.

The Material and Plasma Evaluation System (MAPES) in EAST, which locates at the mi-plane port of H sector as outboard manipulator, is a very useful tool to do PWI experiments. This equipment is manipulated by a remote control system. Samples for doing PWI experiments can be handled by the MAPES and pulled into the tokamak vacuum chamber, and then they can be exposed to the SOLs of dedicated plasma discharges for shot sequences. The maximum sample weight can reach to as much as 20kg and the sample holder moving velocity is adjustable from 1 to 15mm/s. There are lots of local PWI diagnostics during the exposure of the experimental samples such as Langmuir probes, thermocouples, spectroscopy, CCD camera and IR camera. In the following, some experiments proposer by using the MAPES will be introduced. One of the experiments is about W melting research. As we know, the castellation structure W materials are about to be melted as considering the large heat loads to the leading edges. An ITER-like castellation structure W sample would be exposed to the plasma. During the exposure time, the in-situ diagnostics as introduced before will be used to observe the evolution of the sample. After exposure this sample will be measured by some post-mortem analysis. The research focuses on studying the melted surface layer motion and evolution so far as to the influence on plasma performance. Another experiment proposer is material migration experiment. The experiment of $^{13}CH_4$ and WF_6 injection through test limiters can study the C and W migration and re-deposition in the superconducting tokamak. Post-mortem analysis is necessary but need to be supported. The experiment result can compare and benchmark with the ERO modelling. There is a material migration experiment, which is in collaboration with IO and Sandia lab, has been done in which toroidal shape ITER-like BM tile exposed to He plasma. The experimental results indicate asymmetric erosion and deposition profiles, which are found to be due to

the influence by ICRF and movable limiter. After all of the possible causes are considered, the erosion and deposition profiles observed by the experiment can good match with the ERO modelling result. In the coming campaign, a similar experiment will be done with higher heating power and density and more diagnostics tools are foreseen. The following introduced experiment is related to research of impurity deposition in gaps. Some gap samples will be put at divertor and MAPES to collect deposited impurities and deuterium in gaps, and then these samples will be measured by post-mortem analysis such as XPS, NRA, RBS and SIMS which is also need to be supported. The experiment results can be compare and benchmark with the PIC-EDDY simulation. There are many modelling codes can be used to simulate the PWI experiments. For example, local erosion and redeposition can be simulated by ERO [7]; OEDGE which is in collaboration with University of Toronto is a large scale C/W migration code; SOLPS provides a realistic boundary plasma condition; material transport and deposition in gaps can be modelled by PIC-EDDY; and ANSYS is a useful thermal analysis tool. By studying with both experiments and modelling, the mechanism of the PWI and edge plasma physics can be better understood.

The divertor heat load due to large heat flux is a critical issue for magnetic confined fusion energy research, because the heat load that the existing materials can sustain cannot be higher than 10MW/m^2. However, the present Type I ELMs in EAST can lead to a peak heat load of about 10MW/m^2. In contrast, for Type II small ELMs observed in long pulse H-modes the peak load is below 2MW/m^2 [8]. In the next campaign with more than 20MW H&CD power the divertor heat load will be a great challenge. There are some approaches can reduce the divertor heat load. Such as the edge magnetic topology changed by LHCD generates a secondary strike point thus plasma wetted areas are larger and heat flux is reduced [9]. Formal experiments find the Supersonic Molecular Beam Injection (SMBI) controls ELM by strong decreasing the amplitude and increasing frequency. Increasing SMBI pulse length leads to smaller ELMs with higher frequency [10]. Demonstration for the first time ELM pacing by innovative Li-granule injection indicates that each pellet triggers an ELM during ELM free phase after L-H transition and much lower particle flux on divertor target than intrinsic giant ELMs [11]. In the past EAST operation campaign long pulse H-mode over 30s has been achieved with small ELMs to minimize transient heat load. The shot has the predominantly small ELMs with H_{98}~0.9 between type-I and type-III. The target heat load is largely below 2MW/m^2. A new Quasi-Coherent Mode which can continuously remove heat and particles has been observed with the long pulse H-mode [12]. Deeper research on reducing divertor heat flux is necessary on the basis of the previous study.

In conclusion, the progress related to the PWI and edge plasma physics in EAST is introduced. Firstly, the ITER-like W/Cu-PFCs have been installed as the upper divertor for the coming campaign. Long pulse and steady-state plasma operation at EAST can study ITER-relevant physics. Secondly, W-related PWI issues are critical for ITER. PWI experiments and modeling on EAST can help to understand the underlying physics and make good predictions for ITER. At last, various techniques for divertor heat flux control have been successfully developed on EAST.

Acknowledgements

The authors gratefully acknowledge supports by National Magnetic Confinement Fusion Science Program under Contract No.2013GB105003 and National Natural Science Foundation of China under contract No.11175205. This work was partly supported by the JSPS-NRF-NSFC A3 Foresight Program in the field of Plasma Physics (NSFC: No.11261140328, NRF: No. 2012K2A2A6000443).

References

[1] J. Roth et al., J. Nucl. Mater. 390-391 (2009) 1-9.

[2] H.Y. Guo et al., J. Nucl. Mater. 207-311 (2011) S369-S374.

[3] H.Y. Guo et al., Nucl. Fusion 54 (2014) 013002 (9pp).

[4] K. Kireger et al., J. Nucl. Mater. 266-269 (1999) 207-216.

[5] T. Pütterich et al., Plasma Phys. Control. Fusion 55 (2013) 124036.

[6] B. Lipschultz et al., Phy. Plasmas 13 (2006) 056117.

[7] A. Kirschner et al., Nucl. Fusion 40 (2000) 989.

[8] L. Wang et al., Nucl. Fusion **53** (2013) 073028.

[9] Y. Liang et al., PRL **110**, 235002 (2013).

[10] X. L. Zou et al., 24th IAEA FEC, San Diego.

[11] D. Mansfield et al., Nucl. Fusion 53, 113023 (2013).

[12] J. Li et al., Nature Physics 2013, 9(12), P817.

Effect of neutrals localized at torus inboard side on the impurity transport in edge stochastic magnetic field layer of LHD

S.Morita[1,2], H.M.Zhang[2], T.Oishi[1,2], M.Kobayashi[1,2], M.Goto[1,2], X.L.Hunag[2], G.Kawamura[1] and E.H.Wang[3]

[1]National Institute for Fusion Science, Toki 509-5292, Gifu, Japan

[2]Graduate University for Advanced Studies, Toki 509-5292, Gifu, Japan

[3]Institute of Plasma Physics, Hefei 230031, Anhui, China

Abstract

Two-dimensional (2-D) distribution of impurity line emissions has been measured in Large Helical Device (LHD) based on the 2-D extreme ultraviolet (EUV) spectroscopy for studying the edge impurity transport in stochastic magnetic field layer with three-dimensional (3-D) structure. The impurity behavior in the vicinity of two X-points at inboard and outboard sides of torus becomes separately visible with the 2-D measurement. As a result, it is found that the carbon location changes from inboard to outboard X-points when the plasma axis is shifted from R_{ax}=3.6m to 3.75m. A 3-D simulation with EMC3-EIRENE code agrees with the result at R_{ax}=3.75m but disagreed with the result at R_{ax}=3.60m. The discrepancy between the measurement and simulation at R_{ax}=3.60m is considerably reduced when the effect of neutral hydrogen localized at the inboard side is taken into account, which can modify the density gradient and friction force along the magnetic field.

1. Introduction

Study of edge impurity transport is one of the most important physics issues in fusion research based on magnetically confined toroidal plasmas. The current edge impurity transport study is strongly motivated by the requirement of mitigating the heat flux coming onto divertor plates with edge impurity radiation. Based on this requirement the radiative divertor experiment using impurity line emissions has been extensively studied [1,2] in addition to the control of impurity influx and active use of the impurity screening. In the Large Helical Device (LHD) the edge magnetic field is characterized by the presence of stochastic magnetic field, called 'ergodic layer', consisting of fully three-dimensional (3-D) structure, while the scrape-off layer of tokamaks has a two-dimensional structure [3]. Recently, an experiment using resonant magnetic field perturbation coils has been carried out in many tokamaks to mitigate giant edge localized mode and to reduce the divertor heat flux. The experiment also enhances the importance of the edge plasma transport with 3-D magnetic fields. In order to study the edge impurity transport in 3-D stochastic magnetic field layer of LHD the 2-D spectroscopy has been developed in the field of extreme ultraviolet wavelength range at which most of charge states of impurity ions can be observed. A clear difference is observed in the 2-D impurity distribution between two different magnetic axis configurations of R_{ax}=3.60m and 3.75m. Results are presented with analysis based on 3-D edge plasma transport code.

2. Edge stochastic magnetic field layer and two-dimensional EUV spectroscopy

The impurity line radiation in the ergodic layer is dominantly emitted in the EUV range ($10 \leq \lambda \leq 600$Å) because the electron temperature ranges in $10 \leq T_e \leq 500$eV. The 2-D EUV spectroscopy is developed for the edge impurity transport study in the ergodic layer of LHD [4]. A space-resolved EUV spectrometer is installed at a distance of 9.5 meters from the plasma center of R_{ax}=3.60m configuration through a cubic extension manifold to observe the full vertical profile of impurity emissions. The 2-D distribution of impurity line emissions is then measured by horizontally scanning the optical axis of the spectrometer during a steady phase of discharges [5,6]. The horizontal scan is usually necessary for three or five seconds to exposure a sufficient number of image frames. A bird's-eye view of the LHD outboard port and toroidal plasma is shown in Fig.1. The observation range of 2-D EUV spectroscopy denoted with diamond solid line is approximately determined by the outboard port size (horizontally 0.7m and vertically 1.1m), which is a simple projection of the outboard port with diamond shape (invisible in the figure). The cubic extension manifold is connected to the backside rectangular port (horizontally 0.5m and vertically 1.1m) through bellows and insulator flanges.

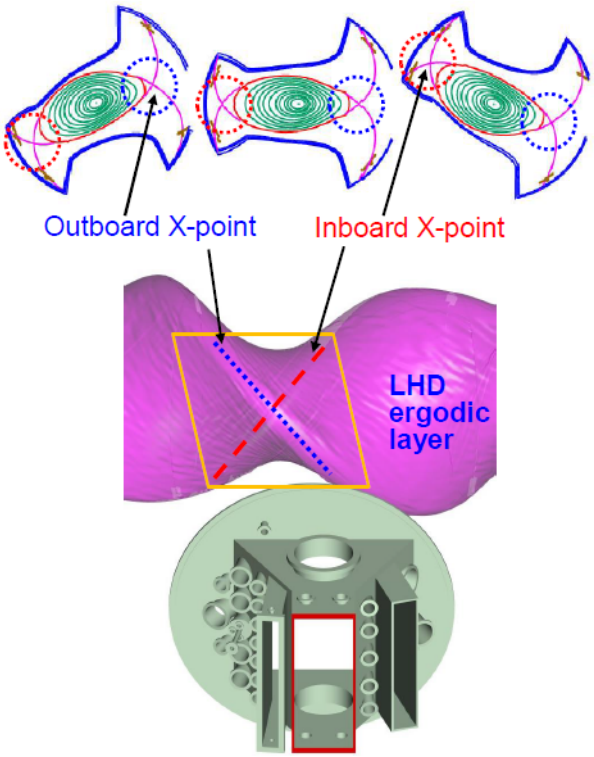

Fig.1 Schematic view of LHD plasma and X-point trajectories (outboard X-point: dotted line and inboard X-point: dashed line). Diamond shape with solid line denotes observation range by 2-D EUV spectroscopy. Three poloidal plasma cross sections show positional change of elliptical LHD plasma within the observation range.

The LHD elliptical plasma significantly rotates within the observation range because of a large toroidal pitch number (M=10) of a set of helical coils (ℓ=2), which resultantly leads to a large rotational transform of $\iota/2\pi$ =5 at plasma edge boundary. A poloidal cross section of the elliptical plasma is also shown in Fig.1 with three different toroidal angles at which the toroidal position is within the observation range of 2-D EUV spectroscopy. Thus, one can understand that two X-point trajectories at inboard and

outboard sides can be distinctively observed by the present 2-D spectroscopy system. The position of inboard and outboard X-points is indicated with dotted circles and the two X-point trajectories at inboard and outboard, which are intrinsically created by a set of helical coils, are also indicated with dashed and dotted lines, respectively. The X-points poloidally rotate in clockwise direction when a point of view toroidally moves in anticlockwise direction.

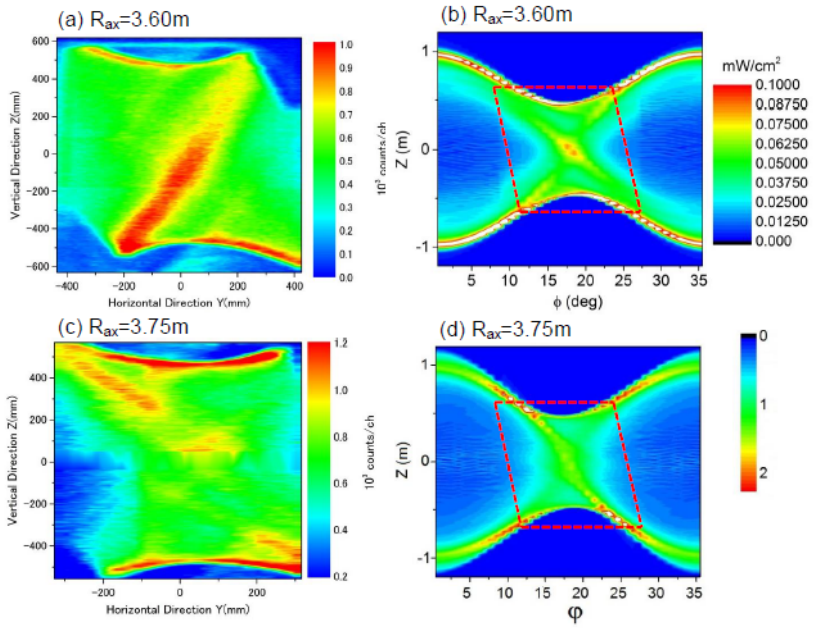

Fig.2 2-D distributions of CIV EUV line emissions at 312Å; measurement ((a) R_{ax}=3.60m and (c) R_{ax}=3.75m) and 3-D simulation ((b) R_{ax}=3.60m and (d) R_{ax}=3.75m). Diamond shape with dashed line denotes observation range by 2-D EUV spectroscopy.

The stochastic magnetic field in the ergodic layer has a variety of magnetic field connection lengths of $10 \leq L_c \leq 2000$m which correspond to 0.5-100 toroidal turns of the LHD torus. There is a space with shorter L_c ($L_c \leq 10$m) outside the ergodic layer called 'open magnetic field layer' [7]. Until now any plasma has not been observed in the open magnetic field layer because the divertor configuration is intrinsically created at edge boundary of the ergodic layer as seen in Fig.1. All the particles coming out the ergodic layer basically reach one of four sets of divertor plates. Since the divertor plate is made of graphite, the source of carbon impurity is believed to originate in the divertor plate. The vacuum vessel of LHD is covered by square protection tiles made of stainless steel forming the first wall. Therefore, the carbon and iron can be observed basically in all the discharges as an intrinsic impurity. However, the amount of iron in LHD plasmas is usually very low ($n_{Fe}/n_e \leq 10^{-4}$) because the impurity screening due to the ergodic layer works well for heavier impurities [8], while the amount of carbon is considerably high ($n_C/n_e \geq 10^{-2}$) [9] despite the existence of the impurity screening [10]. As a result, the carbon emissions are a good tool for the present 2-D EUV spectroscopy. It is noted that the total radiation at plasma edge is very roughly comparable between carbon and iron.

3. Results and discussions on 2-D measurement at R_{ax}=3.60m and 3.75m configurations

The 2-D distribution of CIV at 312Å is measured from low-density discharges ($n_e \sim 1 \times 10^{13}$cm^{-3}) at two different magnetic axis configurations of R_{ax}=3.60m and 3.75m, as shown in Figs.2 (a) and (c), respectively.

It is noticed that the range of horizontal axis is a little different between Figs.2 (a) and (c) due to a different operational parameter setting for the 2-D measurement. From the figures it is clear that the CIV is dominantly emitted from plasma edge and X-point. The edge emission at the top (Z=450mm) and the bottom (Z=-450mm) in the 2-D distribution is enhanced by a relatively long emission volume along the observation chord, which is a normal feature for line emissions of impurities localized at the plasma edge. Then, the 2-D CIV distribution from plasma edge is similar between the two configurations of R_{ax}=3.60m and 3.75m. On the other hand, the X-point emission is entirely different between the two configurations. The X-point emission at R_{ax}=3.60m is dominated by the inboard X-point trajectory, while the outboard X-point trajectory seems to be dominant at R_{ax}=3.75m. In order to understand the change in the X-point trajectory the CIV distribution is simulated with three-dimensional transport code, EMC3 [11] –EIRENE [12,13]. The result is shown in Figs.2 (b) and (d) for R_{ax}=3.60m and 3.75m cases, respectively. The observation range is denoted with diamond dashed line as well as Fig.1. A clear discrepancy is seen between the measurement and simulation in the result of R_{ax}=3.60m configuration, whereas the simulation at R_{ax}=3.75m shows a good agreement with the measurement. The simulation always tends to enhance the emission along the outboard X-point trajectory. It is probably caused by a relatively large plasma volume in the vicinity of outboard X-point. The reason why the inboard X-point trajectory is enhanced at R_{ax}=3.60m is examined by considering a specific feature of R_{ax}=3.60m configuration.

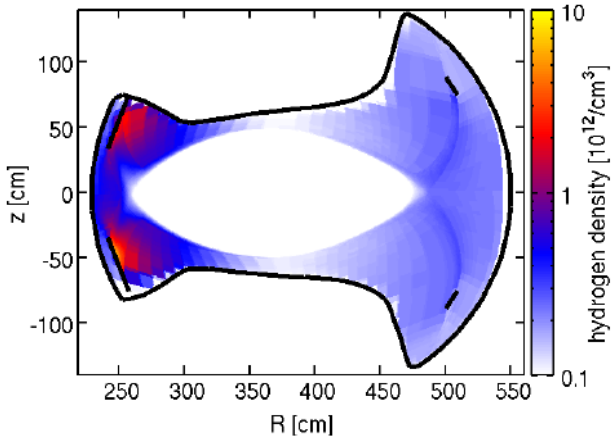

Fig.3 Neutral hydrogen density distribution at R_{ax}=3.60m configuration.

In LHD the inboard side of the torus forms a closed space because the elliptical plasma of LHD poloidally rotates five times during one toroidal rotation and the distance between the plasma edge and the first wall is very narrow at the inboard side of vertically elongated plasma cross section. The distance as a function of R_{ax} is minimal at R_{ax}=3.60m configuration, i.e. ~2cm and the plasma begins to interact with the first wall at R_{ax}=3.55m. Therefore, the inboard side space of the torus is practically divided into ten closed spaces, since the LHD toroidal plasma has ten horizontally and vertically elongated plasma cross sections (see Fig.1). Here, it should be mentioned that the highest confinement performance in LHD is obtained at R_{ax}=3.60m configuration because of the largest plasma volume and smaller deviation of high-energy particle orbit from magnetic surfaces. Until now no significant plasma-wall interaction has been observed at R_{ax}=3.6m configuration.

Figure 3 shows an example of neutral hydrogen distribution at R_{ax}=3.60m calculated with 3-D

EMC3–EIRENE code [14]. The neutral density at inboard side is an order of magnitude higher than that at outboard side. If the neutral is poloidally localized in such an open divertor system like LHD, the local density source becomes big at the neutral ionization depth. The local density gradient along magnetic field is enhanced due to the increased local density. The change in the density gradient can modify the local impurity transport in the ergodic layer through a change in the friction force working as motive force of the impurity screening.

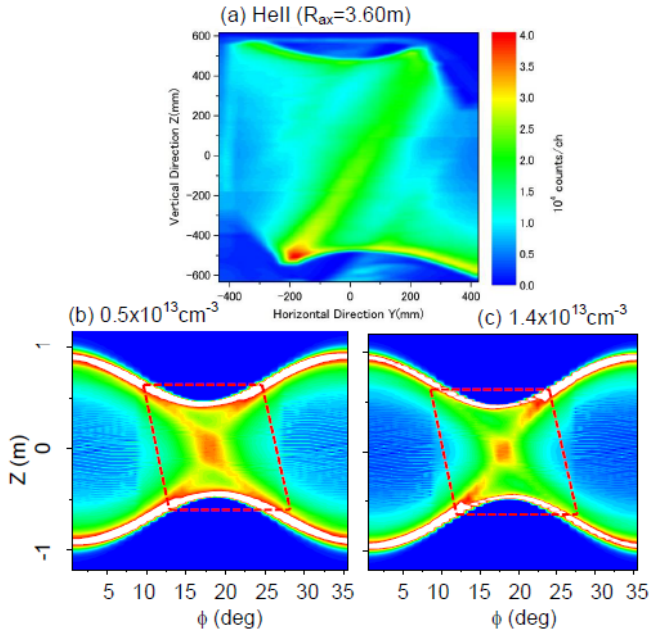

Fig.4 2-D distributions of HeII EUV line emissions at 304Å; (a) measurement and 3-D simulation with (b) n_{LCFS}=0.5x10^{13}cm^{-3} and (c) n_{LCFS}=1.4x10^{13}cm^{-3}.

Figures 4(a) shows a 2-D HeII distribution measured at R_{ax}=3.60m. The simulated result to the measurement is shown in Fig. 4(b). It indicates that the simulation disagrees with the measurement and the result is very similar to the CIV case in Figs. 2(a) and (b). In order to make sure of the neutral effect mentioned above, the 3-D simulation of HeII is done by mandatorily increasing the neutral density. The edge density is increased to 1.4x10^{13}cm^{-3} to reproduce a high neutral recycling at the inboard side. In the EMC3- EIRENE code the divertor field called 'divertor legs' in LHD is not explicitly expressed, but the divertor function is practically included by considering the particle movement between the ergodic layer and divertor plates. The result is shown in Figs.4 (c). The X-point trajectory is clearly changed to the inboard side. The result seems to be more persuasive for explaining the measurement, if we include further effect of the local neutral hydrogen in the simulation. The HeII emission moved outside is condensed into smaller region near inboard X-point which is caused by an enhanced friction force.

4. Summary

It is observed that the impurity differently behaves in the vicinity of inboard and outboard X-points between R_{ax}=3.60m and 3.75m configurations. The effect of neutrals localized at the inboard side on the edge impurity behavior is examined as a possible candidate to explain the discrepancy observed at R_{ax}=3.60m configuration. The friction force enhancement caused by an increase in the neutral density can

possibly modify the edge impurity transport. In order to calculate more precisely the effect of neutrals on the impurity transport EMC3-EIRENE code is probably necessary for introduction of a divertor simulation code.

Acknowledgements

The authors thank all the members of the LHD team for their cooperation through the LHD experiment. This work was partially carried out under the LHD project financial support (NIFS13ULPP010) and partly supported by the JSPS-NRF-NSFC A3 Foresight Program in the field of Plasma Physics (NSFC: No.11261140328).

References

[1] C.Giroud, G.Maddison, K.McCormick et a., Nucl. Fusion 52 (2012) 063022.
[2] M.Kobayashi, S.Masuzaki, I.Yamada et al., Phys. Plasmas 17 (2010) 056111.
[3] M.Kobayashi, S.Morita, C.F.Dong et al., Nucl. Fusion **53** (2013) 033011.
[4] C.F.Dong, S.Morita, M.Goto and E.H.Wang Rev.Sci.Instrum. **82** (2011) 113102.
[5] E.H.Wang, S.Morita, M.Goto, C.F.Dong Rev. Sci. Instrum. **83** (2012) 043503.
[6] S.Morita, E.H.Wang, C.F.Dong et al., to be published in IEEE Transactions on Plasma Sci.
[7] S.Morita, E.H.Wang, M.Kobayashi et al., to be published in Plasma Phys. Control. Fusion 56 (2014).
[8] S.Morita, C.F.Dong, M.Kobayashi et al., Nucl. Fusion **53** (2013) 093017.
[9] H.Y.Zhou, S.Morita, M.Goto and C.F.Dong, Jpn.J.Appl.Phys. **49** (2010) 106103.
[10] M.B.Chowdhuri, S.Morita, M.Kobayashi et al., Phys. Plasmas **16** (2009) 062502.
[11] Y.Feng, F.Sardei, J.Kisslinger et al., Contrib. Plasma Phys. **44** (2004) 57.
[12] D.Reiter, M.Baelmans and P.Börner Fusion Sci. Technol. **47** (2005) 172.
[13] M.Kobayashi, Y.Feng, S.Morita et al., Fusion Sci. Tech. **58** (2010) 220.
[14] G.Kawamura, Y.Feng, M.Kobayashi et al., Contrib. Plasma Phys. **54** (2014) 437.

VUV Spectroscopy in Wavelength Range of 500-2200 Å for Line Spectrum and Ion Temperature Measurements of Tungsten Ions at Low Ionization Stages in Large Helical Device

T. Oishi[1,2,a)], S. Morita[1,2], X. L. Huang[2], H. M. Zhang[2], M. Goto[1,2] and the LHD Experiment Group
[1] *National Institute for Fusion Science, 322-6, Oroshi-cho, Toki, 509-5292, Japan*
[2] *Department of Fusion Science, Graduate University for Advanced Studies, 322-6, Oroshi-cho, Toki, 509-5292, Japan*

Abstract
Vacuum ultraviolet (VUV) spectra of emissions released from tungsten ions at lower ionization stages were measured in the Large Helical Device (LHD) in the wavelength range of 500 to 2200 Å using a 3 m normal incidence spectrometer. Tungsten ions were distributed in the LHD plasma by injecting a pellet consisting of a small piece of tungsten metal and polyethylene tube. Many lines having different wavelengths from intrinsic impurity ions were observed just after the tungsten pellet injection. Doppler broadening of a tungsten candidate line was successfully measured and the ion temperature was obtained.

I. INTRODUCTION

Tungsten is regarded as a leading candidate material for the plasma facing components in ITER and future fusion reactors. Thus, behavior of tungsten in toroidal plasmas has attracted attention[1-3]. Considering tungsten impurity transport in ITER, the following three transport processes need to be evaluated: (1) release of neutral tungsten atoms from the divertor plates; (2) transport of tungsten ions at lower ionization stages in the edge plasmas; and (3) accumulation of tungsten ions at higher ionization stages in the core plasmas. Therefore, diagnostics for tungsten impurity ions in magnetically-confined high-temperature plasmas have been intensively conducted, such as visible spectroscopy for neutral tungsten atoms in the wavelength range around 4000 Å and extreme ultraviolet spectroscopy for highly-ionized tungsten ions in the wavelength range around 60 Å[4]. However, tungsten ions at lower ionization stages have not been measured except for several cases of vacuum ultraviolet (VUV) spectroscopy in basic plasma experiments even though it is necessary for accurate evaluation of tungsten influx and comprehensive understanding of the tungsten impurity transport in high temperature plasmas[5,6]. In the present study, VUV spectra of emissions released from tungsten ions are measured using a 3 m normal incidence spectrometer in the Large Helical Device (LHD) in the wavelength range of 500 to 2200 Å. Identification of lines which are useful for diagnostics of tungsten ions at low ionization stages in ITER is attempted for the study of transport phenomena of tungsten ions in the edge plasmas.

II. EXPERIMENTAL SETUP

In this study, tungsten ions are distributed in the LHD plasma by injecting a polyethylene pellet containing a small piece of tungsten metal. Figure 1 is a schematic drawing of VUV spectroscopy in impurity pellet injection experiments. LHD has the major/minor radii of 3.6/0.64 m in the standard configuration with maximum plasma volume of 30 m^3 and toroidal magnetic field of 3 T. The coil system consists of a set of two continuous superconducting helical coils with poloidal pitch number of 2 and toroidal pitch number of 10 and three pairs of superconducting poloidal coils. Figure 1(a) illustrates the top view of the instruments together with the optical axis of the VUV spectrometer and the incident orbit of the impurity pellet. The enlarged view of the vertical view angle of the VUV spectroscopy and the pellet orbit on the horizontally-elongated cross section of the magnetic field in LHD are also illustrated in Fig. 1(b). The tungsten impurity pellet consists of a small piece of tungsten wire covered by a polyethylene tube. The length and diameter of tungsten wire is 0.6 mm and 0.15 mm, respectively. The polyethylene tube has a dimension of 0.6 mm in length, 0.6 mm in outer diameter, and 0.3 mm in inner diameter[7]. The pellet is accelerated by pressurized He gas of 10-20 atm. The pellet injection orbit is located on the midplane of the plasma having a 12° angle from the normal to the

toroidal magnetic axis[8]. The 3m normal incidence VUV spectrometer (McPherson model 2253) is installed on an outboard midplane diagnostic port which is the same as the impurity pellet injector[9,10]. The working wavelength range of the spectrometer is of 300 to 3200 Å. A mirror unit which consists of a convex mirror and a flat mirror is mounted in front of the entrance slit of the spectrometer, which expands the view angle so that the elliptical plasma of LHD can be fully observed at the horizontally-elongated plasma cross section. A back-illuminated CCD detector (Andor model DO435-BN: 1024 × 1024 pixels) is placed at the position of the exit slit of the spectrometer. CCD was operated in the "Full-binning" mode in which all 1024 vertical pixels are replaced by a single channel. Then, the spatial resolution is entirely eliminated. A slit for spatial resolution mounted between the entrance slit and the grating was fully opened to increase S/N ratio. Each spectrum can be taken with a time interval of 50 ms. The width of the entrance slit is set to 50 μm and the instrumental function is 0.194 Å in the full width of half maximum. A high wavelength dispersion of 0.037 Å/pixel enables measurements of the Doppler broadening of the impurity lines to obtain the ion temperature. The wavelength interval which can be measured in a single discharge is about 37 Å. Therefore, we conducted measurements by scanning the wavelength shot by shot between the wavelength range of 500-2200 Å in this study[11].

III. LINE SPECTRA AND ION TEMPERATURE MEASUREMENT

Figure 2 shows VUV spectra measured in the time frame just after the tungsten pellet injection in hydrogen discharge in LHD. The plasma was initiated by the electron cyclotron heating, and three neutral hydrogen beams based on negative ion sources with total port-through power of 8 MW were injected. Central electron density and temperature just before the pellet injection was 2×10^{13} cm^{-3} and 3 keV, respectively. In Fig. 2, well-known intrinsic impurity lines used for absolute wavelength calibration are indicated by solid arrows[12]. Except for those intrinsic impurity lines, several bright lines have been successfully observed, such as 605.93 Å in Fig. 2(a), 639.66 Å in Fig. 2(b), 677.72 Å in Fig. 2(c), and 1168.15 Å in Fig. 2(d). These lines have wavelengths almost identical to WVI lines with the wavelengths of 605.926 Å, 639.683 Å, 677.722 Å (5d-6p), and 1168.151 Å (6s-6p)[12]. The second order emission of 605.93 Å, 639.66 Å and 677.72 Å lines were also observed as shown in Figs. 2(e-g). In this experiment, those lines appeared at the time frame just after pellet injection and almost all of them disappeared immediately. Therefore, they are considered to be tungsten emission from the pellet ablation process. Those newly found tungsten candidate lines will be useful for spectroscopic study because they have a relatively large intensity and are isolated from other intrinsic impurity lines. On the other hand, a few tungsten candidate lines including 677.72 Å line existed for a finite time after the pellet injection. This means that tungsten ions are distributed in plasmas. The temporal evolution of the line emission was investigated, as shown in Fig. 3. In this discharge, the heating scenario was the same as stated above. When the pellet is injected, the electron temperature drops and the electron density increases rapidly. Figure 3(b) shows the temporal evolution of line emission intensity evaluated by the area of the spectral peak and the ion temperature, T_i, obtained from the Doppler broadening of the spectrum when the atom mass is assumed to be that of tungsten. The line intensity

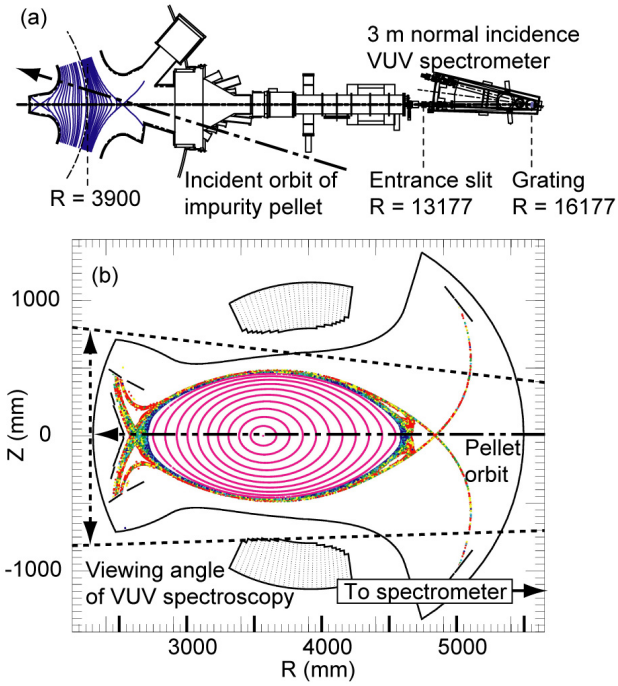

FIG. 1. Schematic drawing of VUV spectroscopy in impurity pellet injection experiments. (a) Top view of the instruments together with the optical axis of the VUV spectrometer and the incident orbit of the impurity pellet. (b) Vertical viewing angle and the pellet orbit on the poloidal cross section of the magnetic field in LHD.

indicated by opened circles increased once at the timing of the pellet injection and turned to decrease down to 4.3s, and finally disappeared. During the period 4.0-4.3s in which the line existed, T_i increased from 400 eV to 700 eV. However, some arguments remain for the reasonability of these values of T_i if this line is assumed to be WVI. During the high density period after the pellet injection, a condition of $T_e = T_i$ is achieved because of the high collisionality. Therefore, impurity ions in a certain charge state cannot exist in a region in which T_i is much higher than the ionization potential, E_i, for the charge state. However, T_i obtained from the Doppler broadening of W 677.72 Å line ranging from 400 eV to 700 eV is much larger than E_i (W^{5+}) of 64.8 eV. At present, the reason for this contradiction has not yet been clarified. Several reasons may be considered, such as emission from an unidentified line of tungsten ion at higher ionization stages or other broadening mechanisms of the spectra, which should be investigated in future studies. Figures 3 (c) and (d) show line intensities and ion temperatures evaluated from CIII 690.52 Å ($1s^22s2p$-$1s^22s3s$) and OIII 703.85 Å ($2s^22p^2$-$2s2p^3$) lines, respectively, measured in the same wavelength range to W 677.72 Å line. Signals were averaged over every 250 ms because of low intensities. The values of T_i for these lines were likely to be measured correctly because they ranged around their ionization potentials, E_i (CIII) of 47.9 eV and E_i (OIII) of 54.9 eV. Figure 4 shows enlarged wavelength spectra of W 677.72 Å line in several time frames after the pellet injection. We can find that broadening of the spectra was measured under adequate wavelength resolution and signal-to-noise ratio. These results indicate validity of the measurement and analysis methods applied in this study to obtain temperatures of impurity ions. In addition to strong lines discussed above, we found many tungsten candidate lines in this study. Their wavelengths will be summarized and compared to references, calculations, and basic experiments for accurate line identification. We also intend to propose the useful tungsten line for the spectroscopic study in ITER edge plasmas based on the progress of this study.

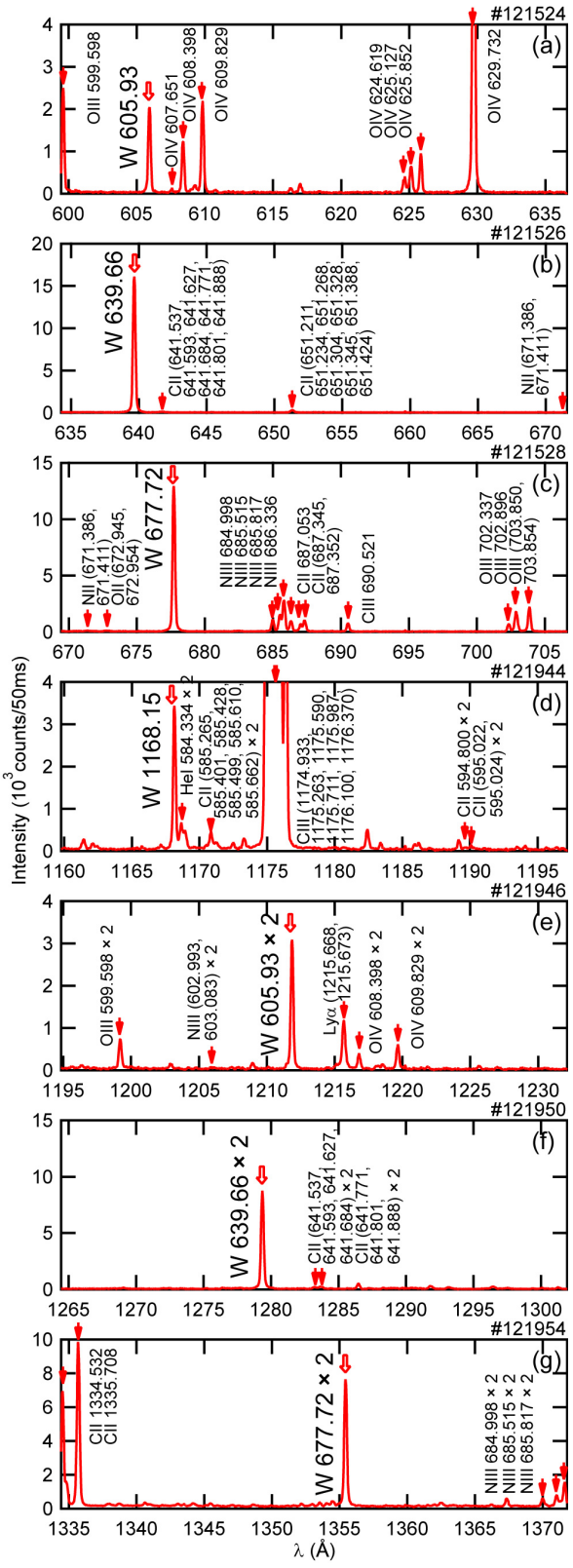

FIG. 2. VUV spectra including tungsten candidate lines.

IV. SUMMARY

A VUV spectroscopy using a 3 m normal incidence spectrometer was applied to measure VUV lines from tungsten ions at lower ionization stages in the wavelength range of 500-2000 Å. Many lines having different wavelengths from intrinsic impurity ions were observed just after the tungsten pellet injection. 605.93 Å, 639.66 Å, 677.72 Å, and 1168.15 Å were clearly identified as tungsten candidate lines, which have the possibility to be useful lines for spectroscopic study in the ITER edge plasmas. While the Doppler broadening of 677.72 Å line was successfully measured, identification of the charge state based upon a comparison between obtained T_i and the ionization potential requires further discussion.

ACKNOWLEDGMENTS

The authors thank all the members of the LHD team for their cooperation with the LHD operation. This work is partially conducted under the LHD project financial support (NIFS13ULPP010). This work was also supported by Grant-in-Aid for Young Scientists (B) 26800282 and partially supported by the JSPS-NRF-NSFC A3 Foresight Program in the field of Plasma Physics (NSFC: No.11261140328, NRF: No.2012K2A2A6000443).

REFERENCES

[1]ITER Physics Basis Editors *et al.*, Nucl. Fusion **39**, 2137 (1999).

[2]R. Neu *et al.*, Nucl. Fusion **45**, 209 (2005).

[3]J. Roth et al., *Plasma Phys. Control. Fusion* **50**, 103001 (2008).

[4]S. Morita *et al.*, AIP Conf. Proc. **1545**, 143 (2013); *Proceedings of ICAMDATA-2012*, Gaithersburg, 30 September–4 October 2012.

[5]R. Radtke *et al.*, *Atomic and Plasma-Material Interaction Data for Fusion* (IAEA, 2007), Vol. 13, p. 45.

[6]J. Clementson *et al.*, J. Phys. B: At. Mol. Opt. Phys. **43**, 144009 (2010).

[7]X. L. Huang *et al.*, "Coaxial Pellets for Metallic Impurity Injection on the Large Helical Device", Rev. Sci. Instrum. (submitted)

[8]H. Nozato *et al.*, Rev. Sci. Instrum. **74**, 2032 (2003).

[9]T. Oishi *et al.*, Plasma Fusion Res. **8**, 2402093 (2013).

[10]T. Oishi *et al.*, J. Korean Phys. Soc. **64**, 840 (2014).

[11]T. Oishi *et al.*, "Line spectrum and ion temperature measurements from tungsten ions at low ionization stages in large helical device based on vacuum ultraviolet spectroscopy in wavelength range of 500–2200 Å", Rev. Sci. Instrum. (in press)

[12]A. Kramida *et al.*, *NIST Atomic Spectra Database*, Version 5.1 (National Institute of Standards and Technology, Gaithersburg, MD, 2013), see http://physics.nist.gov/asd.

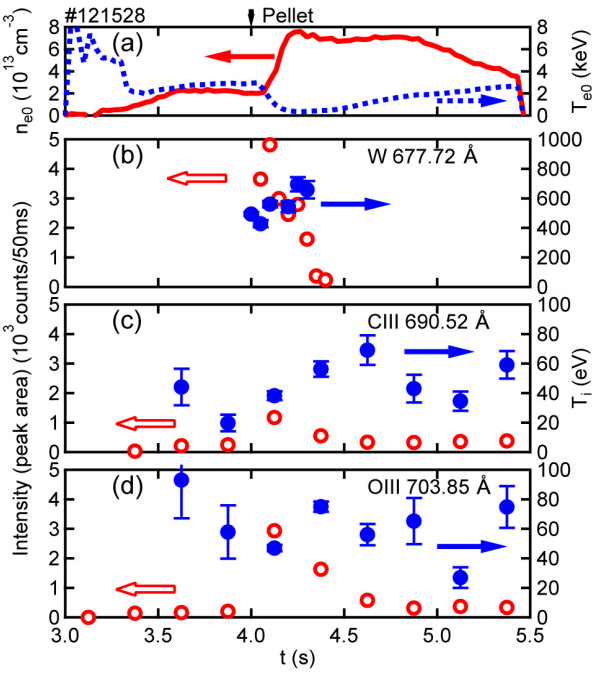

FIG. 3. (a) Temporal evolutions of central electron density and temperature in a hydrogen discharge with tungsten pellet injection. Line intensities and ion temperatures were evaluated from (b) tungsten candidate line located at 677.72 Å, (c) CIII 690.52 Å and (d) OIII 703.85 Å.

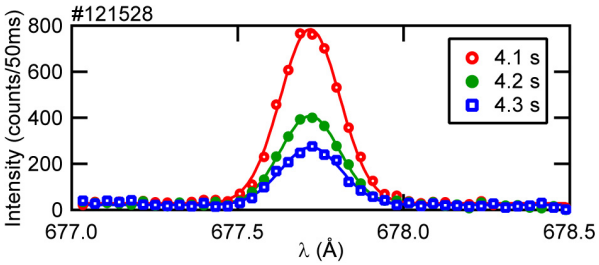

FIG. 4. Enlarged wavelength spectra of W 677.72 Å line in several time frames after the pellet injection.

Spectroscopic modeling for tungsten EUV spectra

Izumi Murakami[1], Daiji Kato[1], Hiroyuki A. Sakaue[1], Chihiro Suzuki[1], Shigeru Morita[1], Motoshi Goto[1], Akira Sasaki[2], Nobuyuki Nakamura[3], Norimasa Yamamoto[4], Fumihiro Koike[5],
and LHD Experimental Group[1]

[1] National Institute for Fusion Science, 322-6 Oroshi-cho, Toki, Gifu 509-5292, Japan
[2] Quantum Beam Science Directorate, Japan Atomic Energy Agency, 8-1-7 Umemidai, Kizugawa, Kyoto 619-0215, Japan
[3] Institute for Laser Science, The University of Electro-Communications, Chofu, Tokyo 182-8585, Japan
[4] Center of Applied Superconductivity and Sustainable Energy Research, Chubu University, Kasugai, Aichi 487-8501, Japan
[5] Faculty of Science and Technology, Sophia University, 7-1 Kioicho, Chiyoda-ku, Tokyo 102-8554, Japan

Abstract

We have constructed an atomic model for tungsten extreme ultraviolet (EUV) spectra to reconstruct characteristic spectral feature of unresolved transition array (UTA) observed at 4-7 nm for tungsten ions. In the tungsten atomic modeling, we considered fine-structure levels with the quantum principal number n up to 6 as the atomic structure and calculated the electron-impact collision cross sections by relativistic distorted-wave method, using HULLAC atomic code. We measured tungsten EUV spectra in Large Helical Device (LHD) and Compact Electron Beam Ion Trap device (CoBIT) and compared them with the model calculation. The model successfully explain series of emission peaks at 1.5–3.5 nm as n = 5–4 and 6–4 transitions of W^{24+} – W^{32+} measured in CoBIT and LHD and the charge state distributions were estimated for LHD plasma. The UTA feature observed at 4–7 nm was also successfully reconstructed with our model. The peak at ~5nm is produced mainly by many 4f–4d transition of W^{22+} – W^{35+} ions, and the second peak at ~6 nm is produced by 4f–4d transition of W^{25+} – W^{28+} ions, and 4d–4p inner-shell transitions, $4p^5 4d^{n+1}$ – $4p^6 4d^n$, of W^{29+} – W^{35+} ions. These 4d–4p inner-shell transitions become strong since we included higher excited states such as $4p^5 4d^n 4f$ state, which ADAS atomic data set does not include for spectroscopic modeling with fine structure levels.

Keywords: tungsten, spectroscopy, collisional-radiative model, EUV spectra

1. Introduction

Tungsten is planned to be used as plasma-facing material of divertor target for ITER and future fusion reactors, because of high melting point, low sputtering yield by hydrogen, and low tritium inventory. However, once tungsten is sputtered from target by some impurities, it is transferred into main plasma and causes radiation power loss to cool plasma. Tungsten is not fully ionized even in the core of ITER plasma with electron temperature of 15–20 keV, where tungsten is ionized up to W^{71+} (Li-like tungsten), and radiation power of such tungsten ions is large. It is also important for the stable operation of ITER to study the influx and edge transport of tungsten ions. Tungsten behavior in plasmas can be studied with spectroscopic method and we need a reliable atomic model for tungsten to analyze spectral data.

Previous studies on tungsten atomic modeling have not fully explained tungsten extreme ultraviolet (EUV) spectra, e.g., an unresolved transition array (UTA) seen at 4.5–7.0 nm in plasma with $T_e < 1.5$ keV [1], which corresponds to edge plasma temperature for ITER. Since the UTA is composed of numerous inseparable emission lines, it has been difficult to analyze the UTA quantitatively. Especially, the second peak of UTA at ~6 nm was not reproduced by Pütterich et al. [1] and they explained that this peak could be produced by lower-charged tungsten ions or via dielectronic recombination processes which they did not included in their atomic model, since there were no significant emission peaks observed in Berlin EBIT spectra [2]. However, the atomic data used in the model of Pütterich et al. did not consider detailed atomic structure and number of energy levels were limited up to ~2000 for one ion. Electron impact excitation cross sections were calculated with Coulomb-Born approximation, which was reliable only at high collision energy. Therefore their model was not sufficient to analyze spectra in detail. The charge state distributions in the Berlin-EBIT experiments were not so well controlled [2].

We have developed a tungsten atomic model with detailed atomic structure and validated the model by comparing with EUV spectra measured from LHD plasmas with tungsten pellet injection and compact electron beam ion trap (CoBIT) plasmas [3] with tungsten hexacarbonyl vapor. The LHD discharge is entirely stable for substantial amount of tungsten injection exhibiting no MHD instabilities. The CoBIT experiments well control the charge distribution of tungsten ions by changing the electron beam energy which determines the highest charge state in the plasma and by controlling vapor gas pressure of hexacarbonyl. The information from CoBIT spectra is absolutely helpful to identify the EUV lines in LHD.

In the following sections, our tungsten atomic model is explained in section 2, and the spectroscopic experiments in CoBIT and LHD are shown in section 3. We discuss the results for the UTA in section 4 and summarize in section 5.

2. Tungsten atomic model

As the tungsten atomic model, we have constructed a collisional-radiative (CR) model for tungsten ions. In the CR model, we solve rate equations for population densities $n(i)$ of excited states with quasi-steady state assumption for given electron temperature and density. We include electron-impact ionization, excitation and de-excitation processes, and radiative decay in the rate equations. The rate equation for the excited level i is described as

$$\begin{aligned} dn(i)/dt = &\sum_{j<i}\{C(j,i)n_e n(j)\} + \sum_{k>i}\{F(k,i)n_e + A(k,i)\}n(k) \\ &-[S(i)n_e + \sum_{k>i} C(i,k)n_e + \sum_{j<i}\{F(i,j)n_e + A(i,j)\}]n(i), \end{aligned} \tag{1}$$

where $C(j,i)$ and $F(k,i)$ are electron-impact excitation and de-excitation rate coefficients, n_e is electron density, $A(k,i)$ is radiative transition probabilities, and $S(i)$ is electron-impact ionization rate coefficient. The recombination processes are ignored since these processes are not important for plasmas considered here. Energy levels, radiative transition probabilities, electron-impact excitation and ionization cross sections are calculated with HULLAC code [4]. In the HULLAC code, atomic structure is calculated with Dirac Hamiltonian using parametric potential method and configuration interaction is included. Collision cross sections are calculated with a relativistic distorted wave method. We consider fine-structure levels including inner-shell excited states with principal quantum number n up to 6. So we treat about 4000 – 20,000 levels for one ion in the CR model. Rate coefficients for electron-impact excitation and ionization processes are obtained by averaging with electron velocity distribution as $C(i, j) = \langle s(i,j)\, \boldsymbol{v} \rangle$,. We use the Maxwellian velocity distribution to compare with spectra taken in LHD, and use mono-energy distribution for CoBIT spectra. The rate equations (eq.(1)) are solved with the quasi-steady state assumption as $dn(i)/dt = 0$ for excited levels, because the relaxation timescale of the population densities is fast enough compared to the timescales for changes in electron density and temperature.

Here we consider W^{q+} ions with q = 20–45 and they are N-shell ions, i.e. the outermost electron is in n = 4 shell for the ground state. Namely, the ground states are 4s for W^{45+}, $4s^2$ for W^{44+}, $4s^2 4p^k$ with k =

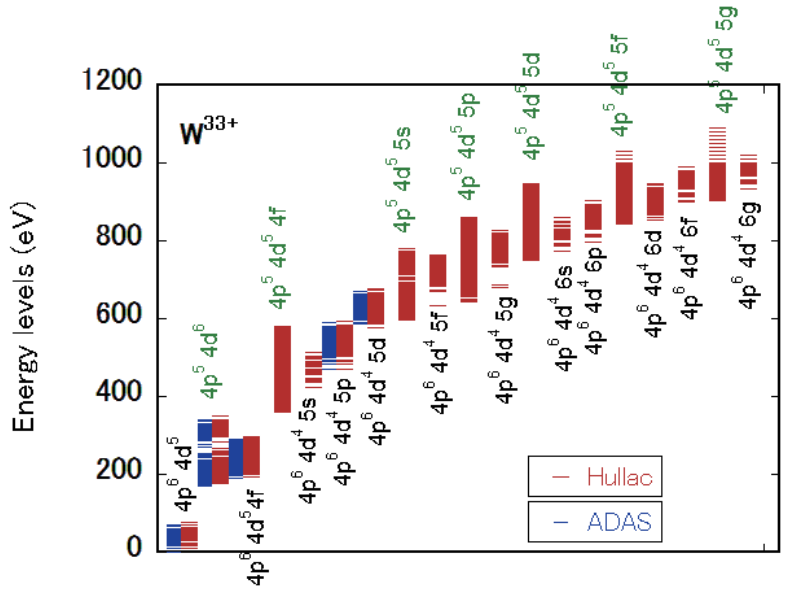

Fig.1 Energy levels for W^{33+} ion, calculated with HULLAC code (black) in our model and data in ADAS database (gray) which Pütterich et al. used [1]. Data in ADAS considers only 5 configurations.

1–6 for W^{43+} – W^{38+}, $4s^24p^64d^k$ with k = 1–10 for W^{37+}– W^{28+}, and $4s^24p^64d^{10}4f^k$ with k = 1–8 for W^{27+} – W^{20+}. Ionization potentials for these ions are 543–2,414eV [5] and they can be seen in LHD plasmas. In the CR model, we consider the excited states including inner-shell excited states. For example, for the case of W^{33+} ion, we consider $4s^24p^64d^5$, $4s^24p^54d^6$, $4s^24p^64d^4nl$ (n = 5–6 and l = 0–4), $4s^24p^54d^55l$ (l = 0–4) states as electron configurations and 14,050 fine structure levels in total (Fig. 1).

Spectral line intensities are obtained with the population densities of the upper level for the transition

$$I(i, j; T_e, n_e) = n(i)\, A(i, j)\mathrm{DE}(i,j), \qquad (2)$$

where DE(i,j) is the transition energy and $n(i)$ is obtained from the CR model. We give electron density n_e and temperature T_e to solve the rate equations.

3. Experiments

3.1 Spectroscopic measurements in CoBIT

Tungsten EUV spectra are measured for plasma in CoBIT [6]. Tungsten hexacarbonyl vapor is introduced into CoBIT, and tungsten is ionized sequentially by the electron beam and trapped by electrostatic potential well in the axial direction and by electronic space charge potential in the radial direction. EUV spectra at 1.5–4.5 nm wavelength region were measured with various electron beam energy and the charge states of observed emission peaks are determined. In this wavelength region, several emission peaks were observed and their peak wavelengths are shifted with the charge state. Using the CR model, we calculate EUV spectra with the physical condition of CoBIT, i.e., $n_e = 10^{10}$ cm^{-3} and mono-energy electron distribution with the beam energy. Figure 2 shows the measured EUV spectrum in CoBIT with electron beam energy 1,170 eV and calculated spectra by the CR model. To synthesize spectrum we determined the ion abundances to fit with the measured spectrum. We obtain good agreement between the measured and synthesized spectra. In this case, peaks at 2.0–2.4nm are 5f–4d transitions of W^{29+}– W^{25+} ions, and peaks at 2.7–3.6nm are 5g–4f and 5p–4d transitions. Figure 3 shows the peak wavelength shifts depending on the charge state q of W^{q+}. Peaks at shorter wavelengths are 5f–4d transitions for q>27 and 6g–4f transitions for q < 28. Peaks at longer wavelengths are 5g–4f and 5p–4d transitions. This indicates that the charge state dependence of the peaks can be used to determine charge state distribution in LHD plasmas.

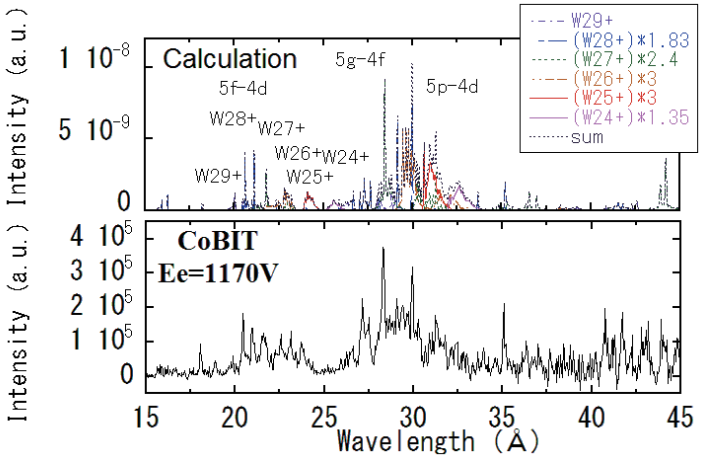

Fig. 2 Tungsten EUV spectra measured in CoBIT (lower) with electron beam 1170eV and calculated with our CR model (upper).

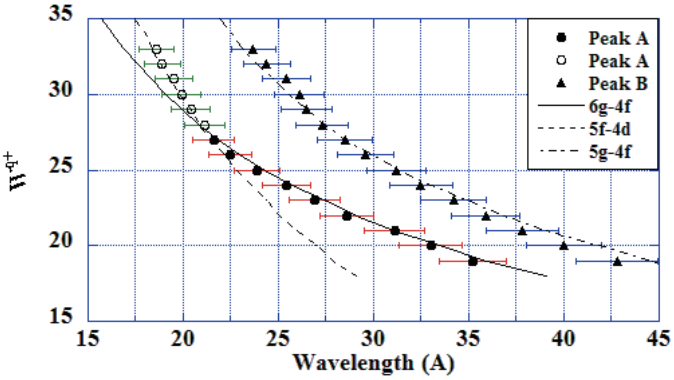

Fig.3 The wavelength shift of EUV emission lines for Tungsten ions measured in CoBIT [6].

3.2 Spectroscopic measurements in LHD

In LHD plasmas tungsten is injected as an impurity pellet. A pellet is ablated and tungsten is ionized and is maybe transferred into a core plasma region for discharges with typical central electron density n_e ~ a few 10^{13}cm^{-3}. Radiation from tungsten reduces electron temperature of a core plasma.

We measured EUV spectra at 1–7 nm wavelength region using an EUV spectrometer. At 1.5–3.5 nm we obtain similar spectra to ones measured in CoBIT and spectra change according to the change of central electron temperature. In order to explain the measured spectra, we calculate spectra using our CR model with the plasma condition of LHD, i.e., n_e ~ 5 ×10^{13} cm^{-3} and the Maxwellian electron velocity distribution with given electron temperature. Figure 4 shows EUV spectra measured in CoBIT and LHD, and calculated spectra for two cases. Namely, lower temperature case (central electron temperature T_0 = 0.7 keV) and higher temperature case (T_0 = 1.5 keV). Emission peaks observed in LHD show very similar structure to peaks measured in CoBIT, so they can be identified. The former spectrum has emission peaks of 6g–4f and 5g–4f transitions of W^{23+} – W^{28+}, and the latter has emission peaks of 5f–4d, 5g–4f, and 5p–4d transitions of W^{28+} – W^{34+}. We can reproduce the LHD spectra with our CR model calculations well as shown in Fig. 4. To fit with the LHD spectra, we determine charge state distribution of tungsten ions as shown in Fig. 5. For the lower temperature case, W^{24+} and W^{25+} ions are abundant, and W^{29+} and W^{30+} are abundant for the higher temperature case.

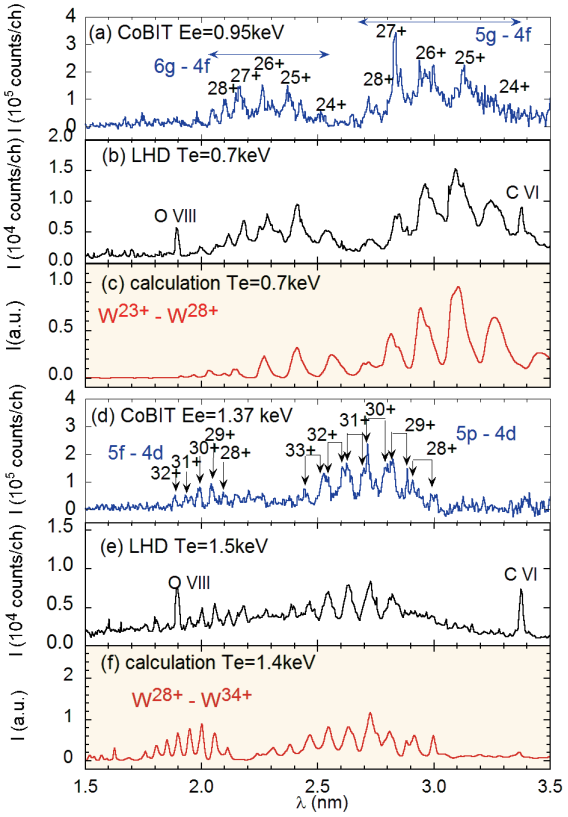

Fig. 4 EUV spectra of tungsten ions; (a, d) CoBIT with two electron beam energies *Ee*, (b, e) LHD with different electron temperature *Te*, and model calculations for (c) W^{23+} – W^{28+} and (f) W^{28+} – W^{34+} ions. Wavelengths in calculation at (c) are shifted by -0.15 nm to fit the position to measurements.

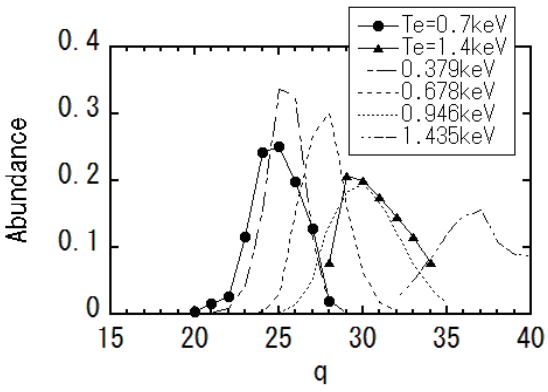

Fig. 5 Charge distribution of tungsten ions obtained by fitting to the measure LHD spectra (● and ▲), and calculated ones in ionization equilibrium [7].

Sasaki and Murakami [7] constructed a large-scale collisional-radiative model with configuration averaged levels to calculate tungsten ion densities in ionization equilibrium condition. Many autoionizing levels were included and dielectronic recombination process was treated explicitly as electron-capture to autoionizing levels, followed by radiative decay to bound levels. Ionization rate coefficients were calculated with Lotz's empirical formula [8]. We can compare their ion density distribution in the ionization equilibrium with our obtained distribution. Figure 5 shows that their equilibrium ion abundance distributions with the similar electron temperature are shifted toward higher charge states than our obtained one from the measurements. The similar abundance distributions are shifted to lower electron temperature, i.e., $T_e \sim 0.4$ keV for $T_0 = 0.7$ keV case, and $T_e \sim 0.9$ keV for $T_0 \sim 1.4$ keV case. These discrepancies indicate that 1) tungsten ions in LHD would not be in ionization equilibrium and behind the equilibrium, 2) tungsten ions would not accumulate in the center, but stay at lower temperature region, or 3) ionization equilibrium calculation would not be correct. Observed time variation of the EUV spectra follows the change of central electron temperature very well, so it is not easy to believe that the ionization stage would be behind the equilibrium. We need further investigation on the charge distributions.

4. Discussion

Now using the obtained charge distribution, we can calculate spectra at 4–7 nm wavelength region, where the UTA is seen. Figure 6 shows calculated spectra at 1–7 nm wavelength region. The characteristic two-peak UTA feature is reproduced: the first peak at ~5 nm is produced with $4d^{n-1}4f$–$4d^n$ transition (4f–4d transition) and the second peak at ~ 6 nm is produced with $4d^9 4f^{n+1}$–$4d^{10}4f^n$ transition of W^{25+} - W^{28+} ions (4f–4d transition) and $4p^5 4d^{n+1}$–$4p^6 4d^n$ transition of W^{29+} – W^{34+} ions (4d–4p transition). These inner-shell transitions are important to reproduced 6nm peak.

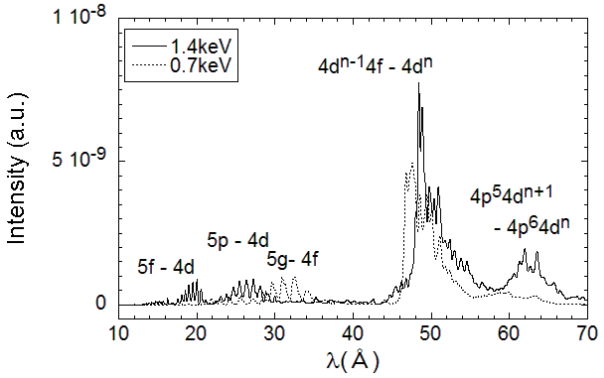

Fig. 6 Calculated spectra for Te = 0.7 and 1.4 keV with obtained charge distributions. Electron density $5 \times 10^{13} cm^{-3}$ is assumed in the calculation.

Pütterich et al. [1] used ADAS atomic database and their atomic data do not include many higher excited states, since they limited total number for energy levels up to ~2000 for dataset with J-resolved energy levels. As shown in Fig.1, only 5 configurations are considered for W^{33+} ion, for example. The $4p^5 4d^6$– $4p^6 4d^5$ inner-shell transition can be occurred even with the ADAS dataset, but higher excited states related to this upper level, such as $4p^5\ 4d^5\ 4f$ are not included. Two-step processes of the electron-impact excitation from $4p^6\ 4d^5$ to $4p^5\ 4d^5\ 4f$ and following de-excitation from $4p^5\ 4d^5\ 4f$ to $4p^5\ 4d^6$ are important to populate the $4p^5\ 4d^6$ levels larger and to produce stronger emissions at ~ 6 nm than the model without these

processes. Therefore it is very important to include higher excited states especially inner-shell excited states to reproduce measured spectra in plasmas.

5. Summary

We have constructed the tungsten atomic model including many fine structure levels and we can use the model for detailed analysis of spectra to examine tungsten behavior in fusion plasmas. The atomic model is validated by comparing calculated spectra with measured ones with CoBIT and LHD. We obtained good agreement for EUV spectra of W^{20+} – W^{33+} ions at 1.5–4.5 nm wavelength region for the CoBIT measurements and the model calculation. Using spectral peaks at 1.5–3.5 nm of n = 5– 4 transitions we can determine charge state distribution for W^{20+} – W^{33+} ions for the LHD plasma. These ions are produced in plasma with electron temperature from ~ 0.3 keV to ~ 1.5 keV. This temperature region corresponds to peripheral plasma in ITER.

Our model can reproduce the two-peak characteristics of the UTA at 4–7 nm. The second peak at ~ 6 nm is produced with $4d^9 4f^{n+1}$–$4d^{10} 4f^n$ transition of W^{25+} – W^{28+} ion and $4p^5 4d^{n+1}$–$4p^6 4d^n$ transition of W^{29+} –W^{34+} ions. Higher inner-shell excited states and the transitions between the inner-shell excited states are important to reproduce the ~ 6 nm peak.

We can apply our model to analyze spectra at longer vacuum ultraviolet wavelength regions for further study of tungsten behavior in LHD plasmas in future.

Acknowledgement

The authors acknowledge all members of LHD experiment group for their technical support and fruitful discussions. This work is supported partly by JSPS Grant-in-Aid for Scientific Research (A) 23246165 and (B) 23340183 and by the JSPS-NRF-NSFC A3 Foresight Program in the field of Plasma Physics (NSFC: No. 11261140328).

References

[1] T. Pütterich *et al*., AIP Conf. Proc. 1545 (2013) 132.
[2] R. Radtke *et al.*, Phys. Rev. A **64** (2001) 012720.
[3] N. Nakamura *et al*., Rev. Sci. Instrum. **79** (2008) 063104.
[4] A. Bar-Shalom *et al.*, J. Quant. Spectr. Rad. Transfer 71 (2001) 169-188.
[5] A. Kramida, Yu. Ralchenko, J. Reader, and NIST ASD Team (2013). *NIST Atomic Spectra Database* (ver. 5.1), [Online]. Available: http://physics.nist.gov/asd [2014, July 7].
[6] H. A. Sakaue *et al*., AIP Conf. Proc. **1438** (2012) 91.
[7] A. Sasaki and I. Murakami, J. Phys. B: At. Mol. Opt. Phys. **46** (2013) 175701.
[8] W. Lotz, Z. Phys. **216** (1968) 241.

Evaluation of ionization and recombination rate coefficients of tungsten ions in LHD plasmas by using UV-visible M1 lines

D. Kato[1], H.A. Sakaue, I. Murakami, M. Goto, T. Oishi, S. Morita, C. Suzuki
National Institute for Fusion Science, Toki, Gifu 509-5292, Japan

N. Nakamura
Inst. Laser Science, Univ. Electro-Communications, Tokyo 182-8585, Japan

A. Sasaki
Japan Atomic Energy Agency, Kyoto 619-0215, Japan

F. Koike
Sophia University, Tokyo 102-8554, Japan

X.-B. Ding, C.-Z. Dong
Northwest Normal University, Lanzhou 730070, China

1. Introduction

Electron temperatures in the core plasma of the Large Helical Device (LHD) is a few keV or lower using neutral beam injection (NBI) heating. We can, therefore, investigate tungsten line emissions of the lower charge states with the LHD, which are anticipated in peripheral regions of ITER. A novel idea of this work is to use forbidden lines in UV-visible ranges to measure the tungsten ion distributions in the core plasma of the LHD. Inherently narrow natural width of the forbidden lines is a suitable feature for identifying a specific charge state of ions in emission spectra.

We have observed a visible magnetic-dipole (M1) line emission from W^{26+} ions in the previous LHD experiments [1]. Recently, an M1 line of W^{27+} ions has also been identified, and its intensity distribution on a poloidal cross section was measured. The measured intensity distribution was compared with W^{27+} ion distributions calculated using available data of the ionization and recombination rate coefficients at electron temperatures measured by Thomson scattering.

2. LHD experiments

Discharges for present measurements were started with electron cyclotron heating followed by hydrogen NBI heating. Then, a solid pellet containing tungsten was injected into background hydrogen plasmas. We used the impurity pellet [2] which has a cylindrical carbon shell (diameter of 1.2 mmφ) with tin coating. Solid tungsten is contained inside a hole at the center of the carbon shell. Size of the solid tungsten in the

[1] E-mail: kato.daiji@nifs.ac.jp

pellet is 0.15 mm in diameter and 0.6 mm in length. Using the density of the solid tungsten, i.e. 19.25 g/cm^3, number of tungsten atoms in the single pellet is estimated to be 6.9×10^{22}. The impurity pellet is injected at speeds of 30 ~ 300 m/s by using a pneumatic pellet injector with helium gas.

Time-resolved (sampling times for 38 ms at every 100 ms) measurements of emission lines were performed using Czerny-Turner UV-visible spectrometers equipped with a CCD detector (10-O port). The pellet is injected at the same port with the observation port. An optical fiber array of 40 lines of sight was used to measure vertical profiles (Z-profiles) of photon emission in a horizontally elongated poloidal cross section.

3. Results and Discussion

In a steady state before the pellet injection, a peak electron temperature at the plasma center is sustained at about 3 keV by NBI heating. Fig. 1 depicts electron temperature and density profiles changing after the pellet injection at 4.0 s. The peak temperatures are decreased after the tungsten injection, while the electron densities are increased: line-averaged densities are increased from 2×10^{19} m^{-3} to 4 $\times10^{19}$ m^{-3}. The radial distribution of the temperature before the pellet injection shows a steep gradient at the edge. After the pellet injection, the density increase is pronounced in the edge region. Since tungsten is mainly deposited in the plasma edge region, the change in the electron temperature and density profiles can be ascribed to ablation of the tungsten pellet, ionization of the ablated tungsten particles and cross-field transport of the tungsten ions.

Fig. 2 shows an emission line spectrum measured during t=4.1 – 4.138 s in the discharge #121534. Its wavelength resolution is approximately 0.045nm. Wavelength calibration is done with the hydrogen

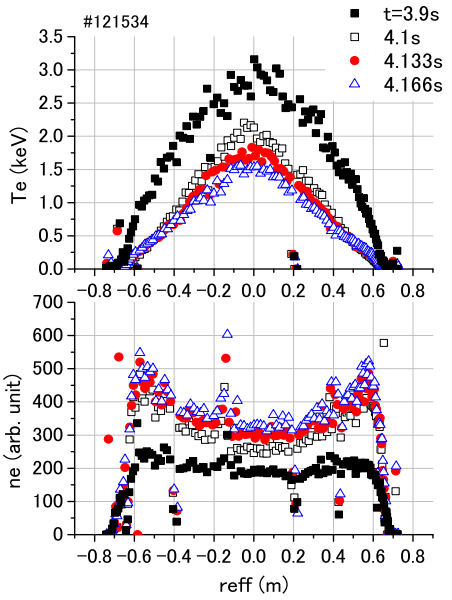

Fig. 1 Electron temperature and density profiles as a function of effective minor radius measured at the LHD (#121534) by Thomson scattering. A tungsten pellet is injected at t=4.0 s.

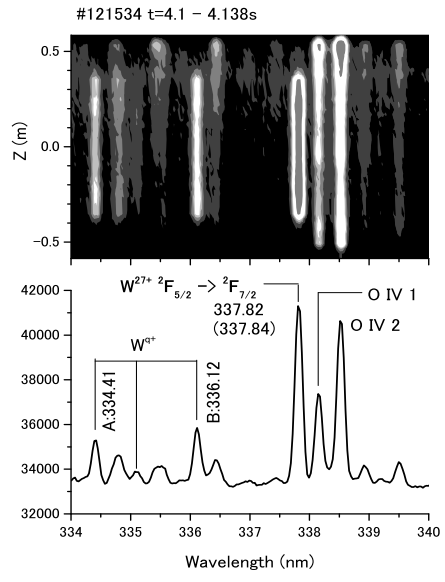

Fig. 2 Line emission measured after a tungsten pellet injection (t=4.1-4.138 s). Upper: A CCD image for Z-profile of an emission line spectrum. Lower: the emission line spectrum.

Balmer series of lines emitted in the last phase of the same discharge. The line at 337.82 nm is identified as the ground-term M1 transition, $4d^{10}4f\ ^2F_{5/2}$ - $^2F_{7/2}$, of W^{27+} ions. This M1 line has been discovered by using an electron beam ion trap (EBIT) at Fudan University [3]; its wavelength was determined to be 337.84 nm. Z-profile of the M1 line emission indicates a line intensity distribution localized inside the core plasma where electron temperatures are high enough to produce the W^{27+} ions (the ionization energy of W^{26+} is about 830 eV). Two lines from O^{3+} ions adjacent to the M1 line are identified, which show a border distribution in Z. In the spectrum, another three lines are also identified as emission lines of W^{q+} ions, because its Z-profiles are similar to that of the M1 line at 337.82 nm.

Fig. 3(a) shows a Z-profile of the line-integrated intensity of the M1 line at 337.82 nm and a simulation of the Z-profile which is an integral transformation of the given radial distribution depicted in Fig. 3(b) on a horizontally elongated poloidal cross section. The radial distribution has the maximum at around 0.3 m in the effective minor radius where a local electron temperature is measured to be about 1 keV. We investigate the present results in terms of predicted ion distributions of W^{27+} assuming the ionization equilibrium. We assume the ionization equilibrium, because a time-scale for ionization and recombination processes is believed to be much smaller than that of cross-field ion transport inside the core plasma.

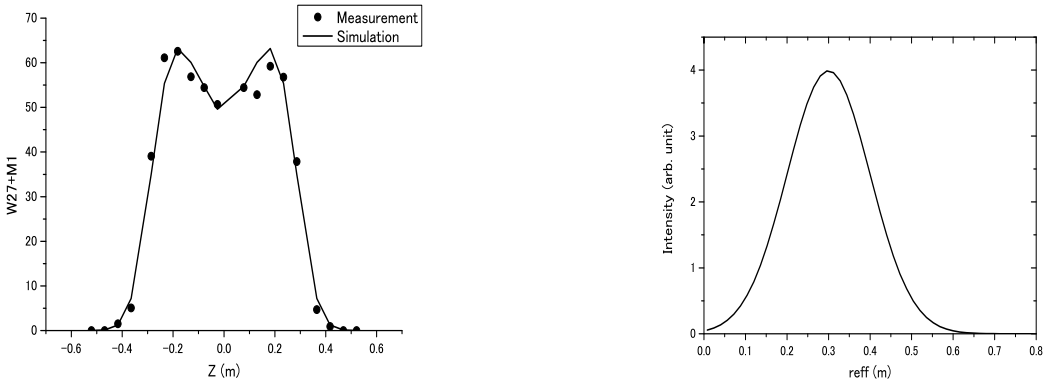

Fig. 3(a) left) Z-profile of line-integrated intensity of the W^{27+} M1 line at 337.82 nm. (b) right) Radial distribution of the line intensity on a horizontally elongated poloidal cross section.

A rate equation of local ion density n_q is written using ionization rate coefficients α and recombination rate coefficients β at a given local electron temperature,

$$\frac{\partial n_q}{\partial t} = -\left(\alpha_q + \beta_q\right) n_e n_q + \beta_{q+1} n_e n_{q+1} + \alpha_{q-1} n_e n_{q-1},$$

where q stands for charge states of ions and n_e is electron density. The coupled rate equations are integrated numerically using the implicit differencing method with the initial condition,

$$n_q(t=0) = \begin{cases} 1 & q = 0 \\ 0 & otherwise \end{cases}.$$

Fig. 4 shows a comparison of the radial distribution of the W^{27+} M1 line intensity and two ion distributions $n_{q=27}(t=\infty)$ calculated with different sets of data for the ionization and recombination rate coefficients. One set is obtained by using a fitting formula of ADPAK data [4], the other uses data calculated by Sasaki [5]. ADPAK data appears to give the ion distribution consistent with the measured distribution of the M1 line intensity, while Sasaki's data gives the distribution whose maximum is located at a lower local electron temperature. This is puzzling, because Sasaki's data are believed to be improved by including detailed indirect processes, e.g. excitation auto-ionization, dielectronic recombination, using HULLAC code [6] (ADPAK data is calculated assuming a simple screened hydrogenic model for the atomic states). This inconsistency is hardly ascribed to the cross-field ion transport, because in the core plasma it is believed to take place much slower than the ionization and recombination processes.

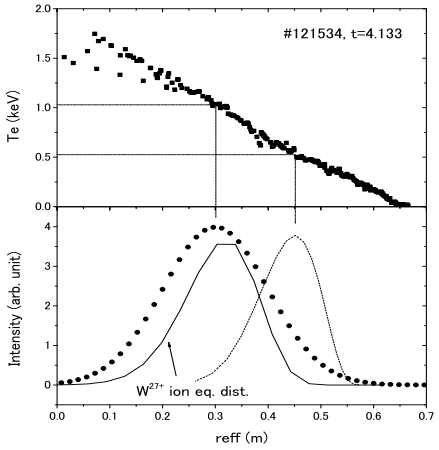

Fig. 4 An intensity distribution of the M1 line at 337.82 nm along the effective small radius. Upper: Electron temperature distribution. Lower: Radial distributions of the M1 line intensity (dot) and W^{27+} ions calculated assuming the ionization equilibrium with ionization/recombination rate coefficients, ADPAK (solid) [4] and Sasaki (dashed) [5].

Acknowledgement

The authors acknowledge all members of the LHD experiment group for their technical supports. This work is performed with the support and under the auspices of the NIFS Collaboration Research program (NIFS13KLPF032) and JSPS-NRF-NSFC A3 Foresight Program in the field of Plasma Physics (NSFC: No.11261140328, NRF : No. 2012K2A2A6000443).

Reference

[1] D. Kato et al., Phys. Scr. T156 (2013) 014081.

[2] H. Nihei et al., Rev. Sci. Instrum. 71 (2000) 3747.

[3] Z. Fei et al., Phys. Rev. A 86 (2012) 062501.

[4] K. Asmussen et al., Nucl. Fusion 38 (1998) 967.

[5] A. Sasaki and I. Murakami, J. Phys. B: At. Mol. Opt. Phys. 46 (2013) 175701.

[6] A. Bar-Shalom, M. Klapisch and J. Oreg, J. Quant. Spectrosc. Radiat. Transfer 71 (2001) 169.

Spectroscopic data of highly charged tungsten ions obtained with an electron beam ion trap

NAKAMURA Nobuyuki

Institute for Laser Science, The University of Electro-Communications, Tokyo 182-8585, JAPAN

INTRODUCTION

An electron beam ion trap (EBIT)[1] is a powerful device to obtain the atomic data of highly charged ions needed for understanding and controlling high temperature plasmas, such as fusion plasmas and the solar corona. It can trap highly charged ions interacting with a monoenergetic electron beam for many hours. It is thus regarded as a well-defined simple plasma consisting of unidirectional monoenergetic electrons and trapped ions with a narrow charge state distribution. Consequently the EBIT plasma is an unique and ideal source for high resolution spectroscopic studies of highly charged ions. Spectra from an EBIT are useful to survey and identify previously unreported lines, and also to provide benchmark for plasma models. An EBIT can also be used as a device to study the interactions of electrons with highly charged ions. Such spectroscopic and collisional data can be obtained for ions over wide ranges of charge state and atomic number; any ion of any element can practically be studied. Interaction energy between ions and electrons can also be varied over a wide range, such as 100 eV to more than 100 keV.

In this paper, we introduce two types of EBITs at the University of Electro-Communications; one is a high-energy EBIT called the Tokyo-EBIT[2] and another is a low-energy, compact EBIT called CoBIT[3]. Recent results with them are also presented.

ELECTRON BEAM ION TRAP (EBIT)

An EBIT[1] was developed at the Lawrence Livermore National Laboratory based on the principle of an electron beam ion source (EBIS)[4] developed at Joint Institute for Nuclear Research in Dubna. Figure 1 shows the schematic principle of an EBIT. An EBIT consists of a Penning-like ion trap and a high-energy, high-density electron beam going through the trap. Its main components are an electron gun, a drift tube (ion trap), an electron collector, and a superconducting magnet. The drift tube is composed of three (or more) successive cylindrical electrodes where a well potential is applied for trapping ions axially. Radial ion trap is achieved by the combination

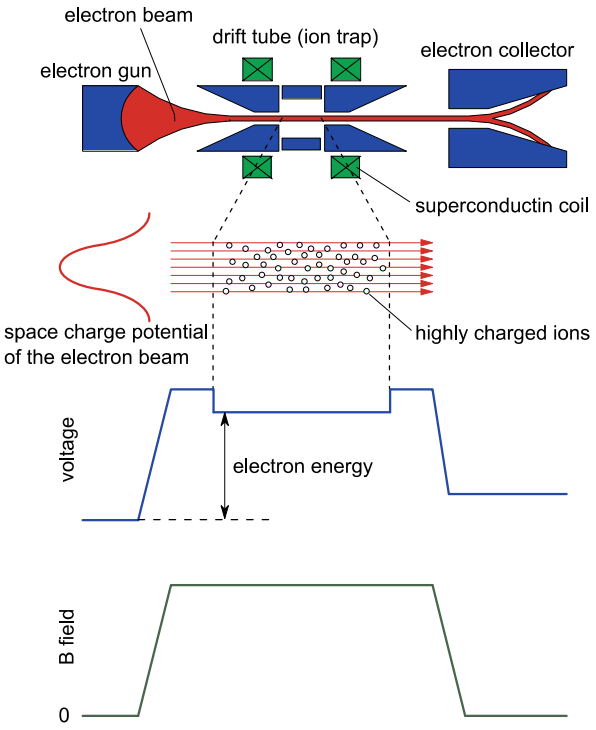

Fig. 1 Schematic principle of an electron beam ion trap.

of the strong axial magnetic field produced by the magnet and the space charge potential of the high density electron beam compressed by the magnetic field. Highly charged ions are produced by successive electron impact ionization of the trapped ions. Emission of highly charged ions excited by the electron beam can be studied spectroscopically through a slit opened at the middle of the drift tube. Since the trapped ions are produced and excited by an (quasi-)monoenergetic electron beam, an EBIT has following advantages over plasma sources. (1) A narrow charge state distribution can be obtained with a dominant charge state controlled by the electron energy. (2) Electron energy dependent emission processes, such as resonant excitation, can be studied. (3) There is no Doppler shift and less Doppler broadening. (4) Polarization of radiation excited by a unidirectional electron beam can be studied. We have developed a high-energy EBIT called the Tokyo-EBIT[2] in 1995 and a compact low-energy EBIT called CoBIT[3] in 2007. The former can be operated with electron energies of 1 to 200 keV, and the latter can be operated with electron energies of 0.1 to 2 keV. The complementary use of them enables spectroscopic studies of tungsten ions with a wide range of charge state.

An element of interest is usually introduced through the slit on the drift tube as a molecular beam. Not only rare gases and molecular gases, compounds which have a relatively high vapor pressure can also be used. For example, for producing tungsten ions, tungsten hexacarbonyl ($W(CO)_6$) are used respectively.

TUNGSTEN SPECTRA IN VISIBLE RANGE

Tungsten is considered to be the main impurity in the ITER plasma, and thus spectroscopic data of tungsten ions are necessary to diagnose and control the high temperature plasma in ITER[5]. In particular, there is strong demand for emission lines in the visible range in the diagnostics of the edge plasmas[6]. Since efficient optical components, such as mirrors, lenses, optical fibers, etc., are available, efficient and effective diagnostics can be expected with the visible range. Until recently, however, only one visible emission line[7] has been reported for tungsten ions with a charge state higher than two. Survey and identification of previously unreported visible lines of tungsten ions are thus in strong demand. An EBIT is a suitable device for such a purpose. As an example, tungsten spectra obtained with CoBIT are shown in Fig. 2. As seen in the figure, observed lines revealed strong dependence on electron energy, i.e., they appeared at a certain threshold energy and their intensity became weak when the

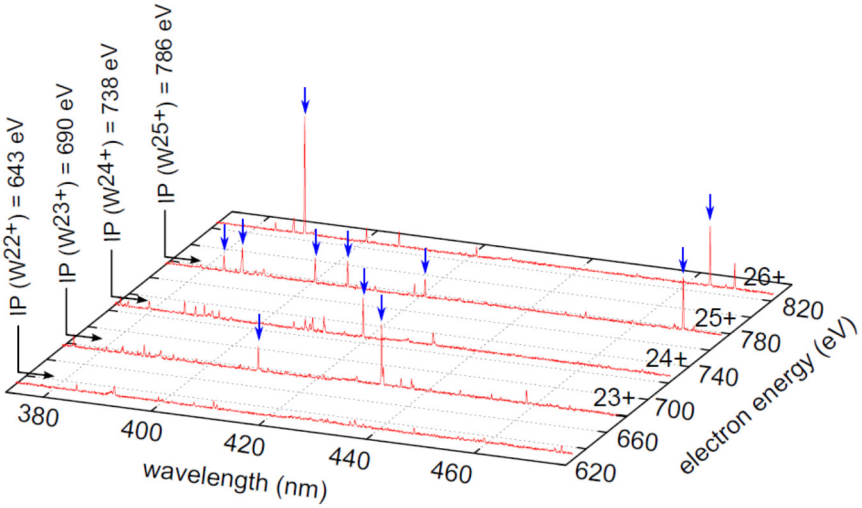

Fig. 2 Visible spectra of highly charged tungsten ions observed with CoBIT. IP(W^{q+}) represents the ionization potential of W^{q+}.

energy was further increased. This strong dependence reflects the charge distribution in the trap. For example, after the electron energy was changed from 630 eV to 675 eV, production of W^{23+} became available because the ionization energy of W^{22+} is 643 eV[8]. The lines at around 409 and 432 nm, appeared at 675 eV, are thus considered to be emission lines from W^{23+}. When the energy was further increased to 725 eV, which is higher than the ionization energy of W^{23+} (690 eV), the intensity of these lines became small because the number of W^{23+} was decreased due to further ionization, and the line from W^{24+} appeared at around 419 nm. The validity of such identification based on the appearance energy has been confirmed through several previous experiments[9]. Consequently, the lines indicated by arrows in the figure are assigned to be the transition of tungsten ions shown in each spectrum. Since transitions between different electronic configurations in highly charged heavy ions should fall in shorter wavelength range, such as EUV and x-ray, transitions in the visible range can be assigned as M1 transitions between fine structure levels. The detailed identification of the fine structure levels should be done through comparison with theoretical calculations. Although it is rather difficult to calculate fine structure splitting precisely for many electron heavy ions, some lines in Fig. 2 have been identified through the comparison with detail calculations[10]. Survey of previously unreported lines is also possible with plasma sources, but observation of spectra excited by a mono-energetic electron beam in an EBIT is quite useful for the identification of the responsible charge state as shown here.

TUNGSTEN SPECTRA IN X-RAY RANGE

Collisions of highly charged ions with electrons are the most important atomic process in hot plasmas. Various parameters and behavior of plasmas are modeled based on the cross sections for electron collisions, such as excitation, ionization, recombination, etc. For the most simple example, the ion density ratio at the ionization equilibrium is determined from the ratio between ionization and recombination rates. However, even for this simple example, different theories sometimes give quite different results[11]. It is thus obviously important to measure cross sections experimentally and examine the theories with them. In an EBIT, a quasi-monoenergetic electron beam interacts with trapped highly charged ions. Collision processes, such as excitation[12] and ionization[13] can thus be studied by observing emission from an EBIT or charge state distribution in an EBIT. In particular, resonant processes, such as dielectronic recombination

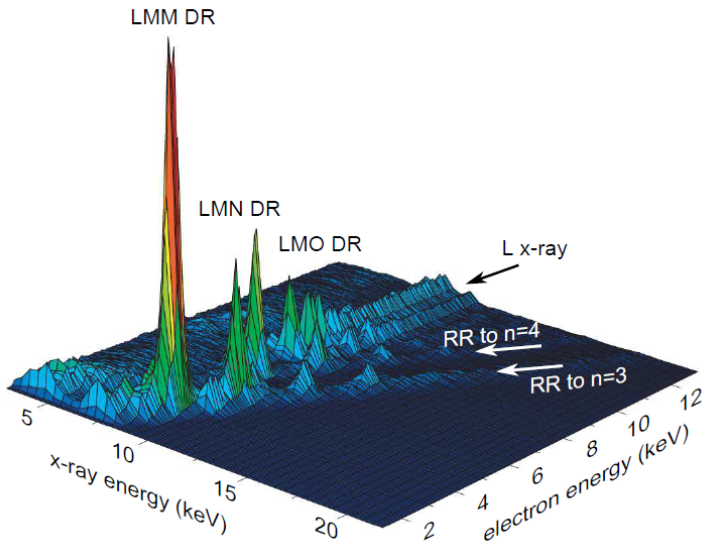

Fig. 3 X-ray spectra of highly charged tungsten ions observed with the Tokyo-EBIT while scanning electron energy between 1.5 and 14 keV.

(DR) can be studied efficiently by observing the dependence on electron energy. For example, Fig. 3 shows the x-ray spectra of tungsten ions observed with a Ge detector while scanning electron energy between 1.5 keV and 14 keV. As seen in the figure, x-ray intensity is prominently enhanced due to DR at some electron energies. For example, at an electron energy of ~3 keV, *L* x-rays are enhanced by the *LMM* DR resonance. *LMM* represents the process where a doubly excited state is produced by capturing the incident electron into the *M* shell while exciting a *L* shell electron to the *M* shell. For heavy ions, since the doubly excited state decays by emitting x-ray with a probability near unity, x-ray intensity is enhanced at the resonant energy. On the other hand, x-rays whose energy increases with the gradient of unity as a function of electron energy are due to non-resonant recombination (radiative recombination: RR). DR resonant strengths can be obtained by normalizing the x-ray intensity from DR to that from RR, for which reliable cross section can be calculated because there is no need to include electron correlation. For example, so far such a method was used to obtain DR resonant strengths for H-like Kr[14], He-like Ti[15], etc.

SUMMARY

As shown in this paper, an EBIT is an unique and versatile device for studying spectra and collision processes of highly charged ions. Three EBITs (the Tokyo-EBIT and two CoBIT) in Japan and over ten EBITs in the world are currently in operation for accumulating the atomic data of highly charged ions relevant to hot plasmas. Spectroscopic data of tungsten ions over a wide range of charge states have been accumulated under the IAEA Coordinated Research Projects “Spectroscopic and Collisional Data for Tungsten from 1 eV to 20 keV” for making a contribution to the future diagnostics of the ITER plasma. An EBIT is a powerful device also for studying collisional processes of highly charged ions, and the monoenergeticity of the electron beam enables ones to study resonant processes, such as dielectronic recombination which strongly affects the ionization balance and the emission of plasmas.

ACKNOWLEDGMENTS

This work was performed with the support and under the auspices of the NIFS Collaboration Research program (NIFS09KOAJ003) and JSPS KAKENHI Grant Number 23246165, and partly supported by the JSPS-NRF-NSFC A3 Foresight Program in the field of Plasma Physics (NSFC: No.11261140328).

REFERENCES

[1] R. E. Marrs et al., Phys. Rev. Lett. 60, 1715 (1988).

[2] N. Nakamura et al., Phys. Scr. T73, 362 (1997).

[3] N. Nakamura et al., Rev. Sci. Instrum. 79, 063104 (2008).

[4] E. D. Donets and V. P. Ovsyanniko, Sov. Phys. JETP 53, 466 (1981).

[5] N. J. Peacock et al., Can. J. Phys. 86, 277 (2008).

[6] C. H. Skinner, Can. J. Phys. 86, 285 (2008).

[7] H. Watanabe et al., Phys. Rev. A 63, 042513 (2001).

[8] A. E. Kramida and T. Shirai, At. Data Nucl. Data Tables 95, 305 (2009).

[9] A. Komatsu et al., Phys. Scr. T144, 014012 (2011); J. Yatsurugi et al., Phys. Scr. T144, 014031 (2011).

[10] X. B. Ding et al., J. Phys. B 44, 145004 (2011).
[11] T. Nakano and The JT-60 Team, J. Nucl. Mater. 415, S327 (2011).
[12] N. Nakamura et al., J. Phys. Soc. Jpn. 69, 3228 (2000).
[13] B. O'Rourke et al., J. Phys. B 34, 4003 (2001); H. Watanabe et al., Nucl. Instrum. Methods B 205, 417 (2003).
[14] Z. Hu, Y. Li, and N. Nakamura, Phys. Rev. A 87, 052706 (2013).
[15] B. O'Rourke et al., J. Phys. B 37, 2343 (2004).

Progress in fast-ion loss detector project in EAST

Kunihiro Ogawa[1], Mitsutaka Isobe[1,2]
[1] *National Institute for Fusion Science, Toki, Japan*
[2] *The Graduate University for Advanced Studies(SOKENDAI), Toki, Japan*
Jiafeng Chang[3], Guoqiang Zhong[3], and Liqun Hu[3]
[3] *Institute for Plasma Physics, Chinese Academy of Sciences, Hefei, China.*

1. Introduction

To achieve a high-temperature and high-density plasma, additional heating by means of energetic ion produced by neutral-beam injection and/or ion cyclotron heating is applied in the middle or large-sized magnetic confinement fusion device. At the institute of plasma physics in China, the EAST will soon be equipped with neutral beam injectors. Therefore, by means of strong neutral beam injections, a study of the loss process of energetic ion due to magnetohydrodynamic (MHD) mode becomes possible. In a fusion device, energetic ions such as fusion-born alpha particles might excite MHD mode such as Alfvén eigenmodes. These instabilities are predicted to cause enhanced energetic-ion transport leading to a localized damage on plasma facing components. Understanding of the interaction of Alfvén eigenmodes and energetic ions through experimental observation in existing devices is necessary to find a way to reduce the energetic-ion loss in a fusion reactor. A scintillator-based fast-ion loss detector (FILD) has been installed on tokamaks such as TFTR [1,2], NSTX [3], JET [4] ASDEX Upgrade [5], DIII-D [6], KSTAR [7], Alcator C-mod [8], and HL-2A [9] and helical devices/stellarators such as CHS [10], Wendelstein7-AS [11], and LHD [12] and used to study the energetic-ion loss process. A FILD in EAST will be a powerful tool for a comprehensive understanding of energetic-ion loss physics in torus devices. This paper describes the progress of FILD project in the EAST.

2. Search a position for FILD

A FILD is a type of a magnetic spectrometer using the magnetic field of magnetic confinement device. The set of apertures is designed to get only an energetic ion. Scintillator emits a light due to the bombardment of an energetic ion. The position of the bright spot gives us the energy (E) and pitch angle (χ) of the energetic ion. The installation position for FILD is searched by means of Lorentz orbit code. The code solves the equation of motion of a charged particle with sixth order Runge-Kutta solver on a static magnetic field condition. The procedure for finding of a position suitable for

the FILD is as follows. At first, energetic ions are launched from a candidate position of the FILD head. Second, the trajectory of each ion is followed backward in time using the Lorentz orbit code. Finally, we judge whether the ion can enter the plasma domain without hitting the vacuum vessel. If the energetic ion reaches the plasma region, it means that the lost energetic ion is measured by the FILD. Figure 1 shows the typical energetic-ion orbit calclucated on the MHD equilibrium file of g030707.03800. In this calculation, E and χ of energetic-ion at the FILD position are 75 keV, and 84.3 degrees, respectively. We found that the upper position on an outer port is first choice to detect escaping ions having banana orbit in the case of the experiment with counter-clockwise direction, looking down from the top, of toroidal magnetic field.

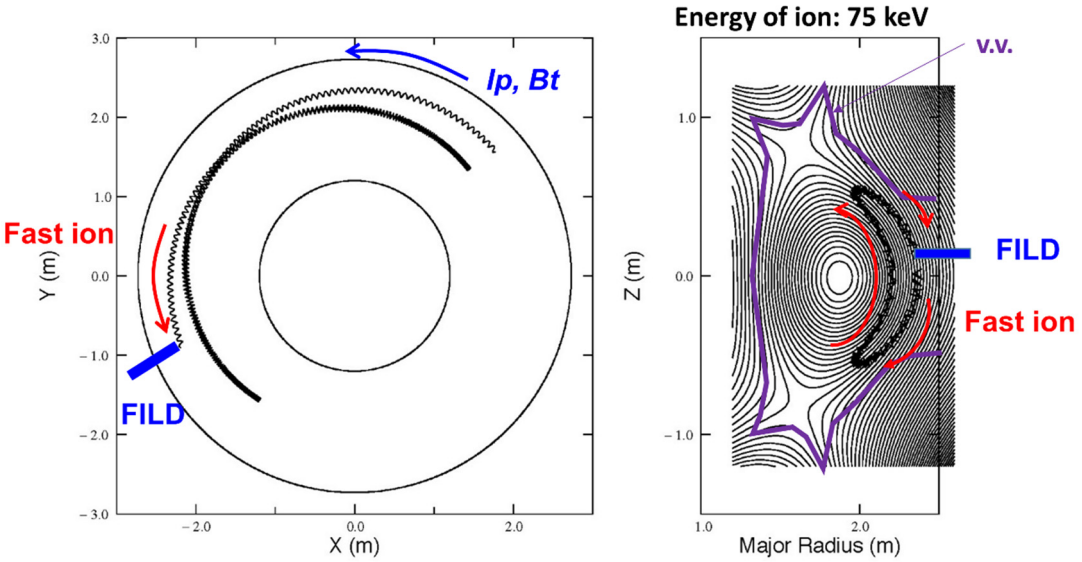

Fig.1 Typical trajectory of energetic ion can be measured by FILD in the EAST.

3. Design of FILD

Figure 2(a) shows the schematic view of the system of a FILD together with J port. The length of the probe is about 3 m, and can move horizontally by 2.5 m by means of servo motor. Note that the distance from the last closed flux surface to the waiting position of the probe head is 2.3 m. Figure 2(b) shows a FILD driving system. Note that the design of supporting structure is changed slightly from that in Fig. 2(a) due to the interference with other diagnostics (Fig. 2(c)). The design of the head is shown in Fig. 3. The width of first aperture and second aperture are 2 mm and 40 mm, respectively. The distance between two apertures is 10 mm. The height of the center of

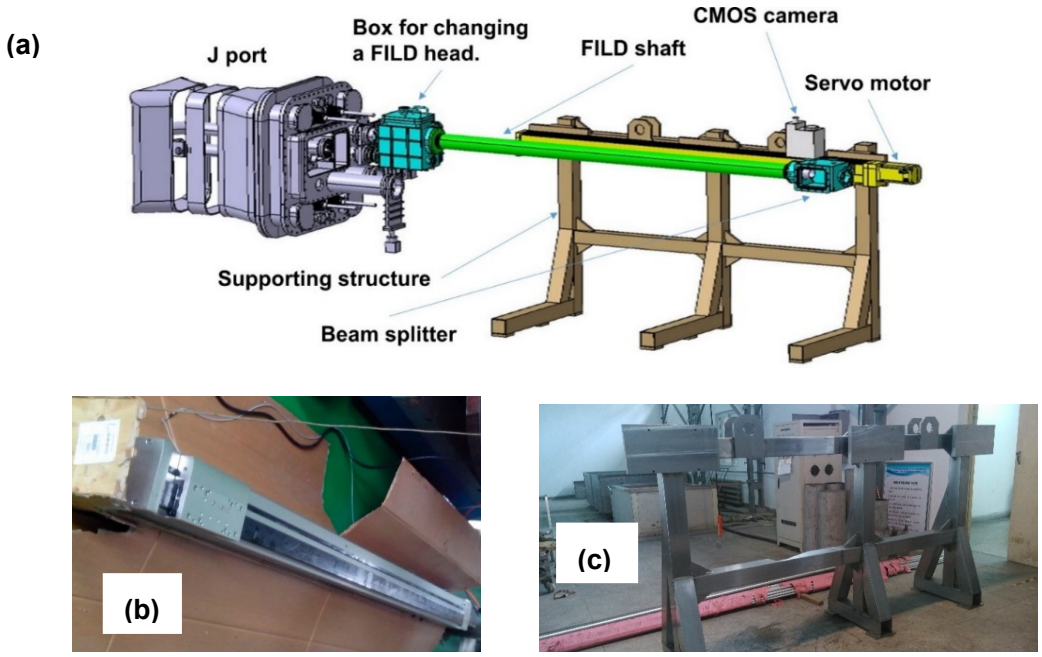

Fig.2 (a) The schematic view of FILD together with J-port. (b) FILD driving system. (c) FILD support structure.

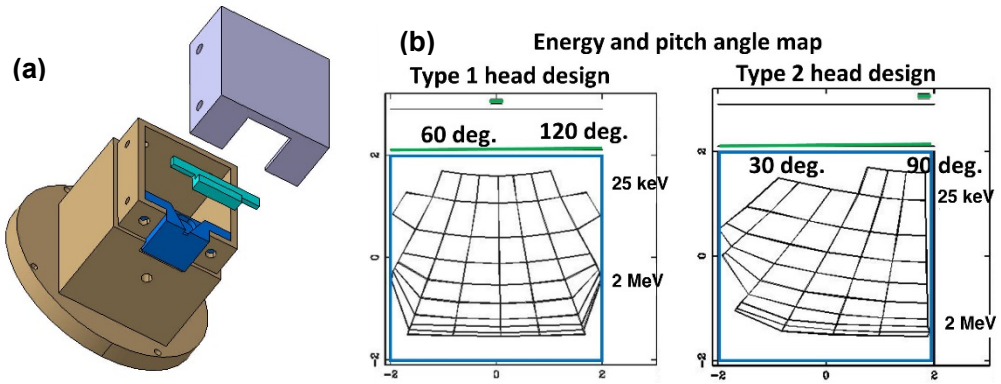

Fig.3 (a) Design of FILD probe head. (b) Energy and pitch angle map of two FILD heads.

these apertures from scintillator screen is 6 mm. The size and position of the aperture and the scintillator is decided according to grid map calculation as shown in Fig. 3 (b). The size of the scintillator is chosen so as to measure deuterons up to 2 MeV. Note that the magnetic field strength on the plasma axis and that on the FILD position are 2.0 T and 1.6 T, respectively. We will prepare two types of heads having different aperture positions. One is to measure energetic ions having χ of 60 degrees to 120 degrees and another is to measure energetic ions having χ of 30 degrees to 90 degrees. The block diagram of an acquisition and a controlling system is shown in Fig. 4. The thermocouple is for measurement of the temperature at the probe head to avoid melting the probe tip. The scintillation image is recorded by photomultiplier (PMT) (H10493, Hamamatsu

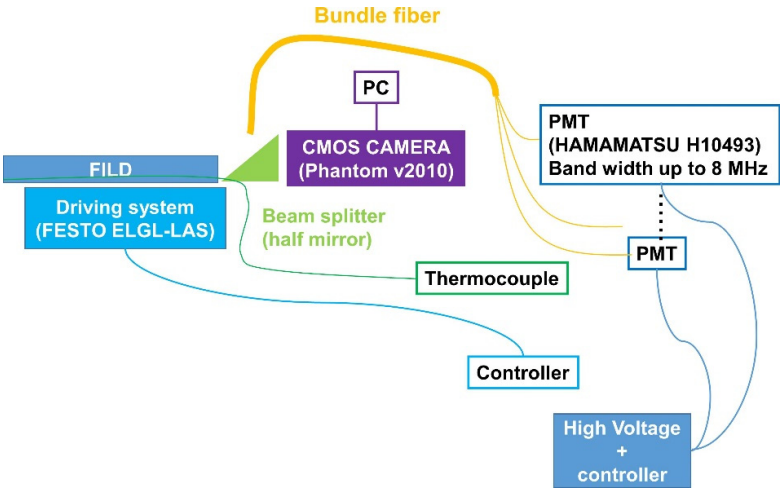

Fig. 4 Data acquisition and control system for FILD

Photonics) and a CMOS camera (v2010, Phantom: up to 22 k frames per second at 1280×800 pixels resolution). We will use 5×5 PMT to follow rapid events associated with energetic-ion-diven MHD instabilities with high-time resolution. The high-speed camera is used to obtain highly resolved energy and pitch-angle pattern on the screen for escaping energetic ions.

4. Summary

Fast-ion loss detector project for EAST is now ongoing as a collaboration between NIFS and ASIPP in the support of A3 foresight program. We chose an upper position on outer port to detect energetic ions escaping from a EAST plasma. Two types of FILD heads have been designed according to energy and pitch-angle grid map calculation. The FILD will be installed on EAST in 2014, being a powerful tool to reveal energetic-ion loss processes in EAST plasmas.

Acknowledgements

This work was partly supported by the JSPS-NRF-NSFC A3 Foresight Program in the field of Plasma Physics (NSFC: No.11261140328).

References

[1] S. J. Zweben, Nucl. Fusion **29** 825 (1989).
[2] D. S. Darrow *et al*., Rev. Sci. Instrum. **66** 476 (1995).
[3] D. S. Darrow, Rev. Sci. Instrum. **79** 023502 (2008).
[4] S. Baeumel *et al*., Rev. Sci. Instrum. **75** 3563 (2004).

[5] M. García-Muñoz *et al*., Rev. Sci. Instrum. **80** 053503 (2009).
[6] R. K. Fisher *et al*., Rev. Sci. Instrum. **81** 10D307 (2010).
[7] J. Kim *et al*., Rev. Sci. Instum. **83** 10D305 (2012).
[8] D. Pace *et al*., Rev. Sci. Instrum. **83** 073501 (2012).
[9] Y. P. Zhang *et al*., Rev Sci. Instrum. **85** 053502 (2014).
[10] M. Isobe *et al*., Rev. Sci Instrum. **70** 827 (1999).
[11] A. Weller *et al*., Rev. Sci. Instrum. **72** 780 (2001).
[12] K. Ogawa *et al*., J. Plasma Fusion Res. SERIES **8** 655 (2009).

Experimental observations of fast-ion loss in KSTAR

Junghee Kim[1,2], Jun Young Kim[2], T. N. Rhee[1], S. W. Yoon[1], M. Isobe[3], K. Ogawa[3], M. García-Muñoz[4], Y. M. Jeon[1]
Email : kimju@nfri.re.kr

[1] *National Fusion Research Institute, 305-806 Daejeon, Korea*
[2] *Korea University of Science and Technology, Daejeon, Korea*
[3] *National Institute for Fusion Science, Toki, Japan*
[4] *Universidad de Sevilla, 41004 Seville, Spain*

1. Introduction

Confinement of the fast ions generated by the auxiliary heating (NBI, ICRH) and the fusion products is essential to realize the commercial fusion reactor. In reality, some amount of fast-ions, which can be the source of the fusion reaction, can be lost, depending on the fast ion distribution. Although the relative number of lost fast-ions is small, the impact of the fast ion loss on the fusion devices causes significant damage [1] on the first-wall due to its high energy. Moreover fast ion loss can lead to degradation of fusion performance, hence understanding of fast ion loss mechanism becomes important mission for the future fusion plasma research.

2. Fast ion loss detector (FILD)

In KSTAR, a fast ion loss detector (FILD) has been operated since 2011 experimental campaign [2]. KSTAR FILD is based on the scintillator which can represent the energy (Larmour radius) and the pitch-angle of the escaping fast-ions. In particular, the shape of the front surface of the FILD head is resembled with the plasma boundary shape so as to reduce the heat load on the detector head. This design prevents saturation of the heat-induced ionoluminescent emission. Since 2012 experimental campaign, a 16ch PMT (photo-multiplier tube)-based 'fast-measurement' system has been used to observe the correlation between the fast-ion loss and the internal MHD instabilities. (Figure 1)

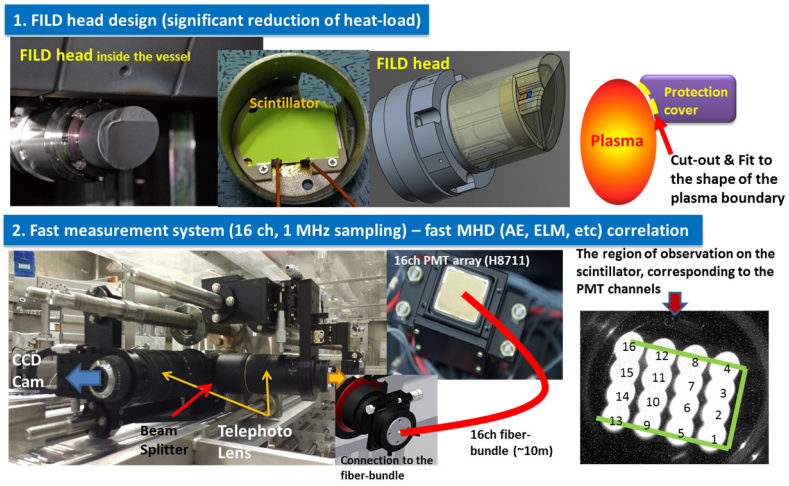

Figure 1. Design of the KSTAR FILD head is shown on the top figure, and the fast measurement system based on the PMT was added and the positions of the measurement segments on the scintillator plate were calibrated.

3. Fast ion loss associated with the edge activity (ELM)

Almost fast ions escaping from the bulk plasma are responding to the edge activities such as profile changes or the edge-localized modes (ELMs) since the orbits of the escaping fast-ions are travelling along the edge / SOL (scrape-off layer) region. One of the most active phenomena at the boundary plasma is the edge-localized mode (ELM). Like on other major fusion devices, strong correlation with the ELM burst is observed on the FILD signal [3]. The distinctive point seen in the ELM-associated fast-ion loss is the spread of the pitch-angle distribution and the multiple peaks in the PMT signal during a single ELM burst event. Multiple-peaks during a single ELM burst (right on the Figure 2) may be the signature of the interaction between the fast-ion orbits and the ELM filaments. The broaden pitch-angle distribution captured by the scintillator plane may be due to integration of the multiple pitch-angles of the bombarding fast-ions for 5 msec (left on the Figure 2). Temporal difference between adjacent peaks in the FILD PMT signal is order of 0.1 msec. It is planned to use the ultrafast camera (~ 10000 frame/sec) to match the phase-space (pitch angle) of each scintillation spot with the timing of ELM filamentation.

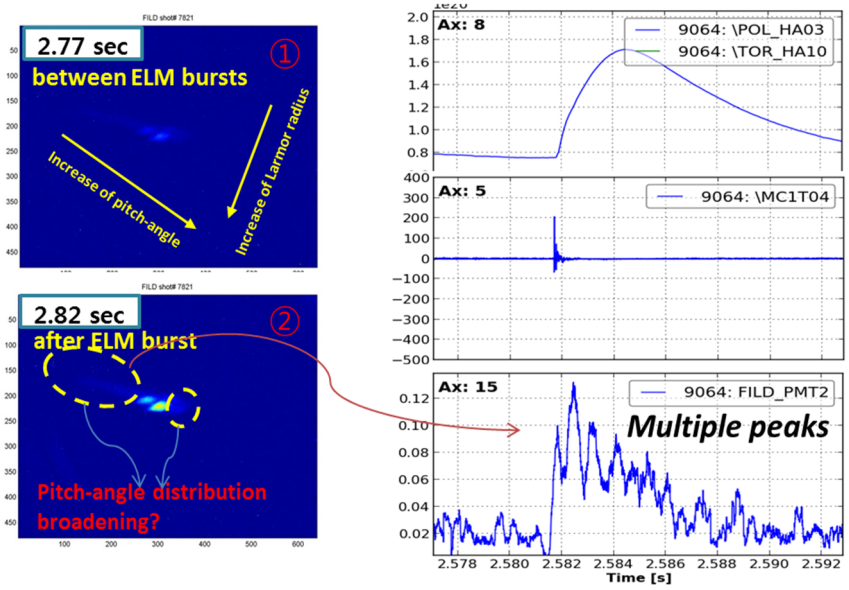

Figure 2. Fast-ion loss signal is shown on the left: CCD camera (scintillator screen, 5msec integration image) and the right: PMT signal (top: Dα signal during a type-I ELM burst, middle: magnetics, bottom: FILD PMT signal from the low-pitch angle side of the scintillator screen).

4. Fast ion loss change in response of the resonant magnetic perturbation (RMP)

It has been found that the intended (resonant) edge magnetic perturbation can mitigate or suppress the ELM activity [4]. However it is known and found that symmetry breaking of the equilibrium lead to the localized enhancement of the fast-ion loss to the wall [5]. Toroidal non-axisymmetry of the fast ion loss pattern has been observed by the single FILD via the experiment changing the polarity of the RMP coil current (B_r direction) [6]. Figure 3 shows the experimental result of the non-axisymmetric fast-ion loss in KSTAR. Left is the case of the inward B_r application, hence the FILD signal during RMP-on phase drops to almost zero-level. On the other hand, outward B_r perturbation enhances the fast-ion loss on the FILD position.

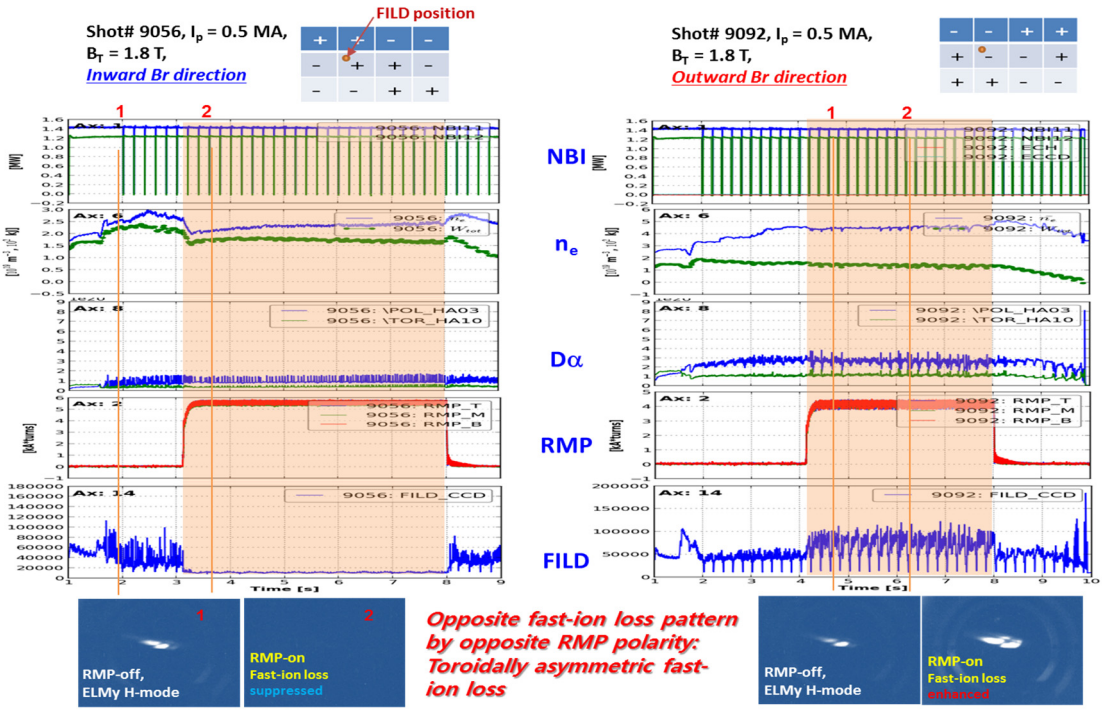

Figure 3. Toroidally asymmetric fast-ion loss pattern is shown. Left figure represents the inward B_r perturbation case and the suppressed FILD signal, and the right one (outward B_r perturbation) shows the local enhancement of the fast-ion loss.

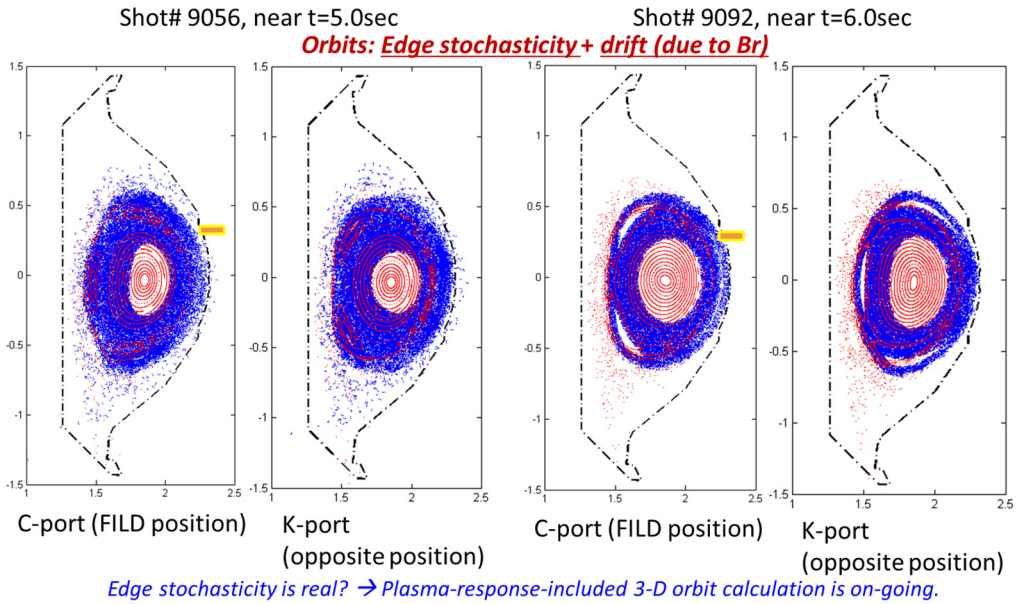

Figure 4. Poincare section plots of the fast-ion orbits (blue) overlaid on the perturbed magnetic field (red).

Simulation works (Figure 4) supporting the experimental results shown in have been performed with the 3-D orbit-following Lorentz-orbit code (LORBIT) [7]. As shown in left two figures in Figure 4, only rare fast-ion orbits (blue dots in the Poincare section) are intersecting with the FILD head. On the right two figures in Figure 4, outward B_r perturbation increases the number of intersection between the orbits and the FILD head, which is consistent with the results shown in Figure 3. Mechanism of the fast-ion loss in the presence of the toroidally asymmetric field is as follows. RMP produces the edge stochasticity, and then the orbits travelling through the edge plasma are perturbed and drifted to the bad-curvature region via stochastic ripple loss [8]. In this paper, 'ripple' is regarded as an alternative expression of the 'stochasticity'. If the RMP field strength is weak, thin or no stochastic region is generated and it does not affect to the fast-ion orbit whose gyro-radius is 3 – 4 cm. Drifted orbits by the stochastic field structure faces the relatively significant radial perturbation field when the orbit approaches the RMP coil. If the perturbation direction near the FILD position (SOL) is outward, drifted orbits are going to the outside. However, drifted orbits can be pushed into the inward direction when the drifted orbits experience the inward B_r perturbation.

5. Fast ion loss associated with the core MHD activity

In addition to the fast-ion loss associated with the edge activity, core MHD instability-induced fast-ion loss has been observed. It is difficult that the confined fast-ion orbits perturbed in the core region are lost. Instead, redistribution of the fat-ion density is occurred. However in some cases, core activity-induced fast-ion can be lost. Simple drift of the orbit cannot fully explain these losses. For the trapped fast-ions existing in the core, it is easy to escape to the outside of the plasma when the toroidal precession frequency of the orbit has integer ratio with island rotation frequency. Pitch-angle of the escaping fast-ion orbit can be varied since the banana tip position is moving when the magnetic moment is

conserved (adiabatic invariant) [9]. In particular, orbit behaviour of the passing fast-ions is sensitive to the magnetic island position. If m/n=2/1 or 3/2 island position is close to the plasma boundary (i.e. q-profile is broad.), core fast-ions can be lost easily. Experimental results depicted in Figure 5 Shows the evidence that the fast-ion loss is associated with the tearing mode. FILD spectrogram shows the same frequency track of the magnetics. Gradual increase of the FILD signal, capturing a specific part of the scintillator screen to eliminate the prompt loss signal, implies the fast-ion loss intensity is proportional to the width of the island. Another example of the core activity is fishbone (ion fishbone). Figure 6 represents the m/n=1/1 fishbone-associated fast-ion loss signal on the spectrograms. Perturbation location of the fishbone is at the deep-core region (near the q=1 surface), hence the resonant interaction between the orbit precession/circulation and the fishbone (kink) frequency is the main mechanism of the fast-ion loss.

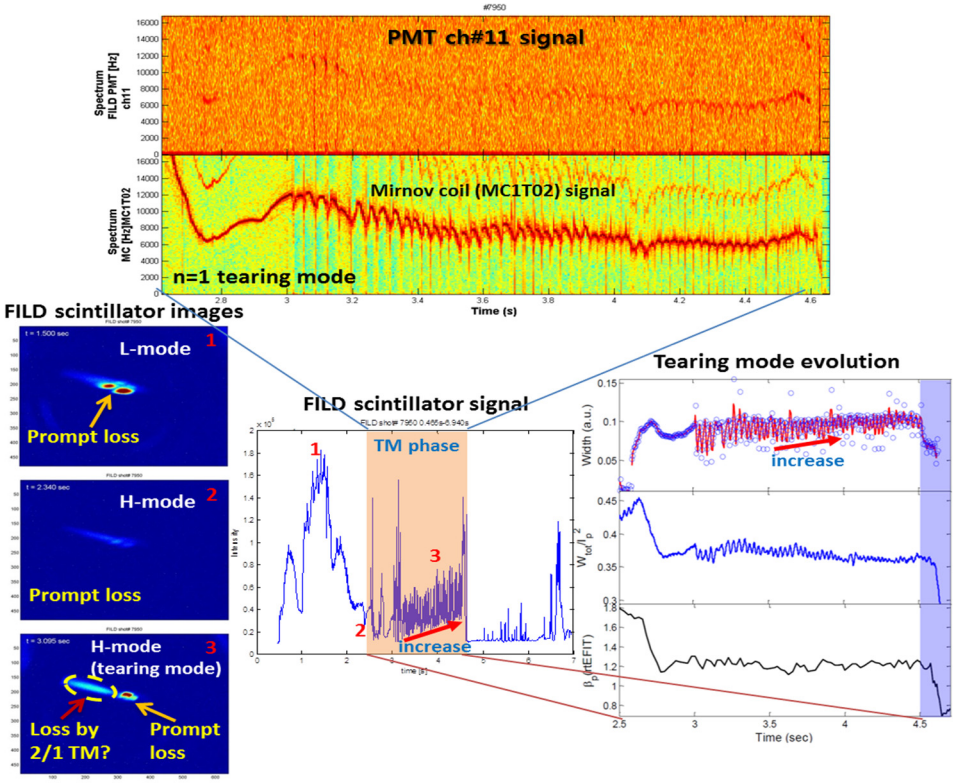

Figure 5. Tearing mode-associated fast-ion loss signal is presented. FILD spectrogram is strongly correlated with the magnetics spectrogram. In addition, FILD signal intensity is proportional to the island width.

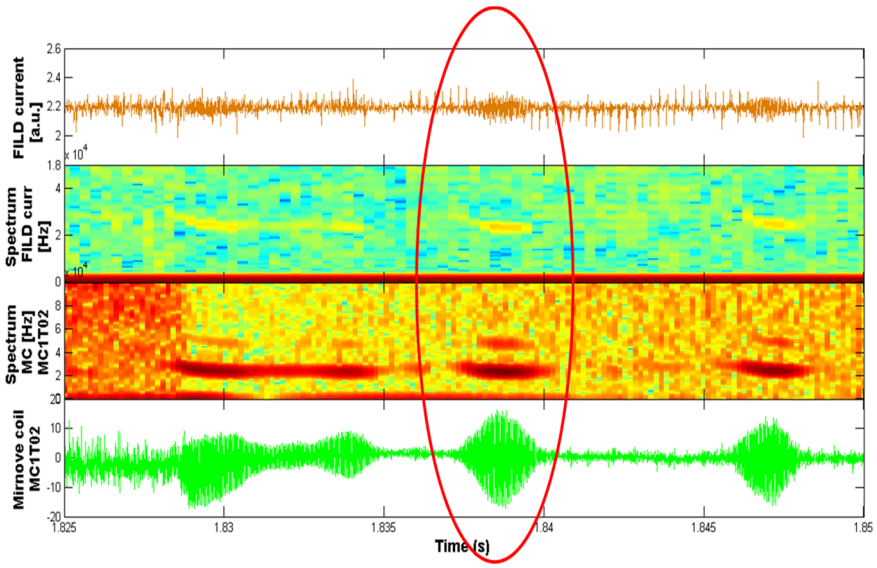

Figure 6. Fast-ion loss signal whose spectrogram is correlated with that of magnetics.

6. Conclusion

Various fast-ion loss cases are introduced. Two representative edge-activity-induced fast-ion loss phenomena are observed, which are the ELM-associated and the RMP-associated loss patterns. Seen on both the FILD scintillator plane and the PMT signal peaks, multiple pitch-angle may be due to interaction with the ELM filament that can produce significant density fluctuation or magnetic fluctuation near the edge/SOL fast-ion orbits. Main mechanism of the fast-ion loss due to edge magnetic perturbation at the edge is composed of stochastic ripple loss due to edge stochasticity and the drift by the radial perturbation direction. It is considered that the stochastic layer can make a 'short-circuit' between the edge and the SOL, causing direct loss (drift) to the wall. In addition to the fast-ion loss at the edge, core MHD instability-induced fast-ion losses are observed. Principal origin of the loss of the core fast-ions is the resonant interaction between the fast-ion orbit precession and the rotating island. In particular, drifting orbit caused by the presence of the tearing mode islands is sensitive to the loss when the q-profile shape is broad. Sophisticated analyses with the plasma-response-included simulations (MHD codes as well as 3-D orbit following codes) with the 3-D equilibrium (HINT2 [10]) will be done.

Acknowledgement

This research was supported by Ministry of Science, ICT, and Future Planning under KSTAR project and was partly supported by the JSPS-NRF-NSFC A3 Foresight Program in the field of Plasma Physics (NSFC: No. 11261140328, NRF: No. 2012K2A2A6000443).

References

[1] S. Putvinski *et al*., in Plasma Physics and Controlled Nuclear Fusion Research 1994 (Proc. 15th Int. Conf. Seville, 1994), Vol. 2, IAEA, Vienna (1995) Paper E-P4.

[2] J. Kim *et al*., Rev. Sci. Instrum. **83**, 10D305 (2012).

[3] M. Garcia-Munoz *et al*., Nucl Fusion. **53**, 123008 (2013).

[4] Y. M. Jeon *et al*., Phys. Rev. Lett. **109**, 035004 (2012).

[5] J. Y. Kim *et al*., in: Proc. 28th EPS conference, Berlin, 21-25 June (2014). P4.067

[6] J. Kim *et al*., 10th ITPA Energetic Particle Physics Topical Group Meeting (2013).

[7] M. Isobe *et al*., J. Plasma Fusion Res. SERIES, Vol. **8**, 330 (2009).

[8] R. J. Goldstone *et al*., Phys. Rev. Lett. **47**, 647 (1981).

[9] S. J. Zweben *et al*., Nucl Fusion. **40**, 91 (2000).

[10] Y. Suzuki et al., Nucl Fusion. **46**, L19 (2006).

Operational status in KSTAR NBI and plan of off-axis neutral beam line development

Young-soon Bae[a], J.S. Kim[a], H.T. Park[a], D.H. Kim[a], W. Cho[a], K.S. Lee[a], H.K. Kim[a], Y.M. Park[a], N.H. Song[a], Y.B. Chang[a], S.W. Kwak[a], L. Terzolo[a], H.L. Yang[a], J.G. Kwak[a], Y.K. Oh[a], S.H. Jeong[b], D.H. Chang[b], T.S. Kim[b], S.R. In[b], K. Watanabe[c], A. Kojima[c], M. Kashiwagi[c], M. Dairaku[c], M. Hanada[c], T. Inoue[c], H.S. Kim[d], Y.S. Na[d], S. Matsuda[e],

[a]National Fusion Research Institute, Daejeon, Korea
[b]Korea Atomic Energy Research Institute, Daejeon, Korea
[c]Japan Atomic Energy Agency, Naka, Ibaraki 311-0193, Japan
[d]Seoul National University, Seoul, Korea
[e]Tokyo Institute of Technology, Tokyo, Japan

Email : ysbae@nfri.re.kr

Neutral beam injector (NBI) is playing an important role in supporting the physics studies and long pulse discharge as well as in the beam-based diagnostics such as CES and MSE using beam modulation in KSTAR tokamak. The first NBI (NBI-1) is designed to support the long pulse KSTAR operation with three co-tangential neutral beams with each neutral D0 beam power of 2 MW at 100 keV in the horizontal midplane of KSTAR tokamak with characteristics of nearly on-axis current drive. The long pulse design requirement requires the large beam sources and efficient water-cooling beamline components collimating beam to allow three beams in effective aperture in the port duct. Presently, NBI-1 has been operated with two beam sources at maximum 2.4 MW beam power with duration of 20 s (3.5 MW for short pulse). The NBI-1 system is under upgrade for the last third beam source for the plan of longer H-mode discharge in KSTAR. Also, the multi-beam aperture accelerator of two beam sources is being modified to enhance the beam transport efficiency by beam steering from the outermost beam apertures. Goal of the KSTAR second phase operation requires new off-axis beamline to develop the advanced operation modes (hybrid and steady state operation modes) since the broad current profiles peaked off-axis are beneficial for steady-state high performance using off-axis NBI in DIII-D experiments [1, 2]. Therefore, the second NBI for KSTAR is under design to have the off-axis beamline of upward and downward beams tilted in vertical plane. This paper presents the operation performance and upgrade of the first NBI system and the design results of new off-axis NBI with integrated tokamak modeling code for the hybrid and steady state operation.

1. Introduction

The KSTAR first neutral beam injector (NBI-1) system is designed with three co-tangential neutral beams [3, 4]. Figure 1 shows the NBI-1 beam line containing three beams from each ion source. All three beam sources have been developed by positive beam based, arc discharge ion source and multi-hole accelerator grid structure without the beam focusing and steering. Two side beams are injected with 4-deg steering angle from the centered beam so that beams cross at the middle of beam duct as shown in fig. 1. NUBEAM code simulation shows, as shown in fig. 1, the NBI-1 has the characteristics of on-axis current drive. Presently, the NBI-1 is equipped with two beam sources; first beam source at the center, the second beam source at the right side looking to the tokamak. The third beam source at the left side will be installed to KSTAR in July, 2014 before the next campaign. Other systems such as high voltage power supply and beam line components are installed for the third beam source.

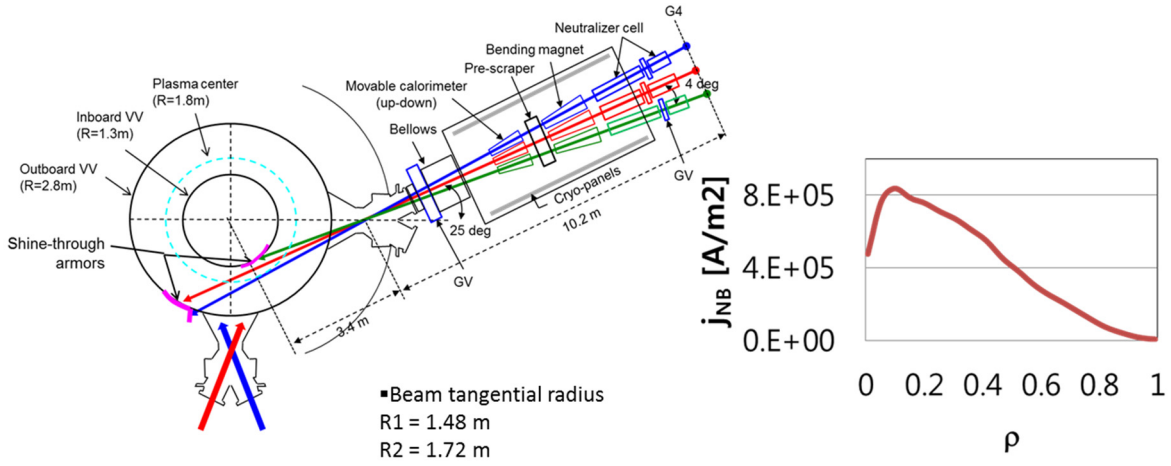

Fig. 1. Design of KSTAR first co-tangential neutral beam injector with three ion sources and the characteristics of on-axis current drive by 6 MW NBI obtained by NUBEAM simulation with double null plasma equilibrium with the plasma current 1 MA and the toroidal magnetic field of 2 T (the major radius of plasma of 1.8 m, and the minor radius of 0.5 m, elongation κ = 1.8, the respective central electron and ion temperatures of 3 keV and 2.5 keV, the line-average density of 4x10^{19}/m^3). The plasma current and the toroidal direction both are set to direction of counter-clockwise.

In 2013, the two beam sources are operated reliably except some heat excess problem in second beam source. The long pulse capable neutral beam enabled to achieve the longer H-mode discharge in 2013 campaign. In this long pulse H-mode discharge at the plasma current of 0.5 MA and the toroidal magnetic field of 2 T, total NBI heating of 2.4 MW is injected with two ECH heating power injection of ~ 1 MW at the later part of the discharge. The pulse length of this long pulse H-mode discharge is limited by available grid electricity (MVAr).

2. Operational status and upgrade

The first beam source is designed to be capable of maximum 4 MW D+ beam power at 100 kV with nominal perveance of 1.2-1.3 microP. It has been conditioned with 3 MW D+ ion beam extraction at 90 kV with the pulse duration of 50 s in 2013. No limitation of pulse duration is known in the first beam source. The second beam source has been developed with a larger diameter of beam aperture holes than the first beam source with the nominal beam perveance of 1.6-1.7 microP. Instead, the number of aperture holes is reduced. It has been conditioned with 2 MW D+ ion beam extraction limited at 70 kV with maximum pulse duration of 30 s. The pulse duration at the high power in second beam source is limited by the heat excess at the ion source collimator positioned after the accelerator of the ion source, and by the heat excess at the backplate of the ion source chamber. The ion source collimator has been used for the purpose of scraping outer diverged beamlets in KSTAR NBI. The high heat excess at the backplate of the ion source chamber during the beam extraction results from the back-streaming electrons. The large diameter of beam aperture holes probably results in the high flux of back-streaming electrons. In the second beam line channels for second beam source, neutralizers and the entrance scraper of the bending magnet also have high heat load leading to lowered transport efficiency than the first beam source beam line channel.

For 2014 KSTAR campaign, we will resolve the high heat excess problems and low transport efficiency in the second beam source and upcoming the third beam source as well which is identical to the second beam source. The ion source collimator is replaced by new one made by CuCrZr alloy machined with improved water cooling channels inside the collimator to resist the heat excess problem. To enhance the transport efficiency, the partly beam focusing is introduced by the displaced apertures in three outermost rows and columns in the deceleration grid (G3). All the beamlet focusing is prohibited to avoid the excessive power flux at the calorimeter and the ion beam dump. In addition to the modification of G3 grid aperture holes, the shape of aperture holes is a bit changed to reduce the backstreaming electron flux at the backplate of the ion source by proper electric field lines around the aperture providing no acceleration of the secondary electrons generated from the aperture surface back to the ion source. The backplate is also replaced by new

CuCrZr plate with enhanced water cooling capacity to have secure operating condition with low temperature increase. The thermocouple sensors are installed at the surface of the backplate to monitor the temperature and for the interlock during the beam extraction.

3. Long pulse beam extraction performance

In order to provide the beam power as highest as possible with longest pulse duration, each beam source has been conditioned during every campaign period. Figure 2 shows the beam heat load ratio in the beam line channel measured by calorimetric circuit of water cooling channel with respect to the ion beam power ($P_{ion} = V_b \times I_b$) in the first and second beam source. Highest beam heat load is at the bending magnet (BM) entrance scraper and at second neutralizer (N2) for first and second beam source, respectively. The second beam line channel has higher beam heat load ratio than the first beam line channel. Presently, the first beam line channel has 75-80% beam transport efficiency, and the second beam line channel has 65-70% beam transport efficiency. But, recent upgrade of the accelerator in second ion source increased the transport efficiency to 80% by reducing the heat excess at the ion source collimator, neutralizers, and bending magnet scraper. Figure 4 shows the temperature data of water cooling channel of internal components and back-plate surface for 80 kV beam extraction with pulse duration of 10 s. The heat load in ion source collimator (or scraper), neutralizers, bending magnet input scraper is decreased, while the delivered power to the calorimeter is increased. The thermocouple sensor at the back-plate of the ion source is not too high. This reduced heat load will support the longer pulse operation at higher power rating.

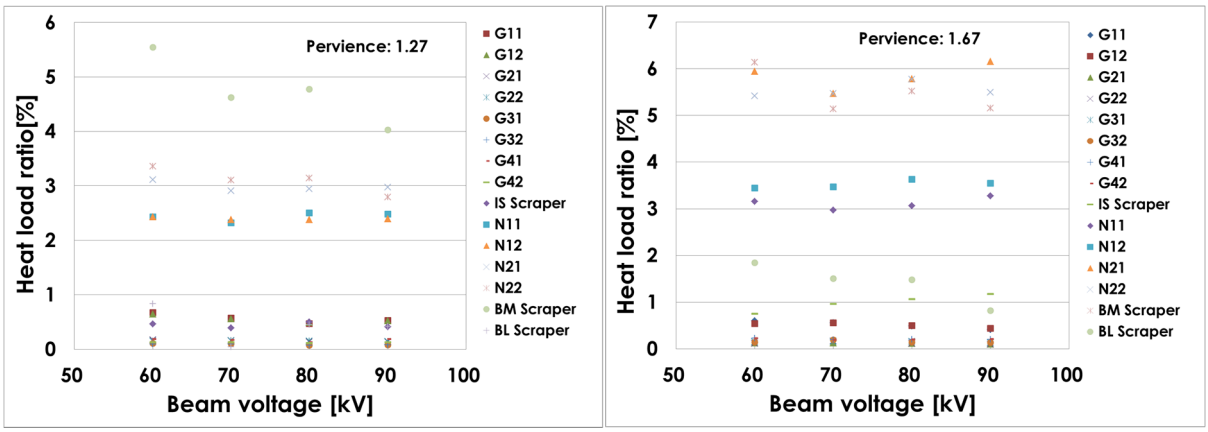

Fig. 2. The heat load ratio of beam line channel corresponding to first and second beam source.

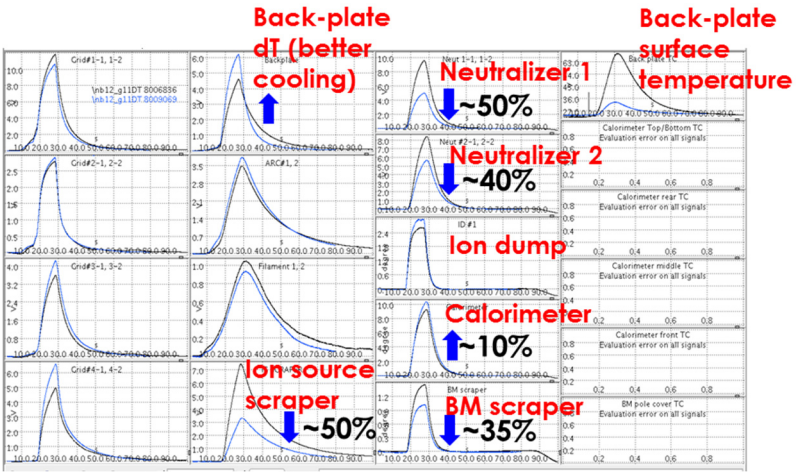

Fig. 3. The temperature of water cooling channel of internal beam-line components and the back-plate surface for 80 kV beam extraction with pulse duration of 10 s. The black and blue curves are for before and after the modification of ion source accelerator, respectively.

4. Plan of second NBI

The second NBI is being considered as a tangential off-axis neutral beam injection to have the center of the two beam sources aimed at a sufficient vertical offset from the geometric center of the plasma. The physics goal of off-axis NBI is for the access to steady state high performance operation mode in KSTAR. Ideally the system should be made such that the beam is injected in the same horizontal plane at an elevation below or above the median plane. So the off-axis plan by tilting the beam angle in vertical plane is an expedient method. Figure 5 shows the present pre-conceptual design (tentative) of off-axis second NBI which is designed to have a maximum steering angle of the beam source from the horizontal plane at about 7.5 deg with elevated ion sources at about 1.35 meters. In this steering angle, the beam transport ratio is calculated by 85% using the superposition of Gaussian beam profile of each beam-let with a divergence angle of 1 deg with all beam-let focusing and the beam source size same as the present beam source in NBI-1. The maximum vertical steering angle is mainly limited by the maximum acceptance of port duct and passive stabilizer. However, the optimized beam steering angle should be investigated for the maximum effect of the high performance of advanced operation mode using integrated simulation code [5]. Figure 6 shows 4 MW off-axis NBI-driven current density profile calculated by NUBEAM code. The total current drive efficiency in present design of off-axis NBI-2 is enough as high as that in existing on-axis NBI-1. In this calculation, the double null plasma equilibrium is used for counter-clockwise plasma current and toroidal magnetic field. So, downward beam is more efficient in current drive than upward beam regarding the beam alignment to the magnetic pitch angle.

It will be challenging to design new internal components such as the deflecting magnet and the residual ion dump with a special shielding structure of stray vertical magnetic field generated by poloidal field coil current and plasma current, the calorimeter beam dump, the cryogenic system for the focused vertical two beams each tilted upward and downward. Additionally, the balanced neutral beam scheme for the low torque relevant to ITER and fusion reactor requires the axis rotation system for the opposite injection angle because the present co-tangential NBI-1 cannot be rotated for the counter beam injection. This requires the change of the plasma current direction to counter-clockwise direction as well as the rotation of off-axis NBI to counter-clockwise direction for the preferable co-tangential off-axis current drive. The rotation of full system will require the flexible support system of many cryogenic lines and water-cooling lines. More detailed design work is going to be carried out in 2014.

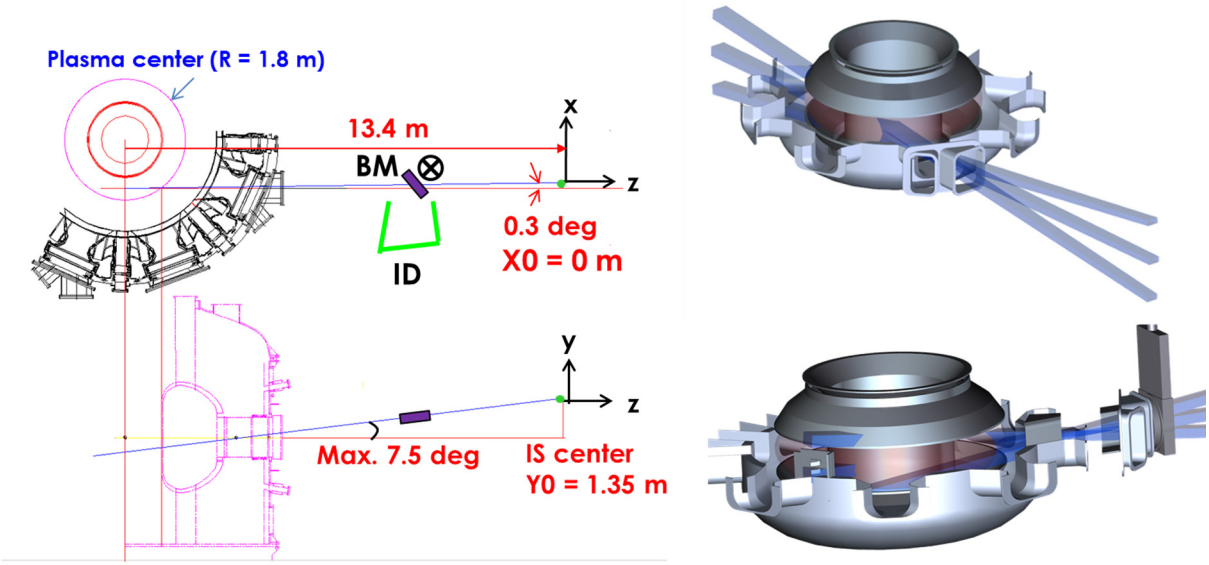

Fig. 4. The tentative pre-conceptual design of off-axis NBI-2 with three beams in vertical plane.

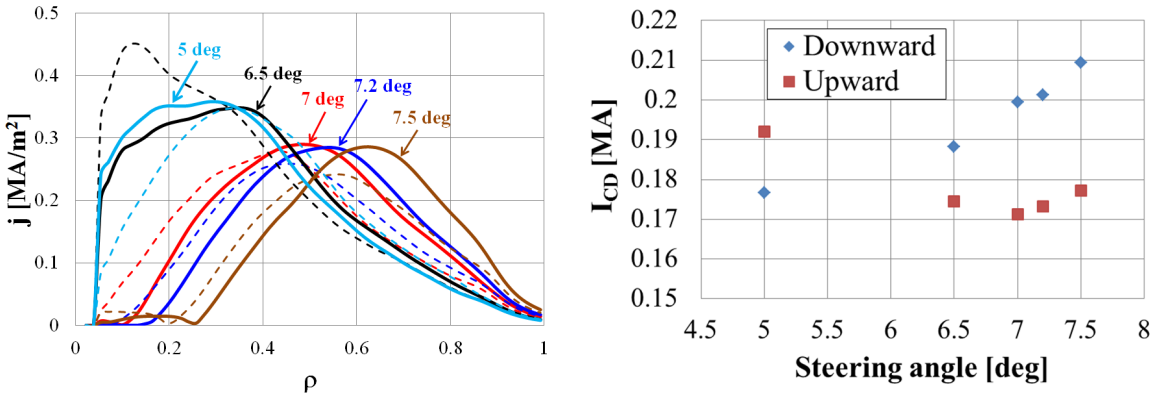

Fig. 5. (Left) Physics validation by NUBEAM code simulation for the off-axis current profile for several vertical steering angles based on the pre-conceptual design in fig. 4 with double null plasma equilibrium with the plasma current 1 MA and the toroidal magnetic field of 2 T. (Right) The total driven current from each beam source vs steering angle.

Acknowledgement

This research was supported by Ministry of Science, ICT, and Future Planning under KSTAR project and was partly supported by the JSPS-NRF-NSFC A3 Foresight Program in the field of Plasma Physics (NSFC: No.11261140328, NRF : No. 2012K2A2A6000443).

References

[1] D.N. Hill et al., Nucl. Fusion 53, 104001 (2013).
[2] C.T. Holcomb et al., EX/1-5, IAEA FEC, San Diego, Oct. 8-13, 2012.
[3] D.H. Chang et al., Fusion Eng. Design 86, 244 (2011).
[4] Y.S. Bae et al., Fusion Eng. Design 87, 1597 (2012)
[5] H.S. Kim et al., A3 workshop, June 23-26, Kagoshima, Japan (2014).

Recent Progress in Experimental Studies of Energetic-Ion-Driven Global Modes on LHD

K. Toi and LHD Experiment Team
National Institute for Fusion Science, Toki, Japan

Abstract

In a stellarator/helical device LHD (Large Helical Device), interaction between energetic ions and MHD modes is intensively studied, because it can destabilize global modes and they can enhance radial redistribution and/or losses of energetic ions noticeably. In this paper, recent progresses of experimental studies on the following main topics on LHD are summarized: (1) MHD spectroscopy using energetic ion driven modes, (2) Characteristics of energetic ion driven geodesic acoustic mode, and (3) Destabilization of MHD modes by helically trapped energetic ions.

1. Introduction

Good confinement of energetic ions is crucial for sustaining D-T burning and avoiding damages of plasma facing components by lost energetic ions in a fusion reactor. Energetic ions can destabilize global modes via resonant interactions in toroidal plasmas such as tokamaks and stellarator/helical devices, and in turn these modes can enhance radial transport such as redistribution and losses. In a tokamak plasma, energetic ion orbits are classified into “passing” and “trapped” orbits. The trapped energetic ions travel toroidally by precessional motions. On the other hand, energetic ion orbits in the Large Helical Device (LHD) are classified into “passing”, “helically trapped” and “transition” orbits. Helically trapped ions have a pitch angle close to ~ 90 ° and are trapped in helical ripples of the LHD magnetic configuration. They travel poloidally and toroidally along a helical ripple well. Passing and helically trapped energetic ions can destabilize global modes in LHD plasmas, since these energetic ions are well confined and the pressure can increase appreciably. Transition particles are not well confined in LHD and would not destabilize global modes. Accordingly, we should pay much attention to interaction of MHD modes with passing and helically trapped energetic ions.

In LHD, toroidicity induced Alfven eigenmoes (TAEs) are routinely excited in moderate density plasmas of $\langle n_e \rangle \lesssim 5\times10^{19}$ m^{-3} at toroidal field strength B_t=0.5 ~ 2.75T by passing energetic ions of ~180 keV [1]. Reversed shear Alfven eigenmodes (RSAEs) are also observed in a reversed magnetic shear (RS-) plasma produced by counter neutral beam injection (NBI) [2]. Helicity induced Alfven eigenmodes (HAEs) which are excited due to non-uniformity of the field strength

coming from helical fields only in stellartor/helical plasmas are detected in the frequency range of 200 kHz to 400 kHz at low toroidal field $B_t \lesssim 1$ T, where the HAE frequency is by a factor of ~8 higher than the TAE frequency [3]. Moreover, global Alfven eigenmodes (GAEs) can be destabilized by passing energetic ions in LHD plasmas having relatively low magnetic shear in a wide core region [1]. The mode frequency of these Alfven eigenmodes (AEs) depends on the rotational transform ($\iota/2\pi$) or the safety factor (q) as well as ion density. The character enables us to predict the $\iota/2\pi$ or q-profile with good accuracy when ion density profile is known, of which idea is called "MHD spectroscopy". The recent progress is described in Section 2. In a RS-plasma produced by counter NBI, a peculiar energetic ion driven mode with toroidal mode number n=0 is observed together with RSAEs [2]. This mode is an energetic ion driven geodesic acoustic mode (EP driven GAM) and is a global mode in contrast to GAM excited by drift wave turbulence. Recently, the characteristics of the EP driven GAM and spontaneous increase of bulk ion temperature have been investigated in the RS plasma. These results are summarized in Section 3. Since the 2011 experimental campaign of LHD, high power neutral beams having relatively low energy E~40 keV are injected to a plasma, perpendicular to the toroidal field line, for bulk ion heating. The perpendicular NBIs generate helically trapped energetic ions appreciably. Then, destabilization of resistive interchange modes by helically trapped energetic ions has been observed clearly, of which instability exhibits a short burst of ~ 2ms having rapid frequency chirping-down. The results are summarized in Section 4. Section 5 summarizes the results of these three topics and discusses future extension of the above experimental studies on LHD to the KSTAR and EAST tokamaks.

2. MHD Spectroscopy using energetic ion driven Alfven eigenmodes

Global modes that can be applied to MHD spectroscopy are required to satisfy the following characteristics [4]: (i) The dispersion relation depends on plasma equilibrium quantities such as q-profile, (ii) The phase velocity should be away from ion and electron thermal velocities to avoid strong Landau damping, (iii) The frequency range does not include the components of large fluctuations due to micro turbulence, and (iv) The amplitude should be in detectable level, but not be

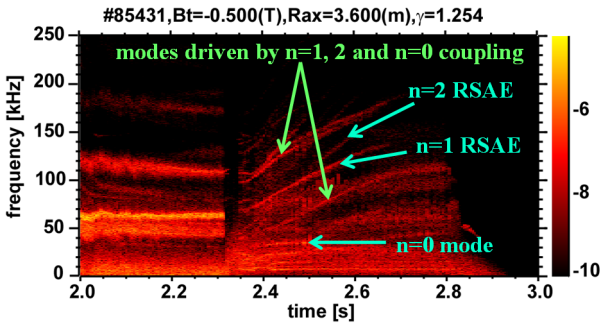

Fig.1 Spectrogram of magnetic probe signal in a medium beta RS plasma.

too large to minimize radial transport of energetic ions. Alfven eigenmodes satisfy these conditions. In particular, RSAEs and GAEs can be effectively used for MHD spectroscopy, because the mode frequency and mode location precisely provide the information of $\iota/2\pi$ or q-profile and mass ratio with help of experimentally obtained density profile. Figure 1 shows the spectrogram of magnetic probe signal in a RS plasma of the averaged toroidal beta $<\beta_t>\sim 1.2$ %. The upward frequency sweeping of the n=1 and n=2 modes from t=2.4 s to t=2.8 s is caused by time evolution of the $\iota/2\pi$ profile, since the line averaged electron density is kept constant during the frequency sweeping. In this medium $<\beta_t>$ plasma, n=1 and n=2 RSAEs are concurrently excited, while only n=1 RSAE is excited in low beta RS plasma ($<\beta_t> \lesssim$ 0.5 %) [2]. In this shot, frequency sweeping modes generated by nonlinear mode coupling between n=1/ n=2 RSAE and n=0 mode, which is geodesic acoustic mode (GAM) driven by energetic ions and discussed in the next Section. The time evolution of the $\iota/2\pi$ profile in a RS plasma can be derived from the time evolution of the mode frequency. The radial information of the mode improves the prediction of the $\iota/2\pi$ profile further. MHD spectroscopy was first proposed for a tokamak plasma, based on utilization of RSAEs [5]. In LHD, the $\iota/2\pi$ profile tends to have an off-axis minimum with the increase of the Shafranov shift due to enhanced plasma beta. In the RS plasmas of LHD, RSAEs would be destabilized by passing energetic ions and enable us predict the $\iota/2\pi$ profile accurately.

3. Characteristics of energetic ion driven geodesic acoustic mode

In counter NBI heated RS plasmas of LHD, geodesic acoustic mode (GAM) having the toroidal mode number n=0 is often destabilized by energetic ions produced by counter NBI [2]. This EP driven GAM is a global mode and accompanies appreciable magnetic fluctuations. A typical example of the spectrogram of magnetic probe signal is shown in Fig.2, where EP driven GAM having ~17-19 kHz in the phase is excited quasi-stationary. At t~5.1 s, two EP driven GAMs

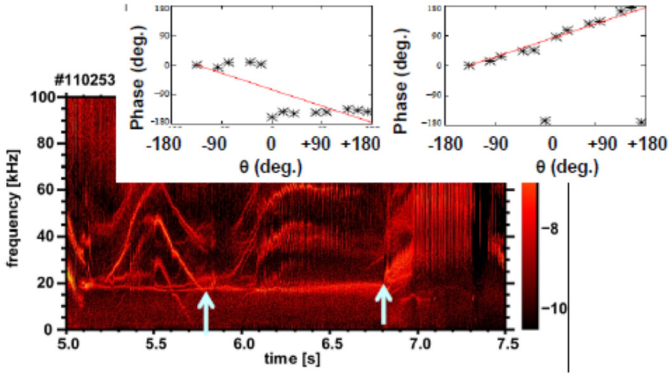

Fig.2 Spectrogram of a magnetic probe signal together with the phase shifts between magnetic probe signals of a poloidal probe array in poloidal direction for the n=0 mode (#1 GAM)

having slightly different frequency are simultaneously excited. While one of GAMs (#1 GAM) is excited having nearly constant frequency of ~18 kHz, the other GAM (#2 GAM) evolves increasing the frequency from ~19 kHz to ~25 kHz and is suppressed. From t~5.5 s, two EP driven GAMs are again excited in a similar manner to that in the phase from t~5.1s. Magnetic fluctuations of these GAMs have standing wave structure poloidally, but sometimes exhibit m=1 rotating mode structure, as shown in Fig.2. The potential fluctuations induced by this mode are measured by a heavy ion beam probe (HIBP). The spectrogram of the coherence γ^2 between magnetic and potential fluctuations at two radial locations is shown in Fig.3. High coherence is found at EP driven GAMs. The higher frequency GAM (#2 GAM) is only detected in an inner region of r/a$\lesssim$ 0.2, while the

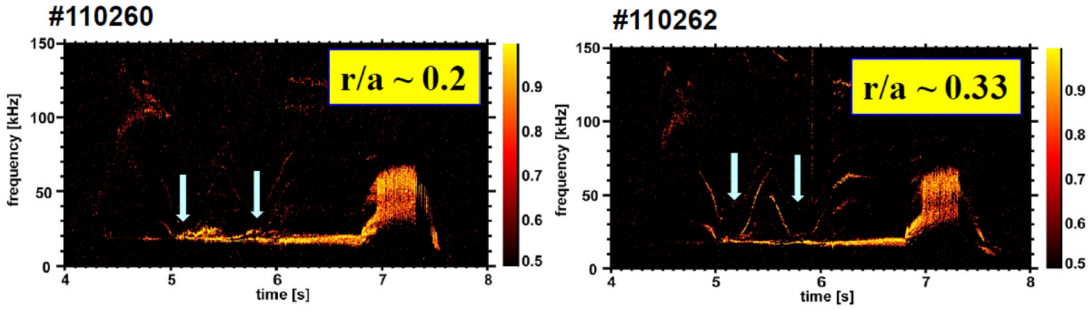

Fig.3 Fig.3 Spectrogram of the coherence γ^2 between plasma potential and magnetic fluctuations where the probe bema of HIBP is placed at two radial positions r/a ~0.2 and 0.33. ECH is applied from t=6.8 s to t=7.3 s.

lower frequency mode (#1 GAM) is more radially extended up to at least r/a~0.33. In the RS plasma where RSAEs and EP driven GAMs are excited as shown in Fig.2 or Fig.3, bulk ion temperature at the plasma center T_{io} shows a characteristic time evolution. In Fig.4, T_{io} evolves oscillatory in time and the start of large increase seems to correlate with the time that $(\iota/2\pi)_{min}$ passes the rational value 1/3. It should be noted that the frequency of the EP driven GAM does not respond to the T_{io} rise in the RS plasmas. On the other hand, the mode frequency clearly increases with the increase in electron temperature during ECH, as shown in Fig.2 and 3. The different

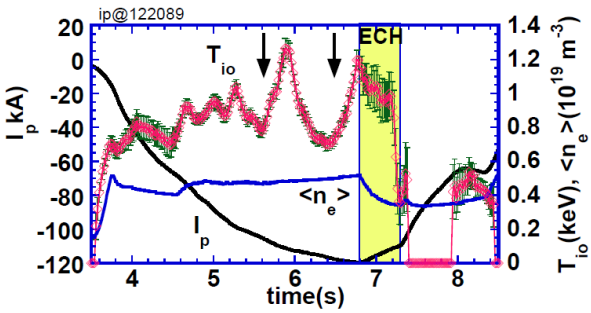

Fig.4 Time evolutions of T_{io}, the line averaged electron density and plasma current driven by counter NBI in a RS plasma.

responses to temperature increase on the EP driven GAM frequency and the mechanism of the above-mentioned spontaneous T_{io} rise are interesting topic and are under investigation.

4. Destabilization of MHD modes by helically trapped energetic ions

At high toroidal field of Bt $\geq$ 2. 75T, helically trapped ions generated by perpendicular NBI, of which beam energy is E~36 keV, are confined well and go around an LHD plasma along helical ripple well of the magnetic field strength. When the beam pressure reaches a certain threshold, a bursting mode having rapid frequency chirping-down is excited as shown in Fig.5 [6]. The radial structure of the destabilized mode measured by a soft X-ray detector array is quite similar to that of usual pressure driven resistive interchange mode (RIC) which is weakly unstable in magnetic hill region in plasma peripheral region of LHD. The eigenfunction derived from the data localizes at the $\iota/2\pi=1$ rational surface. The observed bursting mode is thought to be RIC destabilized by helically trapped energetic ions, and is called Energetic ion drive InterChange (EIC). The EIC propagates in electron diamagnetic drift direction with electron diamagnetic drift frequency and counter direction to the toroidal field in the plasma frame. The initial frequency is determined by the resonance condition with helically trapped energetic ions as $f=(m+\mu)f_{EP\theta}-(n+\nu N)f_{EP\varphi}=-1.2\ f_{EP\theta}$, where m=1, n=1, μ=0, ν=1 and N=10. The poloidal and toroidal rotation frequencies of helically trapped energetic ions of E=36 keV are about – 6.9 kHz (ion diamagnetic drift direction) and $f_{EP\varphi} = (\ell/N)\ f_{EP\theta}$ (counter toroidal field direction), where ℓ is the polarity of helical field and ℓ=2 for LHD. Note that the positive sign of $f_{EP\theta}$ and $f_{EP\varphi}$ indicates electron diamagnetic drift and counter toroidal field directions, respectively. The mode frequency calculated from the above-mentioned resonance condition agrees well with the observed frequency [6]. The EIC bursts induce large drop of plasma potential uniformly in plasma core region. This result shows formation of large edge radial electric field. This is thought to be due to non-ambipolar radial transport of helically trapped energetic ions by EICs. This potential change induces large change of toroidal flow near the EIC mode center, and also clear suppression of edge micro turbulence [6]. Characteristics of EICs and the impacts on

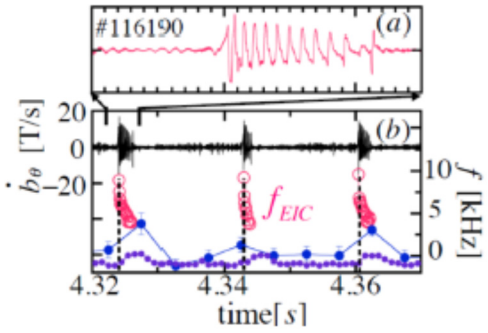

Fig.5 Time evolution of magnetic fluctuations induced by EIC bursts and the mode frequency and plasma rotation frequencies (large squares: poloidal, small circles: toroidal).

bulk plasma are studied in detail.

5. Summary and future plans

Experimental studies on the following three topics on energetic ion physics in LHD have progressed significantly in FY2013: (1) MHD spectroscopy using energetic ion driven Alfven eigenmodes, (2) Characteristics of energetic ion driven geodesic acoustic mode, and (3) Destabilization of MHD modes by helically trapped energetic ions. These topics will be studied in FY2014 more quantitatively on LHD. These studies are planned to extend to KSTAR and EAST tokamaks. In KSTAR, MHD spectroscopy using GAEs and also RSAEs may be applied to development of advanced tokamak scenario for predicting the q-profile evolution. Comparison study between EIC bursts with fishbone instabilities excited by tangential NBI in KSTAR is interesting and important for better understanding of these burst mode characters and their impacts on energetic ions and bulk plasma. In ESAT, high power ICRF heating and NBI heating have high potentiality to excite AEs and fishbone instabilities. Comparison studies among LHD, KSTAR and EAST on energetic ion physics are significant for the better understanding and developing control techniques of these instabilities for steady-state sustainment of high performance plasmas.

Acknowledgements

This research is performed with the support and under the auspices of the *NIFS Collaboration Research Program* (NIFS12KLPH016). This research is also supported in part by the Grants-in-Aid for Scientific Research from JSPS (No. 24360386) and the *JSPS A3 Foresight Program on Critical Physics Issues Specific to Steady State Sustainment of High-Performance Plasmas* and by the *Japan-Korean Collaboration Program*.

References

[1] K. Toi et al., Plasma Phys. Control. Fusion **53** (2011) 024008.

[2] K. Toi et al., Phys. Rev. Lett. **105** (2010) 145003.

[3] S. Yamamoto et al., Phys. Rev. Lett. **91**(2003) 245001.

[4] A. Fasoli et al., Plasma Phys. Control. Fusion **44** (2002) B159.

[5] S.E. Sharapov Phys. Lett. A **289** (2001)127.

[6] X.D. Du et al., 13th IAEA TM on Energetic Particles in Magnetic Confinement Systems, Beiging, 2013, and submitted to PRL

Error Field and its Correction Strategy in Tokamaks

Yongkyoon In
National Fusion Research Institute, Daejeon, Korea
Email : yongkyoon@nfri.re.kr

While error field correction (EFC) is to minimize the unwanted kink-resonant non-axisymmetric components, resonant magnetic perturbation (RMP) application is to maximize the benefits of pitch-resonant non-axisymmetric components. As the plasma response against non-axisymmetric field increases with beta increase, feedback-controlled EFC is a more promising EFC strategy in reactor-relevant high-beta regimes. Nonetheless, various physical aspects and uncertainties associated with EFC should be taken into account and clarified in the terms of multiple low-*n* EFC and multiple MHD modes, in addition to the compatibility issue with RMP application. Such a multi-faceted view of EFC strategy is briefly discussed.

1. Introduction

The presence of the non-axisymmetric fields in tokamaks is so critical to determine whether steady-state, high-performance fusion plasmas can be achieved and sustained in reactor-relevant regimes [1]. While it has been recognized for more than two decades that the unwanted non-axisymmetric field [called 'error field (EF)'] should be minimized, such a conventional paradigm needs to be reconsidered to reflect the benefits of intentionally applied non-axisymmetric field [often described as 'resonant magnetic perturbation (RMP)')]. In general, the n=1 EF and $n > 1$ RMP may be configured not to pose a conflict to differentiate two functions in fusion plasmas. Here, n refers to a toroidal mode number. However, when both EF and RMP use the same toroidal mode number, it might not be straightforward to differentiate two separate roles without addressing the relevant physical mechanisms. In particular, the recent successful operation of n=1 RMP-driven ELM-suppression in KSTAR [2] shows a good evidence that the n=1 non-axisymmetric field itself should not be regarded solely as 'error field', in that it can be also tailored to maximize the beneficial effects of RMP application. Thus, it would be desirable to re-examine the prevailing error field correction (EFC) strategy, while taking into account a variety of non-axisymmetric field aspects. At the same time, the uncertainties and limitation in the present understanding of the EF and its EFC strategy should be also factored in establishing the non-axisymmetric field control.

Thus, this paper delineates a strategic view of physical aspects associated with error field and its correction in tokamaks, which is not limited to certain conditions, but could be directly applicable to enhance the performance of advanced tokamak regimes where the presence of EF could be significantly influential.

In Section 2, a brief description of feedback-controlled error field correction is presented as a promising candidate of EFC strategy, followed by the discussion to incorporate multiple low-n EFC and MHD stabilization needs. In Section 3, the compatibility issues with the RMP application and other uncertainties are discussed. A short summary is given in Section 4.

2. Feedback-controlled Error Field Correction

Feedback-controlled error field correction [also known as dynamic error field correction (DEFC)] is one of the promising EFC strategies that can be practically used for steady-state, high-performance fusion plasmas. Typically, an intrinsic non-axisymmetry (i.e. error field) is investigated in each toroidal device, and then its correction waveform is empirically

constructed, which is usually determined in low-beta plasmas [3]. However, as beta increases, the plasma response against the presence of non-axisymmetric (NA) field increases. Thus, an empirically determined pre-programmed EFC waveform based on low-beta plasmas becomes inherently uncertain in high-beta plasmas. On the other hand, taking advantage of the increased plasma response against non-axisymmetric field in real-time detection system, the feedback-controlled error field correction is configured to nullify the measured non-axisymmetry as minimal as possible using the non-axisymmetric EFC coils [4]. Hence, this DEFC keeps reducing the ever-present uncorrected error field continuously. Considering that high-beta plasmas are accompanied by stronger plasma response against non-axisymmetric fields than low-beta plasmas, ***the DEFC is expected to be much more effective in advanced tokamak regimes***. For example, in DIII-D, the n=1 DEFC has been developed and tested in high-beta plasmas, showing affirmative results [5]. Thus, even if there are multiple low-n EF (e.g. as measured in DIII-D and NSTX), the expansion of the DEFC for multiple low-n EFC is not expected to be technically difficult to deploy the necessary multiple low-n compatible DEFC strategy.

But, caution should be exercised in several areas as follows;

First, the impact of n > 1 fields in high beta plasmas differs quite substantially from that of n = 1 field. Fundamentally, all the existing EFC strategy has been laid out based on the assumption of a single dominant mode, where the spatial distribution of predominant least-stable mode remains the same even if the mode amplitude may change (i.e. single-mode rigidity). However, the accumulative effects of multiple low-n modes may not be understood in the frame of such a single mode assumption. Specifically, there is a vastly different dependence of plasma rotation influenced by n = 1 field, in comparison with n > 1 field. For example, the reducing rotation coming from an increased n=1 NA field often results in a mode-locking, while an increased n > 1 NA field is accompanied by globally reducing rotation without mode-locking. The former is thought to be primarily due to the resonant components at integer rational surfaces, while the latter is predominantly due to the non-resonant components associated with neoclassical toroidal viscosity (NTV). In practice, there are very few (if not none) models that could be consistent with the resonant torque experimental results, though the NTV-related associated non-resonant torque calculations appear in good agreement with experimental observations [6].

Second,, the DEFC should be also compatible with the RMP application as a pre-requisite. Considering that the main purpose of EFC is to minimize the non-axisymmetric field, this requirement appears to conflict with the RMP application that is designed to maximize the benefits of the NA field for ELM-suppression. However, these two non-axisymmetric field control methods are differentiable, in that the DEFC should emphasize the reduction of the kink-resonant components, while the RMP requires sufficient strengths of the pitch-resonant components. Thus, for example, when the n=1 DEFC is used to avoid the kink-resonant response in high beta plasmas, the accompanying n > 1 RMP is expected to be safely configured to maximize the pitch-resonant components necessary for ELM suppression (e.g. [7]).

Third, the DEFC is desirable to have the capability of stabilizing multiple MHD modes. Such a stringent requirement about the non-axisymmetric field control system could be much more easily resolved than might have been imagined. Specifically, while the needs of EFC and RMP application would remain in a low frequency range, various MHD modes (e.g. resistive wall modes (RWM)) that usually grow in fast time scales would require the magnetic feedback in a high frequency range. Thus, a system equipped with broadband power supply should be able to provide a hardware solution for both low and high

frequencies of non-axisymmetric field control [8]. But, the remaining concern lies in the difficulty of how to with cope with *noise issues*. Although several special schemes (e.g. Kalman filtering [9]) and model-based controller design studies (e.g. [10]) are promising, further studies should be made to verify and validate various relevant physics-models, as well as to demonstrate the benefits of model-based controllers in experiments.

Last but not least, such experimental observations and expectations are not necessarily consistent with mathematical/theoretical perspectives, in which the use of the non-axisymmetric control coils would increase, rather than decrease, the resonant components in experimentally optimized fusion plasmas [11]. That is one of the important reasons why further studies of EFC should be made to clarify several unresolved discrepancies between experiment and theory.

3. Compatibility issues of EFC with RMP application

Ever since the n=3 RMP-driven ELM-suppression was reported from DIII-D [12], the relevant physics mechanism has been vigorously investigated in various devices. While a majority of the tokamaks were able to achieve ELM-mitigations with non-axisymmetric fields (such as JET, AUG, and MAST), KSTAR is the only device that additionally achieved full ELM-suppression with RMP application [2]. In particular, the n=1 RMP-driven ELM-suppression in KSTAR is very unique, in that no other machine has ever succeeded with n=1 RMP ELM-suppression so far. (To be fair, both DIII-D and KSTAR recently accomplished the n=2 RMP ELM-suppression, as well.). Although no definitive answer about the physical mechanism has been found, a leading theory [e.g. [13]] and experimental results suggest that RMP-driven stochastic fields form island overlaps on top of edge pedestal, enhancing the particle transport (observed with density pump-out) and avoiding the destabilizing conditions of ELMs.

As mentioned earlier, ***as long as the kink-resonant components of EFC do not conflict with the pitch-resonant components of RMP application, the compatibility issue between them could be minimal.*** In this regard, the extremely low intrinsic n=1 error field in KSTAR [14] is thought to be one of the key contributing factors that helps us explain the n=1 RMP-driven ELM suppression. Since no or little intrinsic n=1 EF in KSTAR implies that the kink-resonant components would be also negligible, the KSTAR would be much more resilient against n=1 mode-locking, until the pitch-resonant components of n=1 RMP exceeds the threshold necessary for ELM-suppression. Considering that similar attempts in DIII-D with the n=1 RMP application were not successful due to strong n=1 mode-lockings [15], the minimization of the kink-resonant components seems to be quite critical, while securing the sufficient strengths of pitch-resonant components necessary for ELM-suppression. In fact, the pitch-resonant phasing (i.e. +90 degree) of n=1 RMP application between RMP coil arrays in KSTAR was very effective in ELM-suppression, while the kink-resonant phasing (i.e. +180 degree) was plagued by mode-lockings [16]. As a result, it is foreseen that the dominantly pitch-resonant n=1 RMP application might work for ELM-suppression even in other tokamaks, as long as the intrinsic kink-resonant components can be controlled (or corrected) to be low enough to avoid early mode-lockings.

Nonetheless, before making definitive conclusions, we should be able to differentiate the roles of kink-resonant and pitch-resonant components in experiments more rigorously in the near future. In particular, it is worthwhile to note that recent experiments in DIII-D suggested the n=2 RMP-driven ELM suppression appeared rather keen on the kink-resonant components, though they did not rule out the possibility that such kink-components were

potentially used to enhance the total pitch-resonant components necessary for ELM-suppression [17].

4. Summary

The prevailing EF and its correction strategy needs to be re-examined, as the understanding of the non-axisymmetric field is being enhanced. While static pre-programmed EFC waveforms are empirically developed to minimize the intrinsic EF typically measured in low-beta plasmas, feedback-controlled EFC appears more adequate in high-beta plasmas, where the plasma response gets strong with beta increase. Although the DEFC can be easily expanded to deal with multiple low-n EFC needs, a few outstanding differences between n=1 and n >1 non-axisymmetric fields in terms of their influences (e.g. plasma rotation) should be taken into account. Also, when the EFC strategy can be easily re-configured to address the needs of multiple MHD modes using a broadband power supply, the inevitably accompanying noise issues and physics model-based controllers should be further studied. Additionally, as long as the EFC strategy is established to minimize the kink-resonant components without interfering with the RMP application that should provide the sufficient strengths of pitch-resonant components, the compatibility issue of the EFC with the RMP application is expected to be none or minimal. ***Nonetheless, further studies are still needed to resolve the discrepancies between experiment and theory, as well as to demonstrate that the aforementioned EFC strategy would be feasible with steady-state, high-performance fusion plasmas in reactor-relevant regimes.***

Acknowledgement
This research was supported by Ministry of Science, ICT, and Future Planning under KSTAR project and was partly supported by the JSPS-NRF-NSFC A3 Foresight Program in the field of Plasma Physics (NSFC: No.11261140328, NRF No. 2012K2A2A6000443).

References

[1] T.C. Hender *et al*., Nucl. Fusion **47,** S12 (2007)
[2] Y.M. Jeon *et al.,* Phys. Rev. Lett. **109,** 035004 (2012)
[3] J.T. Scoville *et al*, Nucl. Fusion **31**, 875 (1991)
[4] Y. In *et al*, Nucl. Fusion **50**, 042001 (2010)
[5] A.M. Garofalo *et al,* Phys. Plasmas **9**, 1997 (2002)
[6] W. Zhu *et al.*, Phys. Rev. Lett. **96,** 225002 (2006)
[7] K. Burrell *et al,* Plasma Phys. Control. Fusion **47**, B37 (2005)
[8] Y. In *et al.,"Error Field Correction in Unstable Resistive Wall Mode (RWM) Regime,*" Proceedings of the 23rd IAEA FEC, Daejeon, Korea (2010); EXS/P5-07
[9] Y. In *et al*, Phys. Plasmas **13**, 062512 (2006)
[10] O. Katuro-Hopkins *et al,* Nucl. Fusion **47**, 1157 (2007)
[11] A.H. Boozer, Fusion Sci. and Technol. **59**, 561 (2011)
[12] T.E. Evans *et al*, Phys. Rev. Lett. **92,** 235003 (2004)
[13] P.B. Snyder *et al*, Phys. Plasmas **19**, 056115 (2012)
[14] Y. In *et al, "Intrinsic Non-axisymmetric Field in Axisymmetric KSTAR"*, presented at the meeting of Korean Physical Society, Division of Plasma Physics, Daejeon, Korea (2014)
[15] R. Buttery, private communication (2014)
[16] Y.M. Jeon *et al,"Aspects and Applications of Non-Axisymmetric Coils on KSTAR"*, presented at the 16th MHD workshop, San Diego, U.S.A. (2011)
[17] M. Lanctot *et al*, Nuclear Fusion **53**, 083019 (2013)

PIC simulations of interactions between radio-frequency waves and plasmas

Nong Xiang*, Chunyun Gan

Institute of Plasma Physics, Chinese Academy of Sciences, Hefei, Anhui 230031, P.R.China

*xiangn@ipp.ac.cn

Abstract:

PIC simulations are performed to study parametric decay process of rf wave in the ion cyclotron range of frequency in an inhomogeneous plasma. It is shown that resonant and nonresonant parametric decays occur near the lower hybrid resonant layer. In the nonresonant decay, the decay ion cyclotron quasi-modes are heavily damped by ions, and ions are heated near the resonant layer. For the resonant decay, waves at half- and second-harmonic frequencies of the pump wave are observed when the selection rules of mode-mode coupling are satisfied. The existence of the input power threshold is found to drive the half-pump frequency mode. The growth rate of the half-pump frequency wave is a few percentages of the launched frequency.

1. Introduction

ICRF wave is one of the most efficient methods for plasma heating in present tokamaks and may play an important role on the next generation of magnetic fusion devices. With the input power of the rf wave up to mega-watt, nonlinear processes such as parametric decay instabilities (PDIs) occur and cannot be ignored.

Observations of PDIs in ICRF heating experiments have been reported in different tokamak devices, such as ASDEX [1], TEXTOR [2], JT-60 [3], Alcator C-Mod [4], DIII-D [5], JET [6], HT-7 [7], et al. Three decay channels have been identified in the ICRF heating experiments: (1) nonresonant decay into an ion Bernstein wave (IBW) and a low-frequency electron quasi-mode, which would heavily damped by electron via Landau damping; (2) nonresonant decay into an IBW and an ion cyclotron quasi-mode (ICQM); (3) resonant decay into two IBWs. Special cases for the resonant decay that half- and second-harmonic frequencies of the pump wave generation are observed during experiments. PDIs degrade plasma heating (current drive), and may generate the energetic ions and increase impurities in SOL.

Theoretically, PDI is the process that a pump wave decays into two daughter waves, which satisfies the selection rules $\omega_0 = \omega_1 + \omega_2$, $k_0 = k_1 + k_2$, where (ω_0, k_0) donates the frequency and wavenumber of the pump wave, (ω_1, k_1) and (ω_2, k_2) of the daughter waves. In the dipole approximation, the growth rates for PDI are calculated by C.S. Liu [8] and Porkolab [9], assuming that the plasma is homogeneous and magnetized and the pump wave is spatially uniform. The validation of these theory

works for the inhomogeneous experimental plasma should be tested. The computer simulation based on particle-in-cell (PIC) approach is a good candidate to fulfill the task.

In the present work, the simulations via the full PIC method in the VORPAL framework [10] have been performed to investigate the collisionless nonlinear interactions between plasmas and ICRF waves. Different decay channels are observed and identified. The simulation results are compared to the experimental PDI observations and reasonable agreement is obtained.

2. Simulation model

The simulation model is shown in Fig. 1(a). We consider a slab model of tokamak plasma with the external magnetic field along the y (toroidal) direction, the magnetic field and density gradient in the x (radial) direction. A pump wave with the frequency of 24MHz is launched by the antenna located at the left boundary. There is a vacuum between the antenna and the plasma edge. Both electrons and ions are treated by a fully kinetic model. We take real ion mass, while the electron mass is three time as much to reduce the calculation time, maintaining the linear dispersion relation almost unchanged. The temperatures of the ions and electrons are 30 eV and 50 eV, respectively. In the simulation, 400 particles per cell are used.

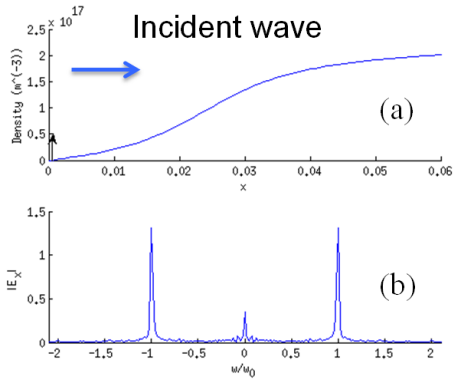

Fig. 1 (a) Density profile
(b) Frequency spectrum of Ex

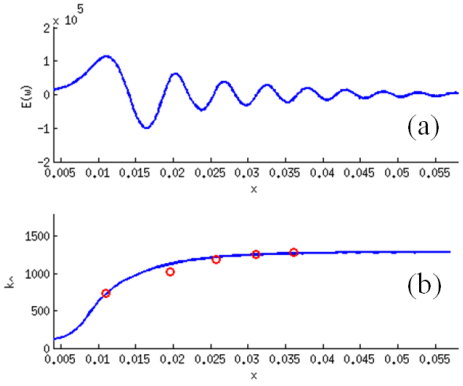

Fig. 2 (a) Spatial distribution of Ex
(b) Linear dispersion curve

3. Simulation results

In a very low incident rf power, PIC simulations obtain the mode converted electrostatic wave as predicted by the linear theory. Good agreement obtained in the comparison justifies our simulation model.

With the input power increasing, PDI occurred in the simulation. Since the driving frequency satisfies $\omega >> k_{//}v_{te}$, where v_{te} is the thermal velocity of electron, the process decay into an IBW plus a low frequency electron Landau damping quasi-mode does not appear in our simulation. Other two types of parametric decay

are found.

3.1 Verification of the simulation model

In order to validate the simulation model, the electric field obtained from the simulation with a lower incident rf power were compared with the predictions of available linear theory.

To reproduce the propagation of the incident wave, we initialized the perturbation current as $J(x,t) = J_0\exp(-(x-x_0)^2/x_0^2)\sin(\omega t)(1-\exp(-\gamma t))^2$, where J_0 = 1e2 A/m^2 and $(1-\exp(-\gamma t))^2$ is a ramped factor used to avoid the excitation of the local modes [11]. Only H ion was contained in this case.

The frequency spectrum of the Ex in Fig. 1(b) indicates that only the peak of the driving frequency appears, no sideband observed. The spatial distribution of Ex has been shown in Fig. 2(a). For the lower input power of the wave, the launched electron plasma wave (EPW) mode transform to IBW and propagate into the plasma. The perpendicular wavenumber from the simulation has been compared with the linear dispersion curve, excellent agreement was shown in Fig. 2(b).

3.2 Second harmonic wave generation

When we rising the input power (J_0=9e2 A/m^2) in the simulation, the second harmonic of the pump is observed near the lower hybrid resonant layer (located at x = 0.02 m) where the match conditions are satisfied. Fig.3 plots the frequency spectrum of this case. The other parameters are the same as above. The perpendicular wavenumbers of both the pump and second harmonic waves calculated from the simulation agree with the linear theory, as shown in Fig.4. No ions heating is observed in this case.

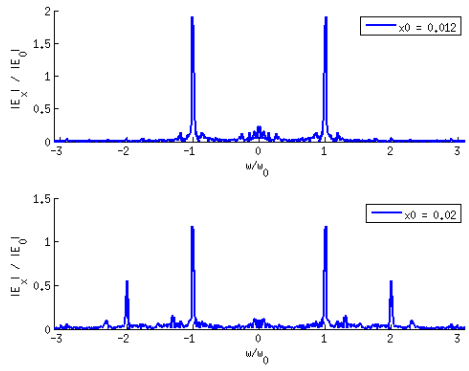

Fig. 3 Frequency spectrum of Ex

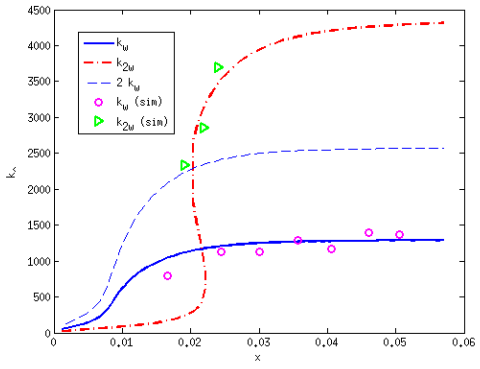

Fig. 4 Dispersion curve

3.3 Parametric decay into ICQM

To explore the PDI processes in the relevant experiments, we set the plasma parameters similar to that used on the HT-7 tokamak [7]. Nonresonant decay into an IBW plus an ICQM is observed in the simulations.

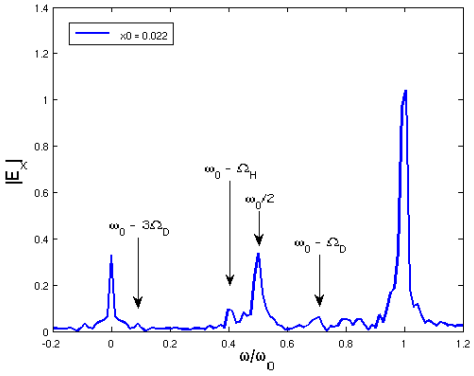

Fig. 5 Frequency spectrum of Ex

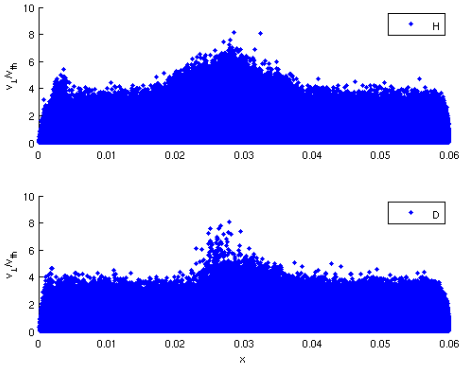

Fig. 6 Spatial distribution of normalized perpendicular velocity of

The frequency spectrum of the Ex (Fig. 5) shows that the peaks of the beat frequency wave between the pump and the ion cyclotron frequencies appear. The ICQMs are heavily damped by ions (including major deuterium and minority hydrogen), and cause ions heating observed near the lower hybrid resonant layer (located at x = 0.024) as shown in Fig. 6.

3.4 Parametric decay into half-pump frequency

When we change the density profile of the decay to ICQM channel in the previous section, the selection rules of mode-mode coupling k_ω=2 $k_{0.5\omega}$ can be match, as shown in Fig. 7. This causes a special case of two decay IBWs are the same modes, i.e. their frequencies are both half of the injected pump wave frequency, found in the simulation.

The frequency spectrum of the Ex in Fig. 8 indicates that, besides the peak of the driving frequency, the harmonics of the half-pump frequency are generated. The spatial distribution of Ex plots in Fig. 9. The perpendicular wavenumber of the half-pump frequency wave from the simulation has been compared with the linear dispersion curve, good agreement is shown in Fig. 7. Fig. 10 shows that a threshold for the electric field of the pump wave is required to drive the half-pump frequency mode. The growth rate of the half-pump frequency wave is a few percentages of the launched frequency.

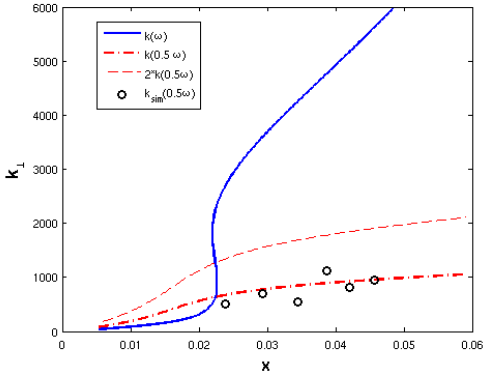

Fig. 7 Linear dispersion curve

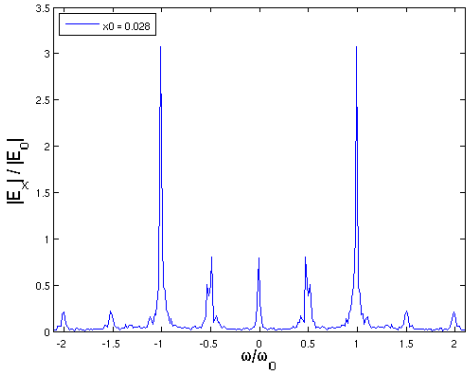

Fig. 8 Frequency spectrum of Ex

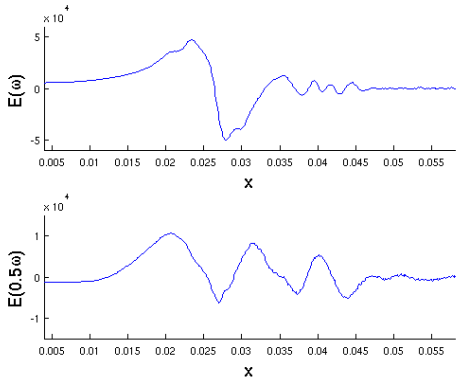

Fig. 9 Spatial distribution of Ex

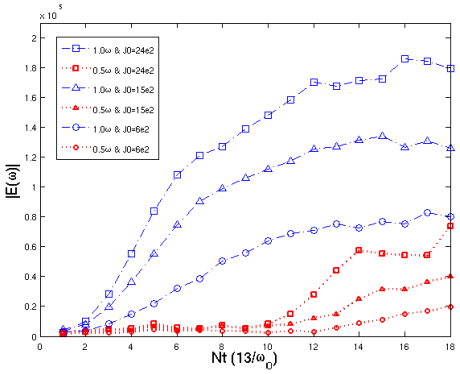

Fig. 10 Time-dependent amplitudes of the electric field

4. Summary and discussions

In the work, PIC simulations are performed to study PDI of rf wave in the ion cyclotron range of frequency in an inhomogeneous plasma. Simulations reproduced resonant and nonresonant parametric decays as observed in HT-7 IBW experiments. Waves at half- and second-harmonic frequencies of the pump wave are observed near the lower hybrid resonant layer when the selection rules of mode-mode coupling are satisfied. Ions heating observed in the simulation of non-resonant decay, which may cause power absorption near plasma edge. Appearance of daughter waves may deposit wave energy at unexpected locations. Ion heating occurs around the place |E| reaches its maximum value, where PDI is most likely triggered. Because most the wave energy is exhausted here, PDI beyond is not significant. The matching condition for k is required or not for the nonresonant decay is still unclear.

This work was partly supported by the JSPS-NRF-NSFC A3 Foresight Program in the field of Plasma Physics (NSFC: No.11261140328, NRF: No. 2012K2A2A6000443).

Reference

[1] R. Vannieuwenhove, et al., Nuclear Fusion, 28, 1603 (1988).

[2] G. Vanoost, et al., Fusion Engineering and Design, 12, 149 (1990).

[3] T. Fujii, et al., Fusion Engineering and Design, 12, 139 (1990).

[4] J.C. Rost, M. Porkolab, and R.L. Boivin, Physics of Plasmas, 9, 1262 (2002).

[5] M. Ono, Physics of Fluids B-Plasma Physics, 5,241 (1993).

[6] J.A. Heikkinen and K. Avinash, Nuclear Fusion, 29, 1307(1989).

[7] J. Li, et al., Plasma Physics and Controlled Fusion, 43, 1227(2001).

[8] C.S. Liu and V.K. Tripathi, Physics Reports, 130(3), 143 (1986).

[9] M. Porkolab, Fusion Engineering and Design, 12, 93 (1990).

[10] C. Nieter, J. R. Cary, Journal of Computational Physics, 196, 448 (2004).

[11] N. Xiang, J. R. Cary, D. C. Barnes, Physics of Plasmas, 13, 062111(2006).

Multi-phase simulation of fast ion profile flattening due to Alfvén eigenmodes in a DIII-D experiment

Y. Todo[1,2], M. A. Van Zeeland[3], A. Bierwage[4], and W. W. Heidbrink[5]

[1] National Institute for Fusion Science, Toki, Japan

[2] The Graduate University for Advanced Studies (SOKENDAI), Toki, Japan

[3] General Atomics, San Diego, United States

[4] Japan Atomic Energy Agency, Rokkasho, Japan

[5] University of California, Irvine, United States

E-mail: todo@nifs.ac.jp

Abstract. A multi-phase simulation that is a combination of classical simulation and hybrid simulation for energetic particles interacting with a magnetohydrodynamic (MHD) fluid is developed to simulate the nonlinear dynamics on the slowing down time scale of the energetic particles. The hybrid simulation code is extended with realistic beam deposition profile, collisions, and losses, and is used for both the classical and hybrid phases. The code is run without MHD perturbations in the classical phase, while the interaction between the energetic particles and the MHD fluid is simulated in the hybrid phase. In a multi-phase simulation of DIII-D discharge #142111, the stored beam ion energy is saturated due to Alfvén eigenmodes (AE modes) at a level lower than in the classical simulation. After the stored fast ion energy is saturated, the hybrid simulation is run continuously. It is demonstrated that the fast ion spatial profile is significantly flattened due to the interaction with the multiple AE modes with amplitude $v/v_A \sim \delta B/B \sim O(10^{-4})$. The dominant AE modes are toroidal Alfvén eigenmodes (TAE modes), which is consistent with the experimental observation at the simulated moment. The amplitude of the temperature fluctuations brought about by the TAE modes is of the order of 1% of the equilibrium temperature. This is also comparable with electron cyclotron emission measurements in the experiment.

1. Introduction

Significant flattening of the fast ion profile was observed during Alfvén eigenmode (AE mode) activity in DIII-D experiments [1]. In the experiments, a rich spectrum of toroidal Alfvén eigenmodes (TAE modes) and reversed shear Alfvén eigenmodes (RSAE modes) driven by ~80keV neutral beam injection is

observed during the current ramp-up phase with reversed magnetic shear. Much attention has been paid to the DIII-D experiments, and many theoretical studies have been devoted. Excellent agreement was found between ideal MHD NOVA predictions and electron cyclotron emission (ECE) measurements of the electron temperature fluctuation amplitude profile due to a TAE mode [2]. It was demonstrated with the ORBIT simulation that multiple low-amplitude AE modes with $\delta B/B$~O(10^{-4}) can account for significant modification of fast ion distributions [3, 4].

For the fast ion transport investigated in Refs. [3,4], resonance overlap was found to be the key mechanism. Resonance overlap of multiple AE modes was predicted to lead to global diffusion of fast ions and enhancement in the AE mode energy [5]. A reduced simulation reproduced TAE bursts and fast ion losses of a TFTR experiment [6]. The fast ion transport mechanism in that work was found to be resonance overlap and overlap of higher-order islands created by a single mode. However, the saturation amplitude in the simulation was $\delta B/B$~2×10^{-2} at the mode peak locations, which is larger than that in the TFTR experiment by roughly one order of magnitude. A nonlinear MHD simulation with fast ion source and slowing down collisions demonstrated that the nonlinear MHD effect reduces the saturation amplitude for the TFTR experiment to $\delta B/B$~5×10^{-3} at the mode peak locations, and $\delta B/B$ ~10^{-3} at the edge region, which is comparable to the experiment [7].

A question that arises is "what is the required AE mode amplitude for considerable fast ion transport?" In the simulation for the TFTR experiment the saturation AE mode amplitude is $\delta B/B$~5×10^{-3} at the mode peak locations, while the inferred amplitude is $\delta B/B$~10^{-4} in the DIII-D experiment. This difference might be attributed to the differences in temporal behavior of AE modes (bursty in TFTR versus steady in DIII-D), and in q-profile (normal shear with q_{min}~1 in TFTR versus reversed shear with q_{min}~3-4 in DIII-D). However, a definite answer to this question is given only by the MHD simulation applied to the DIII-D experiment and motivates us to simulate the DIII-D experiment as realistically as possible.

2. Simulation Results

2.1. Multi-phase simulation with realistic parameters

We have run a multi-phase simulation and a classical simulation for the DIII-D discharge #142111 at $t=525$ms [8]. We use experimental values for collision frequencies, the beam deposition power 4.95MW (for the full energy component), and the beam deposition profile given by the EFIT code. 8 million computational particles are injected at a constant rate over a 150ms time interval, although both the multi-phase and classical simulations are terminated before $t=150$ms.

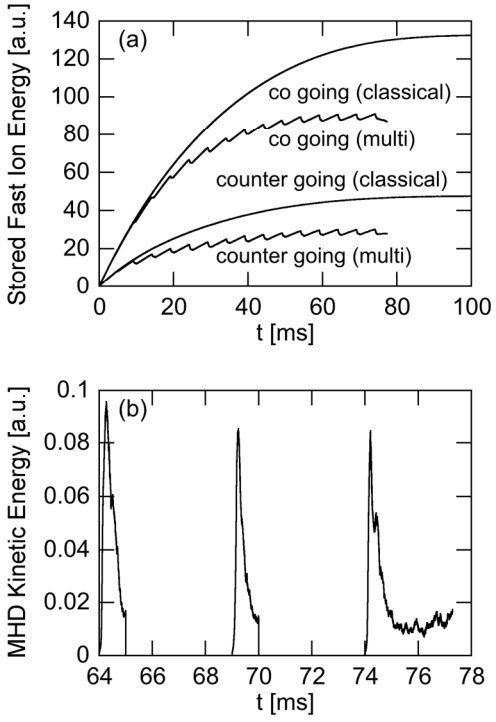

Fig. 1 Time evolutions of (a) stored fast ion energy in multi-phase and classical simulations and (b) MHD kinetic energy in the multi-phase simulation.

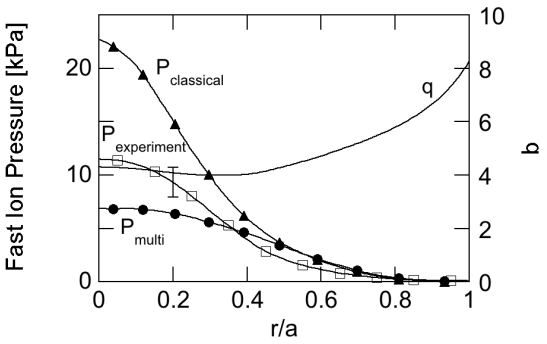

Fig. 2 Comparison of fast ion pressure profile among multi-phase simulation (circle), classical (triangle) simulation, and experiment (square) with an error bar shown in the figure. The random error in the experimental fast-ion pressure associated with subtraction of the thermal pressure is represented by the error bar; the uncertainty in determination of the total pressure from equilibrium reconstructions contributes a comparable systematic error.

The numbers of grid points are (128, 128, 256) for (R, φ, z) coordinates, respectively. We restrict the toroidal mode number of energetic particle drive in the simulation to *n=1-5* in order to reduce the numerical noise. This is supported by the experimental observation that the toroidal mode number of the AE modes is *n=1-5* at *t~525*ms [9]. Here, the dissipation coefficients are set to be $5\times10^{-7}\mathrm{v}_A R_0$. Figure 1 shows the time evolution of stored fast ion energy and MHD kinetic energy. The multi-phase simulation in Figure 1 was run with alternating classical phase for 4ms and hybrid phase for 1ms. This combination was repeated until stored fast ion energy is saturated at *t=75*ms, after which, the hybrid simulation is run continuously. We see the MHD kinetic energy reaches a steady level in Fig. 1(b). The fast ion pressure reaches a steady-state profile after *t=75*ms. Figure 2 compares the fast ion pressure profiles among the multi-phase and classical simulations, and the experiment. The fast ion pressure profile in the experiment is inferred from the equilibrium reconstruction and the subtraction of the thermal pressure. We see in Fig. 2 that significant flattening of fast ion pressure profile takes place in the multi-phase simulation.

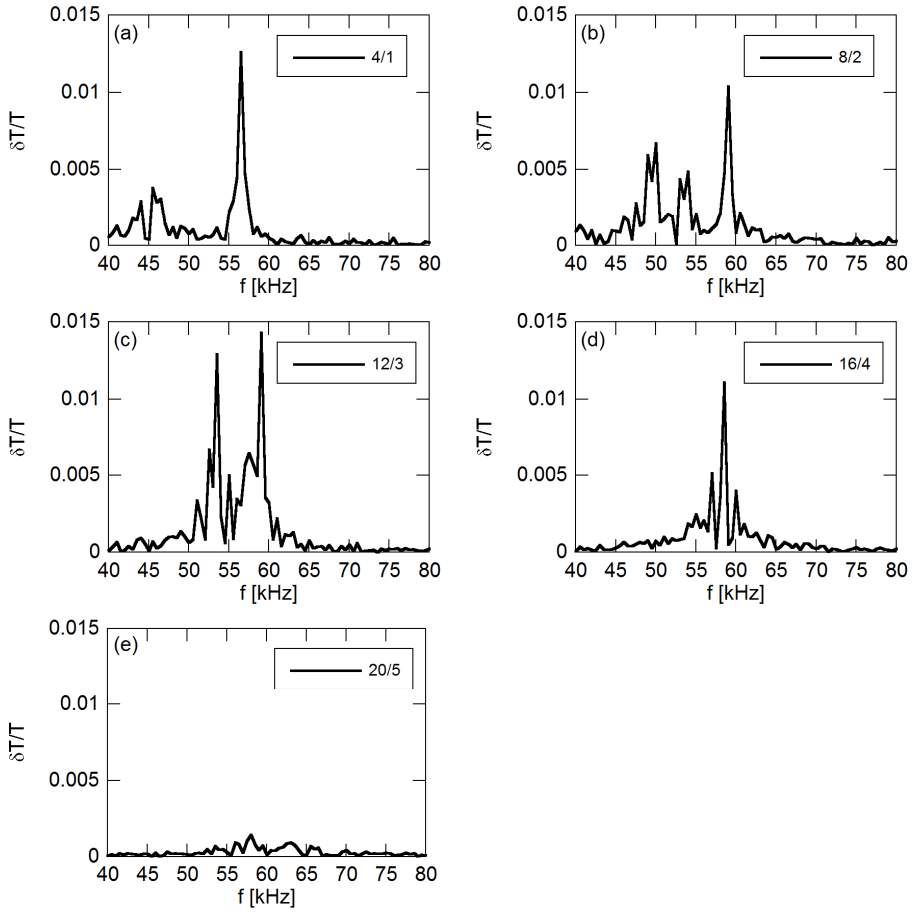

*Fig.3 Frequency spectra of temperature fluctuation at r/a=0.4 for75.0*ms *≤t≤77.3*ms *for (a) m/n=4/1, (b) m/n=8/2, (c) m/n=12/3, (d) m/n=16/4, and (e) m/n=20/5.*

We should note that the half and third energy components, which would increase the fast ion pressure to a level closer to the experiment, are not included in the present simulations, and the total beam deposition power is lower than in the experiment.

2.2. Alfvén eigenmodes and fast ion transport in steady state

Bulk temperature fluctuation spectra with toroidal mode number *n=1-5* at *r/a=0.4* are shown for *75*ms *≤t≤77.3*ms in Fig. 3. The temperature fluctuation is normalized by the equilibrium temperature. At *t=525*ms in the experiment, the TAE modes with *n=1* and *3-5* are observed, whereas the *n=2* TAE mode is not. We should note that *n=2* modes are observed at other times in this discharge.

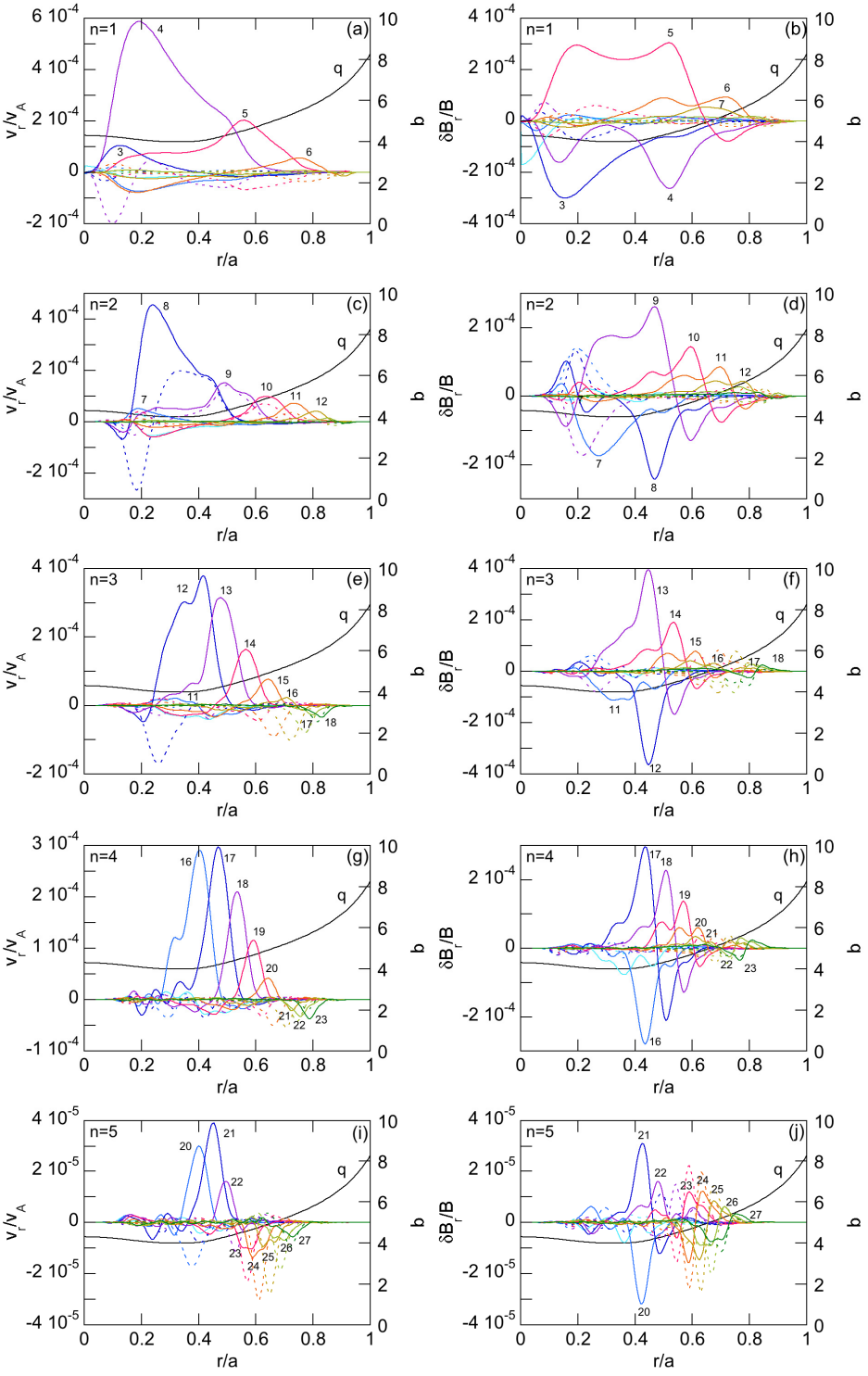

Fig.4 Radial velocity and magnetic fluctuation profiles of TAE modes with toroidal mode number and frequency (a) (b) n=1, f=56.5kHz, (c)(d) n=2, f= 59.0kHz, (e)(f) n=3, f=59.0kHz, (g)(h) n=4, f=58.5kHz, (i)(j) n=5, f=58.0kHz. Solid (dotted) lines represent cosine (sine) components with poloidal mode number labeled in the figure.

We see $\delta T/T \sim O(10^{-2})$ for *n=1, 3*, and *4* that is comparable to the experiment. For *n=5*, the temperature fluctuation $\delta T/T \sim O(10^{-3})$ is lower than that of the experiment. The frequency of the dominant fluctuations is ~60kHz that corresponds to the TAE gap. The spatial profiles of the radial velocity and magnetic fluctuations are analyzed for the dominant frequency of each toroidal mode number, and are shown in Fig. 4. The Fourier decomposition is executed in time for $75\text{ms} \le t \le 77.3\text{ms}$. The spatial profiles shown in Fig. 4 consist of many poloidal hamonics, and the frequency is just above the accumulation point of the lower-frequency continuum of the TAE gap. These indicate that the dominant fluctuations are TAE modes. The n=1 and 2 modes have also a property like energetic particle mode such that their peak is located on the continuum. The amplitude of the TAE modes is $\mathrm{v}_r / \mathrm{v}_A \sim \delta B_r / B \sim 3-6\times10^{-4}$ for *n=1-4* and $\mathrm{v}_r / \mathrm{v}_A \sim \delta B_r / B \sim 4\times10^{-5}$ for *n=5*. From this, we can conclude that the fast ion profile is flattened by the multiple AE modes with amplitude $\mathrm{v}_r / \mathrm{v}_A \sim \delta B_r B \sim O(10^{-4})$.

ACKNOWLEDGMENTS

Numerical computations were performed at the Helios of the International Fusion Energy Center, the Plasma Simulator of National Institute for Fusion Science, and the K Computer of RIKEN Advanced Institute for Computational Science (Project ID: hp120212). This work was supported partly by the JSPS-NRF-NSFC A3 Foresight Program in the field of Plasma Physics (NSFC: No.11261140328, NRF: No. 2012K2A2A6000443).

References

[1] Heidbrink W. W. *et al* 2007 *Phys. Rev. Lett.* **99** 245002

[2] Van Zeeland M. A. *et al* 2009 *Nucl. Fusion* **49** 065003

[3] White R. B. *et al* 2010 *Plasma Phys. Control. Fusion.* **52** 045012

[4] White R. B. *et al* 2010 *Phys. Plasmas* **17** 056107

[5] Berk H. L., Breizman B. N. and Pekker M. S. 1995 *Nucl. Fusion* **35** 1713

[6] Todo Y., Berk H. L. and Breizman B. N. 2003 *Phys. Plasmas* **10** 2888

[7] Todo Y., Berk H. L. and Breizman B. N. 2012 *Nucl. Fusion* **52** 033003

[8] Todo Y. *et al* "Multi-phase simulation of fast ion profile flattening due to Alfvén eigenmodes in a DIII-D experiment" 2014 to appear in *Nucl. Fusion* **54**

[9] Van Zeeland M. A. *et al* 2012 *Nucl. Fusion* **52** 094023

Simulation Study of A New Kind of Energetic Particle Driven Geodesic Acoustic Mode

Hao WANG,[1] Yasushi TODO,[1,2] and Masaki Osakabe[1]
[1]*National Institute for Fusion Science, Toki 509-5292, Japan*
[2]*The Graduate University for Advanced Studies, Toki 509-5292, Japan*

A new kind of energetic particle driven geodesic acoustic mode (EGAM) is investigated using a hybrid simulation code for energetic particles interacting with a magnetohydrodynamic fluid. The energetic particle charge exchange and inertia are considered, and the new EGAM, which has weak bulk plasma temperature dependence of frequency in LHD, is reproduced by simulation. By contrast, the traditional EGAM frequency is proportional to the square root of bulk plasma temperature. Three conditions are found to be important for the transition from the traditional EGAM to the new EGAM: 1) high energetic particle pressure, 2) high charge exchange rate, and 3) low bulk plasma density. A new resonance condition that $\omega_{EGAM} = (l/K)\omega_\theta$ is obtained, where l and K are arbitrary integers. l/K = 2/3 and l/K = 3/5 for most counter- and co-going particles, respectively. The counter-going particles are more dominant for resonance. In addition, it is found that the new EGAM is a kind of typical energetic particle mode (EPM).

A new kind of energetic particle driven geodesic acoustic mode (EGAM), which has weak bulk plasma temperature dependence of frequency, has been found in the Large Helical Device (LHD) experiments [1-2] as shown in Fig. 1. In this work, the new kind of EGAM is investigated with a hybrid simulation code for energetic particles and magnetohydrodynamics (MHD). It is demonstrated in Fig. 2 that the new EGAM in the simulation results has weak bulk plasma temperature dependence of frequency, which is in contrast to the traditional EGAM whose frequency is proportional to the square root of bulk plasma temperature [3-4]. Three conditions are found to be important for the transition from the traditional EGAM to the new EGAM: 1) energetic particle pressure substantially higher than the bulk plasma pressure, 2) charge exchange rate sufficiently higher than the slowing down rate to create a bump-on-tail type distribution, and 3) bulk plasma density is low enough.

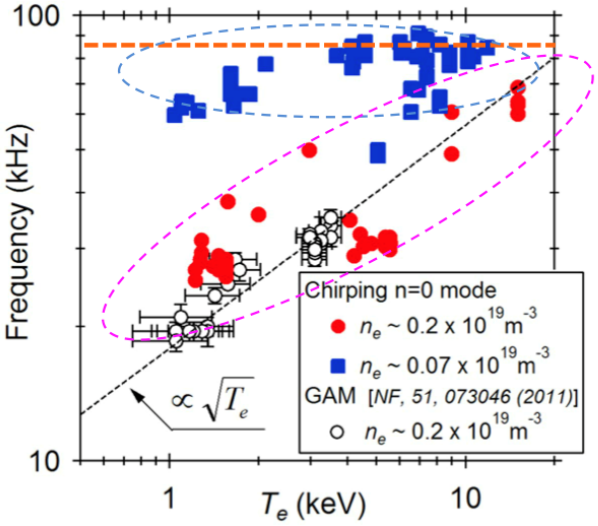

Figure 1. The new EGAM (blue) and traditional EGAM (red and black) in experiment. This figure is from Ref. [1] and [2].

MEGA code [5] is used to simulate the EGAMs in LHD. Since the kinetic geodesic acoustic mode frequency in LHD [6] is close to that in tokamaks, we investigate tokamak type equilibria with concentric circular magnetic surfaces, and with the safety factor profiles and the aspect ratio similar to the LHD plasmas. The tokamak type equilibrium is a

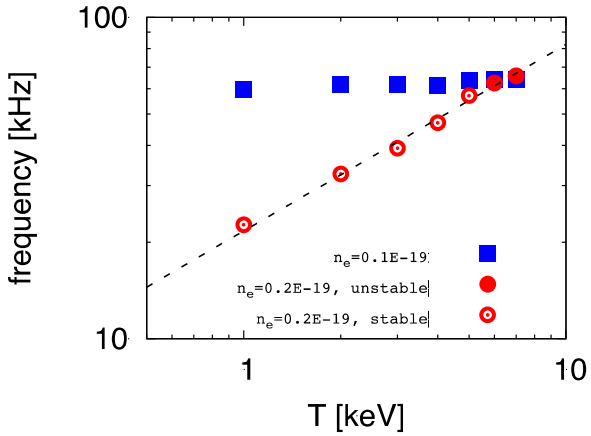

Figure 2 Two kinds of EGAMs are simulated with β_h=3% and τ_{cx}=0.39s. The bulk plasma densities for new (squares) and traditional EGAMs (circles) are $10^{18}m^{-3}$ and $2\times10^{18}m^{-3}$, respectively. The open circles represent stable mode.

reasonable approximation, because we found in our previous work [4,7] that the resonance with EGAM takes place for passing particles. The energetic particle distribution function is characterized by the slowing down time τ_s (=8s in this work) and charge exchange rate ν_{cx} . For high ν_{cx} value, the distribution function has a bump-on-tail shape. The energetic ion inertia term is added into the MHD momentum equation to simulate with energetic particle density comparable to the bulk plasma density. In addition, a Gaussian-type pitch angle distribution is assumed for the energetic ions.

Both the new and traditional EGAMs are reproduced with simulation parameters based on the LHD experiment [1-2], as shown in Fig. 2. The parameters are magnetic field strength B=1.5T, NBI energy E_{NBI}=170keV, energetic particle beta value β_h=3%, and ν_{cx}=2.5s^{-1}. For electron density $n_e=10^{18}m^{-3}$, the new EGAM has weak bulk plasma temperature dependence of frequency. On the other hand, for electron density $n_e=2\times10^{18}m^{-3}$, the traditional EGAM is excited with the frequency proportional to the square root of bulk plasma temperature. The simulated phenomena are very similar to the experimental observation that is shown in Fig. 1.

The resonance condition of the new EGAM is investigated. Normally, when a resonant particle passes one round in the poloidal angle, the phase of the mode should change by a multiple of 2π, then the resonance condition is given by $\omega_{mode}T_\theta - n\Delta\varphi = 2\pi l$, where T_θ is the time to pass one round in the poloidal angle, n is toroidal mode number, Δφ is the toroidal angle, and l is an arbitrary integer. [8] But the new EGAM case is special. When a resonant particle passes not one round but K rounds in the poloidal angle, the resonance condition is given by $K\omega_{EGAM}T_\theta - Kn\Delta\varphi = 2\pi l$, where K is arbitrary integer. n = 0 for GAM, so the resonance condition is $\omega_{EGAM} = (l/K)\omega_\theta$, where $\omega_\theta = 2\pi/T_\theta$. In order to confirm that, the particle which resonates strongest with mode, that means the particle with maximum δf value, is selected from all the half a million particles, and investigated. This particle is counter-going, and $\omega_\theta/(2\pi)$ = 85kHz. The evolution of particle position in z direction is plotted as red curve in Fig. 3(a). When the particle cross the mid-plane, the z value becomes 0, and that means particle moves a half period in poloidal cross section. We also plot the deformed mode amplitude v_θ as blue curve, where deformed v_θ is $v_\theta e^{-\gamma t}$. In Fig. 3(a), particle moves 3 circles while mode oscillates 2 times in the time interval between the 2 black lines, so l/K = 2/3. According to resonance condition, $\omega_{EGAM}/(2\pi)$ = 57kHz, very close to the mode frequency 59kHz. In addition, the particle which is co-going and resonates strongest with mode is also selected and investigated. The

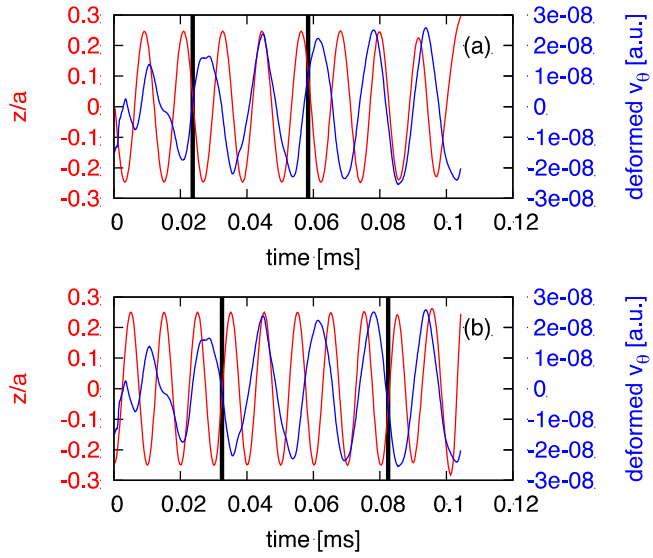

Figure 3 Time evolution of particle position in z direction and deformed amplitude v_θ for (a) the strongest resonant particle in counter-going direction and (b) co-going direction. The simulation condition is corresponding to the blue square with T = 4keV in Fig. 2.

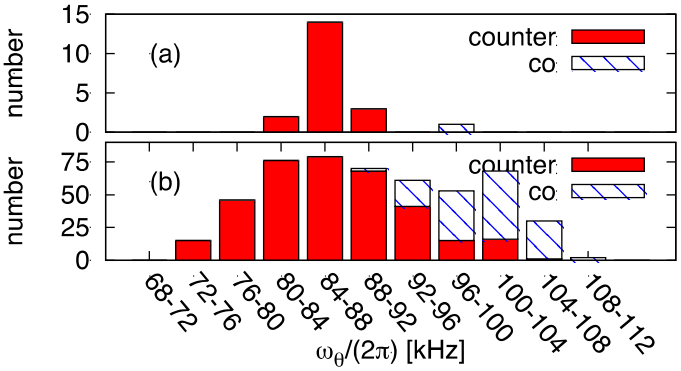

Figure 4 Statistics of the frequency distribution of (a) 20 particles and (b) 500 particles which resonate strongest with mode. Red region and blue shading represent counter- and co-going particles, respectively.

particle frequency $\omega_\theta/(2\pi)$ = 100kHz. In Fig. 3(b), particle moves 5 circles while mode oscillates 3 times in the time interval between the 2 black lines, so l/K = 3/5. According to resonance condition, $\omega_{EGAM}/(2\pi)$ = 60kHz, also close to the mode frequency 59kHz.

In fact, different particles have different l/K values. For confirmation, 20 particles and 500 particles which resonate strongest with mode are selected and analyzed, as shown in Fig. 4. In Fig. 4(a), most particles distribute in the range between 84kHz and 88kHz. Considering mode frequency 59kHz, we know most of particles have same l/K values that equal to 2/3. In Fig. 4(b), the conclusion is similar because the bar around 86kHz is also the highest. In addition, we find that most of co-going particles distribute around the frequency 100 kHz, that means they have same l/K values that equal to 3/5. Moreover, the counter-going particles (red) are more dominant for resonance, and it is consistent with DIII-D experiment [9].

Linear growth properties of the new EGAM are further investigated. Figure 5 shows that frequency increases as the central value of the Gaussian pitch angle distribution decreases, where smaller pitch angle variable corresponds to higher parallel velocity and higher transit frequency. This indicates that the frequency of new EGAM is significantly affected by the energetic particle transit frequency, and the new EGAM is a kind of energetic particle mode (EPM) whose frequency is determined by the energetic particles.

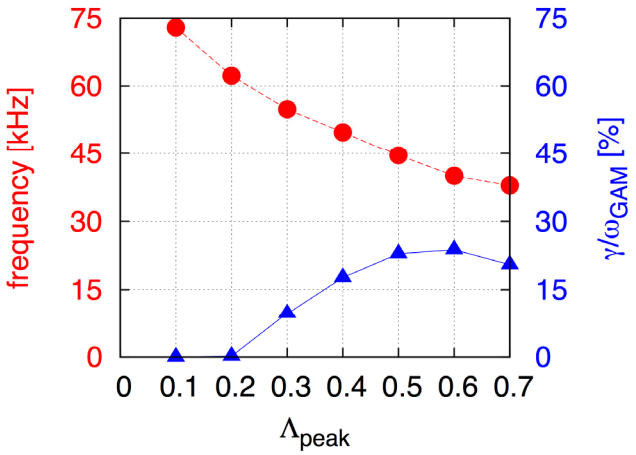

Figure 5. New EGAM frequency (circles) and growth rate (triangles) versus the center of pitch angle variable distribution Λ_{peak} with bulk plasma temperature 4 keV and density $10^{18}m^{-3}$.

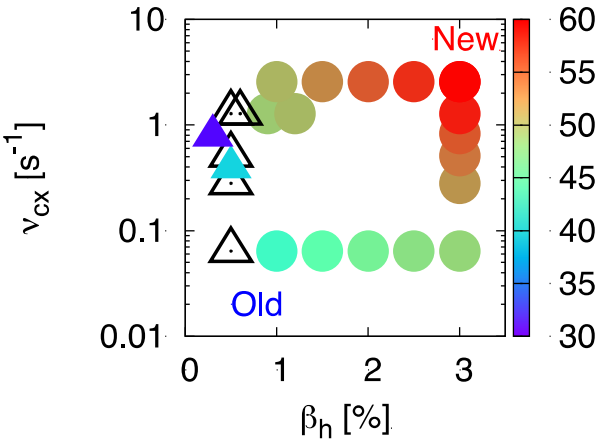

Figure 6. Mode frequency [kHz] is represented by color for various energetic particle beta and charge exchange rate. Circles represent unstable modes, and triangles are stable ones. The frequencies of open triangles are difficult to analyze.

Figure 6 shows the frequency dependence on β_h and ν_{cx}. Growth rate of new EGAM increases as β_h increases similarly with other energetic particle driven instabilities, but the frequency increases as β_h increases. For higher β_h, the effect of energetic particles is enhanced to make the frequency closer to the energetic particle transit frequency. In addition, higher ν_{cx} causes higher growth rate and frequency, because more particles exist in the high energy region of phase space.

In summary, we considered energetic particle charge exchange and inertia, and updated MEGA code to simulate the new EGAM which has weak bulk plasma temperature dependence of frequency in LHD. By contrast, the traditional EGAM frequency is proportional to the square root of bulk plasma temperature. The simulation results are consistent with experiments. The simulation parameters for EGAM excitation of both traditional and new EGAMs are compared and analyzed, and three conditions are found to be important for the transition from the traditional EGAM to the new EGAM: 1) energetic particle pressure substantially higher than the bulk plasma pressure, 2) charge exchange rate sufficiently higher than the slowing down rate to create a bump-on-tail type distribution, and 3) bulk plasma density is low

enough. The resonant particles of new EGAM are investigated, and a new resonance condition, $\omega_{EGAM} = (l/K)\,\omega_\theta$, is obtained. Normally, K = 1 for energetic particle driven instabilities like Alfven eigenmodes, but K can be arbitrary integer for new EGAM, so the new resonance condition in the present work is a stronger form compared with the traditional one. l/K is 2/3 and 3/5 for most of counter- and co-going particles, respectively. In addition, we confirmed that the counter-going particles have stronger resonance than co-going particles, and it is consistent with DIII-D's experiment. Finally, the new EGAM frequency is affected by energetic particles indicating that the mode is a kind of typical EPM.

This work was partly supported by the JSPS-NRF-NSFC A3 Foresight Program in the field of Plasma Physics (NSFC: No.11261140328, NRF: No. 2012K2A2A6000443).

Reference

[1] M. Osakabe, T. Ido, K. Ogawa *et al*, *13th IAEA-TM EP, 17-20 September 2013, Beijing, China*.
[2] T. Ido, M. Osakabe, A. Shimizu *et al*, *24th IAEA-FEC*, 8-13 October 2012, San Diego, USA.
[3] T. Ido, A. Shimizu, M. Nishiura *et al*, *Nucl. Fusion* **51**, 073046 (2011).
[4] H. Wang and Y. Todo, *Phys. Plasmas* **20** (2013) 012506.
[5] Y. Todo, *Phys. Plasmas* **13** (2006) 082503.
[6] H. Sugama and T.-H. Watanabe, *Phys. Plasmas* **13** (2006) 012501.
[7] H. Wang, Y. Todo and C. Kim, *Phys. Rev. Lett.* **110** (2013) 155006.
[8] Y. Todo and T. Sato, *Phys. Plasmas* **5** (1998) 1321.
[9] R. Nazikian *et al*, *Phys. Rev. Lett.* **101** (2008) 185001.

Simulation Study on Dynamics of Runaways in Tokamaks

Jian Liu[1], Hong Qin[1,2], Nathaniel J. Fisch[2]

[1] University of Science and Technology of China
[2] Princeton Plasma Physics Lab

Electrons with high velocities can be accelerated to very high energies by a strong electric field to form runaway electrons. In tokamaks, runaway electrons are produced in many different processes, including the acceleration from the high-energy tail of thermal distribution, through the runaway avalanche, during the rf wave heating and other non-Ohmic current drive, and even in the magnetic reconnection. This proceeding focus on different dynamical problems of runaway electrons in tokamaks.

Introduction to Runaway Electrons in Tokamaks

Runaway electrons are electrons that are accelerated to very high energies by an electric field exceeding the Dreicer field

$$\mathrm{E_D} = \frac{\mathrm{n_e e^3 \ln \Lambda}}{4\pi\epsilon_0^2 \mathrm{T}}. \quad (1)$$

Early in 1959, Dreicer discussed the runaway electron in a fully ionized gas immersed in constant field along the background magnetic field [1]. The collisional friction between an electron and background plasmas will first increase then decrease when the electron's energy rise, which means that there exists a peak value of the friction force. This is an unstable situation. When the external electric force is larger than the firction force, the electron can be accelerated faster and faster, neglecting radiation. For electrons with large velocities, the collision drag cannot balance the electric acceleration any more. The electrons can be accelerated faster and faster by the electric field.

The runaway electrons can be produced in different ways in tokamaks. In normal operations, the thermal distribution of electrons guarantees that there are a number of electrons located in the high-energy tail. These electrons with high energies can easily be accelerated to runaways. In disruption, large number of electrons can be knocked to high velocities by runaways. They thus become new runaway electrons in loop electric field through runaway avalanche process, and the number of runaways grows exponentially. On the other hand, some non-Ohmic current drive method can produce high-energy electrons, and hence the runaway electrons, such as the rf wave heating and rf wave current drive. Besides, many evidences show that runaway electrons can even be created in magnetic reconnection processes. Runaway electrons can also produce runaway positrons through pair production process in tokamaks.

The existence of runaway particles is a severe threat to the tokamak device. Massive runaway particles carrying large energies may damage the plasma-faced components of tokamaks. So it's important to understand the runaway-related physics and study the dynamics of runaway particles.

Runaway Dynamics in Tokamaks

To understand the dynamics of runaway particles in tokamaks, two factors play important roles. On the one hand, the dynamics of runaway particles in 3D configuration space should be considered. This is because both the parallel and perpendicular velocities of runaways effect the collisional drag. At the same time, the 3D geometry of the tokamak magnetic field has significant impact to the dynamics to the runaway particles. On the other hand, the collisional effect, which is critical in the runaway physics, is a random process. It is not quite precise to term an electron as being a runaway or not determinately. Instead, the runaway probability can be rigorously defined to describe runaway phenomena. Both of these factors are reflected in the following problems of runaway dynamics.

The energy limits of runaway particles determined the damages on the tokamak device by the runaways. Since the radiation loss increase with the energy of relativistic particles. Finally the radiation drag will balance the loop electric field acceleration. The radiation drag in the parallel direction are mainly composed of the synchrotron radiation drag

$$F_s = \frac{2}{3} r_e m c^2 \gamma^4 \left(\frac{\sqrt{\gamma^2-1}}{\gamma}\right)^3 \left(\frac{1}{R_0^2} + \frac{\sin^4\theta}{r_g^2}\right) \quad (2),$$

and the bremsstrahlung drag force

$$F_B = \frac{4}{137} n_e m c^2 \gamma r_e^2 (Z_{eff}+1)\left(\ln 2\gamma - \frac{1}{3}\right) \quad (3).$$

The radiation loss gives an energy limit to runaway electrons around several hundred MeVs. Besides, there are also different kinds of loss mechanisms transporting the runaways out of the tokamak plasma before the runaways gain very high energies, such as the ripple magnetic field, the turbulence, and the neoclassical orbit drift. The rapid transport can prohibit the runaways gain enough high energies by shorten their living time within the tokamak plasmas.

Among the loss mechanisms, the slowest one is the neoclassical orbit drift, which comes totally from the neoclassical effect of the 3D toroidal geometry of the tokamak magnetic field. To study the dynamics of runaway particles in phase space, we write down the Lagrangian of the gyrocenters of runaway electrons

$$L = (e\mathbf{A_0} + e\mathbf{A_1} + p_{\parallel}\mathbf{b}) \cdot \dot{\mathbf{x}} - \gamma m c^2, \quad (4)$$

where $\mathbf{A_0}$ corresponds to background magnetic field, $\mathbf{A_1}$ corresponds to the effective electric field as

$$E_{eff} = -\frac{\partial A}{\partial t} = \frac{F_S + F_c + F_B}{e}, \quad (5)$$

where

$$F_c = \frac{n_e e^4 \ln\Lambda\, m}{4\pi\epsilon_0^2}\frac{\gamma^2}{p^2} \quad (6)$$

is the collisional drag force. According to this set of equations, we can obtain the behavior of runaway particles. Besides parallel acceleration, because of the toroidal

geometry, positrons also process an outward drift velocity

$$v_{dr} = \frac{q}{B_0}(E_{\parallel} + E_{eff\parallel}), \quad (7)$$

where the effective electric field

$$E_{eff} = \frac{F_s + F_c + F_B}{e}. \quad (8)$$

Fig.1 presents the evolution of runaway particles in configuration and momentum spaces. The left two figures shows the drift of passing orbit projection in intersection surface perpendicular to toroidal direction in configuration space. The left up one is with collision, and the left down one is without collision. The left two figures compare the time revolution of parallel and perpendicular momentum. These figures show that collisions effect runaway particles in momentum space more than in configuration space.

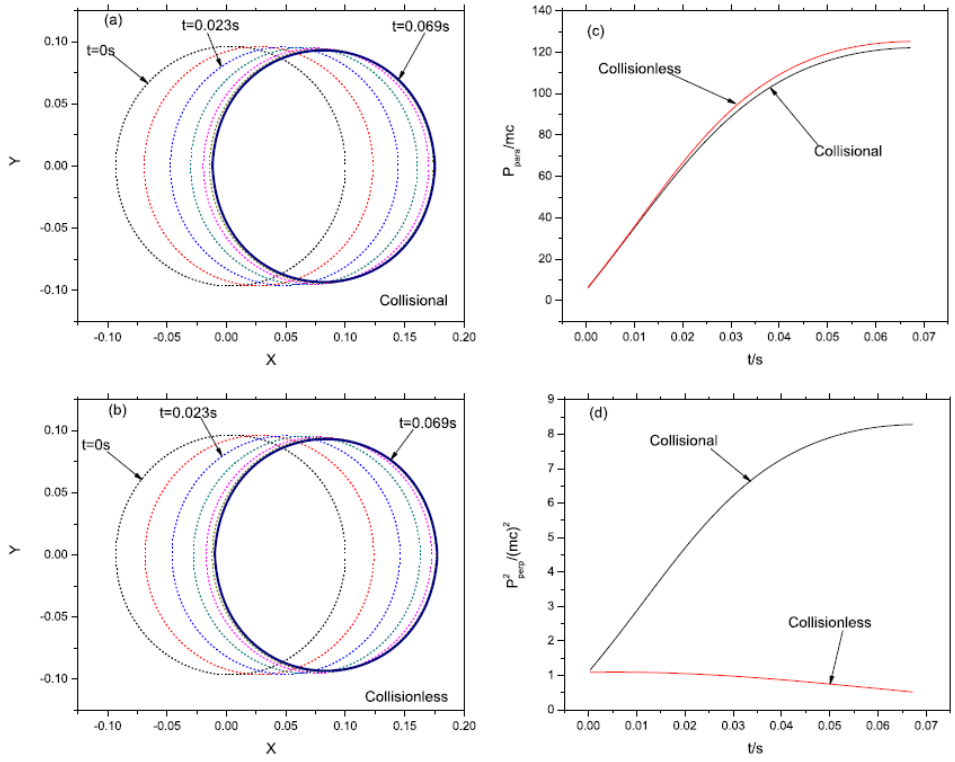

Fig. 1

Fig. 2 shows a case that a trapped particle transits to a runaway particle. The trapped orbit first drifts to the center due to the Ware pinch. Then the particle becomes passing ones and being accelerated to runaway particles. The orbit begins to drift outwards. Numerical results show that for large loop electric field, runaway particles are more likely to drift out a long distance and collide the wall.

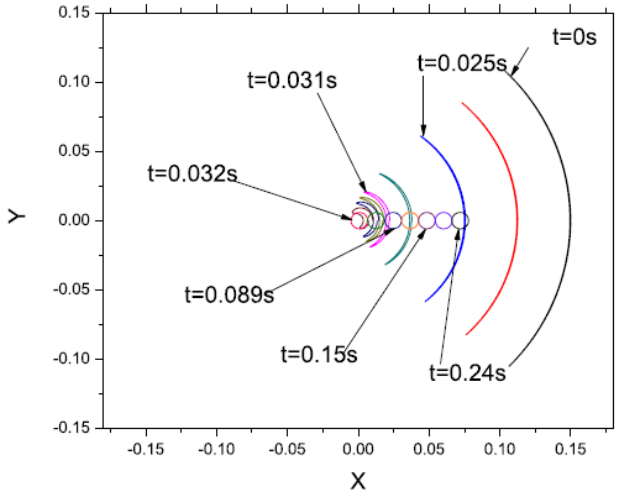

Fig. 2

If the energies carried by runaway electrons are high enough, the positrons can be produced through the pair production process in tokamaks. Pair production is the creation of an elementary particle and its anti-particle when a photon interacts with other particles. In pair production the photon's energy must exceed the total rest mass energy of the two particles. The energy conservation, momentum conservation, electric charge conservation, and many other conservation laws must hold in this procedure. The rest mass energy of electron is 0.51MeV, while in post-disruption plasmas in tokamaks the runaway electrons typically have energy between 10 and 20 MeV. It's sufficient for the pair production of electron and positron

$$\gamma + \gamma \rightarrow e^- + e^+. \quad (9)$$

At high energy, the cross-section of pair-production of electron and positron is approximately [2]

$$\sigma_p = \frac{28(Z_s \alpha r_e)^2}{27\pi} \ln^3 \gamma_e \qquad (\gamma_e \gg 1), \quad (10)$$

where $\alpha = e^2/4\pi\epsilon_0\hbar c = 1/137$ is the fine-structure constant, Z_s is the charge carried by particle species s, $r_e = e^2/4\pi\epsilon_0 m_e c^2$ is the classical electron radius, and $\gamma_e = E/m_e c^2$ is the Lorenz factor for the runaway electrons. Total pair-production cross-section over entire energy range up to 100MeV can be numerically fit as

$$\sigma_{tot} = aZ^2 \ln^3\left(\frac{\gamma_e + x_0}{3 + x_0}\right), \quad (11)$$

where $a = 5.22\mu b$, $x_0 = 3.6$. Thus given the runaway current is $I_r = 0.5MA$, the major radius $R = 1.75m$, the background electron density is $n_e = 3 \times 10^{19}/m^3$, we can estimate the positron production rate in a disruption as

$$S_p = \frac{4\pi R I_r \sigma_p n_e}{e} = 1.1 \times 10^{13}/s. \quad (12)$$

This value is actually an underestimate because the ions with higher Z_s are not considered here. Nevertheless, this value is still much higher than the production rate in accelerators where the dominating Coulomb repulsion hinders the increment of the beam density. Most of the positrons born in the pair-production have Lorentz factors

satisfying $1 \ll \gamma_+ \ll \gamma_e$, which means the original positrons are also relativistic. The annihilation cross-section can be written as

$$\sigma_a = \frac{\pi r_e^2}{1+\gamma_+}\left[\frac{\gamma_+^2+4\gamma_++1}{\gamma_+^2-1}\ln\left(\gamma_+ + \sqrt{\gamma_+^2-1}\right) - \frac{\gamma_+ + 3}{\sqrt{\gamma_+^2-1}}\right], \quad (13)$$

where γ_+ is the Lorentz factor of positron. The total pair-production cross-section σ_{tot}, pair-production cross ultra-relativistic approximation $\sigma_{\gamma\gg1}$, near threshold total cross-section σ_{th}, and annihilation cross-section σ_{an} are numerically plotted in Fig.3[3] for $Z = 1$.

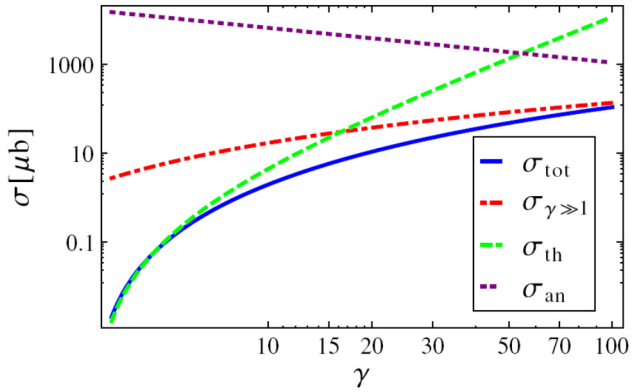

Fig.3

The dynamics of runaway positrons is similar to that of runaway electrons and also interesting. Figure 4 shows the evolution of runaway positrons after birth in the momentum space. After 0.3s, all the parallel momenta reach a steady value around 300mc, as a result of the balance between the loop electric field acceleration and the drag force resistance. The perpendicular momenta also evolve towards a steady value, though a little slower, due to the balance between the radiation loss and the momentum transfer from parallel direction through the pitch angle scattering.

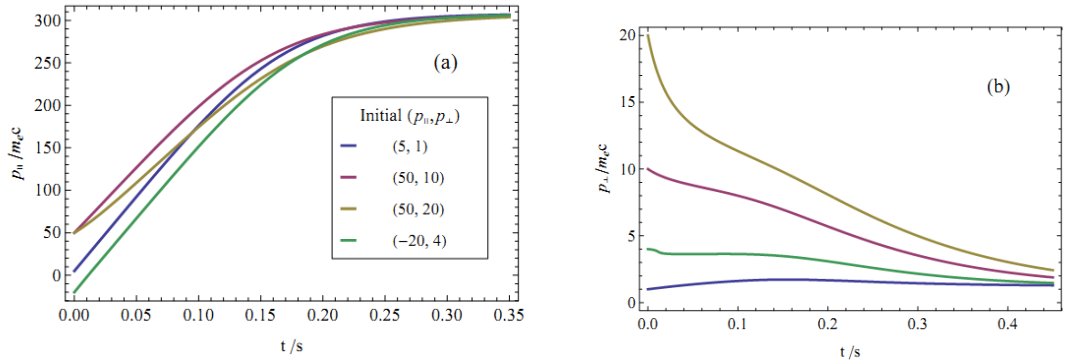

Fig.4

In Fig. 5, the counterclockwise circular orbits are snapshotted for every 0.03s.
The runaway positrons drift out and hit the first wall of the tokamak within about one hundred milliseconds with energy as large as 150 MeV.

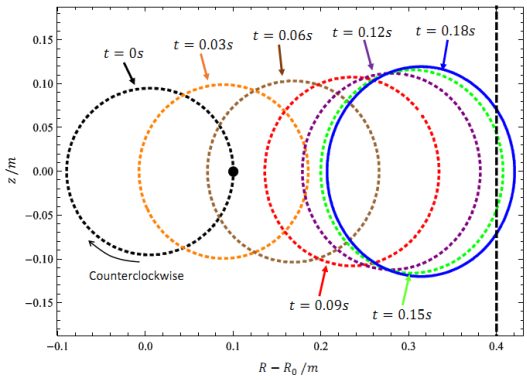

Fig.5

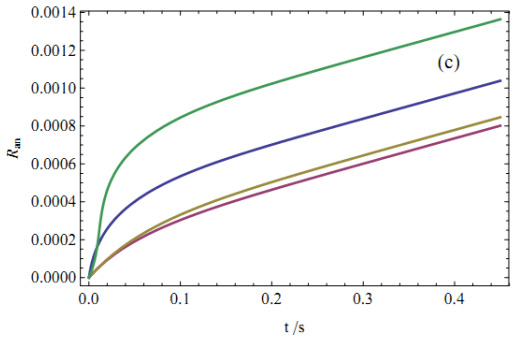

Fig.6

Figure 6 shows the annihilation rate of runaway positrons with different initial states. The backward runaway positrons (green curves) escape from the doom of annihilation for a non-relativistic positron. Though its parallel momentum goes through zero, its perpendicular momentum is still relativistic. The possibility of annihilation for runaway positrons is below 0.1% before drifting out of the plasmas.

Contours of runaway probability on the initial velocity space can be obtained by particle simulation based on stochastic differential equations. The probabilistic descriptions can precisely study the backward runaway phenomena.

Dynamics of runaway particles can be used as potential diagnostic methods. The intensity, breadth, and shift of the annihilation peak in the annihilation spectrum reflect the properties of the plasma that determines the runaway dynamics. Moreover, the time history of the positron annihilation is also an important indication to some events in tokamaks, such as a disruption or rf heating, which produce a burst of positron runaways at a specific time. The annihilation locations on the first wall and the emission directions of the gamma ray provide information about the phase space coordinates of the runaway positrons at the end of their journey, from which we can also infer the trajectories of runaway electrons in the phase space.

Acknowledgement:

This work was partly supported by the JSPS-NRF-NSFC A3 Foresight Program in the field of Plasma Physics (NSFC: No.11261140328, NRF : No. 2012K2A2A6000443).

References:

[1] H. Dreicer, Phys. Rev. **115**, 238 (1959)
[2] P.Helander, and D. Ward, Phys. Rev. Lett. **90**, 135004 (2003)
[3] T. Fulop, and G. Papp, Phys. Rev. Lett. **108**, 225003 (2012)
[4] X. Guan, H. Qin, and N. Fisch, Phys. Plasmas **17**, 092502 (2010)
[5] R. Kulsrud, Y. Sun, N. Winsor, and H. Fallon, Phys. Rev. Lett. **31**, 690 (1973)
[6] J. Wesson, *Tokamaks*, Clarendon Press-Oxford, 2004
[7] C. Surko, et. al., Rev. Sci. Inst. **57**, 1862 (1986)
[8] M. Bakhiari, G. Kramer, and D. Whyte, Phys. Plasmas **12**, 102503 (2005)

MHD instabilities studied by imaging diagnostics in the Large Helical Device

S. Ohdachi[1,2], T. F. Ming[1], K. Toi,[1], and LHD Experiment Group[1]

[1] National Institute for Fusion Science, Toki-shi 509-5292, Japan

2 The Graduate University of Advance Studies. Toki-shi 509-5292, Japan

1. Purpose of study

From the first finding of the sawtooth activities in the ST tokamak [1], measurement of the spatial structure of the MHD activities is key method to understand the MHD phenomena. Using the frame work of the A3 collaboration activities, our group has proposed several tangentially viewing two dimensional (2D) camera systems targeting for MHD study to groups in China and Korea. By introducing the effective analysis method for tangentially viewing 2D camera measurement, the merit and the weak point of the 2D measurement will be presented.

2. Merit of the tangential viewing

The soft x-ray emission from the fusion plasma has been used to estimate the shape of the magnetic surface, assuming that the electron temperature, the electron density and the impurity density is constant on a magnetic surface. From the tomographic reconstruction using several 1D SX detector arrays, the shape of the flux surface can be estimated [2]. Then the modification by the MHD activities is examined. However, the reconstruction process is a kind of differential operation which enhances noises; only large scale structure, e.g. poloidal mode number m =1, 2, ⋯ can be derived with 1D array system. In order to overcome this weak point, tangentially viewing camera system was proposed [3]. Since the most of the MHD activities has very small wave number along the magnetic field lines. MHD mode can be better visualized from the tangential direction where it is close to the direction of the magnetic field lines. Based on this proposal several types of tangentially viewing 2D camera system have been developed [4, 5]. However, the data analysis for the tangentially viewing image is not straightforward.

3. Expansion with orthogonal function

If images at a poloidal cross section can be obtained, Fourier expansion in the poloidal direction can be good tool to study the instabilities. Since the instabilities are analyzed or numerically simulated in the wave number space, comparison with wave number or mode number is the best way to be compared. However, the mode structure is strongly deformed when the structure is observed tangentially (see, Fig. 1).

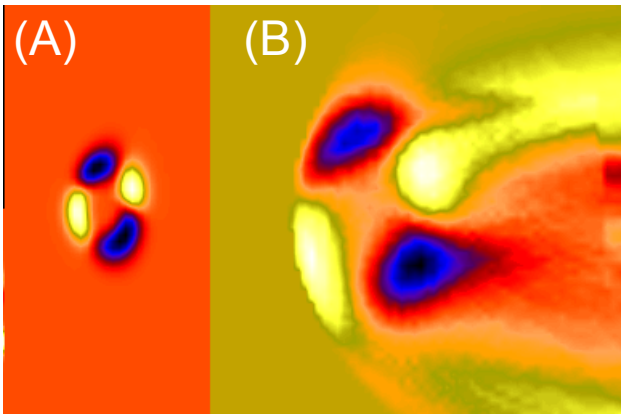

Fig. 1: Example of the mode structure at a poloidal section with poloidal/toroidal mode number m/n = 2/1 (A) and its tangential image (B).DIII-D equilibrium is used.

In order to get effective function for expansion instead of the Fourier series, so-called singular value decomposition (SVD) method [4, 6-8] is found to be quite useful. This kind of method has been used since 1960's with different names in different scientific fields, such as empirical orthogonal functions (EOF) in the meteorology, proper orthogonal decomposition (POD) in fluid mechanics. By SVD, a matrix A(MxN) made up of N time series of M (pixel number) frames (A = ($\mathbf{a}_1$, $\mathbf{a}_2$, $\mathbf{a}_3$, $\cdots$, $\mathbf{a}_n$)) is decomposed into three matrices, U(MxN), V(NxN) and a diagonal matrix W(NxN); A = UWV^t. The columns of U and V are spatial and temporal eigenvectors and are called Topos and Chronos, respectively. Each image in the moving picture $\mathbf{a}_i$ can be expressed as,

$$\boldsymbol{a}_i = w_1 \times v_{i1} \times \boldsymbol{u}_1 + w_2 \times v_{i2} \times \boldsymbol{u}_2 + \cdots + w_m \times v_{im} \times \boldsymbol{u}_m \quad . \quad (1)$$

That means each picture can be express as the summation of the the spatial eigen function Topos times its time evolution Chronos. An example take from the LHD experiments are shown in Fig. 2 [9]. Singular value decomposed components of both time (A) and space (B) from the time evolution of the tangential image are shown. Four larger components A1-A4 and B1-B4 are selected. B1 shows stationary image of the LHD plasma viewed from a tangential port, which can be understood by the fact that this component does not vary in time, as seen from A1. Images of other components are the relative change from the static image of B1 using the color bar shown at the top of the figure. Component 2 shows change of the emission profile at a collapse event happened at 1.288s. Decrease of emission at the center of the plasma and increase in the outer region can be seen in B2. Before this collapse phenomenon, development of an MHD instability having poloidal / toroidal mode number m/n = 2/1 can be seen. Two oscillating component (E3 and E4) with different phase are observed just before the minor collapse event caused by an MHD instability at ~1.3

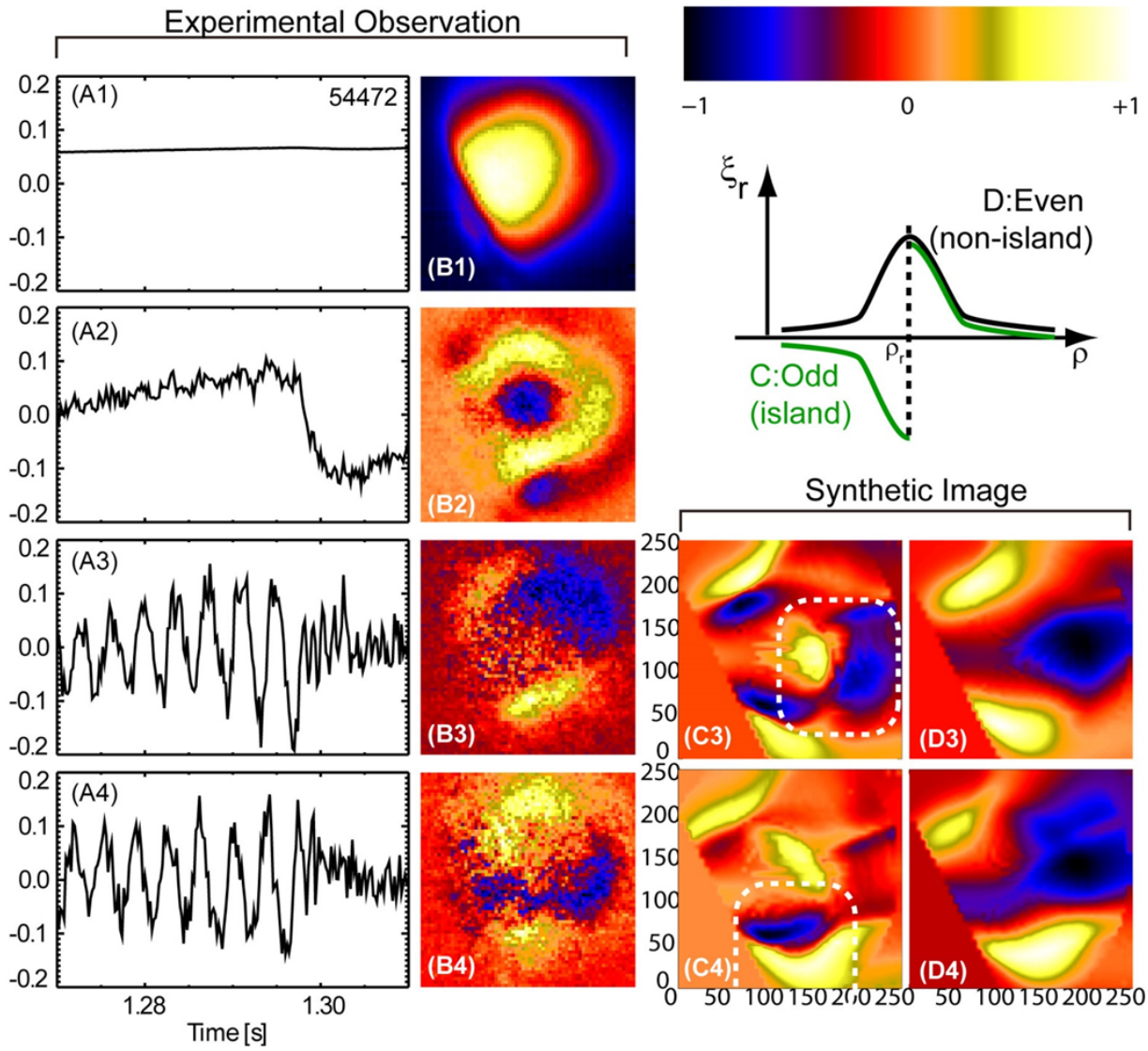

Fig. 2: Singular value decomposed components of both time (A) and space (B) from the time evolution of the tangential image obtained in LHD experiment are shown. Synthetic image assuming island type (C) and no-island type (C) are show also for the comparison.

It is clear that orthogonal spatial pattern, so-called Topos (B) are automatically determined from the experimental data and they work as the basis function for expansion. Each Topos represents different phenomena, e.g., rotation of the mode (B3, B4) and collapse events (B2)

4. How to understand the meaning of the Topos

Then, in order to compare the theory of the simulation, synthetic image should be made in order to compare with obtained Tops. The method to make synthetic image of the fluctuating component based on the MHD instability mode is described here. When we assume the MHD instabilities, the radial displacement ξ_r at the mode rational surface (averaged minor radius $\rho = \rho_r$) can be assumed to be

$$\xi_r = A_0 \exp\left(-\left(\frac{\rho-\rho_r}{w}\right)^2\right) \times f(\rho-\rho_r). \qquad (2)$$

Here, A_0 and w are the amplitude and the width of the perturbation, respectively. $f(\rho) = 1$ for non-island type and $f(\rho) = 1$ $(\rho \geq \rho_r)$, -1 $(\rho < \rho_r)$ for island type (see schematic graph shown in Fig. 2). The flux surfaces are approximated by the small triangles as shown in Fig. 3(A). From this approximation the calculation of the crossing point of the sight line with the flux surfaces become quite simple. The contribution to a pixel from the emission in a layer between the two flux surfaces can be obtained (Fig. 3(B)). Thereby the relation of the radial emission profile and the 2D image is expressed by the matrix form. The deformed structure by the radial displacement (made by eq. 2) is then rotated numerically and the fluctuation component is separated based on the singular value decomposition again.

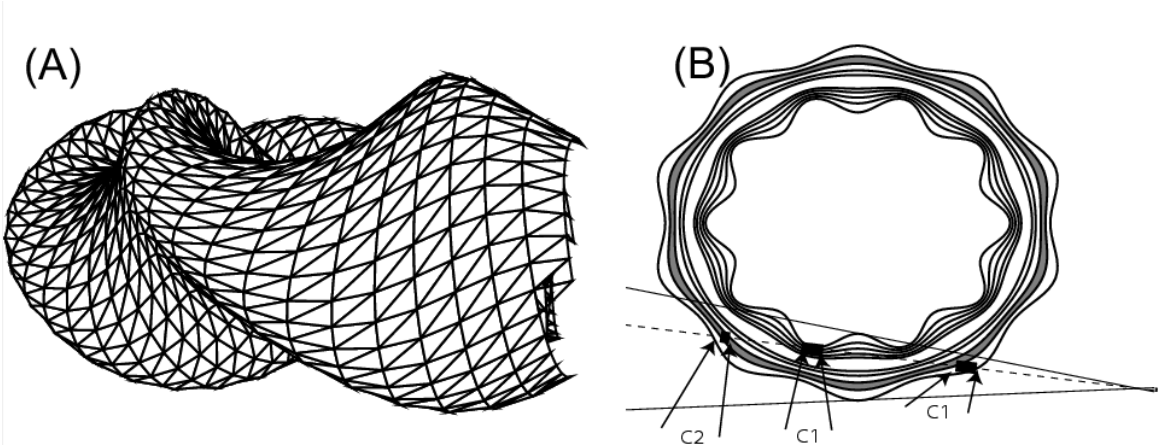

Fig. 3 Shape of the flux surface of the LHD (A) and intersection of the sight lines with the flux surface (B).

The two components are shown in the Fig. 2(C3, C4) and Fig. 2(D3, D4). From the comparison of the synthetic image with experimental ones, one can choose the reasonable model of the MHD instabilities. In this example, there is no small structure showing the phase change (like in the dashed box of C3 and C4) in the experimental image. Experimental image is rather similar to D3 and D4. Therefore, it is concluded that the radial displacement is determined to an even function (non-island type) in this type of LHD plasma even though the amplitude is large enough to make collapse events.

5. Summary

Tangentially viewing imaging diagnostics is a powerful tool since it is quite intuitive to understand the complicated phenomena. Direct decomposition using SV is the most effective way. Even though it is line integrated measurement, comparison of the MHD modeling can be performed. In LHD, the radial displacement at the rational surface is found to be of non-island type. The minimum size, where we can distinguish radial displacement is about 5% of the plasma minor radius. This type measurement will work better in the Tokamak devices, where the shape of the plasma is much simpler.

Acknowledgements

This work was supported by NIFS budget code ULPP021, 028 and is also partially supported by the Ministry of Education, Science, Sports and Culture, Grant-in-Aid for Scientific Research 26249144,by the JSPS-NRF-NSFC A3 Foresight Program (NSFC: No.11261140328, NRF : No. 2012K2A2A6000443)

References

1. Von Goeler, S., Stodiek, W. & Sauthoff, N. Studies of internal disruptions and m= 1 oscillations in tokamak discharges with soft—x-ray techniques. *Physical Review Letters* **33,** 1201 (1974).

2. Ingesson, L. C., Alper, B., Peterson, B. J. & Vallet, J.-C. Tomography diagnostics: Bolometry and soft-X-ray detection. *Fusion science and technology* **53,** 528–576 (2008).

3. Von Goeler, S. *et al.* Tangential imaging for fluctuation studies. *Review of Scientific Instruments* **61,** 3055–3057 (1990).

4. Ohdachi, S. *et al.* High-speed tangentially viewing soft x-ray camera to study magnetohydrodynamic fluctuations in toroidally confined plasmas. *Review of scientific instruments* **74,** 2136–2143 (2003).

5. Stratton, B. C. *et al.* Initial operation of the national spherical torus experiment fast tangential soft x-ray camera. *Review of scientific instruments* **75,** 3959–3961 (2004).

6. Ohdachi, S., Toi, K., Fuchs, G., Team, T. & others. Magnetic islands observed by a fast-framing tangentially viewing soft x-ray camera on LHD and TEXTOR. *Plasma Science and Technology* **8,** 45 (2006).

7. De Wit, T. D., Pecquet, A.-L., Vallet, J.-C. & Lima, R. The biorthogonal decomposition as a tool for investigating fluctuations in plasmas. *Physics of Plasmas (1994-present)* **1,** 3288–3300 (1994).

8. Nardone, C. Multichannel fluctuation data analysis by the singular value decomposition method. Application to MHD modes in JET. *Plasma physics and controlled fusion* **34,** 1447 (1992).

9. Ohdachi, S., Ming, T., Watanabe, K. Y. & Toi, K. Spatial Mode Structure of Magnetohydrodynamic Instabilities Observed by a Tangentially Viewing Soft X-ray Camera in LHD. *IEEE Transactions on Plasma Science* **in press,** (2014).

Features and applications of RMP in KSTAR

YoungMu Jeon and KSTAR team
National Fusion Research Institute, Daejeon, Korea
Email : ymjeon@nfri.re.kr

Recent RMP ELM experiments in KSTAR have successfully demonstrated that ELMs can be controlled and avoided by utilizing low n RMPs, where n is a toroidal mode number being 1 or 2. Unlike DIII-D, it is shown that the effect of RMPs on particle and thermal confinement is directly related to the state of ELMs, otherwise it is proportional to applied field strength. Most importantly, it is observed that the global particle and thermal confinement are improved significantly by suppressing ELMs, so that the typical large degradation of confinement in ELM control by using RMPs can be minimized.

1. Introduction

As the most plausible technique to control the edge localized modes (ELMs) of high confinement mode (h-mode) plasmas, which is critical for ITER and beyond, non-axisymmetric resonant magnetic perturbations (RMPs) have been actively investigated in KSTAR. Since the first success of ELM suppression using n=1 (+90 phase) RMPs in 2011 [1], we have extended its control capability to the case using n=2 (+90 phase) RMPs. Consequently we have demonstrated as shown in Figure 1 that the ELMs can be completely suppressed by properly configuring the RMP spectra for low n RMPs, where n is toroidal mode number and can be 1 or 2 in KSTAR. Also, we have found several interesting, edge-localized phenomena that are thought to be directly linked to the physics mechanism of ELM-suppression, such as a broadband increase of magnetic fluctuation, a saturated evolution of edge electron temperature, and rapidly repeating spikes on the ion saturation current measured from divertor Langmuir probes. It is conjectured that these are as a result of a persistent, rapidly repeating bursty event which is localized in the edge region under RMP fields. A detail description on these observations is found elsewhere [2-3].

A new ITER/DEMO-relevant issue, which is recently highlighted in this ELM-RMP physics, is to mitigate or suppress ELMs with minimal degradation of confinement by RMP fields. According to the DIII-D ELM-RMP experimental results [4], it is shown that the global confinement, particularly particle confinement, is significantly degraded by the strong RMP field that is needed to control the ELMs. This degradation of confinement is roughly proportional to the applied field and is not related to the ELM response or state. In other words, the amount of confinement degradation is just a function of applied RMP field strength and is independent on ELM response. Therefore, it suggests that we need to find out an optimal condition that requires a minimal RMP field to get the ELM-suppression.

However, in KSTAR, we have found a different and conflicting behavior on ELM-suppressed discharges. Interestingly the confinement of both particle and thermal energy is dependent on the ELM state or response as well as the applied RMP field strength. In fact, the confinement was improved as ELMs were suppressed. As a result, the confinement degradation due to the RMP fields was significantly reduced by suppressing ELMs. It is definitely a good aspect of ELM-RMP for application to ITER and beyond. Thus we will describe and discuss these new experimental observations here in detail.

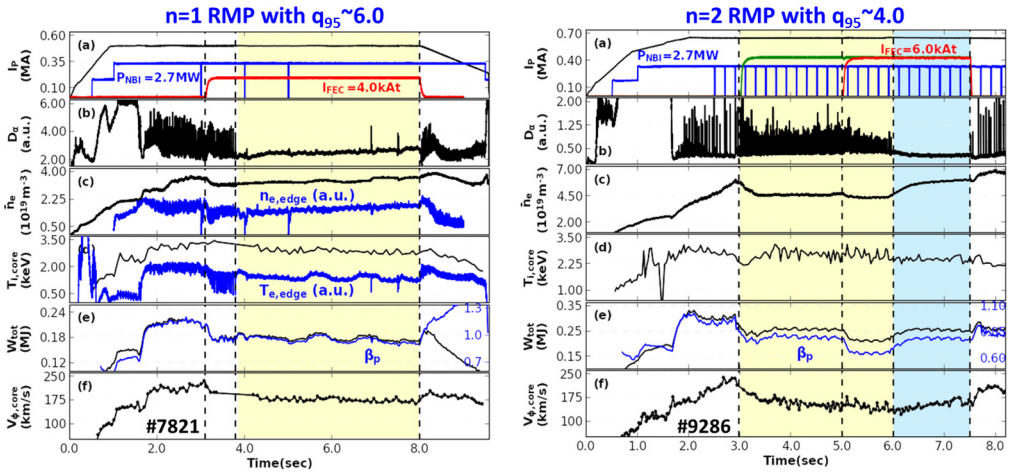

Figure 1. ELM-suppressed discharges using low n RMPs; (a) n=1 RMP at q95~6.0 and (b) n=2 RMP at q95~4.0

2. Typical change of global confinement by RMP fields

One universal observation in ELM-RMP interactions is an increase of particle transport, so called density pump-out. This density pump-out is proportional to applied RMP field strength and has a broad q_{95} window. And thus it seems to be one of fundamental and direct response of plasma to the applied perturbed field. Therefore we can observe this density pump-out in L-mode plasmas [5], in H-mode plasmas without any change of ELMs, and in H-mode plasmas with mitigated or suppressed ELMs [4].

In H-mode plasmas, when a sufficient RMP field was applied under proper q_{95} condition, the ELMs were mitigated or suppressed. Current understanding on this ELM-RMP interaction is that the applied perturbed field leads magnetic island overlapping on rational surfaces and thus produces a stochastic edge region. Then the increased edge transport though the open-field lines reduces the pedestal pressure height (or width). The resultant changes on edge stability and transport make the ELMs mitigated or even suppressed. One important observation according to DIII-D ELM-RMP experiments is that the application of RMP field leads first ELM-mitigation with relatively small field strength and then as the field strength is increased, the ELMs were finally disappeared (i.e. suppressed). It suggests that in a sense, whether the ELMs become mitigated or suppressed is just a matter of RMP field strength. This is the main reason why many of previous studies in various devices have been addressing the physics mechanism of ELM-suppression even though they haven't succeeded in ELM-suppression except DIII-D and KSTAR.

One good and latest example related to the connection between ELM mitigation and suppression under RMP fields in DIII-D is shown in Figure 2 [6], where the changes of electron temperature and density in the pedestal region depending on applied perturbed field strength are shown including ELM-responses. The key message here is that the changes of pedestal plasma parameters are strongly proportional to the applied field strength and there is no clear dependency on ELM response or state. In other words, the change of ELM state didn't make any change on pedestal parameter response. Therefore, it suggests that the increase of edge transport (or reduction of edge confinement) seems to be a fundamental and direct response to applied perturbed field. Thus probably these fundamental responses may not be sufficient to explain the physics mechanism of ELM-suppression (or even ELM-mitigation). In fact, this type of behavior (i.e. seemingly fundamental) can be found in various parameters such as thermal stored energy, beam stored energy, and energy

confinement time. Shortly summarizing, most of global or edge-localized plasma parameters showed a fundamental response (i.e. dependent only on applied field strength and independent on ELM-state) for the case of DIII-D experiments.

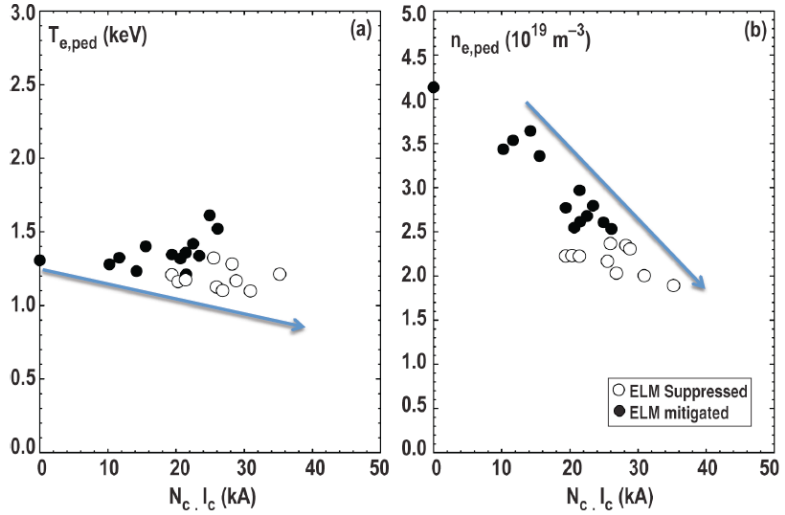

Figure 2. Plasma responses to applied RMP field strength in connection to the ELM-response (mitigated or suppressed) in DIII-D [6]. Here N_c is a number of coil turn and I_c is the coil currents.

3. Distinctive and conflicting observations in KSTAR ELM-RMP experiments

The increase of edge transport (or reduction of edge confinement) is thought to be a universal phenomenon related to RMP interaction as described above. It is valid to the KSTAR plasmas as well, so that some amounts of density pump-out have been routinely observed if the applied field is configured properly (i.e. in resonant condition). In fact, we have used the density pump-out as an indicator whether the perturbed field is resonant or non-resonant to the plasma.

However, contrarily to DIII-D observations, we have found a clear dependence of plasma response on ELM-state. One representative example is shown in Figure 3. There are two types of RMPs applied with same coil currents. One (green line in the first row) was configured using top- and bottom-FEC coils, and the other (red line) was using top-, mid-, and bottom-FEC coils together. The former RMP was less resonant, while the latter one was more resonant. Consequently the ELM-suppression was achieved in the latter RMP phase. As shown, the less resonant perturbation field led ELM-mitigation from 3.0 to 5.0sec with strong reductions of particle (n_e) and thermal energy (W_{tot} or β_p). After that when the stronger RMP field was applied from 5.0 to 7.5sec, the ELMs were initially further mitigated and then suddenly disappeared (i.e. suppressed). Interestingly when the ELMs were suppressed, although the applied RMP fields remained constant and unchanged, the electron density, stored energy, and poloidal beta were increased (i.e. confinement improved). In other words, the global plasma parameters were responded to the change of ELM-state (from

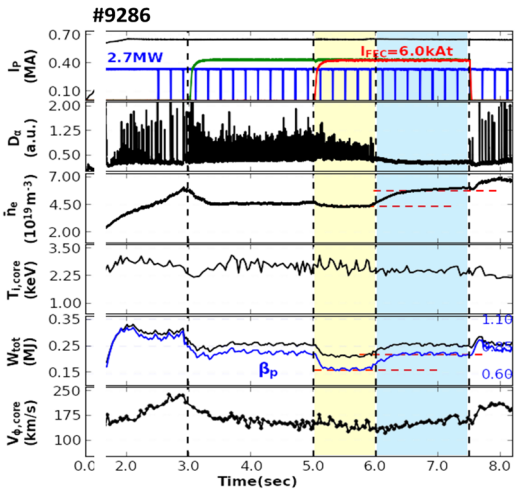

Figure 3. A distinctive plasma response that is dependent on ELM state. Red-dotted horizontal lines show the unusual responses.

mitigated to suppressed). Consequently the reductions of particle and thermal confinements became pretty small, compared with those in ELM-mitigated phase (from 5.0 to 6.0sec) under same RMP fields.

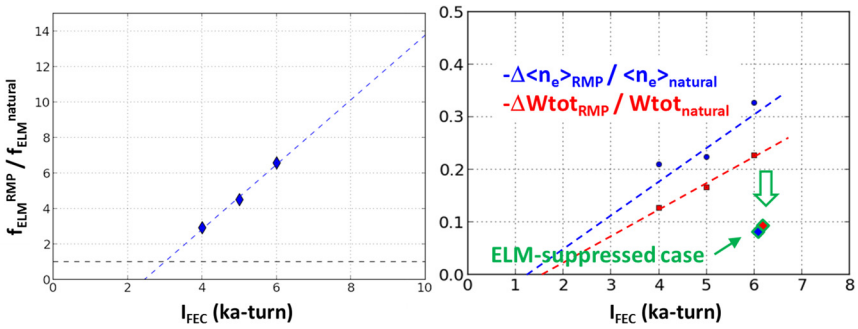

Figure 4. Distinctive response of global plasma parameters to applied RMP fields and ELM-states in KSTAR ELM-RMP experiments

The uniqueness and validity of this dependency on ELM-state is more clearly seen from Figure 4. On the left figure, the ELM frequency was increased linearly proportional to applied field strength, i.e. ELMs were mitigated by applied fields. The corresponding responses of global plasma parameters are shown on the right figure with circle markers. Blue markers with dotted line show the electron density response, while the red markers with dotted line do the total stored energy response. As expected (similarly to DIII-D), the global plasma responses are linearly dependent on applied field strength (i.e. a fundamental response). However, by slightly increasing the RMP field further in the identical discharge, the changes of global parameters were significantly reduced as the ELMs were suppressed (see the diamond marker with green box). According to the observations in DIII-D, the case of ELM-suppression is expected to be marked in-line with those of ELM-mitigation. Thus this result clearly shows a unique response of KSTAR plasmas to the change of ELM state (from mitigated to suppressed). Considering the figure 3, where two distinctive ELM states (ELM mitigation from 5.0 to 6.0sec and ELM suppression from 6.0 to 7.5sec) were sustained stationary, the unusual dependency on ELM state suggests that the ELM-suppression might be a secondary (not fundamental) response that is initiated by a certain triggering mechanism. And this secondary response is a transition phenomenon (from mitigated to suppressed ELMs) that is accompanying an improvement of global confinement.

4. Summary and discussion

Recently the ELM-RMP experiments have been successfully conducted in KSTAR. As results, it has been demonstrated that the ELMs can be mitigated or suppressed by properly configuring the low n (n=1 or 2) RMPs in a wide range of q_{95}. Surprisingly we have found that the global confinement can be improved by suppressing ELMs under RMP fields. A conventional wisdom in ELM-RMP physics is that applying RMP fields leads an increase of edge transport (reduction of edge confinement) and this effect is proportional to the applied fields but independent on ELM-state. It is equally valid in KSTAR if the ELM state doesn't change. If the ELM state is changed in KSTAR plasmas, for instance, if a transition from mitigated to suppressed ELM-state is occurred, then the proportionality of edge transport change to applied field strength is broken and reversed, so that the global confinements are improved significantly. Consequently, it demonstrates that we could achieve the ELM-suppressed H-mode discharge without any significant reduction of global confinements, that is highly required for ITER and beyond.

Acknowledgement
This research was supported by Ministry of Science, ICT, and Future Planning under KSTAR project and was partly supported by the JSPS-NRF-NSFC A3 Foresight Program (NRF No. 2012K2A2A6000443).

References
[1] Y.M. Jeon *et al.,* Phys. Rev. Lett. **109,** 035004 (2012)
[2] Y.M. Jeon *et al.,* submitted to Phys. Rev. Lett. (2013)
[3] Y.M. Jeon *et al.,* ITPA-PEP, IPP, Prague (2014)
[4] T.E. Evans *et al.*, Nucl. Fusion **48** 024002 (2008)
[5] J.W. Coenen *et al.,* Nucl. Fusion **51** 063030 (2011)
[6] D. Orlov, APS invited talk (2013)

Experimental studies on pedestal structure and ELM instability on HL-2A

Y. Huang, C.H. Liu, W.L. Zhong, L. Nie, J.Cheng, K. Yao, X.Q. Ji, Z. Feng, Y.Q. Wang, X.M. Song, Z.Y. Cui, Z.B. Shi, Yi Liu, Q.W. Yang, L.W. Yan, Q.M. Wang, X.T. Ding, J.Q. Dong, M. Xu, Y.H. Xu, X.R. Duan, Yong Liu, and HL-2A team

Southwestern Institute of Physics, P O Box 432, Chengdu 610041, China

E-mail contact of the submitting author: yhuang@swip.ac.cn

H-mode [1] operation is very important for magnetic confinement fusion. On one hand, the study of the L-H transition physics is very important for predictions of the H -mode access in ITER. An intermediate quasi-periodic process, which is called I-phase or limit cycle oscillation (LCO), can often be observed when the heating power is close to the threshold power of L-H transition. On the other hand, many efforts have been spent worldwide on the understanding, mitigation and control of the ELMs, in order to eventually suppress the most destructive ELMs to meet the lifetime requirements on ITER target plates. So the understanding of ELM characteristics is very important to control and mitigate type-I ELMs.

The ELMy H-mode operation is routinely performed since 2009 experiment campaign [2], in HL-2A LSN divertor configuration with the auxiliary heatings of NBI (P_{NBI} < 1.0 MW) and

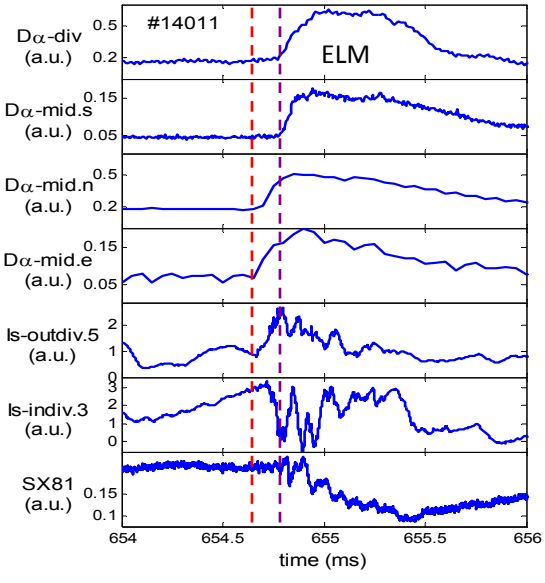

Fig.1 Toroidal asymmetry of ELM perturbation detected by Dα emissions at 3 locations and ion saturation currents of Langmuir probes installed in outer/inner target plates in shot14011

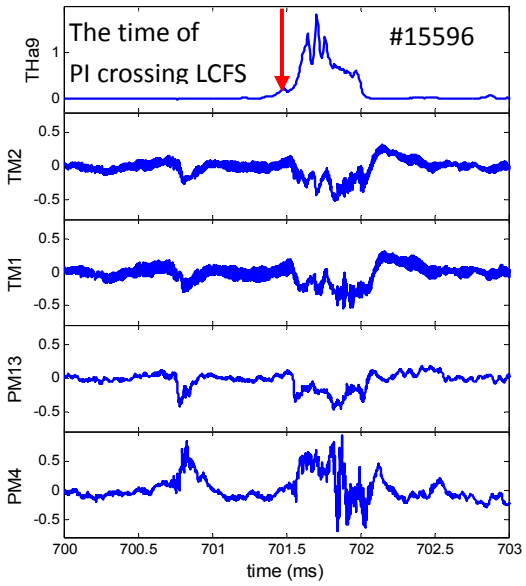

Fig.2 Magnetic perturbations of a spontaneous ELM and an ELM induced by the pellet injected at ~701.4ms in type-III ELMy H-mode plasma of shot15596.

ECRH (P_{ECW} < 3.0 MW, 68 GHz /1s). Recently, microwave diagnostics have been improved

significantly on HL-2A. It allows us gain deeper insights into the pedestal physics, such as dynamical evolution of pedestal structure, temporal-spatial features of pedestal instabilities and so on. The frequency modulated continuous wave (FMCW) reflectometers can measure the entire pedestal structure and monitor the fast evolution of the pedestal density profile, owing to the high temporal resolution. The conventional or Doppler reflectometers can detect the plasma instabilities at different radial positions by choosing suitable launching frequencies. The perturbations of plasma current, plasma density, and stored energy induced by Large ELM bursts are obviously detected on HL-2A tokamak. The total energy loss and line-averaged density perturbations is about 10% ~15% and 6% [3], respectively. Figure 1 illustrates that ELM instability occurs toroidally asymmetric. Here it is detected by Dα emission in midplane east, then detected in north and at last in midplane south with about 150 μs time delay, indicating the instability source locates between the south and the east sections and propagates in co-current direction. Filament structures are demonstrated by the ion saturation current measurements of Langmuir probes installed in outer and inner target plates. The pellet induced magnetic perturbations are distinctly different from those intrinsic magnetic perturbations, as shown by Figure 2 of shot15596. The pellet velocity is measured about 190 m/s. The induced ELM perturbation is detected by Mirnov coils ~150 μs later after the pellet crossing the separatrix at ~701.4 ms.

Figure 3 shows the plasma confinement change induced by pellet injection in shot 17934. Plasma parameters in the shot are: B_t = -1.28 T, P_{NBI} = 0.85 MW (620 ~ 1125 ms). It could be found that electron density, and stored energy and plasma radiation increase obviously after the pellet injection, and D_α radiation in divertor increases as well. After about 8 ms delay, limit-cycle oscillation of 1.5 kHz could be clearly seen on D_α radiation signal. The oscillation lasts about 25 ms, followed by a short ELM-free phase. Electron temperature is higher in I-phase than that in L-mode before pellet injection in r = -33.5 cm region, but it is almost unchanged in r = -38 cm region. After pellet injection, plasma density increases, resulting in the power threshold for L-H transition decrease. Edge transport barrier forms at the inside of the LCFS, and then plasma transport decreases and plasma confinement improves. Plasma operation enters into I-phase. The phenomena also could be

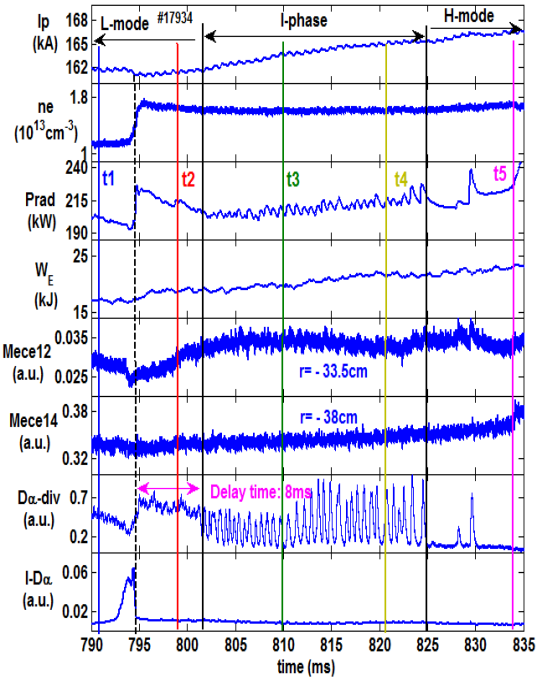

injection from HFS. Fig. 3. Time evolution of main parameters during L-I-H transitions induced by pellet injection from HFS.

explained by the scaling diagram of power threshold (P_{th}) versus line-averaged density in low density branch, where P_{th} decreases with density increasing. Most of the particles of a pellet are deposited near the 1/2 minor radius region, far away from the pedestal. After several milliseconds particle transport from the central region to pedestal region, plasma density profile is steeper step by step from L-mode to I-phase, then to H-mode, and plasma confinement improves gradually.

Distinct precursor modes exhibiting typical frequency of 45~50 kHz, associated with large ELMs crash, are often observed by Mirnov coils on HL-2A. The precursors can also be detected by the edge channels of soft x-ray cameras. The ELM precursors start to grow about several hundred microseconds to several milliseconds before the onset of an ELM [4]. The modes propagate in the electron diamagnetic drift direction. Example for the precursor modes, in shot 14011 and shot 13727, are shown in the upper part and lower part of Fig.4, respectively. In shot 14011 case, the figure shows the signals of the Dα emission in divertor chamber, the measured $\dot{B}_\theta$ of #13 poloidal Mirnov (denoted as PM13) coil located in the outboard mid-plane, the $\dot{B}_\theta$ of PM4 coil located in the inner mid-plane, and the scalogram of the PM13 data analyzed with continuous wavelet transform (CWT). The ELM precursor is observed on the low field side (as in PM13 signals) but not on the high field side (as not in PM4 signals), showing ballooning characteristic. The amplitude and period of the precursor both increase just before the ELM crash. The precursor frequency is about 50 kHz, while its 2nd and 3rd harmonics can also be observed. Not every ELM has corresponding precursor oscillation. In case of shot 13727, the ELM precursors with f~50 kHz last about 10 milliseconds, but their amplitudes do not increase before the onset of ELMs. An ELM crash seems to terminate the coherent magnetic oscillations, which arise again a few milliseconds after the ELM event. In JET tokamak, the time by which the precursor onset precedes the ELM event varies greatly, ranging from 0.2 ms up to several tens of milliseconds.

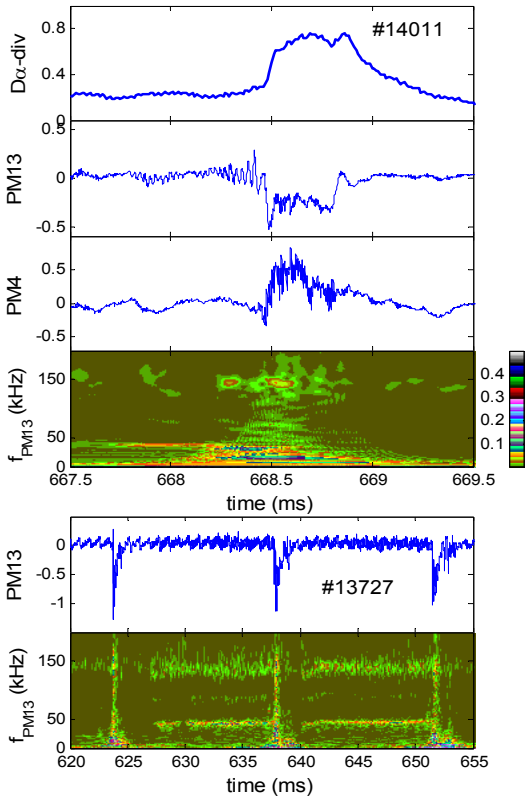

FIG.4. Poloidal magnetic perturbation of the PM13 coil, ELM precursors analyzed by CWT method in shot 14011 (upper) and in shot 13727(lower).

The effect of large ELM burst on long-lived modes and fishbone modes are observed, some MHD modes driven by large ELM bursts on HL-2A are detected. For the ELM

dynamics study, the FMCW results show that pedestal collapses fast when the ELM onsets and then gradually recovers and reaches to the saturation state. Interesting, quasi-coherent modes can be observed in density fluctuations and/or abundant MHD instabilities occur prior to the ELM crash. Preliminary analyses indicate that the excitation of the pedestal instabilities strongly relate to the pedestal density gradient. The role of the edge plasma instabilities in dynamical evolution of pedestal will be further investigated. The two major applications of time-frequency analysis in microwave reflectometry data processing are the detection of group delay from FMCW reflectometry needed for density profile inversion and to characterize the density fluctuations from fixed frequency reflectometry [5]. The tested signal is obtained by the Ka-band(26.5–40 GHz) homodyne reflectometry with a sweep time of 100μs in the HL-2A plasma and is sampled by 2 MHz recorder. The spectrogram of Fig. 5(a) shows several modes identified by broad frequency bands, not having well-defined frequencies because they exist in a broadband frequency range and the trade-off between time and frequency resolution. The CWD (Fig. 5(b)) can give a much more clearly time-frequency spectrum and the modes can be identified more easily and directly (t_{CWD} = 0.08 ms). It is an effective tool for further study the short time and mixed MHD instabilities by using CWD technique.

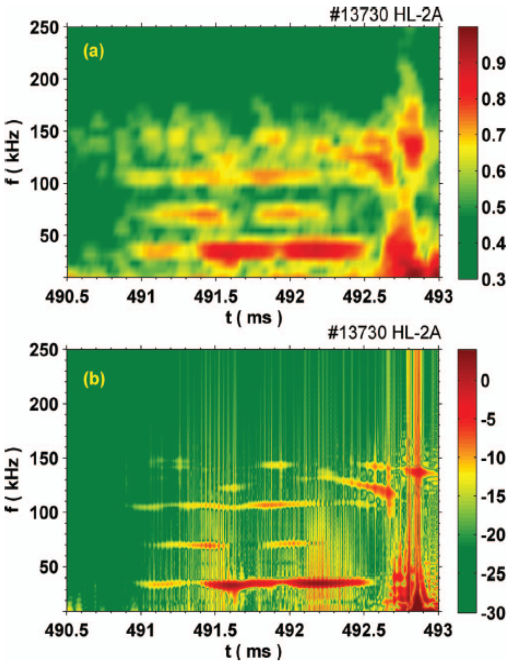

Fig. 5. Time evolution of main parameters during L-I-H transitions induced by pellet

This work was partly supported by the National Natural Science Foundation of China under Grant No. 10990213 and partly supported by the JSPS-NRF-NSFC A3 Foresight Program in the field of Plasma Physics (NSFC: No.11261140328, NRF : No. 2012K2A2A6000443).

[1] Wagner F. *et al* 1982 *Phys. Rev. Lett.* **49** 1408
[2] Duan X.R. *et al* 2010 *Nucl. Fusion* **50** 095011
[3] Liu C.H. *et al* 2012 *Acta Phys. Sin.* **61** 205201
[4] Huang Y. *et al* 2012 *Nucl. Fusion* **52** 114008
[5] Zhong W.L. *et al* 2014 *Rev. Sci. Instrum.***85** 013507

Absolute intensity calibration for ECE measurements on EAST

Yong Liu[1], Xiang Liu[1], Hailin Zhao[1], Xiang Han[1], Erzhong Li[1], Stefan Schmuck[2], Bin Zhang[1], Ang Ti[1], Liqun Hu[1], John Fessey[2], C. W. Domier[3], and N. C. Luhmann Jr.[3]

(1) Institute of Plasma Physics, Chinese Academy of Sciences, Hefei 230031, China
(2) Euratom/CCFE Fusion Association, Culham Science Centre, Abingdon, Oxon. OX14 3DB, United Kingdom
(3) Department of Applied Science, University of California at Davis, Davis, California 95616

Abstract
In this proceeding, the results of the in-situ absolute intensity calibration for ECE measurements on EAST are presented. A 32-channel heterodyne radiometer system and a Michelson interferometer on EAST have been calibrated independently, and preliminary results from plasma operation indicate a good agreement between the electron temperature profiles obtained with different systems.

I. Introduction
Electron cyclotron emission (ECE) measurement is one of the routine diagnostics in magnetically confined plasmas since the 1960s [1]. It provides the temporal evolution of local electron temperature with fairly good spatial and temporal resolution under certain conditions [2] and the information on the electron velocity distribution [3,4].
Technically, the ECE spectrum can be measured by using either optical or microwave method for the reason that the ECE in conventional magnetically confined plasmas is in the microwave range. The Michelson interferometer and the heterodyne radiometer systems are routinely used for ECE measurement in magnetically confined plasmas [5,6,7,8]. The Michelson interferometer has very wide frequency coverage, and the hardware is very simple and robust. Having high light throughput, the system can be easily calibrated. Poor spectral resolution and low temporal resolution are the weak points for the Michelson interferometer, while these are exactly the strong points of a radiometer system. However, the hardware of a radiometer is much more complex. Generally, the radiometer is cross-calibrated with the Michelson interferometer if it is available, or with other diagnostics like Thomson scattering.
The different calibration strategies lead to the motivation of our work. First of all, an independent Te from ECE measurement is essential. The second motivation is to verify the independent intensity calibration for the radiometer system on EAST. It is also essential to validate the cross-calibration between the radiometer system and the Michelson interferometer, because the spectral resolution and the temporal resolution are so different for them.
Comprehensive ECE diagnostics have been commissioned on EAST [9,10,11]. This proceeding will focus on the in-situ absolute intensity calibration for a Michelson interferometer and a 32-channel heterodyne radiometer system on EAST. To validate the cross-calibration between a radiometer system and a Michelson interferometer, they were calibrated independently. Section II of this proceeding focus on the characterization of the systems and the calibration hot source. The in-situ absolute intensity calibration of the two systems is depicted in Section III. In Section IV, preliminary results from plasma operation are given.

II. System characterization

II.I. Stability test of the radiometer system

Before the in-situ absolute intensity calibration is performed, the systems were carefully and fully characterized. For the radiometer, the most concerned is the stability. The radiometer on EAST is placed in a laboratory with controlled temperature and humidity. The system sensitivity is monitored, by measuring the radiation of a hot source within one week. Figure 1(a) shows the variation of the normalized sensitivity within one week for some channels. As illustrated in Figure 1(b), the relative uncertainty for most channels is within 10%.

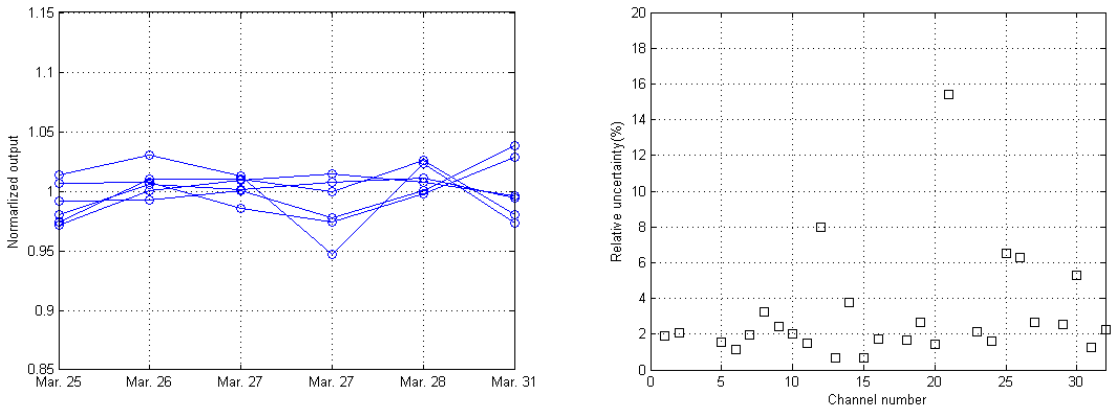

(a) (b)

Figure 1: (a) Evolution of the normalized sensitivity within one week for some channels of the radiometer system; (b) The relative uncertainty for all channels.

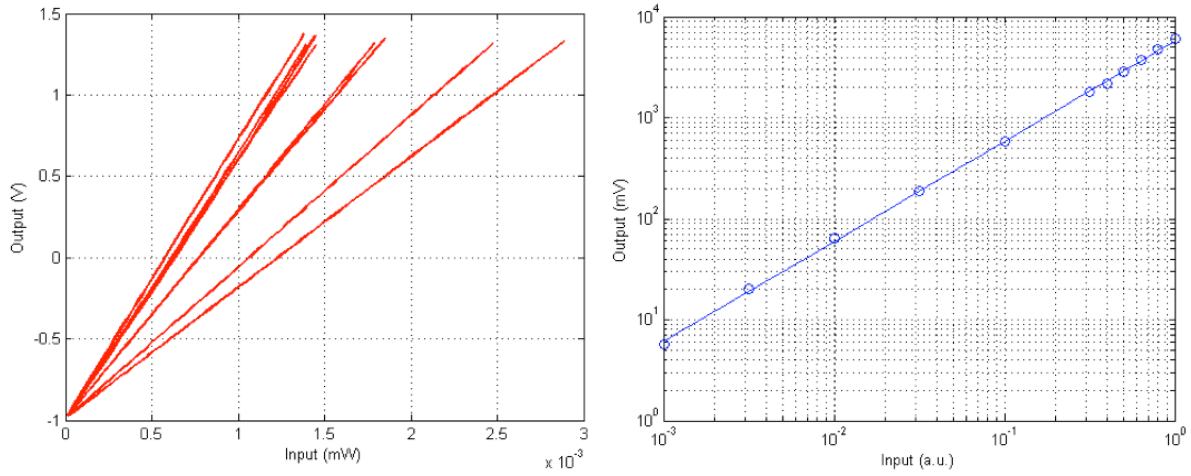

(a) (b)

Figure 2: (a) Linearity measurement results for the IF part (Channels 01-08) of the radiometer; (b) Linearity measurement results for the detector and electronics of the Michelson interferometer.

II.II. Linearity measurement

Linearity is another important issue, because the radiation intensity of the calibration source is weaker than the plasma emission by a magnitude of 4 to 5. Linearity is the precondition to do the extrapolation. For the radiometer system, the components were carefully chosen and arranged to achieve a good linearity. For the Michelson, the linearity is mainly determined by the detector and the electronics. Generally, it is very difficult to characterize the linearity of

the RF part of a radiometer system. The IF part can be characterized by using a sweep source, and the results for some channels are shown in Figure 2 (a). The Linearity measurement results for the detector and electronics of the Michelson interferometer is shown in Figure 2(b). As the results show, the linearity is quite good for both systems.

II.III. Emissivity measurement of the calibration hot source

After characterizing the systems, the emissivity of the calibration hot source was measured. To obtain the emissivit, the hot source and another source with known emissivity were measured separately with the Michelson interferometer. In ECE community, the TK material with pyramidal shape is believed to be an ideal blackbody, and it is used in our case. The measured emissivity and the relative uncertainty for the hot source are shown in Figure 3.

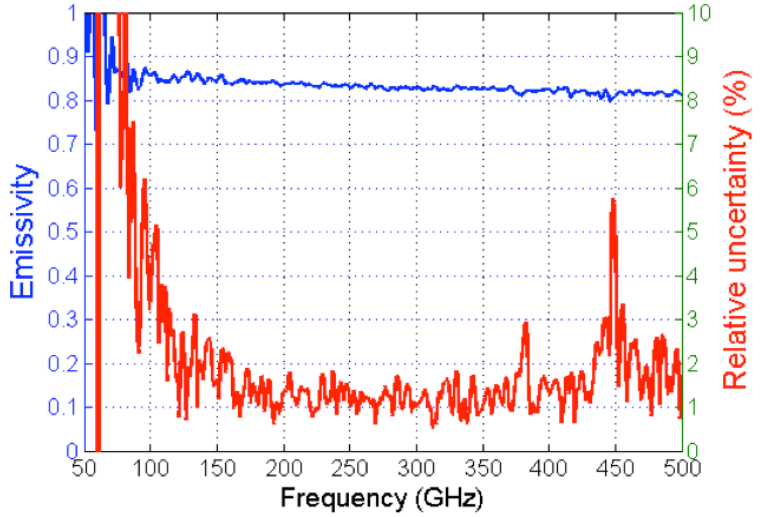

Figure 3: Measured emissivity and the relative uncertainty for the calibration hot source.

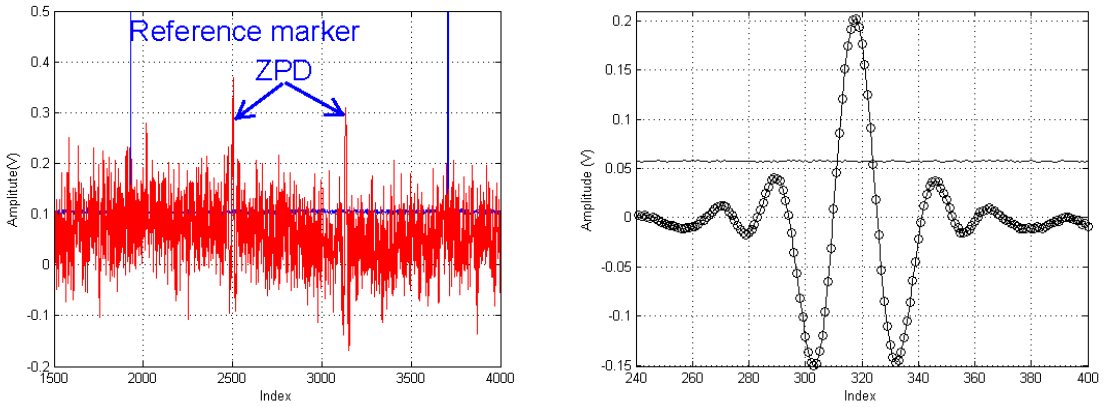

(a) (b)

Figure 4: (a) Original interferograms for one scan measured by the Michelson interferometer; (b) Averaged interferogram for 9000 scans.

III. In-situ absolute intensity calibration

After the systems were fully characterized, the hot source was placed inside the vacuum vessel for the final in-situ calibration. The radiometer and the Michelson interferometer were calibrated independently. The calibration strategies for them are slightly different. For the

interferometer, the calibration was performed at a source temperature of 600 degrees, while different temperatures were used for the calibration of the radiometer system in order to reduce the deviation of the calibration factor.

Figure 4(a) is the raw data of an individual scan from the Michelson interferometer. The two peaks correspond to the zero-path-difference (zpd) where constructive happens for all frequency radiation. Because the gain is much higher than that for the plasma operation, the S/N ratio is bad. Therefore, every 9000 scans are averaged to obtain an interferogram as show in Figure 4(b). In total, 28 averaged interferograms were obtained, and consequently 28 spectra. The averaged spectrum (solid line) and the standard deviation (dashed line) are show in Figure 5.

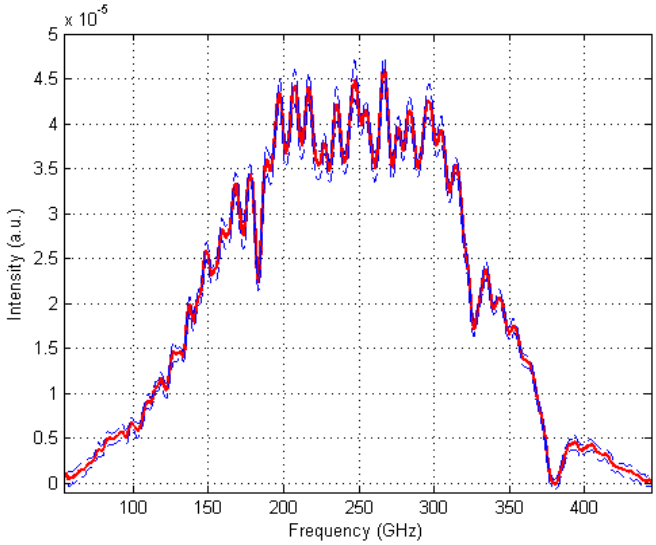

Figure 5: Averaged spectrum (solid line) and the standard deviation (dashed lines) for the calibration hot source from 28 individual measurements by using the Michelson interferometer.

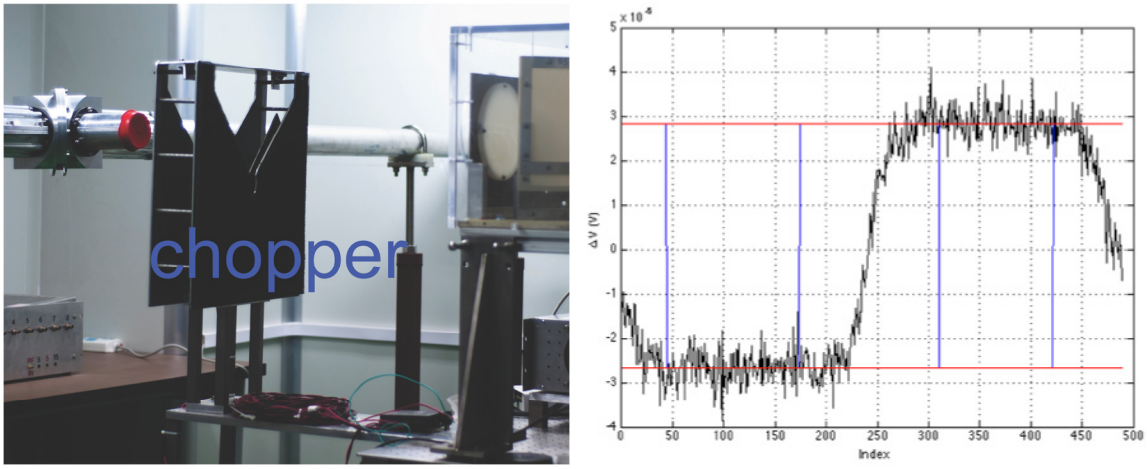

(a) (b)

Figure 6: (a) Chopper adopted for ultra-weak signal detection; (b) Averaged data for one channel of the radiometer system.

Calibration procedure for the radiometer is shown in Figure 6. The input is modulated with a

chopper as shown in Figure 6 (a), and the coherent averaged data for one channel is illustrated in Figure 6 (b). Figure 7 shows the outputs of one channel versus different source temperatures. The calibration factor is obtained by linear fitting.

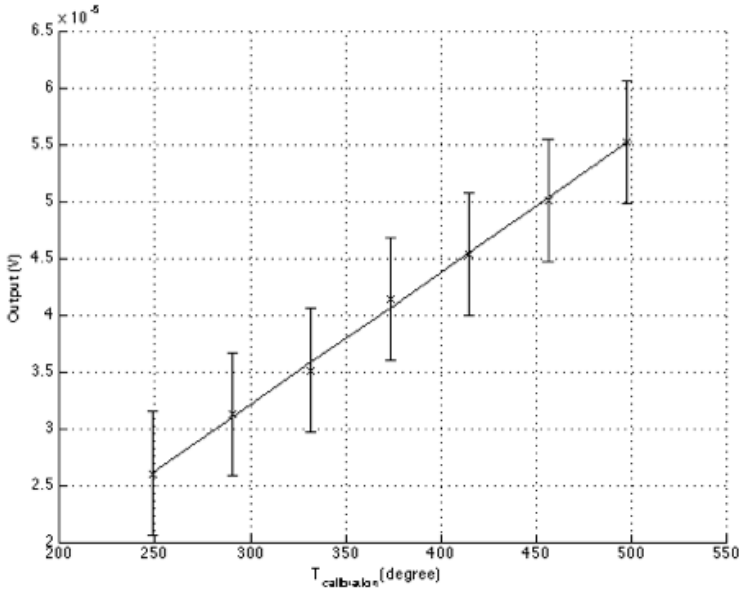

Figure 7: Calibration results for one channel of the radiometer system.

IV. Preliminary results for plasma operation

The 2014 EAST campaign started very lately, and there are only a few discharges with appropriate plasma parameters for ECE measurement. Figure 8 is the ECE spectra of EAST discharge 45273 at the time slice 2 seconds. The spectra were measured separately by the Michelson interferometer (red line) and the radiometer system (square), and there is a good agreement between them. The plasma current and line integrated density are separately 170 kA and $3x10^{19}$ m^{-3} for this discharge.

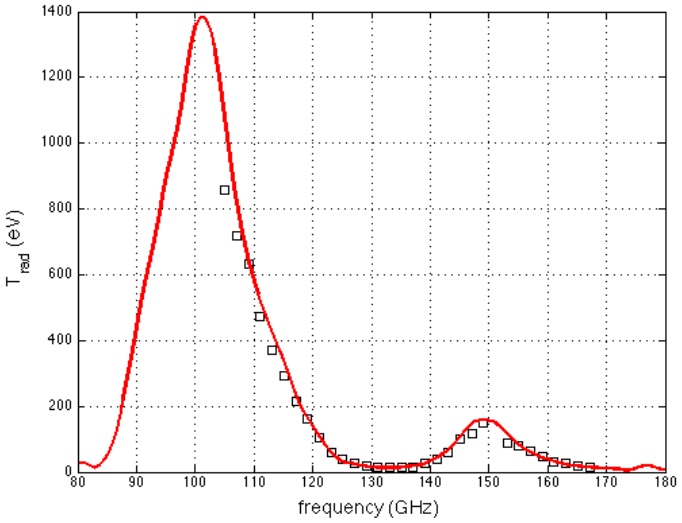

Figure 8: ECE spectra measured by the Michelson interferometer (red line) and the radiometer system (square), 2 seconds at EAST discharge 45273.

V. Summary

The Michelson interferometer and the 32-channel heterodyne radiometer system on EAST have been calibrated independently. Preliminary results from plasma operation indicate that the agreement of the electron temperature profiles measured by the two systems is fairly good.

Acknowledgements

This work was partly supported by the JSPS-NRF-NSFC A3 Foresight Program in the field of Plasma Physics (NSFC: No.11261140328, NRF: No. 2012K2A2A6000443), and the National Magnetic Confinement Fusion Science Program of China under Contracts No. 2011GB107000.

References

[1] Lichtenberg A J et al 1964 Phys. Rev. Lett. 13 387
[2] Hutchinson I H and Komm D S 1977 Nucl. Fusion 17 1077
[3] Kato K and Hutchinson I H 1986 Phys. Rev. Lett. 56 340
[4] Kato K and Hutchinson I H 1987 Phys. Fluids 30 3809
[5] de la Luna E et al 2004 Rev. Sci. Instrum. 75 3831
[6] Schmuck S et al 2012 Rev. Sci. Instrum. 83 125101
[7] Nagayama Y et al 2001 Fusion Engineering and Design 53 201
[8] Isei N et al 2001 Fusion Engineering and Design 53 213
[9] Ti A et al 2007 Int. J. Infrared Milli. Waves 28 243
[10] Liu Y et al 2011 Fusion Sci. and Technol. 59 657
[11] Liu Y et al 2011 Plasma Sci. Technol. 13 352

Integrated disruption avoidance and mitigation in KSTAR

Jayhyun Kim[1], M.H. Woo[1], H. Han[1], N.W. Eidietis[2], Y. In[1], J.G. Bak[1], and the KSTAR team

[1]National Fusion Research Institute, Daejeon, Korea
[2]General Atomics, San Diego, United states

E-mail: jayhyunkim@nfri.re.kr

The final target of Korea Superconducting Tokamak Advanced Research (KSTAR) aims advanced tokamak operation at plasma current 2 MA and toroidal field 3.5 T [1]. In order to safely achieve the target, disruption counter-measures are unavoidable when considering the disruption risks, inevitably accompanied with high performance discharges, such as electro-magnetic load on conducting structures, collisional damage by run-away electrons, and thermal load on plasma facing components (PFCs) [2]. In this reason, the establishment of integrated disruption mitigation system (DMS) has been started for routine mega-ampere class operations of KSTAR since 2013 campaign. The DMS mainly consists of the disruption prediction and its avoidance/mitigation in company with logical/technical integration of them. We present the details of KSTAR DMS and the related experimental results in this article.

1. Introduction

The responses against plasma disruption can be divided in two categories. First one is active avoidance of plasma disruption. Various techniques of the active avoidance have been demonstrated, for instance, electron cyclotron heating (ECH) against density limit disruption. In a broad sense, almost all MHD feedback stabilizations could be included in the active avoidance of plasma disruption such as the magnetic feedback stabilization of resistive wall mode (RWM) and the suppression of neoclassical tearing mode (NTM) by auxiliary current drive.

Second one is so called disruption mitigation. Massive gas injection (MGI) for safe termination of discharge has been studied intensively so far in many devices. MGI mitigation presented promising results against the mentioned disruption risks. However, there are expectations that MGI is not sufficient for the disruption mitigation in reactor scale devices. Thus other mitigation techniques such as shattered pellet injection are studied as well for securing the safety of ITER further.

The above-mentioned techniques require certain response time in reaching satisfactory mitigation level. The response time is governed by both the time scale of plasma phenomena and the reaction time of mitigation hardware. As a result, *early warning*, which guarantees enough response time, becomes a crucial factor in *integrated* disruption avoidance and mitigation. *Early warning* necessitates careful treatments of disruption precursors which are usually originated from disruption-causing instability.

In this article, section 2 describes the disruption prediction in real-time manner. Section 3 depicts the counter-measures against the disruptions. Then section 4 summarizes the mentioned results and discusses possible improvements.

2. Real-time disruption prediction

2.1. Axisymmetric signals and global parameters

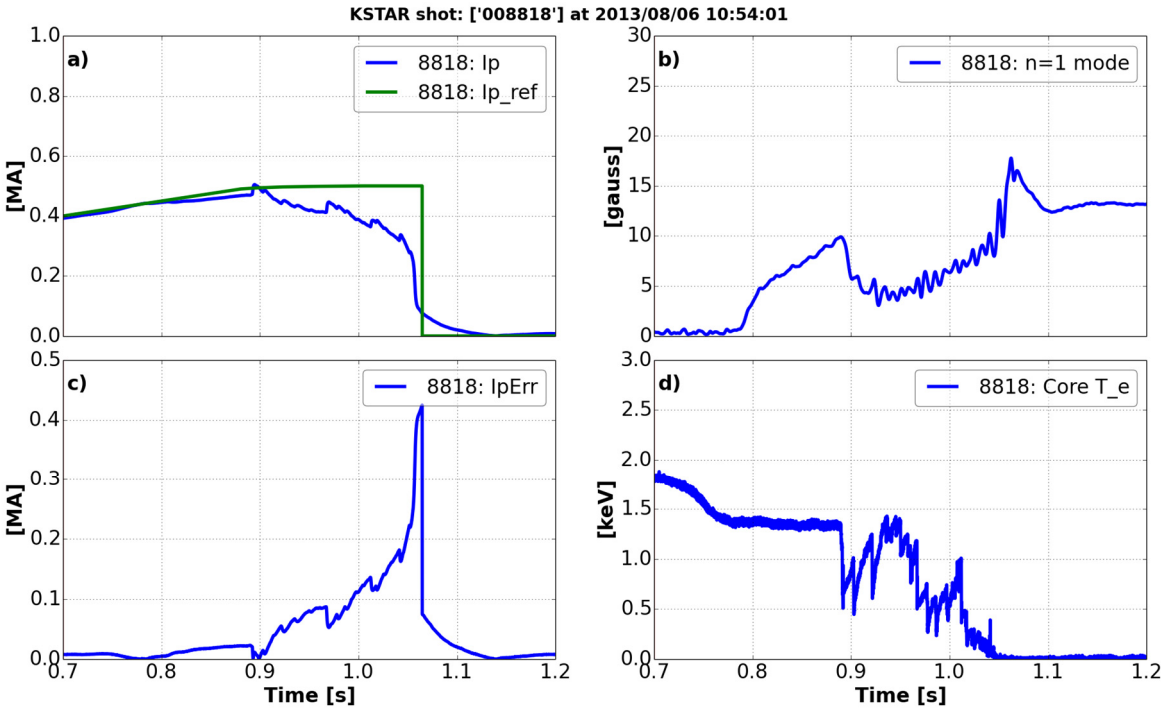

Fig. 1. Detection of locked mode. a) Plasma current. b) Locked mode amplitude. c) Discrepancy between measured plasma current and its feedback target. d) Core electron temperature.

In 2013 KSTAR campaign, we used namely I_p error that is the discrepancy between measured (*i.e.* actual) and feedback target of plasma current as a major disruption precursor. As shown in figure 1, the plasma current became deviated from the target despites of the feedback action when strong locked mode took place. The notable points of figure 1 are different time behaviors among the precursor signals. The amplitude of locked mode depicted starts to grow from t=0.788 s. However, minor disruption at t=0.895 s makes the prediction difficult since the mode amplitude decreases temporally right after the minor disruption and increases again during 150 ms period. On the contrary, I_p error exhibits a steady increase during the period. In the same period, core electron temperature shows sudden drop and slow recovery.

From the observations in figure 1, it can be concluded that we might fail in the prediction and the early warning of disruptions if we solely rely on the mode amplitude that directly causes the disruption. We could recognize the real situation when the global parameters are also taken into account.

KSTAR plasmas typically have highly elongated shapes (*i.e.* elongation κ~2) for pursuing advanced tokamak operations in high beta where beta is the ratio between thermal and magnetic pressures. In this reason, KSTAR discharges are inherently vulnerable to VDE and the largest portion of plasma disruptions in KSTAR has been caused by VDE so far.

In VDE, plasma vertical position Z_P and its time derivative dZ_P/dt correspond to the mode amplitude and the mode growth, respectively. Therefore, the integrated DMS of KSTAR adopts Z_P and dZ_P/dt as precursors of VDE. However, dZ_P/dt, which is typically derived from the numerical differentiation of Z_P, is susceptible to a noise due to the characteristics of numerical differentiation. In order to moderate the noise problem, the DMS considers the current on in-vessel vertical control coils (IVCCs) as an alternative of dZ_P/dt. In the experiment, the determination of VDE is conducted by the logical combination of them

through AND/OR logic with their own thresholds [3].

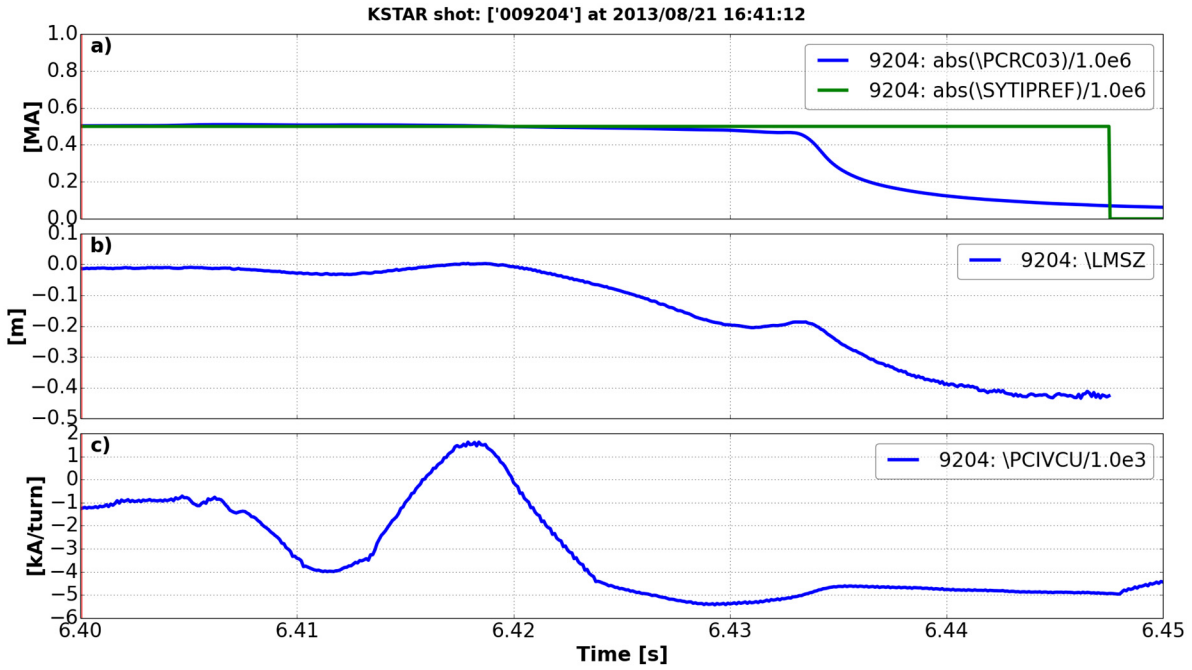

Fig. 2. Typical behaviors of *LMSZ* and *PCIVCU* during the VDE. a) Plasma current (blue line) and its control reference (green line). b) Plasma vertical position. c) Current on IVCC.

2.2. Non-axisymmetric signals

Although locked mode-induced disruptions have not frequently occurred in KSTAR so far, it could be expected that locked mode becomes a serious issue in high performance discharge in conjunction with potential amplification of error field. In 2013 KSTAR campaign, we concentrated on in-situ detection of slowly rotating mode and its integration to the DMS. To detect slowly rotating/non-rotating mode, KSTAR has several picture frame type coils which are sensitive to mode amplitude rather than mode frequency.

Additionally, the real-time prediction of the disruption requires the rejection of equilibrium component in in-situ way. For the purposes, 180° hard-wired pairing configuration was implemented in the picture frame type coils such as locked mode detection coils and saddle loops as depicted in figure 3. The 180° hard-wired pairing configuration is essential for in-situ detection of MHD instability since it inherently rejects n=0 equilibrium component (actually all n=even components) and extracts n=1 instability component (actually all n=odd components). We assume that n=1 mode takes a major portion among all n=odd components [3].

However, we did not utilize the locked mode detector in 2013 experiments because it still needed compensation of pick-ups from poloidal field (PF) coils and even plasma current. The locked mode amplitude depicted in figure 1 is the post processed result and the compensation applied in figure 1 will be implemented in the KSTAR PCS. From next campaign, the KSTAR DMS will be able to take the compensated signal of locked mode in real time.

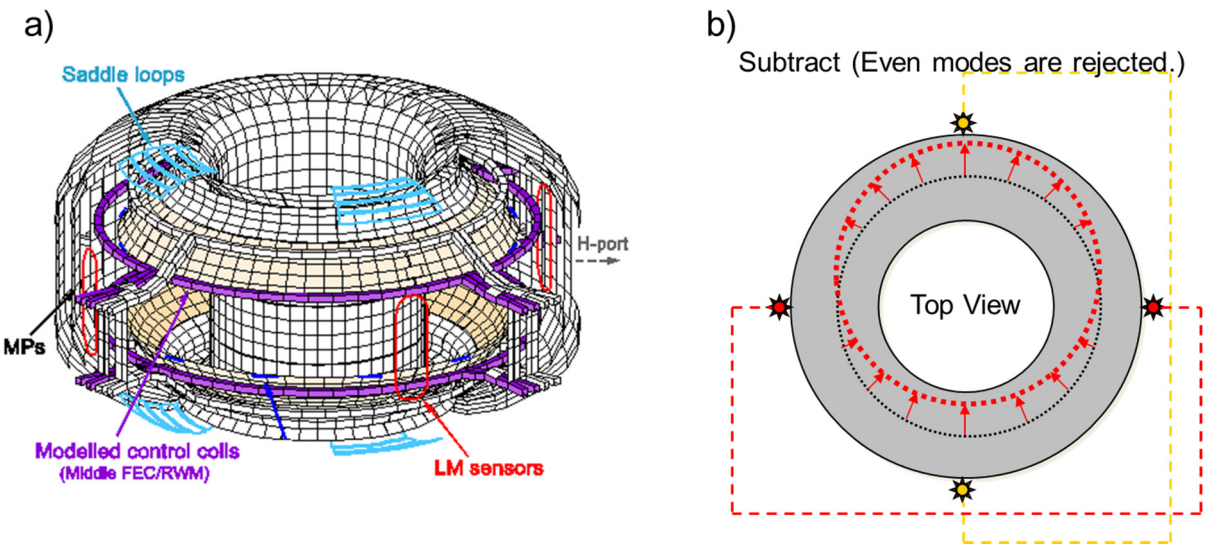

Fig. 3. 180° hard-wired pairing of picture frame type sensors. a) Magnetic sensors installed in KSTAR. b) Schematic view of equilibrium portion rejection.

3. Disruption avoidance and mitigation

3.1. Unplanned ramp-down of plasma current

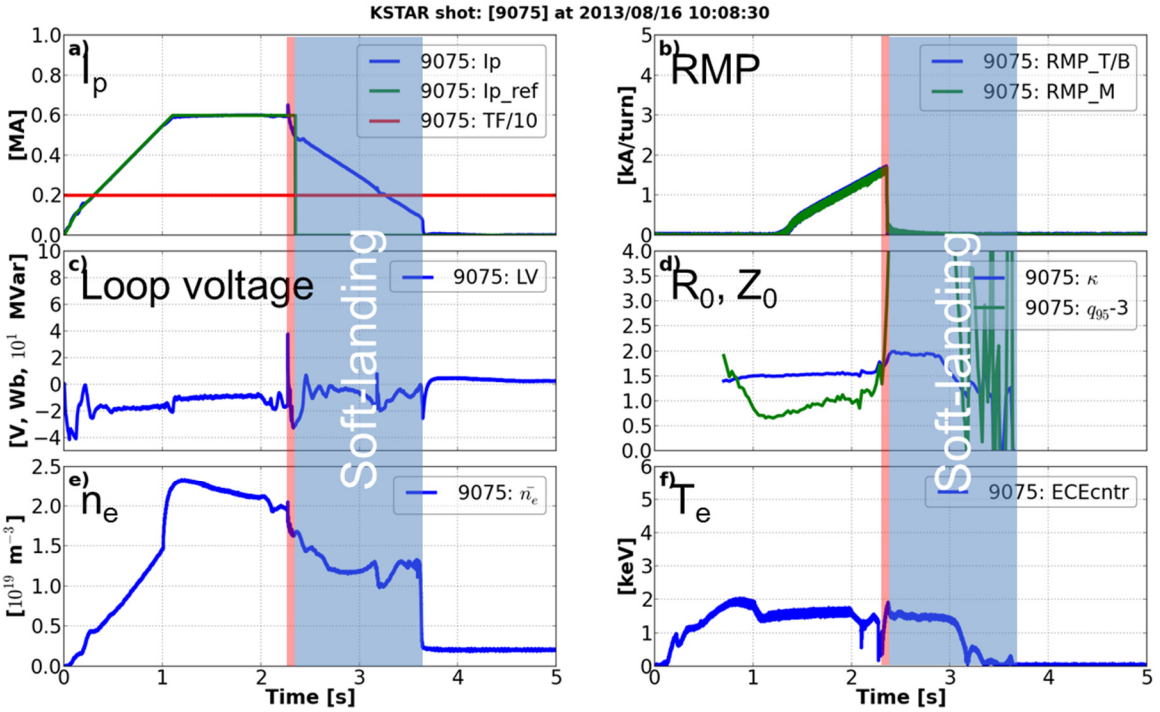

Fig. 4. Asynchronous ramp-down against simulated locked mode. a) Plasma current (blue line) and its control reference (green line). b) Currents of field error correction coils. c) Loop voltage. d) Elongation (blue line) and q_{95} (green line). e) Volume-averaged density. f) Core electron temperature.

In order to realize unplanned I_p ramp-down in KSTAR device, two functions are newly

implemented in KSTAR PCS. First function is the reassignment of control targets after the trigger of the unplanned phase. The control targets include not only preprogrammed target of plasma current but also other targets such as desired plasma shape since the unplanned ramp-down phase is almost identical to the planned ramp-down phase after the transition of phase [4].

Second one is the reprogramming of feedback algorithm and feedforward waveform. This consideration is more crucial in superconducting devices because the responses of superconducting PF coils are much slower than those of normal conductor devices. Thus the well-programmed waveforms of feedforward control are inevitable for compromising narrow gain window of feedback control.

Figure 4 depicts the example of unplanned I_p ramp-down against locked mode occurrence. In detail, the DMS caught the rise of I_p error due to the locked mode and invoked the unplanned ramp-down. One thing should be noticed is that the locked mode was intentionally induced with using resonant magnetic perturbation..

3.2. Massive gas injection

The above-mentioned advantages of unplanned ramp-down may act as a handicap when the allowed response time to plasma disruption is not sufficiently long. For instance, superconducting device KSTAR typically has sub MA/s of I_p ramp-rate and it takes almost second in the ramp-down of MA class discharge below the safe level (*e.g.* I_p<500 kA). On the other hand, VDE only permits several *ms* of the response time in order to prevent severe damage.

In this reason, we implemented fast shutdown technique, MGI as well and it was successfully commissioned within integrated DMS.

4. Summary

In order to achieve stable MA class operation and high performance discharges, integrated DMS was implemented and applied during 2013 KSTAR campaign. Under the integrated DMS framework, various diagnostics and actuators were combined and controlled logically for the purposes of real-time disruption prediction and avoidance/mitigation. In future, the DMS will be upgraded to properly respond to diverse disruption causes which have their own time scale (*i.e.* allowable response time). Through the upgrade, we will pursue to increase the probability of disruption mitigation.

Acknowledgement

This research was supported by Ministry of Science, ICT, and Future Planning under KSTAR project and was partly supported by the JSPS-NRF-NSFC A3 Foresight Program in the field of Plasma Physics (NSFC: No.11261140328).

References

[1] G.S. Lee, *et al*., Nucl. Fusion, **40** (2000) 575.
[2] A.H. Boozer, Phys. Plasmas **19** (2012) 058101.
[3] J. Kim, et al., 2013 Asia Pacific Fusion Association (2013).
[4] M.H. Woo, et al., 2013 KSTAR conference (2013).

MHD Instabilities determining achieved beta value in helical plasma

S.Sakakibara and LHD Experiment Group
National Institute for Fusion Science, Gifu 509-5292, Japan

Abstract

Characteristics of MHD instabilities limiting beta value have been investigated in Large Helical Device. Ideal interchange mode can be destabilized by enhancing magnetic hill or reducing magnetic shear. In enhanced magnetic hill configuration that was realized by magnetic axis position to the inward, m/n = 2/1 mode with a finite frequency appeared, and it led to significant drop of central beta value (~ 30 %), after the stop of the mode rotation. In reduced magnetic shear configuration produced by increasing plasma current, m/n = 1/1 mode was destabilized when the plasma current exceeded a threshold. The mode led to minor collapse after the stop of the rotation as well as the case of the m/n = 2/1 mode. The central beta value was dropped by about 60 %.

1. Introduction

Exploration of available beta regime is one of key subjects for design and configuration-optimization of economical fusion reactor. In tokamaks and RFPs, neoclassical tearing mode and resistive wall mode obviously limit the beta value in experiments, and establishment of the control method is a key issue for ITER and DEMO. In helical devices and stellarators, pressure driven instabilities concern the maintenance of stable plasma. Especially, interchange mode is a key instability because it is easily destabilized in heliotron configuration with magnetic hill. Previous experiments in ideal-stable configurations clarified that saturation level of the interchange mode decreased with the increase in magnetic Reynolds number, S, and the dependence is qualitatively consistent with that of linear growth rate of interchange mode [1]. Also it was found that the amplitudes of the modes observed in Large Helical Device (LHD) with high S were one order smaller than those in Compact Helical System (CHS) with low S [2], which is favorable for stable operation of fusion reactor. However, since the growth rate of the interchange mode has weak

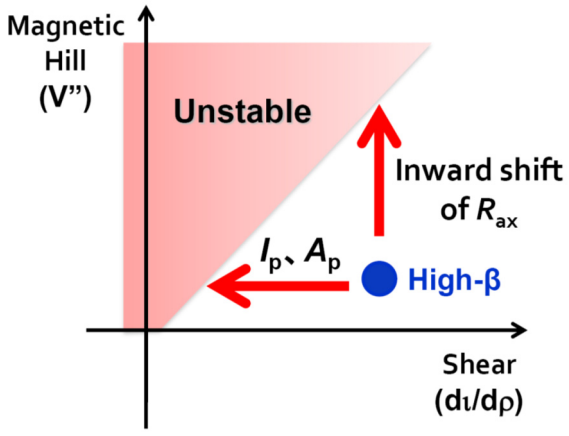

Fig.1 Concept of experiments related to beta limit study

dependence of S when the reactor-plasma is in the ideal-unstable regime, the verification of the effect of the ideal mode on plasma confinement is required for stable operation of the reactor. In heliotron configuration such as LHD, MHD mode is stabilized with the outward shift of magnetic axis position, R_{ax}, whereas transport is improved in the inward shift of R_{ax}. Therefore, available beta in the ideal-unstable regime should be known to optimize magnetic configuration for realization of favorable confinement properties of high energy particles.

Here we have studied characteristics of MHD mode in two kinds of ideal unstable regimes. One is enhanced magnetic hill configuration, which is realized by shifting R_{ax} to the inward during a discharge. The other is reduced magnetic shear configuration. The magnetic shear can be reduced by increasing plasma current and/or plasma aspect ratio. Concept of the experiments is shown in Fig.1. The high-beta experiments (blue circle) have been done in ideal-stable regime where the growth of the mode has clear S dependence. The volume averaged beta of more than 5 % was obtained there [1].

2. Experimental Results

MHD instabilities in enhanced magnetic hill configuration

Figure 2 shows MHD activities in a discharge of the enhanced magnetic hill configuration. The magnetic hill was enhanced by shifting R_{ax} from 3.6 m to 3.5 m during this discharge. The plasma was produced and maintained by injecting three neutral beams. When R_{ax} reached 3.54 m, m/n = 2/1 mode appeared, and the amplitude started to increase with further inward shift of R_{ax}. The frequency of the mode was about 0.5 kHz and abruptly decreased at 3.34 s. Then the mode significantly grew, especially, after the stop of the mode rotation. Although the central beta of about 5 % was kept at the beginning of the discharge, it was decreased to less than 3 % with deceleration of the mode rotation. The mode rotation repeated acceleration and deceleration to the end of

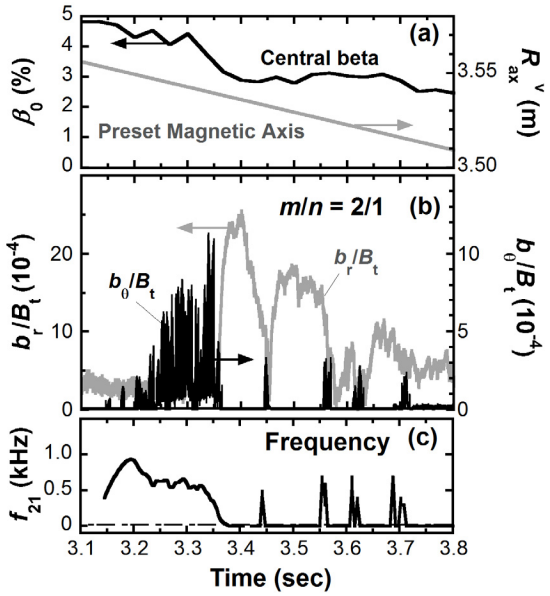

Fig.2 Time evolutions of (a) central beta, preset magnetic axis, (b) radial and poloidal components of m/n = 2/1 magnetic fluctuations, and (c) frequency in enhanced magnetic hill discharge.

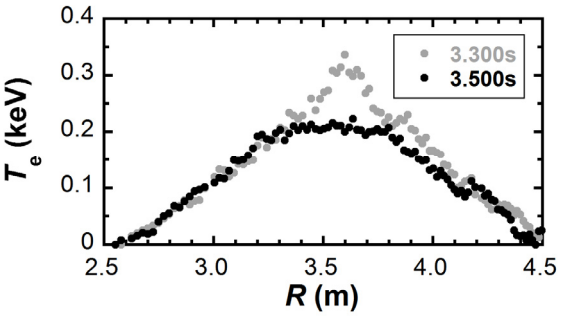

Fig.3 Electron temperature profiles before and after the collapse.

this discharge, whereas no central beta was recovered.

Electron temperature profiles before and after the collapse are shown in Fig.3. At 3.3s, flattening of the electron temperature profile around the $\iota/2\pi = 1/2$ resonance (3.4 m and 3.85 m) was formed. This flattening was extended to the core at 3.5 s. This is a reason for the drop of the central beta.

MHD instabilities in reduced magnetic shear configuration

The magnetic shear was reduced by increasing the plasma current driven by co-neutral beams in high aspect ratio configuration with low magnetic shear. Figure 4 shows an activity of m/n = 1/1 mode in an typical discharge. The m/n = 1/1 mode with low amplitudes appeared at the beginning of discharge, and it was enhanced when the plasma current exceeded a certain value. Then the rotation of the mode gradually slowed down and stopped at 4.46 s. The mode rapidly grew then, which dropped the central beta from 2.1 % to 1 %. Figure 5 shows the electron temperature profiles before and after the collapse. The flattening structure with relatively wide width was formed around $\iota/2\pi = 1$ resonance even before the collapse. The flattening area was extended to the core after the stop of the rotation, which led to significant drop of the central temperature [3, 4].

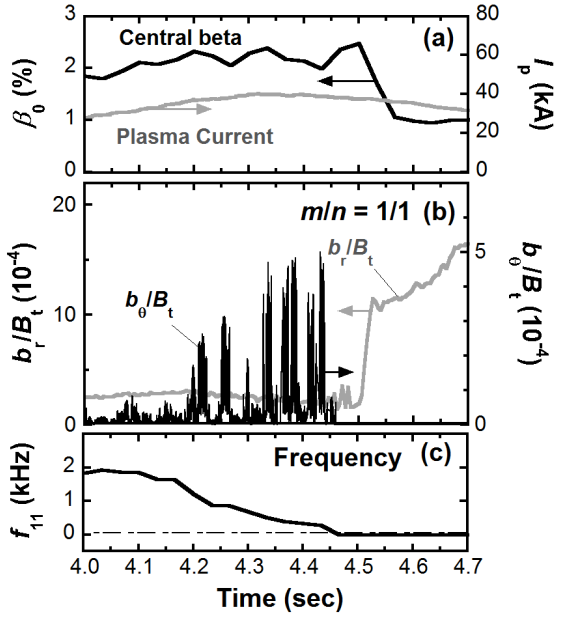

Fig.4 Time evolutions of (a) central beta, preset magnetic axis, (b) radial and poloidal components of m/n = 2/1 magnetic fluctuations, and (c) frequency in reduced magnetic shear discharge.

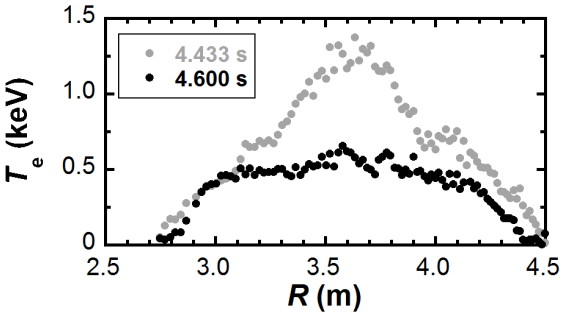

Fig.5 Electron temperature profiles before and after the collapse.

3. Discussion

The beta limits in two kinds of ideal unstable regimes have been studied in LHD. In both enhanced magnetic hill and reduced magnetic shear configurations, low-order MHD modes were destabilized and led to minor collapse. These modes significantly grew after the stop of the rotation, which suggests that the rotation is a key parameter for stabilization of the mode as well as instabilities observed in tokamaks. It has been found out in various experiments

that the onset of the mode is qualitatively consistent with theoretical prediction [3]. The stability analysis based on the equilibrium with plasma flows is required to perform quantitative estimation of the actual stability boundary, which is important for optimization of the reactor configuration.

The experiments show that the rotation of the interchange mode is in agreement with sum of E×B and electron diamagnetic flows [5]. The profile flattening shown in Figs.3 and 5 reduces the diamagnetic flow and radial electric field around the resonance, which might be one of reasons for deceleration of the mode rotation. The error field is one of candidates for the deceleration of the mode and it is well known as the reason for a cause of locked mode in tokamaks. However, the destabilization of the mode causing minor collapse is independent of the existence of the error field [3].

In summary, characteristics of MHD activities determining achieved beta value were investigated in unstable regime of the ideal interchange mode in LHD. The access to the ideal unstable regime was realized by enhancing the magnetic hill or reducing the magnetic shear. In both experiments, low-*n* MHD modes were destabilized and led to core collapse when their rotations were stopped. The maximum drop of central beta value was about 60 %.

Acknowledgements

This work was partly supported by the JSPS-NRF-NSFC A3 Foresight Program in the field of Plasma Physics (NSFC: No.11261140328).

References

[1] S. Sakakibara et al., Plasma Phys. Control. Fusion **50** (2008) 124014.

[2] S. Sakakibara et al., Nucl. Fusion **41** (2001) 1177.

[3] S. Sakakibara et al., Nucl. Fusion **53** (2013) 043010.

[4] Y. Takemura et al., Nucl. Fusion **52** (2012) 102001.

[5] Y. Takemura et al., Plasma Fusion Res. **8** (2013) 1402123.

Quick plasma equilibrium reconstruction based on GPU

Bingjia Xiao[1, 2] Y. Huang[1], Z.P. Luo[1], Q.P. Yuan[1], L. Lao[3]

[1] Institute of Plasma Physics, Chinese Academy of Sciences, Hefei, China

[2] School of Nuclear Science & Technology, University of Science & Technology of China

[3] DIII-D national Lab., General Atomics, USA

Abstract

A parallel code named P-EFIT which could complete an equilibrium reconstruction iteration in 250μs is described. It is built with the CUDA™ architecture by using Graphical Processing Unit(GPU). It is described for the optimization of middle-scale matrix multiplication on GPU and an algorithm which could solve block tri-diagonal linear system efficiently in parallel. Benchmark test is conducted. Static test proves the accuaracy of the P-EFIT and simulation-test proves the feasibility of using P-EFIT for real-time reconstruction on 65×65 computation grids.

1. Introduction

1.1 Background

Optimum performance of tokamak operation needs accurate feedback control of many discharge parameters. However, the values of many parameters, such as shape and current profile, cannot be directly measured but can be evaluated from available diagnostics. The most frequent used method is called equilibrium reconstruction by fitting diagnostic data and solving Grad-Shafranov equation, which describes the force balance of plasma equilibrium. Various equilibrium reconstruction codes has been developed and implemented on tokamak devices. EFIT is an efficient code to reconstruct equilibrium. It has been widely used in various tokamaks in the world. However, the algorithm of EFIT is too computation intensive to be used in real-time control. In reference [1], the real-time version-EFIT (RT-EFIT) is described through using simpler algorithms and relatively lower spatial solutions compared with the off-line EFIT.

The former real-time codes produce solutions at a rate sufficient for discharge control only if the grid number is substantially reduced, but this would low down the precision of reconstruction result. For example, the RT-EFIT used on EAST scales the 2.4m*1.4m rectangle plasma area by 33*33 grids, but the off-line EFIT typically scales the same area by 129*129 grids. In this paper, the parallelized EFIT code based on GPU is described, which significantly accelerate the whole process of the reconstruction. Through efficiently taking advantage of massively parallel GPU cores, P-EFIT accurately reproduces the EFIT reconstruction algorithms at a fraction of computational time cost. Compared with RT-EFIT currently used in EAST, P-EFIT can complete one reconstruction iteration in much less time with better spatial resolution. For now, 65*65 grid version P-EFIT cost about 0.3ms per iteration. In the coming 2014 EAST experiment campaign, P-EFIT is planed to apply in plasma control system.

1.2 Overview of parallel computing with GPU

Driven by the insatiable market demand for realtime, high-definition 3D graphics, the programmable Graphic Processor Unit or GPU has evolved into a highly parallel, multithreaded,

manycore processor with tremendous computational horsepower and very high memory bandwidth, as illustrated by Figure 1 and Figure 2.

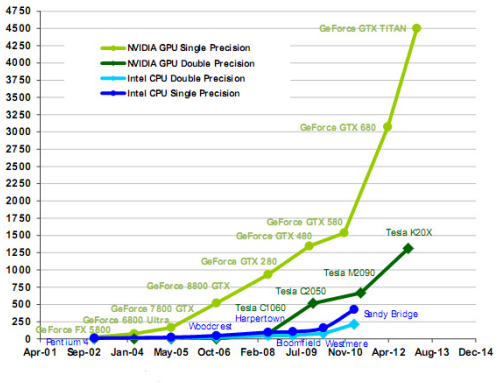

Fig.1. Floating-Point Operations per Second

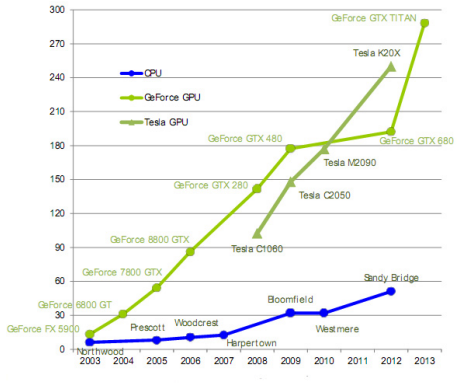

Fig.2. Memory Bandwidth

The reason behind the discrepancy in floating-point capability between the CPU and the GPU is that the GPU is specialized for compute-intensive, highly parallel computation- exactly what graphics rendering is about - and therefore designed such that more transistors are devoted to data processing rather than data caching and flow control, as schematically illustrated by Figure 3. GPU has been proved to be a very good choice for the acceleration of equilibrium reconstruction.

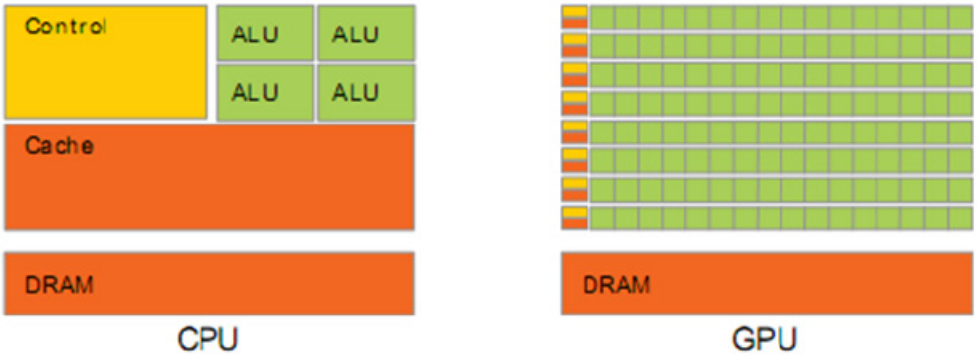

Fig.3. GPU Hardware Design: GPU devotes more transistors to data processing

In November 2006, NVIDIA introduced CUDA(TM), a general purpose parallel computing platform and programming model that leverages the parallel compute engine in NVIDIA GPUs to solve many complex computational problems in a more efficient way than on a CPU. CUDA comes with a software environment that allows developers to use C as a high-level programming language. A detailed description of CUDA(TM) can be found in [2].

2. Parallelization of equilibrium reconstruction algorithms

2.1 Basis reconstruction algorithm

P-EFIT is based on the EFIT framework described in [3,4]. The main task of the reconstruction algorithm in EFIT is to calculate the distribution of both the poloidal flux ψ and the toroidal current density J_ϕ in (R,Z) plane, based on a least squares best fit to the diagnostic data and simultaneous solution of the Grad-Shafranov equation.

$$\Delta^{*}\psi = -\mu_0 R J_\phi \quad , \quad J_\phi = RP'(\psi) + \frac{\mu_0 FF'(\psi)}{4\pi^2 R} \tag{1}$$

Here, ψ is the poloidal magnetic flux per radian of the toroidal angle ϕ enclosed by a magnetic surface, $F = 2\pi R B_\phi / \mu_0$ and B_ϕ are the poloidal current function and the toroidal magnetic field, and $\Delta^* = R^2 \nabla \cdot (\nabla / R^2)$. The equilibrium solution of poloidal flux ψ and toroidal current density of plasma J_T are obtained on a rectangular grid which covers the entire area of the vacuum vessel. The plasma current is modeled as being distributed among the elements of grid points, with linear coefficients α_n and γ_n. As shown in reference [4], the pressure gradient and current flux are modeled as:

$$\begin{cases} p'(\psi) = \sum_{n=0}^{n_p-1} \alpha_n \psi_N^n - \delta \psi_N^{n_p} \sum_{n=0}^{n_{p-1}} \alpha_n \\ FF'(\psi) = \sum_{n=0}^{n_F-1} \gamma_n \psi_N^n - \delta \psi_N^{n_F} \sum_{n=0}^{n_{F-1}} \gamma_n \end{cases} \tag{2}$$

where the normalized flux $\psi_N = (\psi - \psi_0)/(\psi_1 - \psi_0)$ varies between 0 and 1 with ψ_0 the poloidal flux at the magnetic axis and ψ_1 the poloidal magnetic flux at the plasma boundary. p' and FF' are set to be zero at the boundary when $\delta = 1$ at ohmic or L-mode discharge, and set to be finite value at boundary when $\delta = 0$ at H-mode discharge. For the number of coefficients n_p and n_F, it is essential that they should be appropriately chosen to correctly reflect the availability of the measured data [6]. The diagnostic data consist of those of flux from loops and field from magnetic probes outside the plasma and plasma current from a Rogowski loop. Then, the calculated flux and field value on the corresponding measurements are obtained from the Picard iterations:

$$C_i^{(m+1)}(\mathbf{r}_i) = \sum_{n=1}^{n_C} G_{C_i}(\mathbf{r}_i, \mathbf{r}_{en}) I_{en}^{(m+1)} + \int dR'\, dZ' G_{C_i}(\mathbf{r}_i, \mathbf{r}') J_\phi\left(R', \psi^{(m)}, \alpha_n^{(m+1)}, \gamma_n^{(m+1)}\right) \tag{3}$$

where G_{C_i} is the appropriate Green's function corresponding to the i^{th} measurement, $I_{en}^{(m+1)}$ is the current in the external poloidal field coils at the m+1 iteration, n_C is the total number of the external poloidal field coils. During the iteration cycles, α_n and γ_n are readjusted continuously, according to the available measured data, by finding a linearized minimization

$$\chi^2 = \sum_{i=1}^{n_M} \left(\frac{M_i - C_i}{\sigma_i} \right)^2 \tag{4}$$

Where M_i, C_i and σ_i denote the measured value, the calculated value and the error associated with the i^{th} measurement, respectively. n_M is the total number of measurements. The solution is calculated using a new value of normalized flux ψ_N to compute the new set values of the coefficients $\left(\alpha_n, \gamma_n\right)$. The iteration process continues until the latest two successive error, indicated by the largest change in the grid points, is small enough (such as $\varepsilon = 10^{-3}$).

$$\left| \frac{\psi^{(m)} - \psi^{(m+1)}}{\psi_b - \psi_a} \right| \leq \varepsilon \tag{5}$$

Then, the iteration process finishes. The values of the $\left(\alpha_n, \gamma_n\right)$ obtained in the latest iteration are the correct coefficients of the plasma current density. Then the equilibrium parameters, such as pressure p, current flux function F, poloidal flux ψ, poloidal beta β_p, and the parameters of plasma shape and position are obtained.

2.2 Basic parallel algorithms

P-EFIT is based on the EFIT framework but takes advantage of massively parallel GPU cores to significantly accelerate the computation. The main time-consuming computing parts are poloidal flux refreshing (Δ^* Inversion), response matrix calculation and least square fitting.

Equation (1) shows the poloidal flux refreshing (Δ^* Inversion), which calculate the flux on grid points after getting the plasma current distribution. As same in EFIT, finite difference method is used and the partial differential equation transformed into a block tri-diagonal equation. By eigenvalue decomposition, the block tri-diagonal equation is transformed into independent triangular system that could be solved in parallel on GPU. Equation (3), shows the relation between current sources (plasma current and PF coils current) and magnetic diagnostics. Based on the distributed grid points and PF coils, the response matrix between these current sources and diagnostics can be calculated beforehand. This part is mainly consisted of two large matrix multiplications. By dividing the matrix into small parts, the cost of matrix elements multiplications, additions and data accessing are reduced. Least square fitting solves the equation (4), the plasma current parameter and external coil currents is solved. EFIT solves this overdetermined equation by singular-value decomposition. P-EFIT makes use of parallel matrix multiplication, the initial overdetermined equation system is transformed into full rank system and can be solved directly.

As the co-processor, GPU process the compute intensive functions. The basic flow path of

the equilibrium reconstruction code is showed in figure 4. The detailed basis parallel algorithms can be found in [5].

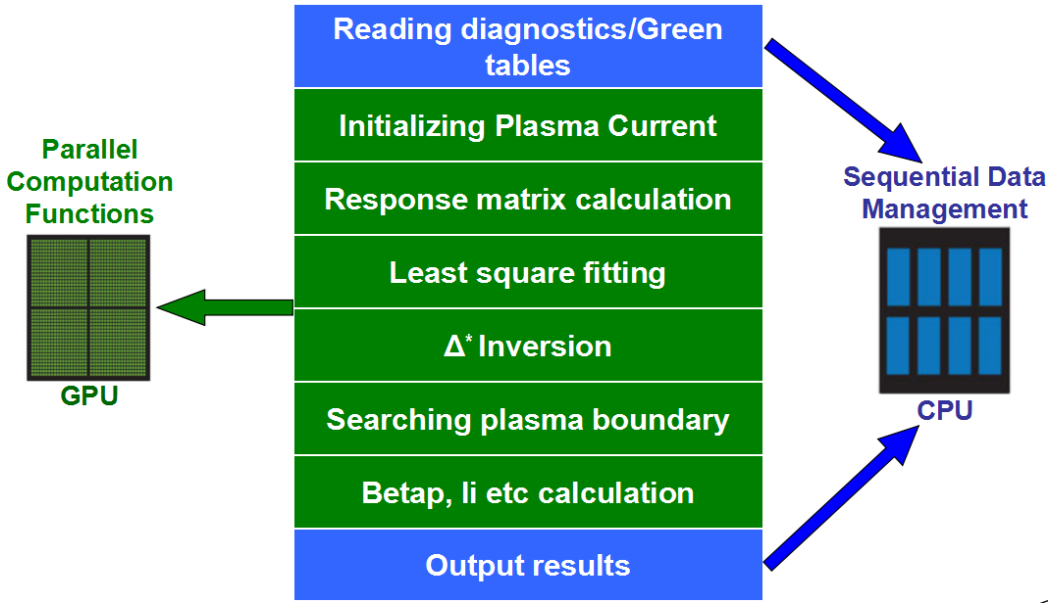

Fig.4. P-EFIT Flow Chart: Optimization of GPU/CPU Interactions

Initial magnetic reconstruction testing results for EAST discharge on 65×65 spatial grids showed that P-EFIT can do one iteration in less than 0.3ms and could obtain a well-converged and accurate enough equilibrium result in 8-9 iterations which would take about 2 ms. Although P-EFIT is more than ten times faster than EFIT, it still can not satisfy the requirement for real-time control in tokamak operation. For this reason, a strategy similar to RT-EFIT is adopted, whose basic premise is to use the equilibrium result of last time-slice as the initial input for next computation, and perform least-square best fit using the most recent diagnostic data. For each computation, only one iteration is conducted.

3. Benchmark and result discussion

3.1 EAST single static equilibrium benchmark test

A set of magnetic measurement data is simulated by off-line EFIT using EFIT fixed boundary equilibrium calculation mode. These measurement data are used as the input data to P-EFIT. To simulate in the actual experimental case, a random relative uncertainty up to 3% is added to the exact data, as figure 5 shows. The reconstruction result is presented in figure 6, which demonstrates that 3% random error did not bring about significant impact on the final reconstruction result.

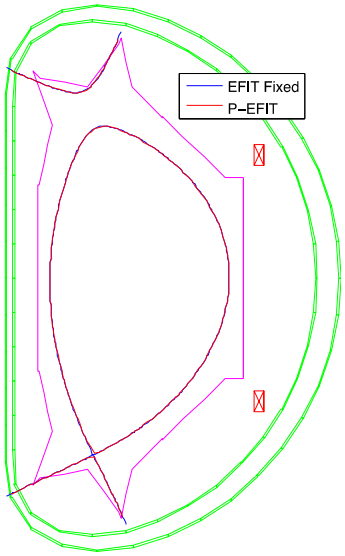

Fig. 5 Comparison between the simulated static equilibrium by offline EFIT and reconstructed by P_EFIT

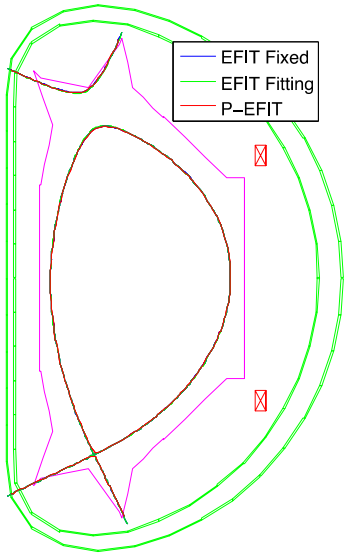

Fig. 6 Comparison among the simulated static equilibrium, reconstructed by offline EFIT and P_EFIT with 3% random error on measurements

1.2 EAST real experiment simulation test

To verify the strategy of P_EFIT for real-time plasma control, another benchmark test is conducted with a set of ideal equilibrium results derived from an ideal discharge shot simulated by TSC [7]. To simulate the real situation, 3% relative error is added to the measurements. Figure 7 illustrated the flux contour map at three time points of this shot. The plasma shape has some obvious changes between during these time points. Figure 8 compares the plasma boundary reconstructed by P-EFIT and the output from TSC, which showed that the boundary reconstructed by P-EFIT using the one iteration strategy was accurate even with 3% noise existed on the measurements. More detailed results and discuss can be found in [5].

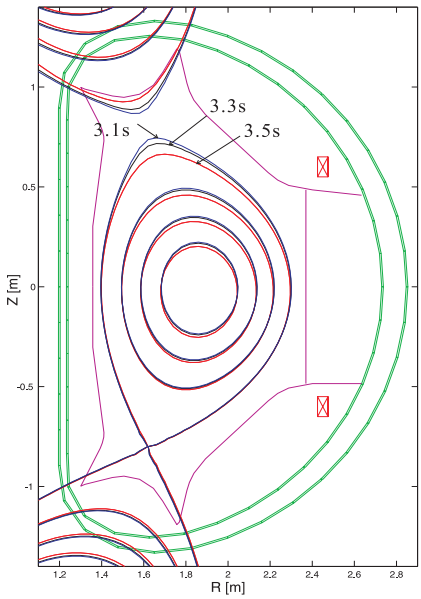

Fig.7. The flux contour maps at three time points of the TSC shot, during which the plasma shape is changing significantly.

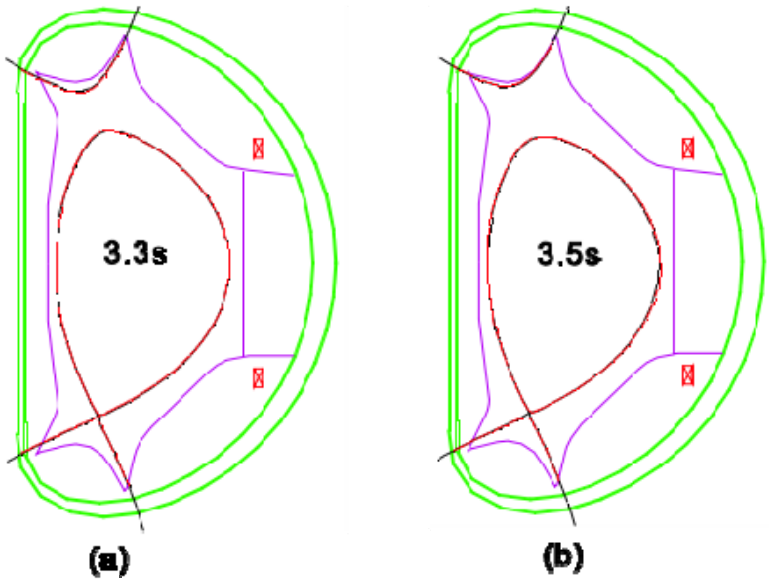

Fig.8. The comparison of P-EFIT reconstruct result (red line) at two time points with the TSC output (black line).

3.3 P-EFIT results on DIII-D

Here, DIII-D experiment discharge data is directly used and the results compared with EFIT. There are also some enhancement in P-EFIT algorithms, which aims at improving reconstruction quality, including truncated least square fitting, more accurately searching x-point and magnetic axis, more robust plasma current profile representation.

Finally, all the results from P-EFIT are compared with EFIT, both results of 65×65 and 129×129 spatial grid size P-EFIT version indicate that P-EFIT could accurately reproduce the EFIT reconstruction algorithms at a fraction of the computational cost. Figure 9 compares the plasma boundary reconstructed by EFIT and P-EFIT. Figure 10 shows the comparison of magnetic diagnostic fitting quality. In figure 11, the plasma current profile and PF coil currents is compared between EFIT and P-EFIT results.

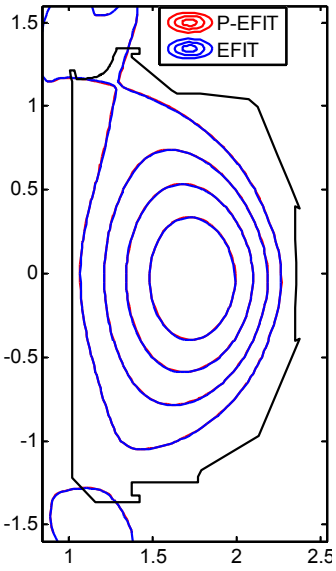

Fig.9. The comparison of reconstructed plasma boundary between P-EFIT (red line) and EFIT (blue line).

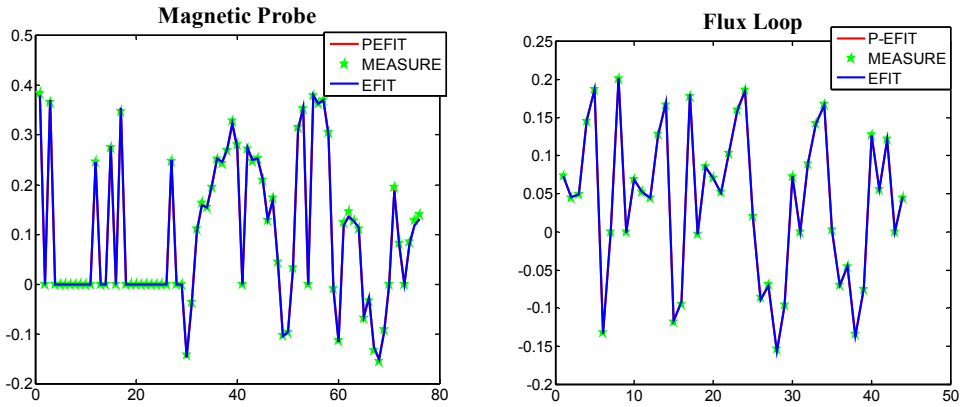

Fig.10. Comparison of magnetic diagnostic fitting quality between P-EFIT (red line) and EFIT (blue line) and measurement (green star).

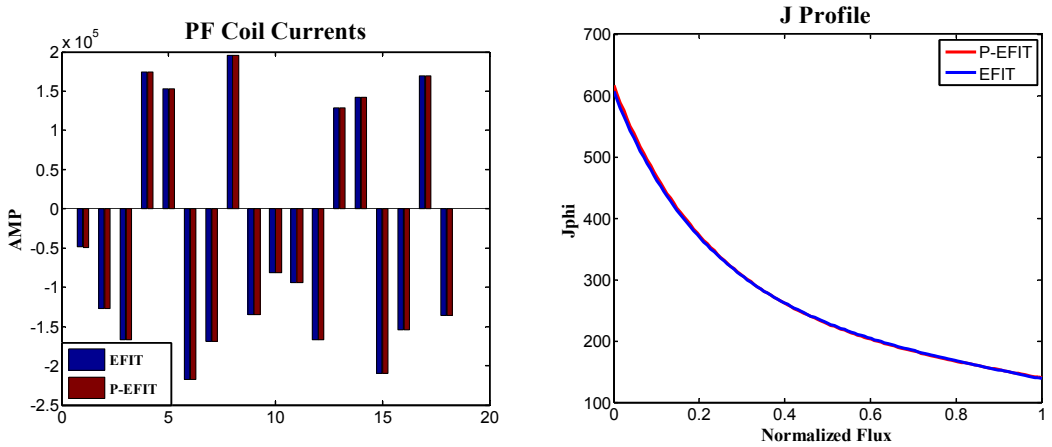

Fig.11. Plasma current profile and PF coil currents from P-EFIT (red) compared with EFIT (blue).

4. Conclusion and future developments

In this paper, we have proved the feasibility of accelerating the equilibrium reconstruction algorithm with CUDA™and described some important implementation details. Initial magnetic reconstruction benchmark results for EAST and DIII-D discharge indicate that P-EFIT could accurately reproduce the EFIT algorithms at a fraction of the computational cost (~ one-tenth cost time).

The GPU accelerated reconstruction code P-EFIT could complete a full iteration in around 250μs, with 65×65 grid number, which is satisfying the real-time control needs. This work provides high-quality real time high spatial grids equilibrium reconstruction results for plasma control and opens a way for more complicated equilibrium problem solver. We will continue work on more experimental measurements, physics constraints and higher resolution spatial grids.

Acknowledgments

This work was supported by the Major State Basic Research Development Program of China (973 program, No 2012GB105000 and No 2014GB103000), the National Nature Science Foundation of China for Youth (No 11205191) and partly supported by the JSPS-NRF-NSFC A3 Foresight Program in the field of Plasma Physics (NSFC: No.11261140328).

References

[1] Ferron J R, Walker M L, Lao L L, et al. Real time equilibrium reconstruction for tokamak discharge control, *Nucl. Fusion* 38, 1055, 1998

[2] NVIDIA 2011 *CUDA C Programming guide* v. 4.0 (Santa Clara, CA: NVIDIA Corporation)

[3] Lao L L, John H S, Stambaugn R D, et al., Reconstruction of current profile parameters and plasma shapes in tokamaks *Nucl. Fusion* 25, 1611-22, 1985

[4] Lao L L *et al 2005* MHD equilibrium reconstruction in the DIII-D tokamak *Fusion Sci. Tech.* 48, 968, 2005

[5] Yue X N, Xiao B J, Luo Z P, et al., Fast equilibrium reconstruction for tokamak discharge control based on GPU *Plasma Phys. Control. Fusion*, 55, 085016, 2013

[6] Lao L L, Ferron J R, Groebner R J, et al., Equilibrium analysis of current profiles in tokamaks *Nucl. Fusion*, 30, 1035, 1990

[7] S C Jardin, N Pomphrey, J. DeLucia, Dynamic modeling of transport and position control of tokamaks, *Journal of Computation Physics*, 66, 481, 1986

Effect of Local Modification of Equilibrium on the Stability of MHD Modes

Ohjin Kwon* and Hyunsun Han**
*Dept. of Physics, Daegu University, Gyungsan, Gyeongbuk, Korea
e-mail : ojkwon@daegu.ac.kr
**National Fusion Research Institute, Daejeon, Korea

We have shown earlier that the *n*=1 global MHD mode onset is extremely well correlated to the crossing of the numerically predicted stability boundaries by calculating the linear growth rate of ideal instabilities for various high beta plasmas in JET. Here, we consider one of such cases and investigate the effect of local modification of pressure gradient and current density profiles on the stability of the *n*=1 mode. When the current density profile is modified to decrease smoothly to zero, a long tail in the stability boundary related with the peeling type instability can be removed. Depending on the position where the pressure profile is flattened, the *n*=1 mode can be either stabilized or destabilized. For the equilibrium considered here, changes at *q*=2 surface due to the modification of pressure gradient profile are found to be important.

1. Introduction

It is necessary to find optimized pressure and current density profiles in order to increase the β limits to improve efficiency in fusion devices since the triple fusion product increases with β. Here, $\beta = 2\mu_0 < p > /B_0^2$ is the ratio of the plasma pressure to the magnetic pressure and $< p >$ is the volume-averaged plasma pressure. For JET high β operations of AT (Advanced Tokamak) [1] and hybrid [2] scenarios, wide range of MHD instabilities are encountered, including fast-particle driven chirping modes, tearing modes, and ideal saturated kink modes [3]. AT scenario operations have reversed magnetic shear, $\hat{s} = \frac{r}{q}\frac{dq}{dr}$, in the core where q is the safety factor, while the hybrid scenario operations have low $\hat{s}$. Both regularly operate near or above the no-wall stability limit. Both have low internal inductance and high non-inductive current portion, and therefore suitable for steady-state operations of fusion devices.

In Ref. [4], we have focused on cases limited by slowly growing *n*=1 internal modes. Stability boundaries of the *n*=1 MHD (Magneto-Hydro-Dynamic) at some time-slices for many shots have been calculated by changing β_p and q_0 with fixed p' and j profiles using the HELENA equilibrium code [5] and the MISHKA-1 linear stability code [6]. Here, n is the toroidal mode number, β_p is the poloidal β, q_0 is the central q value, $p' = dp/d\Psi$, Ψ is the normalised poloidal magnetic flux, and j is the flux-surface averaged current density. The stability boundary in q_0- β_p space is found to change considerably in time. The trajectory of the operating condition of different reconstructed equilibrium in the no-wall stability boundary shows that the plasma enters the unstable region just before the experimentally observed onset of the continuous *n*=1 MHD mode activity in many cases. The example is shown in Fig. 1 (Figure 1 of this paper is same as Fig. 7 of Ref. [4]). The reconstructed equilibrium stays in the stable region before 5.5sec. The transition from the stable region to the unstable region takes place between 5.5sec and 5.9sec. During this time, the stability boundary changes considerably such that the unstable region widens. At the same time, the global equilibrium quantities, especially β_p, also change. It enters the unstable region just before the continuous *n*=1 MHD mode is experimentally observed at 6.2sec. This demonstrates that ideal MHD represents a valid description of the plasma for predicting the onset of global long-lived instabilities in plasmas with broad low-shear q-profiles.

We have also investigated the effect of the plasma boundary shape, p' and j profiles on the stability boundaries in Ref. 4. In general, broader pressure profile, peaked current profile, and more shaped plasma are favorable for the stability. However, detailed profiles are more important. Only whole profile changes were considered in Ref. 4, such as replacing plasma boundary shape, p' and j profiles with ones from different time slices or from different shots. In this study, we investigate the effect of local modification of p' and j profiles on the stability of *n*=1 MHD kink mode, instead of whole profile changes.

2. Current density profile modification

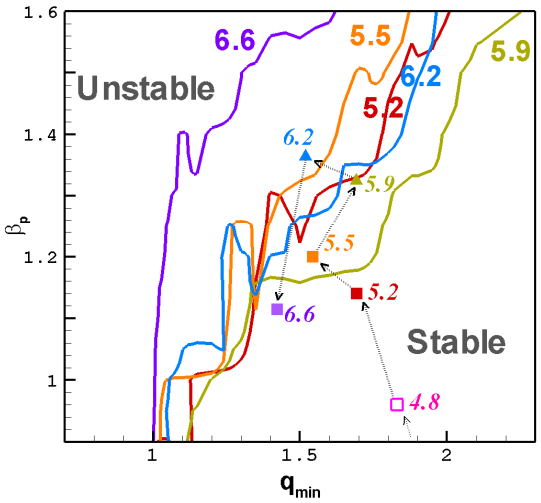

Fig 1. MHD stability boundaries and a trajectory of experimental equilibrium in $\beta_p - q_{min}$ space for JET shot 77877. Numbers correspond to different time slice. This figure is same as the Fig. 7. of Ref. [3]

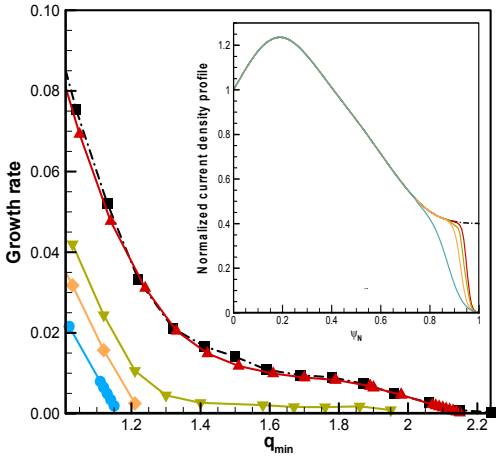

Fig. 2. The $n = 1$ mode growth rate as a function of q_{min} when j is modified. The inserted figure shows how j is varied where the color corresponds to the same color in the main figure.

We have chosen an experimental equilibrium at a time when it is unstable to the n=1 ideal kink mode, using the EFIT equilibrium reconstruction [7] constrained by MSE field line pitch angle measurements and the magnetic probe measurements. The chosen equilibrium has $q_0 \sim q_{min} \sim 1.6$ and finite edge j. The growth rate of the mode, γ, as a function of q_{min} is shown in Fig. 2. It can be seen that γ decreases as q_{min} increases. But the mode is not completely stabilized, having a long tail, for experimental finite edge j equilibrium (black curve). This tail is associated with peeling-mode type instability [8]. We have modified current density profile such that it vanishes to zero at the plasma boundary. Modification of j from four starting positions (Ψ_s=0.75, 0.85, 0.875, 0.9) to the boundary are shown in the inserted figure in Fig. 2. For Ψ_s<0.85, the tail disappears and the equilibrium with β_p=1.46 becomes stable for q_{min}>1.2 (experimental q_{min} is1.6) This is due to the fact that the peeling mode is driven by edge plasma current or edge current gradient and that this destabilizing effect may be removed by the current density profile modification. Ψ_s is important for complete stabilization of the tail.

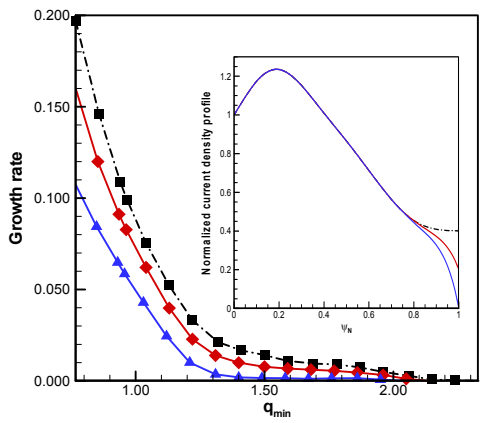

Fig. 3. The $n = 1$ mode growth rate as a function of q_{min} when j is modified. The inserted figure shows how j is varied where the color corresponds to the same color in the main figure.

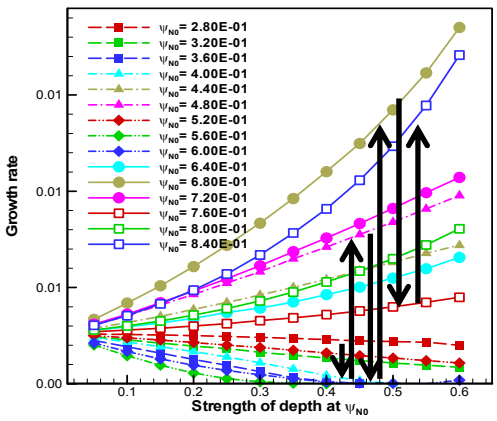

Fig. 4. Dependence of the n=1 mode growth rate on the depth of pressure gradient modification for various values of ψ_0.

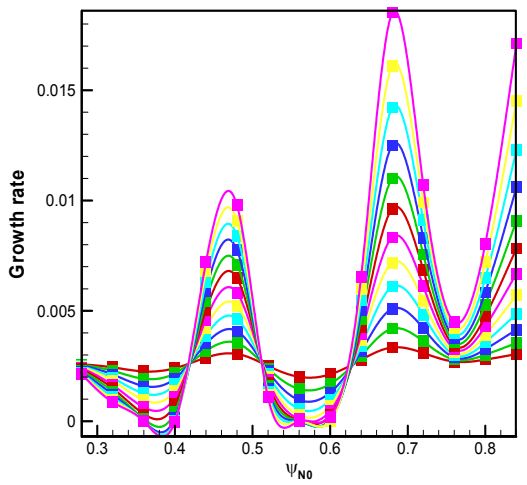

Fig. 5. Dependence of the n=1 mode growth rate on ψ_0 for various values of the depth.

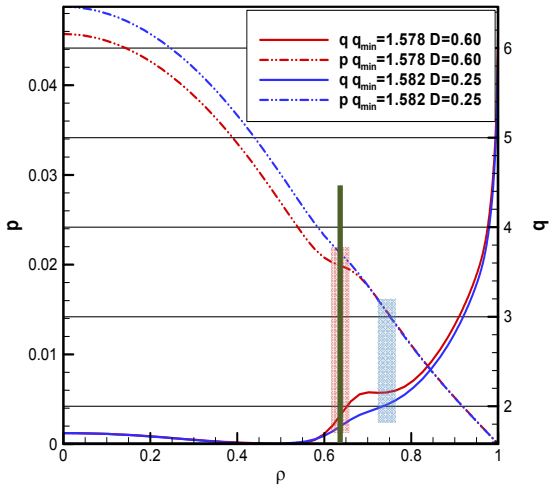

Fig. 6. p and q profiles as a function of $\rho = \sqrt{\psi}$ when p' is modified at ψ_0=0.4. A green line represents the position of ψ_0. Shaded regions represent approximate positions of $q = 2$ surface for two different values of D.

We have tried a different type of j modification as shown in the inserted figure of Fig. 3. Here, j decreases smoothly from Ψ_s=0.75. Both for non-zero current (red curve) and zero current (blue curve) at the boundary, a tail in γ remains. Therefore, even if j decreases from the same Ψ_s=0.75, the way how j decreases determines whether the mode can be completely stabilised (as shown in yellow curve of Fig. 2) or not (as shown in blue curve of Fig. 3) for $1.2<q_{\min}<2.0$. If j at the boundary remains to be finite, even though smaller than reconstructed experiment, γ behaves similarly to the original equilibrium.

3. Pressure gradient profile modification

In HELENA equilibrium code [5], $j(\Psi)$ and $p'(\Psi)=dp/d\Psi$ profiles can be chosen as input. We have chosen j profile as a red curve of Fig. 2 (i.e., $\psi_s = 0.9$) and modified $p'(\Psi)$ profile by adding a Gaussian function of $\Delta p'$ to p', such that

$$\Delta p' = -De^{-\frac{(\psi-\psi_0)^2}{2W^2}}.$$

Here, $\Delta p'$ is characterized by depth (D), width (W), and the central position of modification (ψ_0). This modification will act to flatten p profile locally. The results, γ as a function of D, are shown in Fig. 4, for various positions of ψ_0. Thick black arrows denote the direction of increasing ψ_0, starting from the left. It can be seen from this figure that the mode can be more stabilized (γ decreases) or more destabilized (γ increases) depending on ψ_0. Stabilizing or destabilizing effect increases with D for same ψ_0. Therefore, the position where the pressure profile is flattened is important in determining whether one can stabilize this mode, further increasing attainable β. The effect of ψ_0 on γ is more clearly seen in Fig. 5, where γ is drawn as a function of ψ_0 for various values of D. For $0.3 < \psi_0 < 0.42$ and $0.52 < \psi_0 < 0.63$, the effect of pressure flattening is stabilizing. It is destabilizing otherwise in the range of ψ_0 we have examined.

The reason why the stability property depends on ψ_0 can be explained when we examine changes in p and q profiles due to pressure gradient modification. This is shown in Fig. 6. Here, p and q are plotted as a function of $\rho = \sqrt{\psi}$ for two values of $D = 0.25$ (blue curve) and 0.6 (red curve). Also, since ψ_0=0.4 in this figure, $\rho_0 = \sqrt{\psi_0}=\sqrt{0.4} \approx 0.63$, which is shown in the thick green line. The q profile can be seen to have weakly reversed shear in the core with $q_{\min} \approx 1.6$. Regions shaded in blue and red correspond to the regions where $q = 2$ surface is located for $D = 0.25$ and 0.6, respectively. The current profile is also modified accordingly when the pressure gradient profile is modified, due to the relation in Grad- Shafranov equation which governs the plasma equilibrium. As D increases, the $q = 2$

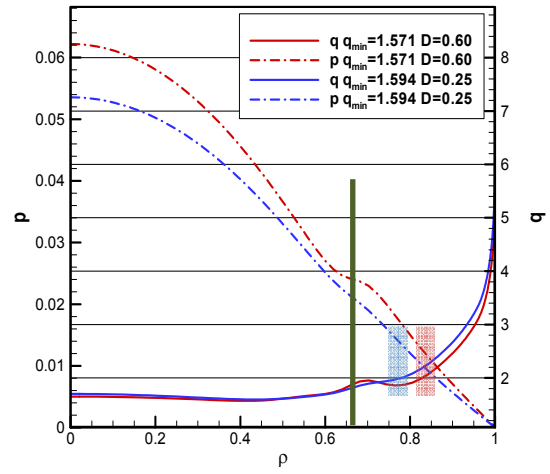

Fig. 7. p and q profiles as a function of $\rho = \sqrt{\psi}$ when p' is modified at ψ_0=0.44. A green line and shaded regions are as explained in Fig. 6.

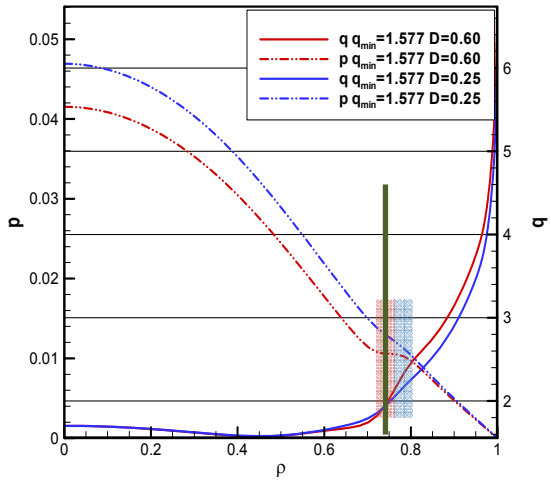

Fig. 8. p and q profiles as a function of $\rho = \sqrt{\psi}$ when p' is modified at ψ_0=0.56. A green line and shaded regions are as explained in Fig. 6.

surface moves inward, closer to ψ_0 (or ρ_0) where the pressure is flattened in Fig. 6. Also, $\hat{s}$ at $q = 2$ surface increases with D, which is stabilizing. Therefore stabilization can be obtained in this case by low the pressure gradient and by high $\hat{s}$, near $q = 2$ resonant surface.

When $\psi_0 = 0.44$, the $q = 2$ surface moves outward, away from ψ_0, as D increases as shown in Fig. 7. This behavior is opposite to the one in Fig. 6, and this makes p' larger at $q = 2$ when D increases, which then makes the mode more unstable. Therefore, if changes of p and q profiles due to p' modification is such that p' becomes smaller (or larger) and that $\hat{s}$ becomes larger (or smaller) as D increases at $q = 2$ surface, the mode becomes more stable (or unstable). Figure 8 shows the results for $\psi_0 = 0.56$, where the effect of increasing D is stabilizing. Here, ψ_0 and modified $q = 2$ surface are almost at the same location. The effect of pressure flattening can be maximized in this case and since $\hat{s}$ becomes rather large, when compared with other cases, stabilization may be obtained. The results for ψ_0=0.76 are shown in Fig. 9, where ψ_0 is located too far out near the edge, away from the original $q = 2$ sufrace. It makes p' larger as D increases at $q = 2$ with little change in $\hat{s}$, which is destabilizing.

4. Summary

We have studied the effect of modifying j and p' profiles on the stability of the $n = 1$ kink mode which is associated with experimentally observed slowly growing mode, encountered in JET high-β AT and hybrid scenario operations. The MHD stability boundaries and trajectories in some timeslices of experimental equilibria for various shots have been calculated previously [4], showing good correlation between the crossing of stability boundary and the onset of the $n = 1$ kink mode.

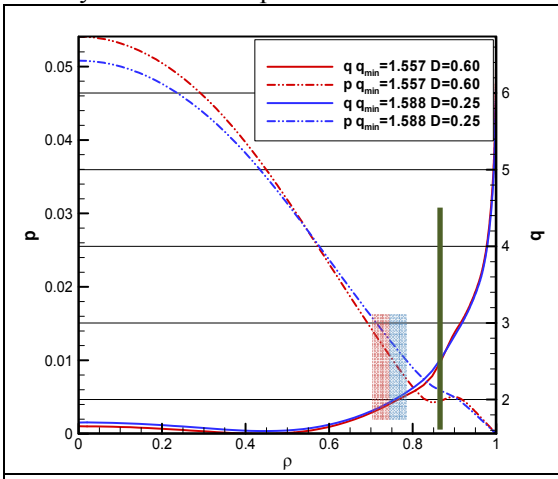

Fig. 9. p and q profiles as a function of $\rho = \sqrt{\psi}$ when p' is modified at ψ_0=0.76. A green line and shaded regions are as explained in Fig. 6.

We have examined the effect of local modification of current density profile and pressure gradient profile on MHD stability. By eliminating the edge current in certain ways, instability which extends to large $q_{\min}$, related to the peeling type mode driven by edge plasma current or edge current gradient, can be removed. Location of the center of the pressure gradient profile modification determines whether modified equilibrium becomes more unstable or less unstable. When the pressure gradient decreases and the magnetic shear increases at the modified $q = 2$ surface, more stabilization can be achieved by pressure gradient modification.

In conclusion, if proper modifications of the current density profile and pressure gradient profile are applied experimentally, better performance can be achieved

Acknowledgement
This work was partly supported by Ministry of Science, ICT, and Future Planning under KSTAR project, and by the JSPS-NRF-NSFC A3 Foresight Program in the field of Plasma Physics (NRF No. 2012K2A2A6000443 and NSFC: No.11261140328).

References
[1] T S Taylor 1997 Plasma Phys. Control. Fusion **39,** B47 (1997)
[2] E Joffrin *et al*., Nucl. Fusion **45**, 626 (2005)
[3] P. Burratti *et al.,* Nucl. Fusion **52**, 023006 (2012)
[4] O J Kwon *et al*., Plasma Phys. Control. Fusion **54,** 045010 (2012)
[5] G Huysmans, J Goedbloed, and W Kerner, Proceedings of the CP90 Conference on Computer Physics, (World Scientific, Singapore), p. 371 (1991)
[6] A B Mikhailovskii, G T A Huysmans, S E Sharapov, and W O Kerner Plasma Phys. Rep. **23,** 844 (1997)
[7] L Lao *et al*., Nucl. Fusion **30**, 1035 (1990)
[8] J W Connor *et al*., Phys. Plasmas **5**, 2687 (1998)

Preliminary experimental results of disruption mitigation using supersonic molecular beam and massive gas injection on J-TEXT and HL-2A

Y.B. Dong[1], Y.P. Zhang[1], Z. Chen[2], L. Zeng[3], H. Zhuang[3], C.Y. Chen[1], X.Q. Ji[1], Y. Liu[1], Y. Xu[1]

1. Southwestern Institute of Physics, PO Box 432, Chengdu 610041, China
2. State Key Laboratory of Advanced Electromagnetic Engineering and Technology, College of Electrical and Electronic Engineering, Huazhong University of Science and Technology, Wuhan 430074, China
3. Institute of Plasma Physics, Chinese Academy of Science, Hefei 23031, China
Corresponding Author's e-mail address: caroldyb@swip.ac.cn

1. Introduction

Disruption is one of major threats in future reactor-size tokamaks. Due to a sudden loss of confinement, plasmas produce excessive heat loads onto plasma facing components, inducing strong electromagnetic forces and currents in the structures, and hence, generating multi-MeV runaway electrons [1, 2]. The potentially damaging consequence of large runaway currents generated by disruptions is a key issue for next generation tokamak. Therefore, disruption mitigation is essential for next-generation fusion devices, including ITER [3]. Massive gas injection (MGI) is one of the candidate methods foreseen to be a standard mitigation tool for future tokamaks. It aims at reducing the deleterious effects of the disruption. So far, MGI experiments have been carried out on several tokamaks, such as TEXTOR [4], DIII-D [5], ASDEX Upgrade [6], Alcator C-Mod [7] and JET [8, 9]. Encouraging results have been obtained. Another possible method to mitigate plasma disruption is the supersonic molecular beam injection (SMBI), which has been developed on the HL-2A [10]. However, the optimization of injection scenario (gas species and amount) is still an open question.

2. Disruption mitigation system

Recently, disruption mitigation experiments with SMBI and MGI have been carried out in the HL-2A and J-TEXT tokamaks to study various injection scenarios and gas jet penetration.

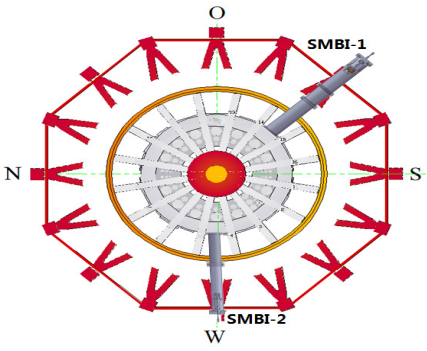

Fig. 1 Location of two SMBI systems and relevant diagnostics on HL-2A.

The improved SMBI system at HL-2A, which has similar mechanical structure with the old ones[10], meets a lot of demanding functional requirements, such as a larger orifice(0.5mm of diameter), a quite shorter opening time (0.2ms), and its maximum throughput is up to 1.0×10^{21} (10ms，50bar). The SMBI clusters are produced at liquid nitrogen during a supersonic adiabatic expansion of moderate backing pressure gases into vacuum

through a Laval nozzle. The SMBI was triggered by a negative voltage spike in the loop voltage signal prior to the thermal quench (TQ). Location of the SMBI systems used for experiments is shown on figure 1.

In support of our disruption mitigation program, a fast massive gas injection valve has been constructed and tested on the J-TEXT tokamak. Figure 2 shows a cross section of the valve: an aluminum stem seals a fueling gas reservoir from the discharge vessel. In this contribution, we demonstrate a valve activated by an eddy current induced on a piston which opens the valve. It is built without ferromagnetic materials and can be operated close to the vessel in the environment of the tokamak fields.

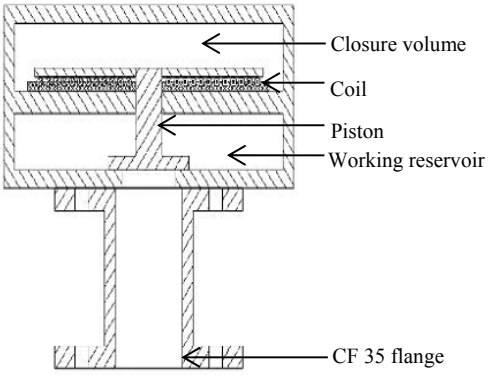

Fig. 2 Cross section drawing of the fast valve

Response time and throughput are the two key characteristics of the fast valve, in order to calibrate them accurately, a kind of non-contact displacement measurement sensor: a magnetic ruler was chosen to take the measurement. The displacement sensor was connected with the piston, when the piston be raised up, the displacement sensor will raised up too, so there will be a signal output, the interval time between the trigger signal and sensor signal is the response time of the fast valve. From the experiment we could get that after trigger signal. Figure 3(a) shows the test results of the opening time and the displacement of the valve, which with the same voltage (600V) and the two different pressure (0.2Mpa and 0.4Mpa). Valve starts to open in 0.25ms with 0.4Mpa pressure after the trigger signal. After about 1 ms, it is nearly completely open and after 2 ms is closed again due to the repulsive pressure in the back volume. Compared different pressure of gas, the response time and the full open time is deeply depended on the pressure of gas and the voltage of capacitor. The throughput of the valve is also strongly depending on the gas pressure and the voltage. In order to calibrate the throughput of fast valve, a test bench is assembled. We have chosen a container as a target vessel whose volume is 100L. The pressure increase can be directly measured in the target volume after the shot. The throughput of the fast valve in different voltage and different gas pressure is shown in figure 3(b). It could be adjust from 0 to 700mbar.L. The throughput of the fast valve is depending on the voltage and gas pressure, by adjusting voltage and gas pressure, it is easily to change the throughput during the experiment.

A dependence of the throughput of the valve on the gas species was observed. The vessel of J-TEXT is the target vessel whose volume is $3.8m^3$. The throughput of the fast valve in different voltage is shown in Figure 4. The backpressure is 0.566 Mpa. Experiments on J-TEXT have shown that already about 6.3×10^{20}(Ar)-3.85×10^{21}(He) particles of a gas is sufficient to generate reliably the disruption. The high pressure in the reservoir guarantees a fast gas stream and a fast reaction time. It could be adjust from, which could absolutely meet the requirement of disruption mitigation on HL-2A and J-TEXT. The valve has been applied successfully on J-TEXT.

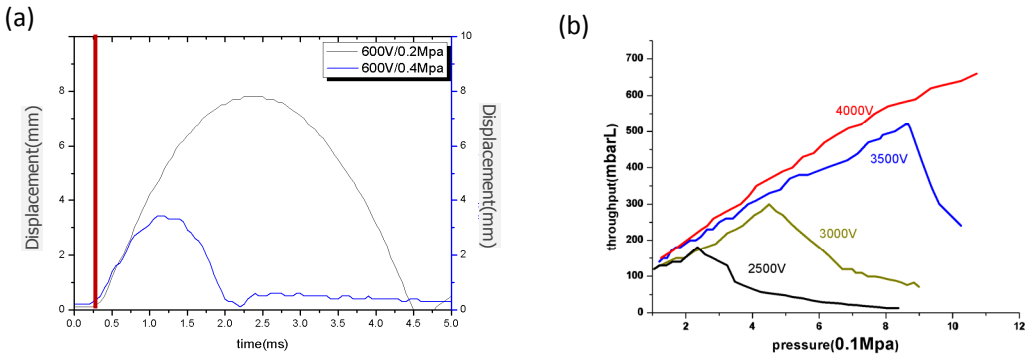

Fig. 3 (a) The opening characteristics of the fast valve. (b) The relationship of throughput and voltage and gas pressure. The curves with different colors represent different voltage.

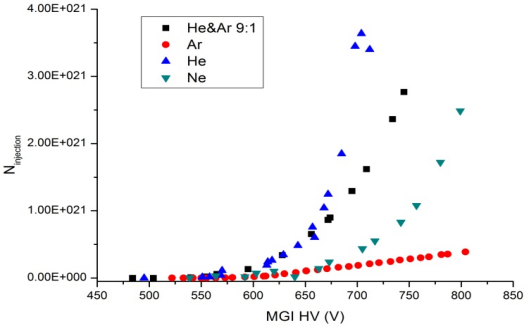

Fig. 4 Number of injected particles vs. voltage for the working volumes. The backpressure is 0.566 Mpa.

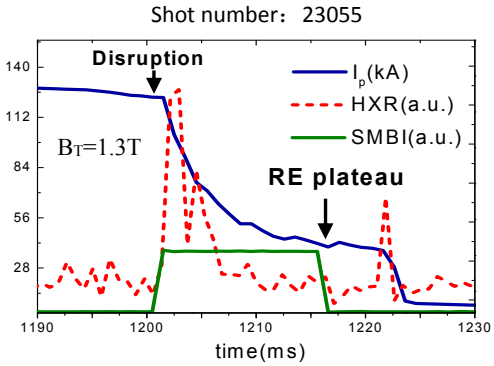

Fig. 5 The time evolution of the plasma current (I_p), hard x-ray radiation (HXR), and the SMBI pulse triggered in a current quench phase at the HL-2A tokamak.

3. Preliminary experiment results

In tokamak experiments, including JET, JT-60U, Tore Supra, and TEXTOR, it has been shown that the runaway electron（RE）generation occurs only above a threshold at $B_T \approx 2$ T independent on machine size. In the present SMBI mitigation experiments at HL-2A, the RE plateau is achieved even at $B_T = 1.3$ T, much lower than the B_T threshold observed in other tokamaks. Figure 5 shows the generation of a RE plateau during a major disruption ($B_T = 1.3$T) after Ar injected by SMBI in a current quench phase. Comparisons of different gas species (Ne and Ar) and their amounts (from 50 to 500 mbar.L) have been made, showing that the heavier gases are easier to generate REs than light ones. Both Ne and Ar gases could create runaway electron at $B_T = 1.3$ T. The maximum conversion rate (I_{RE}/I_P) of the runaway current reach 55% (I_{RE} has been calculated by subtracting an exponential current decay from the measured I_p).

In J-TEXT, disruption is induced by MGI. The RE plateau has also been achieved during major disruption after Ar injected by MGI during pre-TQ phase, as illustrated in Fig.

6(a). By comparing different inject amount, we found that runaway electrons were suppressed by a larger number of Ar atoms. Through scanning B_T and $\bar{n}_e$, both B_T and $\bar{n}_e$ threshold are observed in J-TEXT (Fig. 6(b)). The threshold of B_T is 1.2T, similar to that found in HL-2A. Figure 6(b) also shows that the RE plateau is easier to obtain at lower electron densities.

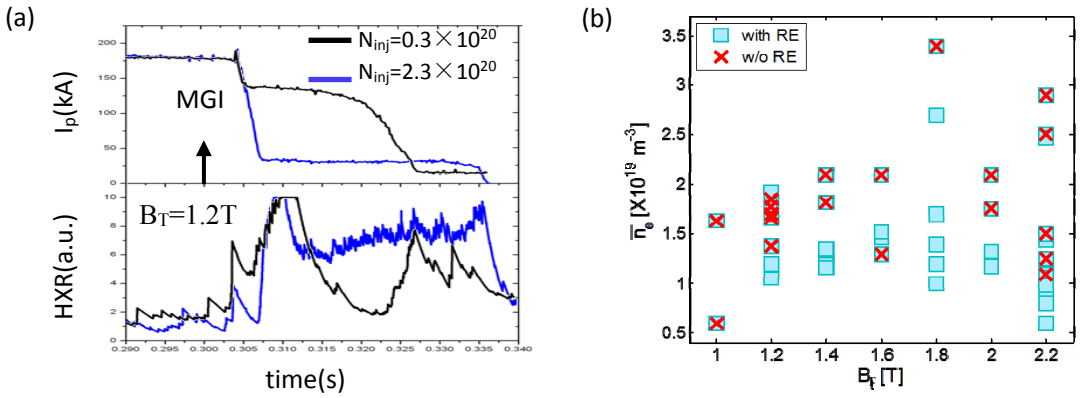

Fig. 6 (a) Suppression of runaway electrons by two different injected amounts of Ar. (b) B_T threshold and electron density threshold are measured in J-TEXT tokamak.

4. Discussion

Gas jet penetration show different features between SMBI and MGI. The shallow penetration of impurities prior to the thermal quench injected by MGI is confirmed by observations of impurity radiation in the visible range [11]. In contrast to of MGI, the SMBI with clusters, which resembles micro-pellets, will be more favorable for deeper injecting and fuelling [10]. The SMBI cluster might be more effective to mitigate disruption than the normal MGI with the same numbers of injected atoms.

Acknowledgement —Support from the National Magnetic Confinement Fusion Science Program of China under Contracts No. 2011GB109003 is gratefully acknowledged.

References:

[1] Plyusnin V.V., et al., 2006 Nucl. Fusion 46 277.
[2] Yoshino R., et al., 1999 Nucl. Fusion 39 151.
[3] Hender T.C. et al 2007. Nucl. Fusion 47 128–200
[4] Bozhenkov S.A. et al 2008. Plasma Phys. Control. Fusion 50 105007
[5] Hollmannn E.M. et al 2005 .Nucl. Fusion 45 1046
[6] Pautasso G. et al 2009. Plasma Phys. Control. Fusion 51 124056
[7] Whyte D.G. et al 2007. J. Nucl. Mater. 363–365 1160–7
[8] Gill R.D., et al 2000. Nuclear Fusion, Vol. 40, No. 2, 163
[9] Lehnen M. et al 2009. 36th EPS Conf. (Sofia, Bulgaria)

[10] LianghuaYao, et al 2007. Nucl.Fusion 47 1399
[11] Reux C., et al 2010. Nucl. Fusion 50 095006

Recent Status of Pedestal Physics Activities in KSTAR

S. W. Yoon[1], Y. M. Jeon[1], J. H. Lee[1], S. H. Hahn[1], W. H. Ko[1], J. G. Kwak[1], G. S. Yun[2], H. Y. Lee[3]

[1] National Fusion Research Institute, Daejeon, Korea

[2] Postech, Pohang, Korea

[3] Korea Advanced Institute of Science and Technology, Daejeon, Korea

E-mail : swyoon@nfri.re.kr

In this paper, as one of the main research thrusters in KSTAR[1], the recent progress of research activities on pedestal physics will be summarized focusing on the several key topics including ELM suppression/dynamics, profile characteristics and L-H transition followed by near term plan in pedestal physics

KSTAR research has been focused on ITER urgent issues such as the first demonstration of ELM suppression with unique n=1 resonant magnetic perturbation (RMP) in 2012[2]. ELM suppression/mitigation experiment has been successful for a wide range of coil configuration and the suppression window in the safety factor q_{95} from 6.5 to 3.9 depending on the configuration, i.e., q_{95}~6.5 for n=1, q_{95}~5.0 for the mixed n=1 & n=2, and q_{95}~4.0 for n=2 indicating the strong impact of resonant component on ELM suppression with degradation of global energy confinement less than 10 %. A unique 2D/3D ECE imaging diagnostics on KSTAR provided the basic underling physics of the ELMs validated with the synthetic image based on the BOUT++ code. The examples are; 1) persisting mode structures accompanied with bursting behaviours in ELM crash-free period, 2) ELM dynamics observed simultaneously at both high and low field sides revealed necessity of the strong Pfirsh-Schlüter flow in pedestal region. There has been a significant progress on understanding of the underlying mechanism on RMP suppression using the measurements of pedestal turbulence fluctuations and modeling of the plasma response especially for n=1 case where the field penetration is global and full response modeling is required including the shielding effect of the toroidal rotation. In parallel, by extending the duration of the ELM suppression upto 4 sec, the long-pulse compatibility of RMP suppresion is tested in terms of global particle balance also. Furthermore, a strong effort is made to develop a full scenario without a single ELM crash approaching ITER relevant pedestal collisionality (ν_e^*~0.1).

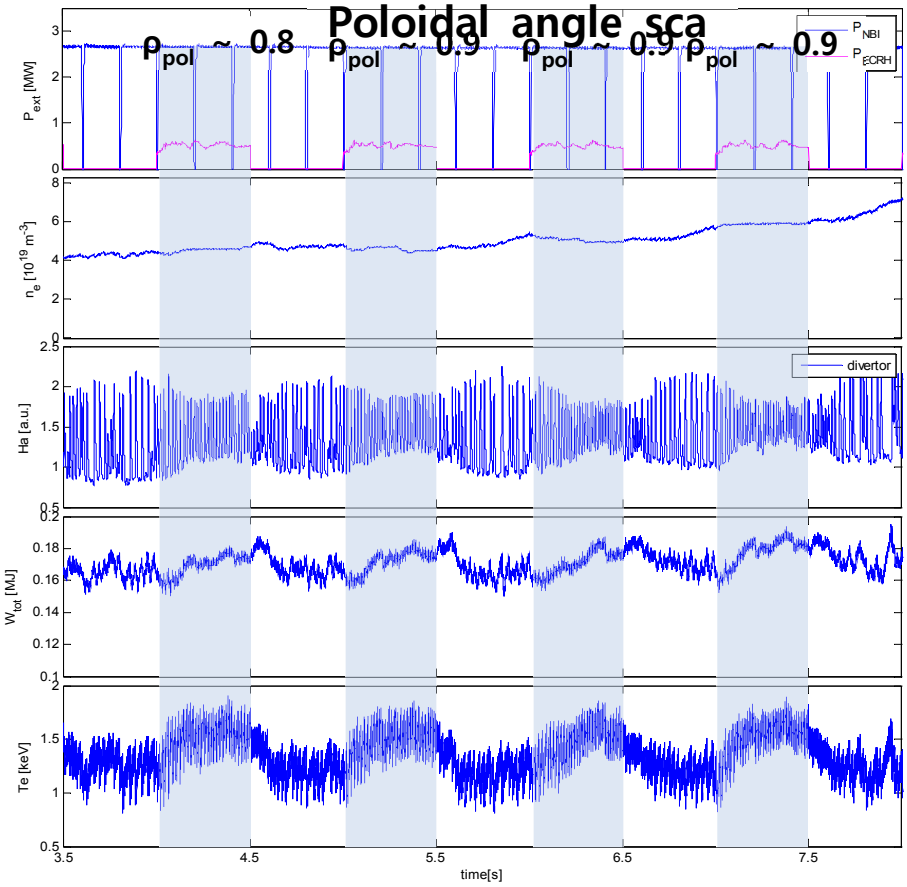

Figure 1. Effect of edge ECH heating on ELM size & frequency. Stronger mitigation is discovered when deposition layer approaches pedestal foot.

Apart from RMP physics, the local heating and current drive in the pedestal region by electron cyclotron heating (ECH) provides a unique tool to perturb the edge characteristics and with proper positioning the resonance layer inside the pedestal, the ΔW_{ELM} is successfully reduced to 10-20 % including factor of three increase of f_{ELM}. Similar to the previous reports from other tokamaks, the increase of the ELM frequency is observed when the enough ECRH is injected in the pedestal region (figure 1). Approaching deposition layers from rho_pol~0.86 to ~.98, the size of ELM is decreased and ELM frequency is also increased. It turned out that the increase of the stored energy is marginal by ECH and most of additional ECH (~ 0.5 MW) is dissipated by additional transport channel by increased low frequency fluctuations in the pedestal region. Alternatively, ELM mitigation is also investigated with Supersonic Molecular Beam Injection (SMBI) technique and additional gas puffing by SMBI was demonstrated to control ELM. The ELM frequency (f_{ELM}) was increased by a factor of 2 - 3 due to SMBI, and the influence time (τ) was about 300 ms which is a few times higher than the global particle confinement time[3]. Density rise by

SMBI is marginal even at low density ($3x10^{19}$ /m^3) and negligible at higher density ($4x10^{19}$ /m^3) implying no significant drawback for density control. During the mitigated ELM phase by SMBI, the pedestal electron pressure (P_e^{ped}) and its gradient were decreased by about 50% and this experimental result suggests that the modification of pedestal profiles by SMBI is closely related to the ELM mitigation.

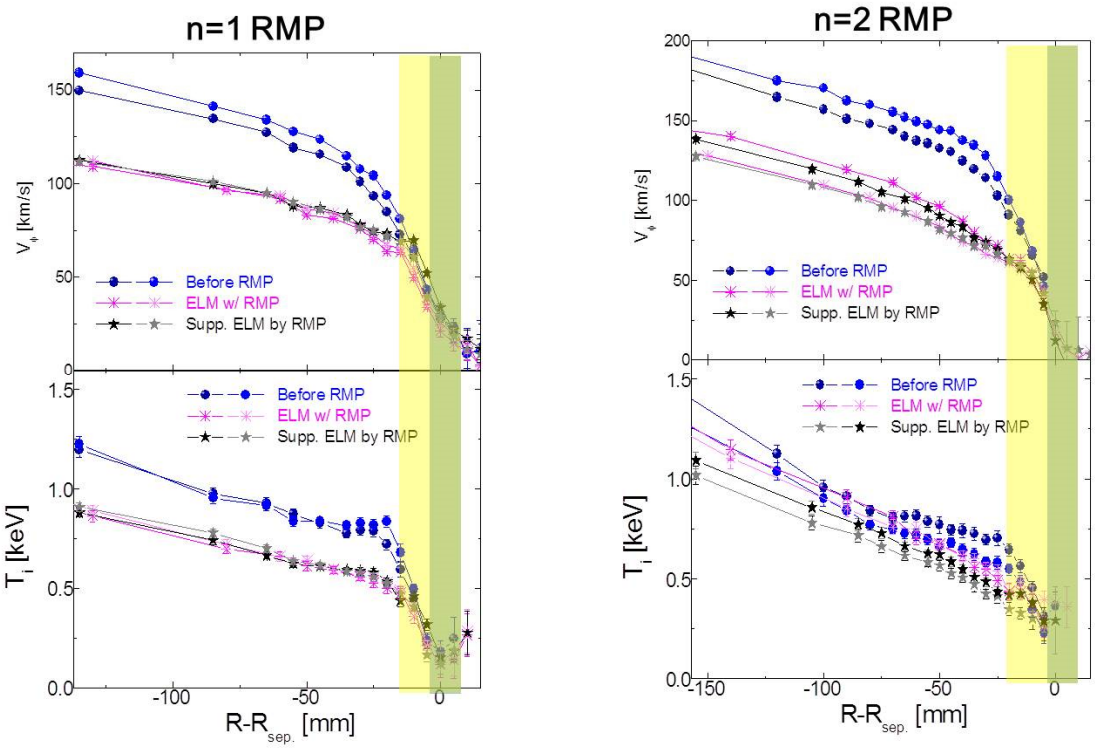

Figure 2. Effect of RMP on pedestal rotation & ion temperature profiles both for n=1 & n=2 RMP ELM suppression

Supersonic molecular beam injection at pedestal foot triggered L-H transition, i.e., stimulated transition rather than conventional transition below threshold power at low density branch and it is in good agreement with 1D radial predator-prey model which includes additional ExB shearing from increased density gradient driven by local SMBI particle source in pedestal foot.

The change of rotation profile by RMP is investigated and the comparison of the toroidal rotation profiles between during ELMy H-mode and during ELM suppression shows 30% decreasing in case of suppression as shown in fig 2. Figure 2 shows the temporal evolution of toroidal rotation and ion temperature profiles during the suppression period of a type-I ELMy H-mode. The whole toroidal rotation during ELMy H-mode before RMPs is higher than that

during the applied RMP and rotation damping rate in the pedestal region is the similar whether ELM is suppressed or not. The profile change of ion temperature is very similar to that of the toroidal rotation and both profiles clearly show the significant decrease in the pedestal region and also indicate the effective pedestal width is decreased more than factor of two. Toroidal rotation speed increased slightly when ELM starts to appear and it is recovered when RMP is removed during at the same stored energy. Qualitatively similar decrease of pedestal width has been also measured during n=2 RMP ELM suppression and for n=2 case, the toroidal rotation responds faster and more strongly when RMP is applied than T_i does in n=2 RMP case which is similar for conventional ELM burst.

The research on pedestal physics will be investigated in KSTAR focusing on ITER application. First of all, the developed techniques for ELM suppression/mitigation will be further validated in ITER relevant edge condition. It will include ITER similar shape, lower pedestal collisionality ($\nu_e^* \sim 0.1$)/T_e by higher P_{ext}. The mechanism of ELM suppression will be further investigated with detailed profile and fluctuation measurements including high resolution Thomson scattering system, 2D ECEI, MIR, Lithium Beam spectroscopy. In parallel, complex dynamical characteristics will be simulated with BOUT++ and M3D-C1. Beside the physics understanding, the long-pulse compatibility of recent finding on pedestal physics and ITER relevant edge operation scenario for ITER will be also tested including L-H transition during Ip ramp-up phase, removal of first ELM, power/particle exhausts in long-pulse H-mode, and benign H-L back transition.

Acknowledgement

This research was supported by Ministry of Science, ICT, and Future Planning under KSTAR project and was partly supported by the JSPS-NRF-NSFC A3 Foresight Program (NRF No. 2012K2A2A6000443).

Reference

[1] S.W. Yoon, J.-W. Ahn, Y. M. Jeon, T. Suzuki, S. H. Hahn, W.H. Ko, K. D. Lee, J.I. Chung, et al., Nucl. Fusion **51**, 113009 (2011)

[2] Y.M. Jeon, J.-K. Park, S.W. Yoon, W.H. Ko, S.G. Lee, et, al., Phys. Rev. Lett. 109, 035003 (2012)

[3] W.W. Xiao *et al*., *24th IAEA-FEC* (Oct. 8-12, 2012) San Diego, USA.

Estimation of Heat and Particle Transport by Means of Transient Phenomena

Tomohiro Morisaki and LHD Experiment Group
National Institute for Fusion Science

1. Background and introduction

Several years ago, the super dense core (SDC) mode with central electron density of more than ~ 1 x 10^{21} m^{-3} was discovered in LHD with the formation of an internal diffusion barrier (IDB) when a series of pellets was injected into the neutral beam (NB) heated plasma under the condition of low edge neutral pressure [1,2]. Recently, with the thorough wall conditioning in the outward shifted configuration, the SDC plasma with central electron density of ~ 2 x 10^{20} m^{-3} can successfully be sustained for more than 3 seconds. In such a high density regime, a large Shafranov shift takes place which strongly modifies the edge magnetic topology. Therefore it is interesting to investigate the transport properties in the modified edge region which surrounds the SDC plasma.

In tokamaks, for the ELM suppression or mitigation, the resonant magnetic perturbations (RMPs) are applied to modify the edge region where the ballooning or peeling/ballooning mode is sometimes unstable [3]. Although the modification of the magnetic topology may change the current profile or heat and particle transport in the edge region, clear physical explanations for the mechanism of the ELM suppression or mitigation have not yet been shown. In LHD, RMP is also applied to further modify the edge magnetic topology to investigate the effect of the stochastization on heat and particle transport in detail [4].

From the opposite viewpoint, it is possible to know the magnetic structure from the transport properties if they are well characterized according to the stochasticity or island structure. Thus it is crucially important to clarify the relationship between transport and magnetic topology.

In this study we focused on the edge particle transport during the SDC discharge in LHD, where the edge magnetic structure is strongly ergodized by the large Shafranov shift. The density pulse generated by the pellet injection was utilized for the transport analysis, measuring its propagation from the core to edge region.

2. Experimental results

The SDC mode can be obtained by the repetitive pellet injection and the strong NB heating. Figure 1 shows the time evolution of the stored energy measured with diamagnetic loop and electron density measured with Thomson scattering at different normalized radii of the typical SDC discharge. Eight pellets were injected to get the maximum central electron density of ~ 5 x 10^{20} m^{-3}. The maximum central electron density n_e and temperature T_e at t = 3.1 s in this typical SDC discharge are shown in Fig. 2. It is found that quite high electron density with steep gradient is maintained in the core region, while gradient in the edge

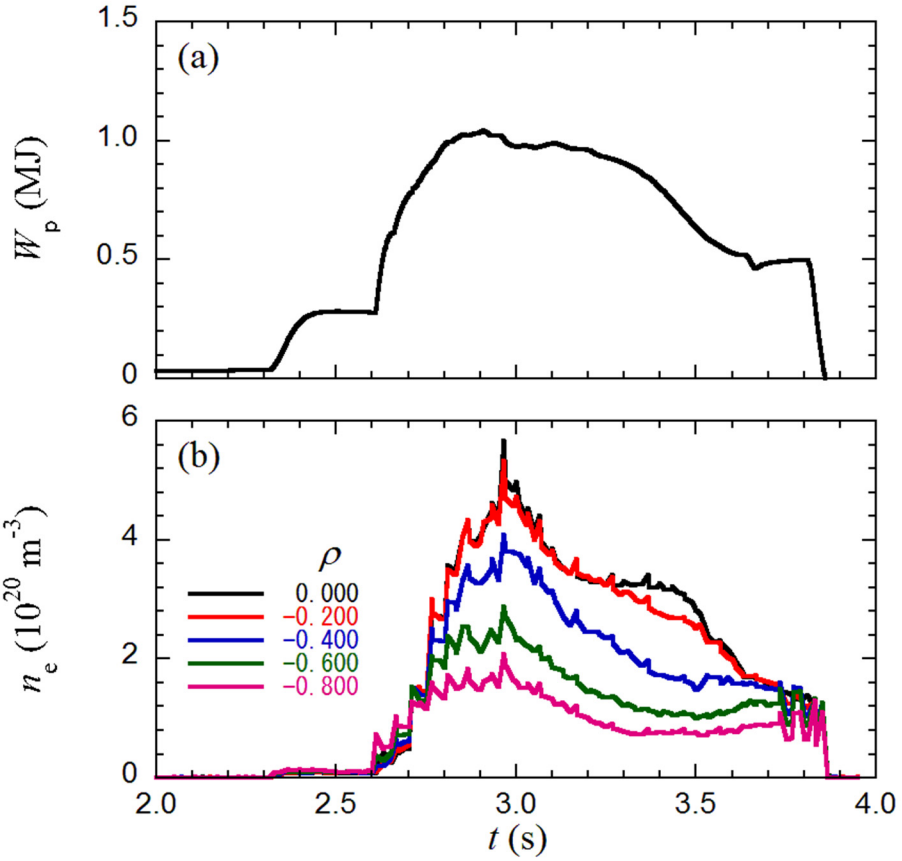

Fig. 1. Time evolution of (a) stored energy measured with diamagnetic loop and (b) electron density measured with Thomson scattering at different normalized radii.

region (mantle) is relatively low. This suggests the formation of the internal transport barrier for particles, namely, IDB. As for the temperature profile, it is almost flat inside the IDB, while it has a steep gradient in the mantle (outside the IDB), which is opposite to the density profile.

The RMPs are also applied to the SDC plasma to further modify the edge magnetic structure in LHD. Ten pairs of small normal conducting loop coils are installed on the top and bottom of the torus to apply the RMPs. With this system, m/n = 1/1 and/or 2/1 RMPs can be applied, where m and n are poloidal and toroidal mode numbers, respectively. It is interesting, in the case with RMP, that n_e in the mantle region is reduced, compared to that without RMP. This phenomenon is similar to the density pump-out observed in tokamak RMP experiments.

In order to see the relationship between the magnetic field structure and the transport properties, one-dimensional particle transport analyses were performed, together with numerical analyses of the magnetic field structure. For the one-dimensional particle transport analysis, time evolutions of electron

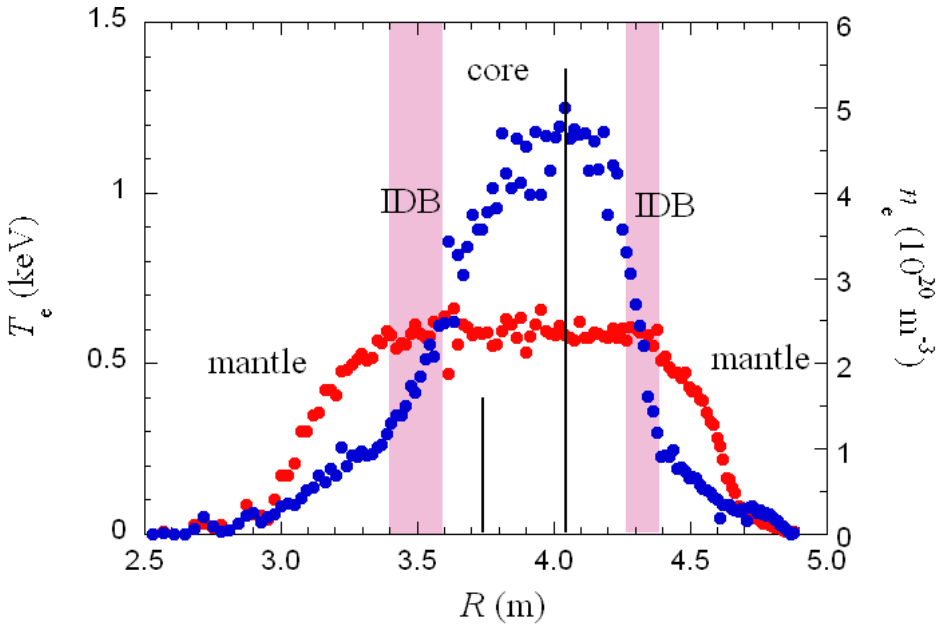

Fig. 2. Typical electron density and temperature profiles in SDC discharge. Original and Shafranov shifted magnetic axis positions are indicated with bars at R = 3.75 m and 4.04 m.

density at different radial positions are analyzed to provide diffusion coefficients and convective velocities at each radial position, according to the following equations,

$$\Gamma = \frac{1}{r}\int_0^r r\left(S - \frac{\partial n_e}{\partial t}\right)\mathrm{d}r \qquad (1)$$

$$\frac{\Gamma}{n_e} = -D\frac{1}{n_e}\frac{\partial n_e}{\partial r} + v. \qquad (2)$$

In Fig. 3, Γ normalized by n_e is plotted as a function of inversed density scale length ($\mathrm{d}n_e$ / $\mathrm{d}r$) / n_e, of which gradient indicates the particle diffusion coefficient D. It can clearly be seen that the diffusion coefficient in the mantle region is higher than that in the core region. Furthermore, D in the mantle region is increased by applying the RMP, while it increases little in the core region. On the other hand, the convection in both region is always small (nearly zero), as shown in Fig. 3, since y-intercepts of Γ/n_e vs. ($\mathrm{d}n_e/\mathrm{d}r$)/$n_e$ lines indicate the convective term of the particle transport, as is known in Eq. (2). These results suggest that modification of the magnetic topology in the mantle region enhances the particle transport, which finally results in the density pump-out effect.

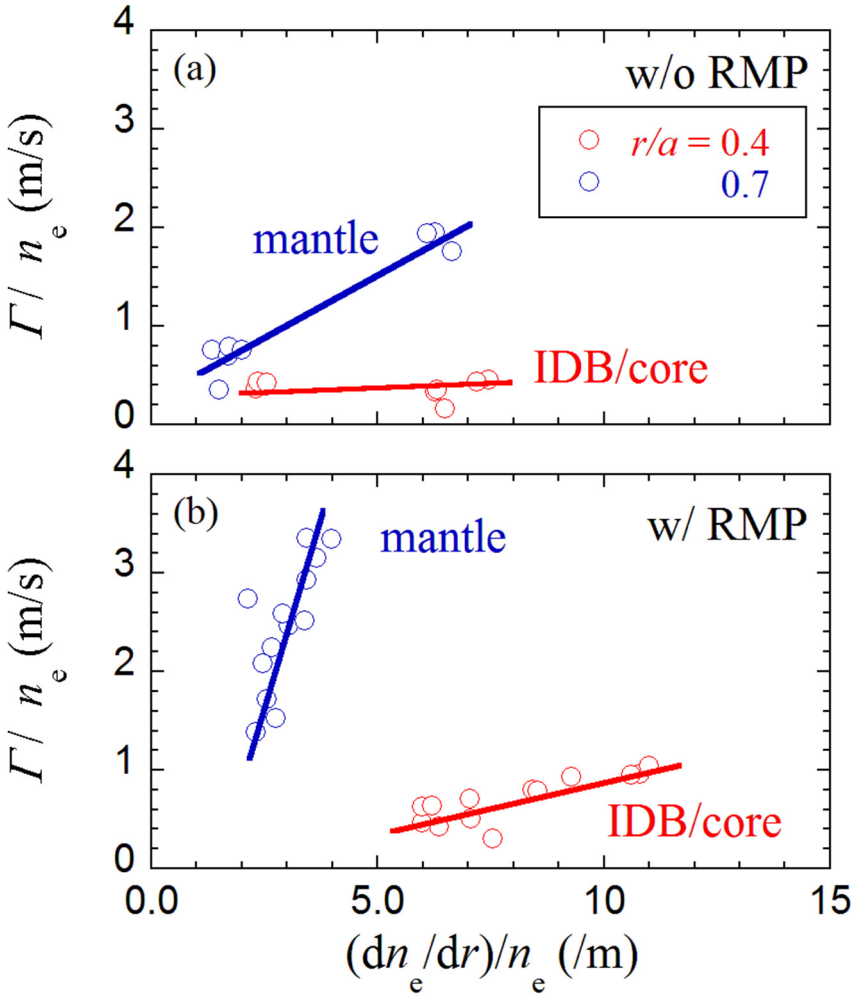

Fig. 3. Density normalized flux vs. density scale length. Gradient indicates diffusion coefficient.

3. Summary and future plan

From the preliminary results obtained in the LHD experiment, it was found that the modification of the magnetic topology affects the particle transport, which could be seen in the changes of diffusion coefficient D. In the mantle region, during the SDC discharge, where the magnetic structure is ergodized by the large Shafranov shift due to the high central pressure (beta value), D is larger than that in the core region. It was also observed that D is further increased by applying the RMP. These results agree well to those expected in the numerical study with the HINT2 code [5].

In this study, D and convection v were derived from the time evolution of the local electron density n_e, i.e. density pulse propagation. On the other hand, this technique can also be utilized as a diagnostic tool for the magnetic structure, e.g., nested surfaces, islands, or stochastic layers. The magnitude of the

modification (stochasticity) may also be measured if precise observation and analysis are available. In this experiment, density pulses were made by the pellet injection. Though it is an easy and reliable technique to introduce the particle source to the core region, disturbance in the plasma along the flight path is relatively large. Thus smaller perturbation in the measurement is required. Recently some new passive methods using MHD activities have been proposed. In the SDC discharge, the core density collapse (CDC) sometimes occurs in the core region, which generates a density pulse propagating from the core to edge region. Thus one can use the CDC pulse as a particle source in the core region. No disturbance is left, introducing the source to the core region. In addition, saw-tooth oscillations destabilized on the inner rational surfaces can also be a candidate for the heat and/or particle source propagating to both directions.

Acknowledgements

This work was partly supported by the JSPS-NRF-NSFC A3 Foresight Program in the field of Plasma Physics (NSFC: No.11261140328).

References

[1] N. Ohyabu, T. Morisaki, S. Masuzaki, et al., "Observation of Stable Superdense Core Plasmas in the Large Helical Device", Phys. Rev. Lett. **97** (2006) 055002.

[2] T. Morisaki, N. Ohyabu, S. Masuzaki, et al., "Superdense core mode in the Large Helical Device with an internal diffusion barrier", Phys. Plasmas **14** (2007) 056113.

[3] T. Evans, et al., "The physics of edge resonant magnetic perturbations in hot tokamak plasmas", Phys. Plasmas **13** (2006) 056121.

[4] M. Kobayasho, et al., "Transport characteristics in the stochastic magnetic boundary of LHD: Magnetic field topology and its impact on divertor physics and impurity transport", Fusion Sci. Technol. **58** (2010) 220.

[5] Y. Suzuki, K. Ida, K. Kamiya et al., "3D plasma response to magnetic field structure in the Large Helical Device", Nuclear Fusion, **53** (2013) 073045-1.

Investigation of divertor particle flux from electric probe measurements during ELMy H-modes in KSTAR

Jun-Gyo Bak[1], Heung-Su Kim[1], Min-Keun Bae[2], Jun-Woo Juhn[1], Dong-Cheol Seo[1], Eun-Nam Bang[1], Kyu-Sun Chung[2] and Suk-Ho Hong[1]

[1]National Fusion Research Institute, Daejeon, Korea
[2]Han Yang University, Seoul, Korea

Email : jgbak@nfri.re.kr

The characteristics of the divertor particle fluxes are investigated from the edge Langmuir probe assembly (ELPA) measurements at the lower divertor region in the lower single null (LSN) configuration during ELMy H-mode discharges in Korea Superconducting Tokamak Advanced Research (KSTAR). Firstly, it is found that the peak amplitude of the divertor particle flux near the strike point during an ELM burst, $\Gamma_{div}{}^{peak}$ decreases by about 20 % as the ELM frequency f_{ELM} increases by a factor of ~ 3 when the plasma elongation becomes higher. In addition, similar trends of the peak amplitude during an ELM phase are observed when the ELMs are mitigated by using several methods as resonant magnetic perturbation (RMP), supersonic molecular beam injection (SMBI) and electron cyclotron heating (ECH): $\Gamma_{div}{}^{peak}$ decreases by about 30 - 50 % as f_{ELM} increases by a factor of 1.4 - 6.8. Secondly, profile of the divertor particle flux, which is mapped to the outboard mid-plane (OMP), is comparable to the upstream scrape-off layer (SOL) profile of the particle flux obtained from a fast reciprocating Langmuir probe assembly (FRLPA) measurement at the OMP. Thirdly, the characteristic e-folding length of the divertor particle flux during an ELM phase is about two times larger than ones at inter-ELM phases, and larger e-folding lengths (λ_{Te} and λ_{ne}) during the ELM phase are also observed from the upstream SOL profile measurements.

1. Introduction

The edge localized modes (ELMs) in H-mode discharges increase the scrape-off layer (SOL) plasma and produce burst-like particle fluxes on the divertor targets which are about ten times larger than the stationary particle flux between ELMs [1]. The large transient divertor heat pulses due to ELMs (especially, type-1 giant ELMs) would impact potentially on the divertor design of the next-step high power tokamak such as ITER because the power load on the divertor target was required to be less than 10 MW m^{-2} [2] due to the thermal engineering limitation in the material as a critical design parameter in the ITER. Up to now, the activities on the ELM control were carried out for reducing the divertor heat flux due to the ELM in several tokamaks such as experiments for investigating effect of plasma shaping on the ELM behavior [1,3] and for ELM mitigations by using methods as resonant magnetic perturbation (RMP) [1,4], supersonic molecular beam injection (SMBI) [5] and electron cyclotron heating (ECH) [1,6]. The experimental investigations of the ELM effect on the profile of the divertor particle flux and the SOL profiles were also carried out to understand the edge particle transport during ELMs in tokamaks [1,7].

Figure 1 shows electric probe diagnostics (EPDs) [8] for the SOL and divertor study in the Korea Superconducting Tokamak Advanced Research (KSTAR). The EPDs consists of a fixed edge Langmuir probe array (ELPA) with 24 single probes at the lower divertor region (called as divertor LPA), another ELPA with 8 probes for triple and Mach probe configurations newly installed at the poloidal limiter (called as limiter LPA) and a fast reciprocating Langmuir probe assembly (FRLPA) at the outboard mid-plane (OMP). Up to now, the divertor particle fluxes were evaluated from the divertor LP measurements for study on the diverter plasmas in the KSTAR tokamak, and the radial profiles of T_e and n_e were measured by using the FRLPA with a maximum speed of 1.5 m/s in the SOL region in order to study the characteristics of the SOL in the KSTAR tokamak. The limiter LPA was used to measure plasma parameters at far SOL region for benchmarking the SOL profile from the FRLPA measurements. After the H-mode plasmas were routinely produced in the KSTAR tokamak, the investigations of divertor heat flux are needed to evaluate the power load on the divertor target in ELMy H-mode discharges because the heating power have been gradually increased for high plasma performance in the KSTAR tokamak. Thus, the initial investigation of the divertor particle flux and the SOL width from the divertor LP and FRLPA measurements in ELMy H-mode plasmas were carried out, and particle and heat fluxes at the far SOL were evaluated from the limiter LP measurements. In this work, the preliminary results of the experimental investigation of divertor particle

flux from the electric probe measurements in ELMy H-mode discharges are presented.

2. Divertor particle flux during ELMs

The particle flux was evaluated by using the relation of $\Gamma_{div} = I_{is}/(eS) \sin\alpha$ from ion saturation current I_{is} measured with the divertor LPA at the outer divertor region in ELMy H-mode discharges under the lower single null (LSN) configuration. Where α ($\alpha = 5°$) is the angle between the magnetic field and the divertor target surface, and S is an effective area of each divertor probe. The characteristics of the divertor particle flux near an outer strike point during ELMs were investigated as following; the peak amplitudes of the divertor particle flux versus the ELM frequencies due to the effect of plasma shaping on the natural ELMs and due to the ELM mitigations by the RMP, the SMBI and the ECH.

The ELM amplitude decreases as the ELM frequency $f_{ELM} = 1/\Delta T_{ELM}$ increases as shown in Fig. 2(a). ΔT_{ELM} denotes the time between two adjacent ELMs. The plasma elongation κ, as one of plasma shaping parameters, is increased from 1.81 to 1.92 in the time range of 2.0 - 3.0 s (I_p = 0.63 MA, B_T = 2.0 T), and the safety factor q_{95} also becomes higher as from 4.96 to 5.76. The stored energy W_{TOT} is nearly constant while f_{ELM} is increased. It is found that f_{ELM} increases from ~ 33 Hz up to ~ 100 Hz and the peaked value of divertor particle flux near a outer strike point during ELMs Γ_{div}^{peak} decreases from ~ 0.5×10^{23} $m^{-2}s^{-1}$ to ~ 0.1×10^{23} $m^{-2}s^{-1}$ as shown in Fig. 2(b). The energy drop due to the ELM normalized to the stored energy $\Delta W_{ELM} / W_{TOT}$ decreases from 3.8 % to 1.3 %. The behavior is similar to the experimental result reported in the DIII-D [3].

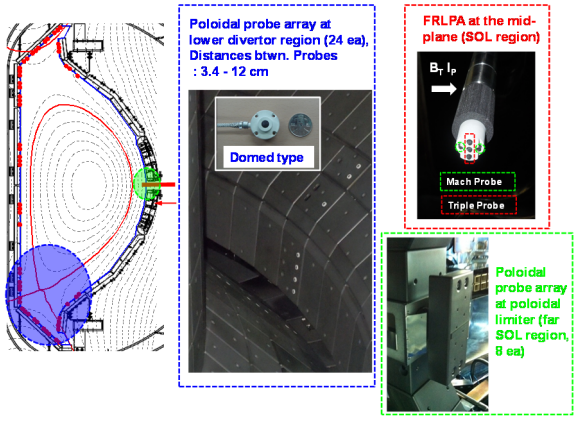

Fig.1. Electric probe diagnostics in KSTAR.

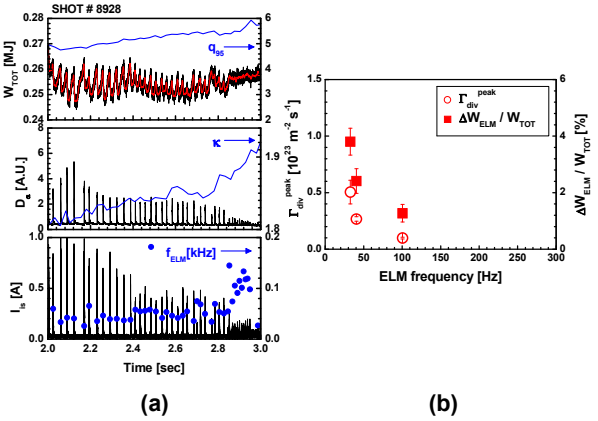

Fig. 2. (a) Time evolutions of stored energy with q_{95}, D_α signal with plasma elongation and ion saturation current with ELM frequency, and (b) peaked value of divertor particle flux near an outer strike point and stored energy drop vs. ELM frequency during ELMs.

The ELM size is reduced as f_{ELM} rises when the ELM is mitigated by the RMP as shown in Fig. 3(a). The RMP (n = 2 field) with a two-step waveform is applied to the plasma edge region in the time range of 2.0 - 6.0 s (I_p = 0.68 MA, B_T = 1.8 T). The ELM mitigation is more effective for higher RMP field. The stored energy decreases from ~ 0.35 MJ to ~ 0.25 MJ and the density pump-out (from 6×10^{19} m^{-3} to 4.4×10^{19} m^{-3}) during an RMP. f_{ELM} increases from ~ 20 Hz up to ~ 135 Hz and Γ_{div}^{peak} decreases from 1.2×10^{23} m^{-2} s^{-1} to 0.55×10^{23} m^{-2} s^{-1} when the RMP is 'ON' as shown in Fig. 3(b). $\Delta W_{ELM} / W_{TOT}$ decreases from 4.1 % to 1.1 %.

The magnitudes of ELM peaks decrease as f_{ELM} becomes faster in ELM mitigations due to the SMBI as shown in Fig. 4(a). Three SMBIs (time duration: ~ 8 ms, ~ 2ms, ~ 3ms) are done for the ELM mitigations in the time range of 3.0 - 3.5 s (I_p = 0.52 MA, B_T = 2.0 T). The stored energy decreases from ~ 0.20 MJ to ~ 0.185 MJ. f_{ELM} rises from ~ 53 Hz up to ~ 240 Hz and Γ_{div}^{peak} decreases from 0.92×10^{23} m^{-2} s^{-1} to 0.47×10^{23} m^{-2} s^{-1} when the SMBI is 'ON' as shown in Fig. 4(b).

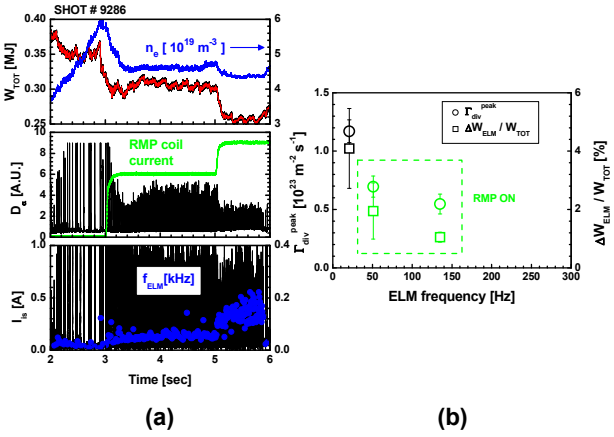

Fig. 3. (a) Time evolutions of stored energy with density, D_α signal with RMP coil current and ion saturation current with ELM frequency, and (b) peaked value of divertor particle flux near an outer strike point and stored energy drop vs. ELM frequency during ELMs for the RMP 'OFF' and 'ON'.

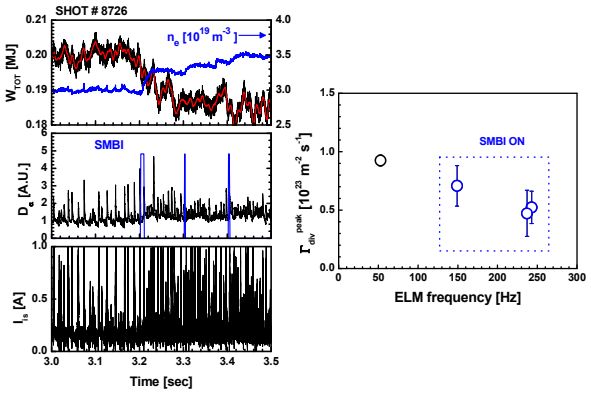

Fig. 4. (a) Time evolutions of stored energy, D_α signal with SMBI pulse and ion saturation current, and (b) peaked value of divertor particle flux near an outer strike point and stored energy drop vs. ELM frequency during ELMs for the SMBI 'OFF' and 'ON'.

The ELM amplitude decrease as f_{ELM} becomes higher in ELM mitigations by the application of the ECH (@ 170 GHz, P_{ECH} = ~ 0.8 MW) as shown in Fig. 5(a). The ECH power was deposited in the plasma edge. The stored energy is nearly constant, and edge temperature rises from ~1.2 keV to ~1.5 keV after the ECH (I_p = ~ 0.5 MA, B_T = 2.3 T). f_{ELM} increases from ~ 57 Hz up to ~ 77 Hz and Γ_{div}^{peak} decreases from 0.81 × 10^{23} m^{-2} s^{-1} to 0.30 × 10^{23} m^{-2} s^{-1} when the ECH is 'ON' as shown in Fig. 5(b). The ELM mitigation was also observed when the ECRH beam was moved towards the plasma separatrix in the TCV [6].

From comparison between particle fluxes at divertor and far SOL regions, it is found that the peaked value at the far SOL Γ_{OMP}^{peak} is less than 0.3 % of Γ_{div}^{peak} as shown in Fig. 6. Thus, it can be estimated that the particle flux toward to the main chamber is less than 1 % of divertor particle flux during ELMs under some experimental conditions. In addition, the peaked value of the heat flux from the limiter LPA measurement q_{OMP}^{peak} decreases from ~ 3.0 kW/m^2 to ~1.0 kW/m^2 in the ELM mitigation due to the RMP.

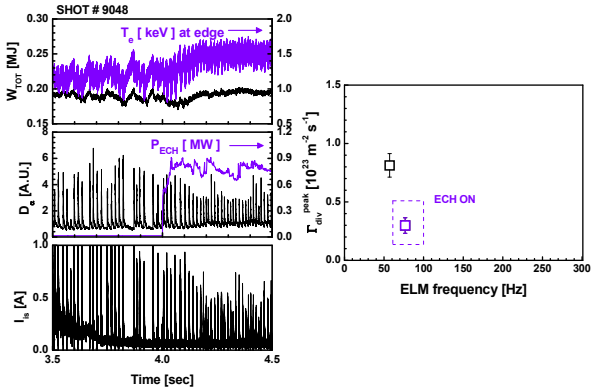

Fig. 5. (a) Time evolutions of stored energy with ECE signal at edge, D_α signal with ECH power and ion saturation current, and (b) peaked value of divertor particle flux near an outer strike point and stored energy drop vs. ELM frequency during ELMs for the ECH 'OFF' and 'ON'.

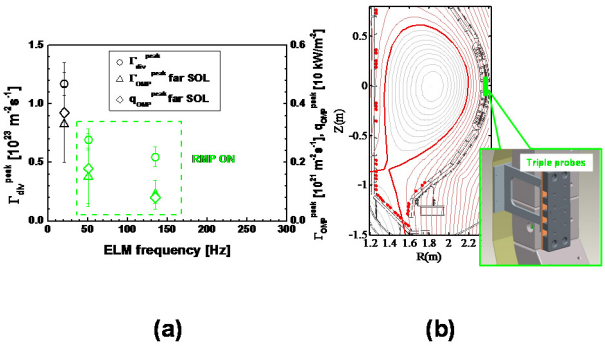

Fig. 6. (a) Peaked value of particle fluxes near an outer strike point in the outer divertor, peaked value of particle and heat fluxes in far SOL vs. ELM frequency during ELMs for the RMP 'OFF' and 'ON', and (b) the EFIT reconstruction for the LSN divertor configuration with limiter LPA for measuring far SOL plasmas for shot # 9286.

3. Profile of divertor particle flux and SOL profiles in ELMy H-mode plasma

The profile of particle flux Γ_{div} from the divertor LPA measurements had low spatial resolution because of large radial distance between two adjacent divertor probes (up to 8.0 cm). Thus, it was noted that the e-folding length $\lambda_{\Gamma div}$ was able to be evaluated from the profile in some LSN configurations during ELMy H-modes although it was difficult to know the exact peak flux and to evaluate the spreading factor of the particle flux in the private region in this work.

Figure 7 shows particle flux profile in the SOL region at the OMP during an ELMy H-mode discharge (2.42 - 2.62 s) for the LSN divertor configuration ($dr_{sep} \approx$ - 5 mm). The divertor particle fluxes from the divertor LPA measurements in the time range of 2.52 - 2.525s are used for the profile because the EFIT reconstruction, as shown in Fig. 7, is sustained for the time range of 2.42 - 2.62 s. The profile of divertor particle flux mapped to the OMP (magnetic flux expansion of ~ 1.9) is comparable to the upstream SOL profile of the particle flux from FRLPA measurement. The parameters in the time range of 2.42 - 2.62 s were $B_T \approx 2.3$ T, $I_p \approx 0.5$ MA, $P_{NB} = 2.67$ MW, $n_e \approx 2.4 \times 10^{19}$ m^{-3}, $\kappa = 1.8$ - 1.9 and $q_{95} \approx 7.3$. The particle flux measured by limiter LPA at far SOL region agrees with the value at the poloidal limiter location in the profile measured with the FRLPA.

For the comparison between the profiles of the divertor particle flux for inter and during ELM phases in an ELMy H-mode discharge ($dr_{sep} \approx$ -0.06 m, $\kappa \approx 1.89$, $I_p = 0.5$ MA, $B_T = 2.3$ T, $q_{95} = 7.3$, $n_e = \sim 2.4 \times 10^{19}$ m^{-3} and $P_{NBI} = \sim 2.67$ MW), a relatively-isolated ELM peak was selected. Here, 1 ms and 0.5 ms time-averaged values were used to get the profiles for inter and during ELM phases, respectively. The value of $\Delta W_{ELM} / W_{TOT}$ was about 6% and f_{ELM} was about 44 Hz, which might indicate the type-I ELM. The maximum particle flux during the ELM is five times (two and a half times) larger than one before (after) the ELM, but the characteristic e-folding length $\lambda_{\Gamma div}$ at the ELM phase is about two times of ones in the inter-ELM phases as shown in Fig. 8(a). The longer e-folding length during the ELM was similar to the experimental result reported in the EAST [7]. In addition, the SOL profiles of T_e and n_e with several spikes due to ELM bursts are obtained from the FRLPA measurement in the ELMy H-mode discharge ($\kappa \approx 1.8$, $I_p = 0.5$ MA, $B_T = 2.0$ T, $q_{95} = 3.4$, $n_e = \sim 2.7 \times 10^{19}$ m^{-3} and $P_{NBI} = 1.35$ MW) as shown in Fig. 8(b). The value of f_{ELM} was about 200 Hz, which might correspond to the type-III ELM. The radial profile from the FRLPA measurement was able to be obtained up to 20 mm outside the last closed flux surface (LCFS) during H-mode discharges. The e-folding lengths during ELMs and inter-ELMs were evaluated from the radial profiles obtained by selecting one data point near each ELM peak and by using 100 data points before each ELM, respectively. Here, 100 data points corresponded to a time difference of 1 ms because the sampling rate in the digitizer for electric probe diagnostic system was 100 kHz. It is found that the e-folding lengths during ELMs ($\lambda_{Te} = 29.9$ mm, $\lambda_{ne} = 15.1$ mm) are broader than ones in the inter-ELM phases ($\lambda_{Te} = 23.0$ mm, $\lambda_{ne} = 10.0$ mm), which is similar to the result reported in JET [1].

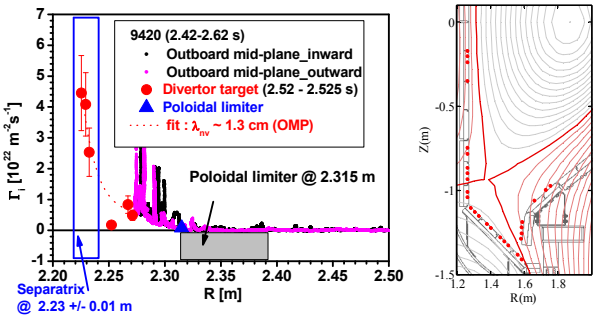

Fig. 7. Radial profile of particle flux at the outboard mid-plane (OMP) and plasma shape from the EFIT reconstruction in an ELMy H-mode discharge. Here, e-folding length $(\lambda_\Gamma)_{mp}$ is obtained from the divertor flux that is mapped to the OMP.

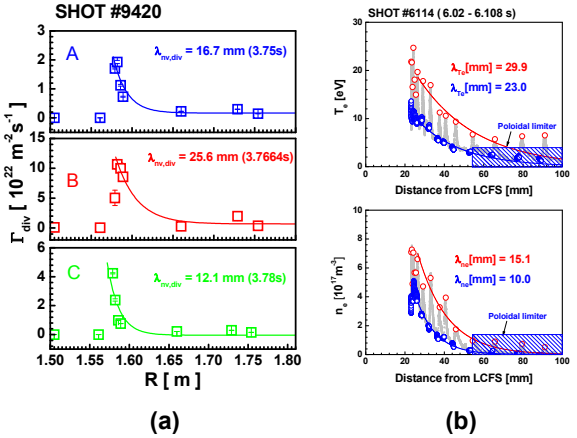

Fig. 8. (a) Divertor particle profiles during and inter ELM and (b) SOL profiles of T_e and n_e in ELMy H-mode plasma.

4. Summary

From the experimental investigation of the divertor particle flux for ELMy H-mode plasmas in the KSTAR tokamak, it was found that the peak amplitude of the divertor particle flux near the outer strike point during an ELM burst decreased by about 20 % as the ELM frequency rose by a factor of ~ 3 when the plasma elongation κ, a factor of the plasma shaping, increased from 1.81 to 1.92. Similar trends of the peak amplitude during an ELM phase are also observed in the ELM mitigations due to RMP, SMBI and ECH as following: the peak amplitude decreased by about 30 - 50 % as the ELM frequency increased by a factor of 1.4 - 6.8. The trend was more clearly shown in the ELM mitigation due to RMP, comparing with the cases of the SMBI and ECH. In addition, it could be estimated that particle flux towards the main chamber was two orders of magnitude smaller than the divertor particle flux under some experimental conditions.

From the experimental investigation of the profile of divertor particle and the upstream SOL profiles, the profile of the divertor particle flux mapped to the OMP was comparable to the upstream SOL profile of particle flux. It was found that the characteristic e-folding length from the profile of divertor particle flux during an ELM was about two times broader than ones in the pre and post ELMs although the spatial resolution of the divertor LPA was not enough to detect an exact peak value in the divertor flux profile. The characteristic e-folding lengths (λ_{Te} and λ_{ne}) during ELMs from the upstream SOL profiles were also longer than ones in the inter-ELM phases.

Further study on the divertor particle flux and the SOL profiles during ELMy H-mode plasmas will be carried out for extended operation conditions to investigate the characteristics of the ELM dynamics (such as the amplitude of divertor particle flux vs. the ELM frequency) more clearly. Eventually, the investigation of the heat flux will be required to estimate how much transient power will be loaded on the divertor target during ELM burst and to understand how the power load will be able to be reduced by using methods for the ELM mitigation. To do this work, the preliminary divertor heat flux will be able to be obtained from the initial divertor infra-red camera measurements and the heat flux near outer strike point will be also evaluated by using T_e obtained from the triple probe configuration in the divertor LPA with more probes in the experimental campaign of 2014.

Acknowledgements

This research was supported by Ministry of Science, ICT, and Future Planning under KSTAR project contract, and was partly supported by the JSPS-NRF-NSFC A3 Foresight Program in the field of Plasma Physics (NSFC: No. 11261140328, NRF: No. 2012K2A2A6000443).

References

[1] D.N. Hill, *Journal of Nuclear Materials*, **241-243** (1997) 182
[2] J. Linke, *Transaction of Fusion. Science and Technology,* **49** (2006) 455
[3] T. Ozeki, et al., *Nuclear Fusion,* **30** (1990) 1425
[4] Y. Liang, et al., *Plasma & Fusion Research,* **5**(2010) S2018
[5] J. Cheng, et al., *Journal of Nuclear Materials*, **438** (2013) S1200
[6] J.X. Rossel, et al., *Nuclear Fusion,* **52** (2012) 032004
[7] L. Wang, et al., *Nuclear Fusion,* **52** (2012) 063024
[8] J.G. Bak, et al., *Contributions to Plasma Physics,* **53** (2013) 69

Feasibility study of advanced operation scenario in KSTAR using CRONOS

H.-S. Kim[1], Y.S. Bae[2], S.H. Kim[3], Y.M. Jeon[2], J.-F. Artaud[4], and Y-S. Na[1*]

[1]Department of Nuclear Engineering, Seoul National University, Seoul, Korea
[2]National Fusion Research Institute, Daejeon, Korea
[3]ITER Organization, France,
[4]Isntitut de Recherche sur la Fusion Magnetique, EURATOM-CEA, France

*Email: ysna@snu.ac.kr

We report the results of predictive modelling of advanced operation scenarios in KSTAR. Firstly, the operation windows are produced to explore the KSTAR advanced scenarios in the condition of upgrading H/CD mix. Using METIS code, the rough ranges of operation condition of I_P and B_T to utilize for the development of advanced operation scenario are determined. Secondly, the advanced inductive and the advanced tokamak operation scenario of KSTAR are developing with the scaling based and the physics based transport model by using CRONOS to make a suggestion to on-going KSTAR experiment. Thirdly, the dependency of the time of L-H transition on q_0 and q_{min} is investigated for the advanced inductive operation scenario. These reliable results can become the useful database for exploring the advanced regime of KSTAR discharges in the future.

1. Introduction

KSTAR mission has a final goal which is an achievement of steady state operation using active profile controls. In addition, another important mission is to support ITER relevant urgent issues such as ELM mitigation, disruption control, and divertor heat loads reduced. During the next five years, KSTAR would be focus on ITER-relevant advanced operation with highly concentrated and optimized our resources. It can be characterized to the regime of long pulse ($> 10\tau_R$) and high performance (β_N~3.0) [1,2]. In order to meet them of KSTAR tokamak, we have to prepare the reliable database before the experiment is conducted. We have studied a feasibility of achieving the advanced operation scenario on the basis of heating and current drive (H/CD) upgrade plan associated with KSTAR H/CD mix by using CRONOS suites [3] as a 1.5-D integrated tokamak plasma transport simulator. Our work is essential to propose a practical guide to achieve the advanced operation.

The predictive modelling has been done to develop the advanced operation of KSTAR in the previous works [2,4]. To improve those results, we consider more practical heating and current drive (H/CD) system. Based on the recent H/CD upgrading plan in KSTAR H/CD systems in next few years, we decide to handle two actuators, NBI H/CD and ECH/CD, to depict the KSTAR operation scenario. The details of available external H/CD based on the H/CD upgrade plan are as follows. We consider three beam lines and 6 MW of delivered beam power in total so that each beam line produces up to 2 MW with 100 keV. We simulate two combinations of NBI H/CD system. One is the combination describing all of beam lines aligned to the on-axis, and the other is the combination describing part of beam lines aligned to the off-axis (two beam lines in off-axis and one beam in on-axis). We also considered 2.4 MW 105 GHz ECH/CD with two radial depositions of on-axis and off-axis.

As mentioned before, we calculate KSTAR operation scenarios simulated by using the CRONOS suites. The CRONOS includes the SINBAD (PENCIL modeling) module and/or NEMO/SPOT (Monte-Carlo modeling) module for NBI H/CD and REMA module for ECH/CD.

2. Operation window for advanced operation in KSTAR

Here, we use the METIS code to produce the operation window for the reference inductive operation and the advanced inductive operation in KSTAR. The METIS code is a fast integrated tokamak simulator tool and it can simulate tokamak plasma evolution using information coming from scaling laws coupled with simplified source models. According to tentative H/CD upgrade plan of phase II operation in KSTAR, we set the condition of H/CD and expect to use P_{NB}=6.0 MW and P_{EC}=2.4 MW. We assume δ=0.7, $\bar{n}_e$=0.3n_{GW}, and $\rho_{\varphi,ped}$=0.95 as control variables in the simulation. As I_P and B_T are changed, q_{95}, f_{NI}, and β_N are produced. Figure 1 (a) presents the distribution of them. Here, we determine the operation window for

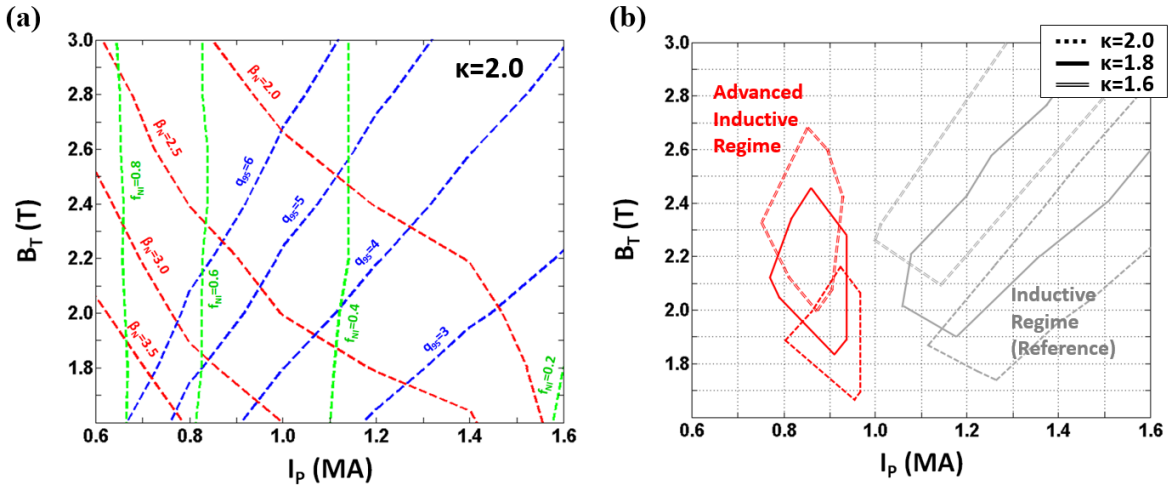

Figure 1 q_{95}, f_{NI}, and β_N against the changes of I_P and B_T (a) and the operation window for reference inductive regime and advanced inductive regime (b).

the advanced inductive operation in KSTAR to the condition of q_{95}=3.9-5.5, f_{NI}=0.5-0.65, and β_N=2.5~3.0. The range of q_{95} is determined for the ITER relevant experiment. Finally, we can deduce the specific operation window of the advanced inductive regime of KSTAR. It is presented in Fig. 1 (b). As a result, we expect that the advanced inductive operation in KSTAR is achieved in the range of I_P=~0.7 MA-1.0 MA and B_T=~1.6 T-2.7 T.

3. KSTAR operation scenarios: reference inductive, advanced inductive, and advanced tokamak

We adopt two approaches to describe the anomalous heat transport in the CRONOS simulation. One is the Scaling Based Model (SBM) like KIAUTO [5] and the other is the Physics Based Model (PBM) like GLF23 [6], CDBM, Weiland, MMM95, etc. When we use SBM, the confinement enhancement factor would be a constraint. That is, if we assume the target H-factor in the simulation, the plasma is controlled by the proportional modification of heat conductivity. It is a kind of inductive approach. Therefore, it is useful to measure the plasma performance/state against the assumed confinement. On the other hand, when we use PBM, the anomalous heat conductivity is determined by the physics based on the micro instabilities like Ion Temperature Gradient (ITG), Trapped Electron Mode (TEM), Electron Temperature Gradient (ETG), Resistive Ballooning Mode (RBM), etc. It is a kind of deductive approach. Here, we use KIAUTO and GLF23 for SBM and PBM, respectively, to develop the KSTAR operation scenarios.

3.1. Reference inductive and advanced inductive scenarios with scaling based model

In our work, based on the operation window as shown in Fig. 1 (b), we are producing three types of the operation scenario of KSTAR using the CRONOS code. One is the reference inductive operation scenario. It is the normal H-mode discharge. It can be characterized to B_T~1.88 T, I_P=1.2 MA, β_N=2.0~2.5, q_{95}~3, $H_{98(y,2)}$~1.0. The on-axis H/CD are used to produce the normal H-mode operation as the reference operation scenario. The other is the advanced inductive operation scenario so called the hybrid operation scenario. It is the longer discharge than the reference inductive operation scenario. It can be characterized to B_T~1.88 T, I_P=1.0 MA, β_N=2.5~3.0, q_{95}~4, $H_{98(y,2)}$~1.1-1.3, f_{NI}>0.8. The last is the advanced tokamak operation scenario which is the fully non-inductive steady state operation. It can be characterized B_T~1.88 T, I_P=0.8 MA, β_N>3.0, q_{95}~5, $H_{98(y,2)}$>1.3, f_{NI}>1.0. The off-axis H/CD are used to produce the advanced inductive and the steady state operation scenarios. Table 1 describes the operation condition and the target plasma performance and confinement of KSTAR operation scenarios.

Firstly we devote to develop the reference inductive and advanced inductive operation scenarios with SBM. The detailed schemes of H/CD are as follows. We inject the 6 MW of NBI with on-axis configuration

Table 1 The operation condition and the target plasma performance and confinement for KSTAR operation scenarios.

	B_T (T)	I_P (MA)	q_{95}	$H_{98(y,2)}$	β_N	f_{NI}	P_{NB} (MW)	P_{EC} (MW)
Reference Inductive operation	1.88	1.2	~3.0	~1.0	2.0-2.5		6 (on-axis)	2.4
Advanced Inductive operation	1.88	1.0	~4.0	~1.1-1.3	2.5-3.0	> 0.8	2 (on-axis) 4 (off-axis)	2.4 (off-axis)
Advanced Tokamak operation	1.88	0.8	~5.0	> 1.3	> 3.0	> 1.0	2 (on-axis) 4 (off-axis)	2.4 (off-axis)

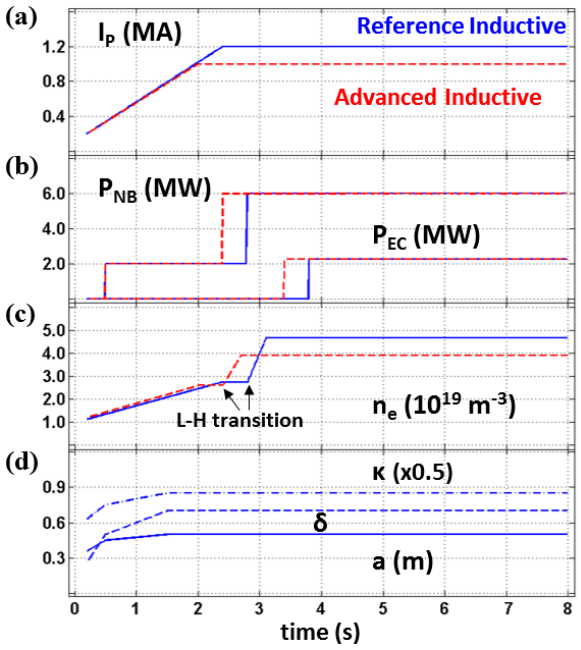

Figure 2 The time traces of plasma operation parameters like I_P, P_{NB}, P_{EC}, n_e, a, κ, and δ of the reference inductive (blue) and the advanced inductive (red) scenarios for KSTAR.

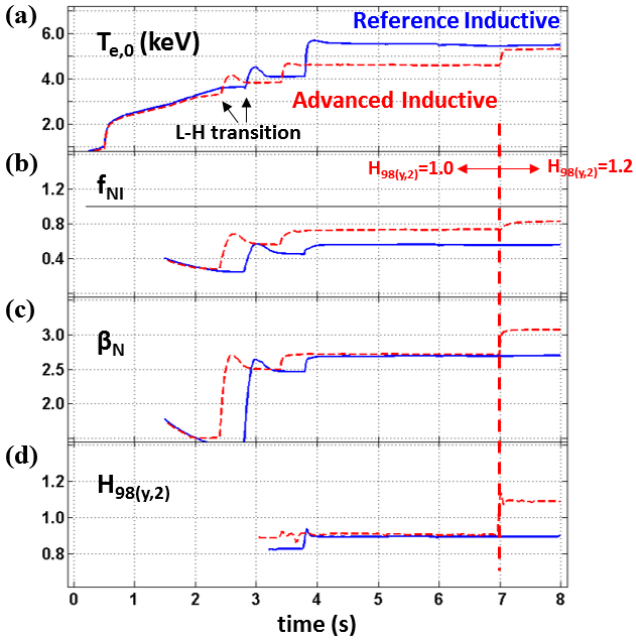

Figure 3 The time traces of parameters describing the plasma performance and the confinement like $T_{e,0}$, f_{NI}, β_N, and $H_{98(y,2)}$ of the reference inductive (blue) and the advanced inductive (red) scenarios for KSTAR.

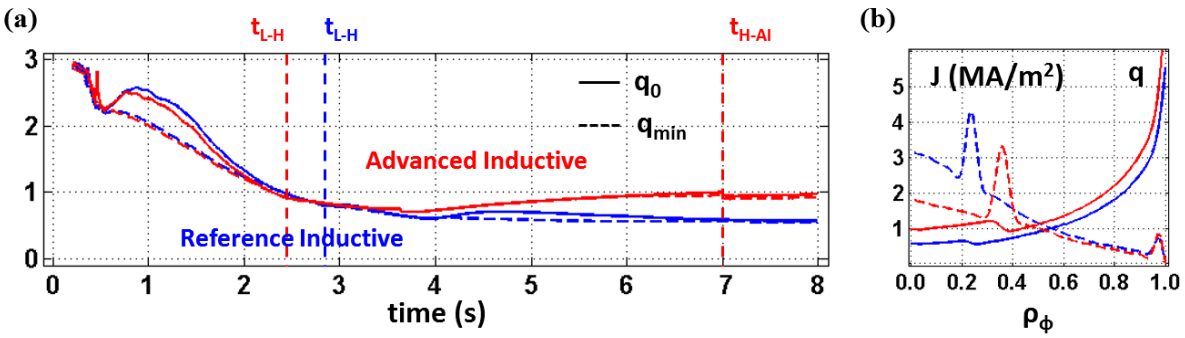

Figure 4 The time traces of q_0 and q_{min} (a) and the profiles of q and current density at 7.0 s (b) in the reference inductive (blue) and the advanced inductive (red) scenarios for KSTAR.

and 2.4 MW 105 GHz X2 ECCD with slightly off-axis configuration ((φ, θ)=(+10°,+10°)) for producing the reference inductive operation scenario. On the other hand, for the advanced inductive operation scenario, we inject 2 MW of NBI with on-axis and 4 MW of NBI with off-axis and 2.4 MW 105 GHz X2 ECCD with further off-axis configuration ((φ, θ)=(+10°,+27°)).

The time traces of plasma operation parameters like I_P, P_{NB}, P_{EC}, n_e, a, κ, and δ for both those scenarios are described in Fig. 2. For both operation scenarios, we set the same schemes of B_T, I_P ramp-up rate (dI_P/dt=0.5 MA), the Greenwald density fraction (f_{GW}=0.3) in H-mode phase, and the plasma shape. We set the beam is injected to the plasma after 0.4 s from the time which I_P plat-top phase is reached and the ECCD is injected after 1.0 s from the time which the NBI is injected. Also we set the L-H transition is occurred with the full injection of NBI. So, L-H transition of each operation scenario is occurred at 2.8 s and 2.4 s, respectively. Note that $\bar{n}_e$ is different between two scenarios in H-mode phase and it is lower in the advanced inductive scenario due to lower I_P.

As mentioned above, we adopt SBM to describe the anomalous heat transport. In the reference inductive operation scenario, SBM is applied in all phase (L- and H-mode) with the assumption of $H_{98(y,2)}$=1.0. In the advanced inductive operation scenario, SBM is also applied in all phase (L- , H-, and AI-mode), so that $H_{98(y,2)}$=1.0 is assumed in L- and H-mode. But $H_{98(y,2)}$=1.2 is assumed in AI-mode to reflect the confinement enhancement. In the scenario, we consider that the plasma is entered to AI-mode from 7.0 s, so that the H-factor constraint is changed from $H_{98(y,2)}$=1.0 to $H_{98(y,2)}$=1.2 as shown in Fig. 3 (d). We can confirm clearly that β_N and f_{NI} increase against the H-factor constraint.

At 8.0, β_N=2.7, f_{NI}=0.55, $H_{98(y,2)}$=0.90, l_i=0.86 (internal inductance) and V_{loop}=114 mV (loop voltage) are achieved in the reference inductive scenario. Compared with reference inductive scenario, β_N (=3.07), f_{NI} (=0.83), and $H_{98(y,2)}$ (=1.09) are improved, l_i (=0.82) is slightly reduced, and V_{loop} (=10 mV) is dramatically reduced in the advanced inductive scenario.

It is worthy to explain here how we can determine whether the plasma is entered into the AI-mode or not. It comes from the q profile. Figure 4 presents the time trace of q_0 and q_{min} and the profiles of q and current density at 7.0 s in the reference inductive and the advanced inductive operation scenarios of KSTAR. In the reference inductive scenario, q_0 decreases gradually and reaches below q_0<1.0 even ECCD is injected to the plasma from 3.8 s. On the other hand, although the time traces of q_0 and q_{min} are similar between two scenarios before ECCD is injected, q_0 increases gradually with ECCD deposited at ρ_φ~0.4 from 3.4 s in the advanced inductive operation scenario as shown in Fig. 4 (a). Then, we can confirm that q profile eventually presents the hybrid-like q profile (not monotonic) at 7.0 s as shown in Fig. 4 (b). So the discharge can be assumed to access advanced inductive regime by manually changing the H-factor constraint to 1.2. Hereafter the shape of q is held in similar. That is, q_0 does not decreases in time and the plasma of the advanced inductive scenarios reaches the stationary condition.

The reduced I_P in the advanced inductive operation scenario is the main reason which the q_0 and q_{min} increase with the off-axis injection of ECCD. In other word, the reduced I_P makes increase the controllability of q_0 and q_{min} by the external H/CD as the non-inductive induced current, because the inductive portion of the total current goes smaller with the reduced I_P.

3.2. Reference inductive and advanced inductive scenarios with physics based model

In the previous section, the reference inductive operation scenario is developing by SBM. Here we report that it is also developing by PBM. Figure 5 presents the comparison between SBM and PBM, which is the time traces of parameters describing the plasma performance and the confinement like $T_{e,0}$, f_{NI}, β_N, and $H_{98(y,2)}$ in the reference inductive scenario of KSTAR. After the L-H transition, the plasma performance with GLF23 model is not much different from one with KIAUTO model. However, q_0 shows different trend and decreases quickly with GLF23 model. It comes from the low T_e in L-mode phase.

Secondly the advanced inductive operation scenario is also ongoing to develop using PBM. Before full simulation of the advanced inductive scenario, the trend of q_0 has to be checked whether it is accessible to the advanced inductive regime or not. When we adopt the GLF23 model, q_0 is below the unity too much so that it is hard to expect to recover q_0 to above the unity even ECCD is injected as shown in Fig. 6. (a). It means that is hard to make the hybrid-like q profile to access the advanced inductive regime. Therefore, in this work, we investigate that how much q_0 would be adjustable by the time of L-H transition in our limited H/CD condition. Figure 6 (b) presents the dependency of the time of L-H transition on q_0 and q_{min}. As the L-H transition is occurred at earlier time, q_0 is elevated more so that the time of q_0=1.0 is delayed more. It means that earlier L-H transition has the controllability more to the hybrid-like q profile to access the

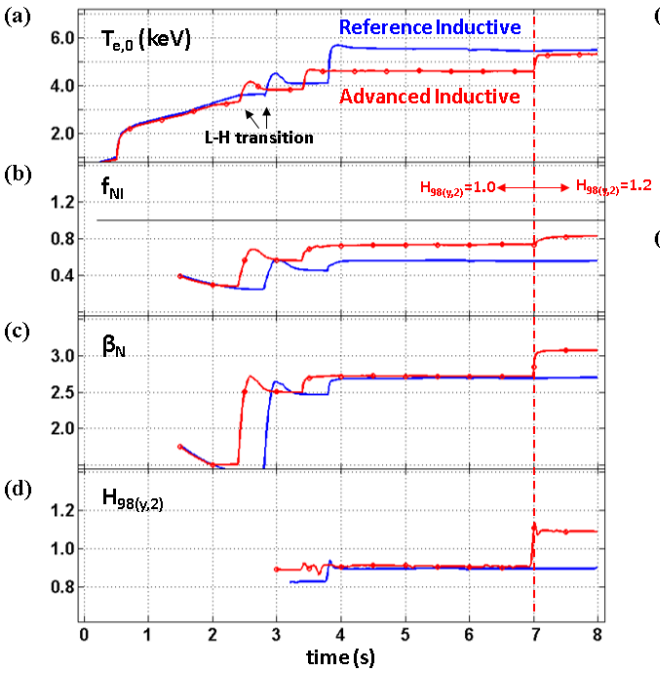

Figure 5 The time traces of parameters describing the plasma performance and the confinement like $T_{e,0}$, f_{NI}, β_N, $H_{98(y,2)}$, and q_0 and q_{min} with SBM (blue) and PBM (red circle) in the reference inductive scenario for KSTAR.

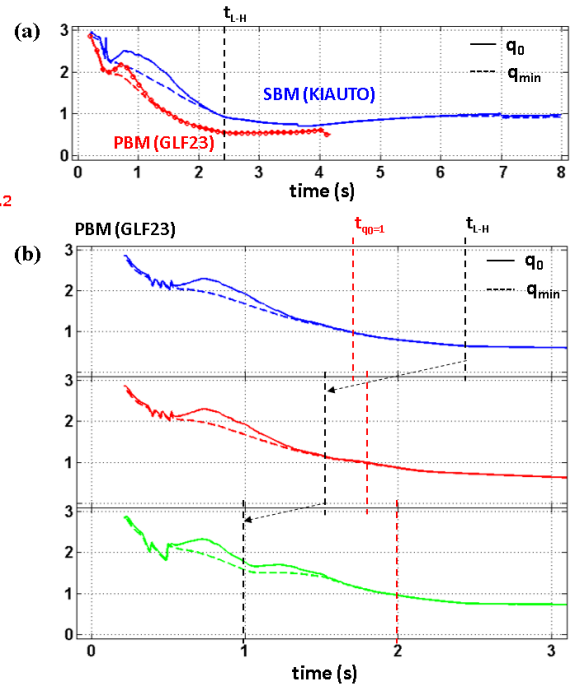

Figure 6 The time traces of q_0 and q_{min} with SBM (blue) and PBM (red circle) in the advanced inductive scenario for KSTAR (a) and the dependency of the time of L-H transition (t_{L-H}) on q_0 and q_{min} (b).

advanced inductive regime. Furthermore, if we inject the ECCD before 2.0 with combination of earlier L-H transition, we can expect the hybrid-like q profile is produced. In conclusion, we cannot determine the advanced inductive regime is achieved with applying PBM even though we simulate the same operation scenario of the SBM case. However we can expect the possibility of achieving the advanced inductive regime with the adjustment of the time of L-H transition and the time of injection of ECCD.

3.3. Advanced tokamak scenarios with both physics based and scaling based model

In this work, we also try to develop the advanced tokamak operation scenario with applying both PBM and SBM. We adopt CDBM as PBM and KIAUTO as SBM. As mentioned before and shown in Fig. 7, we also set the same schemes of B_T, I_P ramp-up rate (dI_P/dt=0.5 MA), the Greenwald density fraction (f_{GW}=0.3) in H-mode phase, and the plasma shape compared with the previous two operation scenarios. We set the beam is injected to the plasma with on-axis 2 MW and off-axis 4 MW at 2.0 s which is the time after 0.4 s from the time of I_P plat-top phase reached, and the ECCD is injected with the toroidal and poloidal injection angle to (φ, θ)=(+10°,+25°) at 3.0 s which is the time after 1.0 s from the time of full injection of NBI. The L-H transition assume to be occurred with the full injection of NBI at 2.0 s. Note that $\bar{n}_e$ is more reduced due to lower I_P (=0.8 MA) in the advanced tokamak operation scenario.

In the advanced tokamak operation scenario, SBM is applied in L- and H-mode phase with assumption of $H_{98(y,2)}$=1.0. If the plasma is satisfied the condition of AT-mode, the anomalous heat transport model is changed KIAUTO with CDBM as shown in Fig. 8. Figure 8 presents the time traces of parameters describing the plasma performance and the confinement like $T_{e,0}$, f_{NI}, β_N, and $H_{98(y,2)}$ of the advanced tokamak scenarios for KSTAR with green colored dashed line. Compared with the reference inductive operation scenario, β_N (=3.11) and f_{NI} (=1.05) are improved and V_{loop} (=-10 mV) exhibit to the negative. That is, the discharge achieves fully non-inductive operation. However, $H_{98(y,2)}$ (=0.94) is not improved significantly. It seems to be required the H/CD power more to get the improved confinement.

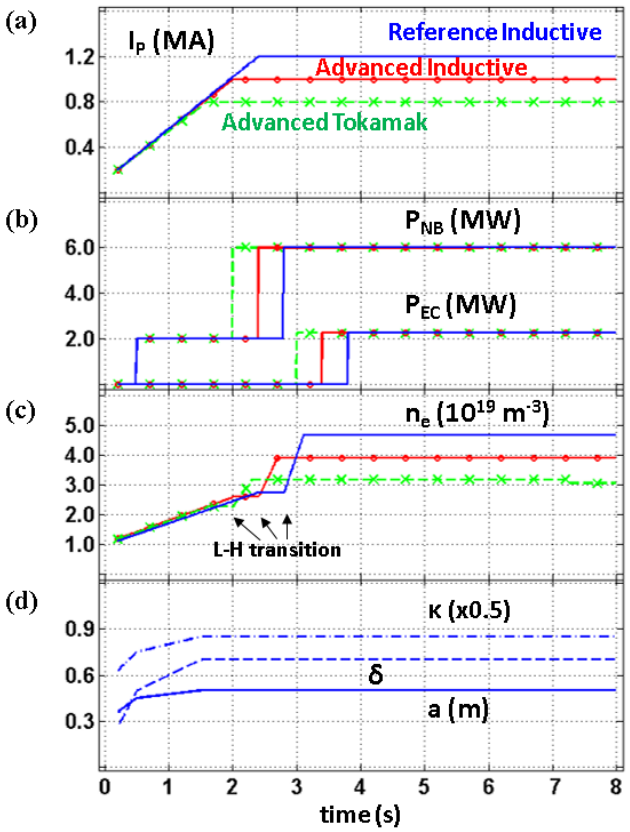

Figure 7 The time traces of plasma operation parameters like I_P, P_{NB}, P_{EC}, n_e, a, κ, and δ of the reference inductive (blue), the advanced inductive (red circle), and the advanced tokamak scenarios (green ex) for KSTAR.

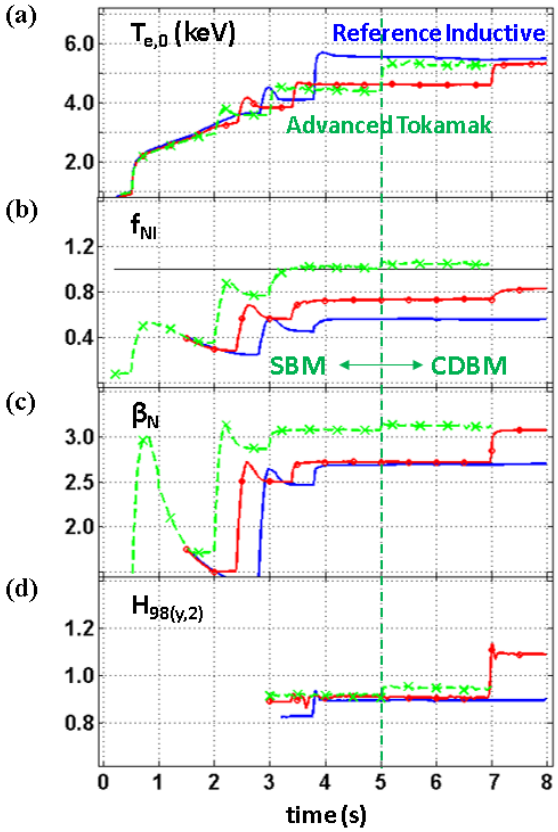

Figure 8 The time traces of parameters describing the plasma performance and the confinement like $T_{e,0}$, f_{NI}, β_N, and $H_{98(y,2)}$ of the reference inductive (blue), the advanced inductive (red circle), and the advanced tokamak (green ex) scenarios for KSTAR.

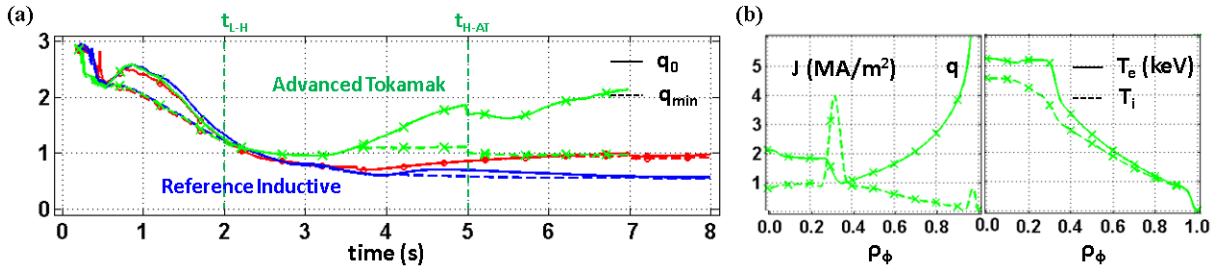

Figure 9 The time traces of q_0 and q_{min} (a) and the profiles of q, current density, electron temperature and io n temperature at 7.0 s (b) in the reference inductive (blue), the advanced inductive (red circle), and the adva nced tokamak (green ex) scenarios for KSTAR.

It is worthy to explain here how we can determined whether the scenario is entered into the AT-mode or not. It comes also from the q profile as we did in the advanced inductive operation scenario. As shown in Fig. 9 (a), from 3.0s, q_0 increases gradually with ECCD deposited at ρ_φ~0.35. We can confirm the q profile is reversed enough in the core at 5.0 s Therefore, from 5.0s, the plasma assumed to be entered into AT regime by manually applying CDBM. Hereafter the shape of q is held in similar and the plasma reaches the stationary condition. As shown in Fig. 9 (b), the internal transport barrier (ITB) is formed in the electron and ion channel as indicated by the high gradient region around ρ_φ~0.35.

4. Summary

In this work, the Operation Windows are produced to explore the KSTAR Advanced Scenarios in the condition of upgrading H/CD mix. Using METIS code, rough ranges of operation condition (I_P and B_T) to use for development of advanced operation scenario could be determined. Based on the operation window, the advanced inductive and advanced tokamak operation scenario of KSTAR are developing with SBM (KIAUTO) and PBM (GLF23, CDBM) transport model by using CRONOS to make a suggestion to on-going KSTAR experiment. The advanced inductive operation scenario are developing with SBM and PBM (GLF23). SBM could make a hybrid-like q profile, but PBM could not. We investigate the q_0 dependency against different timing of L-H transition to find the optimized condition of the advanced inductive operation scenario. As the L-H transition is occurred earlier time, q_0 is elevated more so that the time of q_0=1.0 is delayed more. Finally, the advanced tokamak operation scenario are developing using the combination of SBM (KIAUTO) and PBM (CDBM). Up to now, the discharge achieves fully non-inductive state. However, $H_{98(y,2)}$ (=0.94) is not improved significantly. These reliable results could become a useful database for exploring the advanced regime of KSTAR discharges in the future.

Acknowledgement

This research was supported by Ministry of Science, ICT, and Future Planning under KSTAR project and was partly supported by the JSPS-NRF-NSFC A3 Foresight Program in field of Plasma Physics (NRF No. 2012K2A2A6000443).

References

[1] M. Kwon et al., Nucl. Fusion 51, 094006 (2011)
[2] Y-S. Na et al., Nucl. Fusion 49, 115018 (2009)
[3] J.-F. Artaud et al., Nucl. Fusion 50, 043001 (2010)
[4] Y-S. Na et al., Computer Phys. Communications 177, 134 (2007)
[5] Artaud J.F. et al., 2005 Proc. 32nd EPS Conf. on Plasma Physics (Tarragona, Spain) vol 29C (ECA) p P-1.035
[6] Waltz R.E. et al., Phys. Plasmas 4, 2482 (1997)

Initial result on iron transport analysis using radial profiles measured by space-resolved EUV spectrometer in LHD

X. L. HUANG[1], S. Morita[1,2] , T. Oishi[1,2], M. Goto[1,2], H. M. Zhang[1], I. Murakami[1,2]

[1] *Department of Fusion Science, Graduate University for Advanced Studies, Toki 509-5292, Gifu, Japan*

[2] *National Institute for Fusion Science, Toki 509-5292, Gifu, Japan*

Abstract

The Fe n=3-2 transition array consisting of Fe^{16+} through Fe^{23+} ions is utilized for impurity transport study in the Large Helical Device (LHD). Since the charge states of Fe^{16+} through Fe^{23+} are usually distributed all over the whole volume of LHD plasmas, the impurity transport can be studied without any assumption on the radial structure of transport coefficients. A one-dimensional transport code is employed to simulate the emissivity profile of iron line emissions. The transport coefficient is then determined by fitting the experimental profile of n=3-2 Fe transitions in several ionization stages with the impurity transport code. A preliminary result of the iron transport analysis in high and low electron density discharges is reported.

I. Introduction

Radial transport of impurity ions remains as an important issue in magnetically confined fusion devices, since the plasma performance is significantly affected by radiation loss and fuel dilution caused by impurities. In the Large Helical Device (LHD), the density profile can exhibit a peaked, flat or hollow shape, depending on plasma conditions such as B_t, T_e, and n_e. Therefore, it is of great importance to investigate corresponding impurity transport in the plasma core of LHD[1-4]. With a centrally peaked density profile in high-density LHD discharges, impurity accumulation has been clearly observed and the transport is analyzed based on an assumption of the radial structure of convective velocity[5]. Nevertheless, analysis on the detail structure of transport coefficients is still necessary for better understanding of the radial transport. Formation of the hollow or flat density profile observed in the LHD is quite unique in tokamaks. Therefore, the LHD plasma can give a good opportunity for studying the impurity transport through the analysis of radial structure in the transport coefficient, in particular in relation to the density and temperature gradients.

Iron is an intrinsic impurity in magnetically confined fusion plasmas and therefore is useful for comprehensive study of the impurity transport under different plasma conditions. For the purpose, the Fe n=3-2 Lα transition array, emitted in narrow wavelength range of 10 – 18 Å, is of great advantage because the transition array includes emissions from ions in several charge states of Fe^{16+} through Fe $^{23+}$. In addition, these iron emissions have relatively strong emissivities and are distributed all over the whole plasma volume of the LHD as the ionization energy of corresponding ions stays between 1 keV and 2 keV of which the range is nearly equal to electron temperature in core plasmas of the LHD. Radial profiles of the Fe Lα emissions have been well measured by a space-resolved extreme-ultraviolet (EUV) spectrometer[6]. It is then possible to determine the transport coefficient, i.e. the diffusion coefficient and the convective velocity, from the emissivity profile with the help of impurity transport simulation. It should be noted that the iron transport can be analyzed along the minor radius without any assumption on the radial structure of transport coefficients because the Fe Lα transition with several ionization stages is emitted over wide range of the radial plasma location.

II. Experimental setup and Fe n=3-2 array

The EUV system used for this study is working in the wavelength range of 10-130Å, mainly consisting of an entrance slit, a spatial-resolution slit, a gold-coated concave varied-line-spacing (VLS) laminar-type holographic grating with a groove density of 2400 per mm and a charge-coupled device (CCD) detector with 1024 × 255 pixels, as shown in Fig. 1(a). A relatively long distance between the spectrometer and the plasma is necessary for observing the vertical plasma range of 50 cm. In practice the distance between the central plasma position and the entrance slit of the spectrometer is set to 9157 mm when the plasma axis position is R = 3.90 m. Since the distance between the entrance slit and the CCD detector is roughly 470 mm, which is a weak function of wavelength, we obtain a multiplication factor of 19.5. The EUV spectrometer is installed on a mid-plane port at the backside of rectangular vacuum extension chamber.

The elevation angle of the central viewing chord is exactly determined to make possible the profile measurement at upper half vertical range of the elliptical plasma, i.e., Z = 0–50 cm. Figure 1(b) shows top view of the optical layout in the spectrometer. EUV radiation emitted from LHD plasmas passes through the entrance slit and reaches the grating adjusted at the angle of incidence of 88.6°. The radiation diffracted on the grating is focused on the focal plane and recorded by the CCD detector. The large angle of incidence is necessary for observing the EUV light in such a short wavelength range with high throughput.

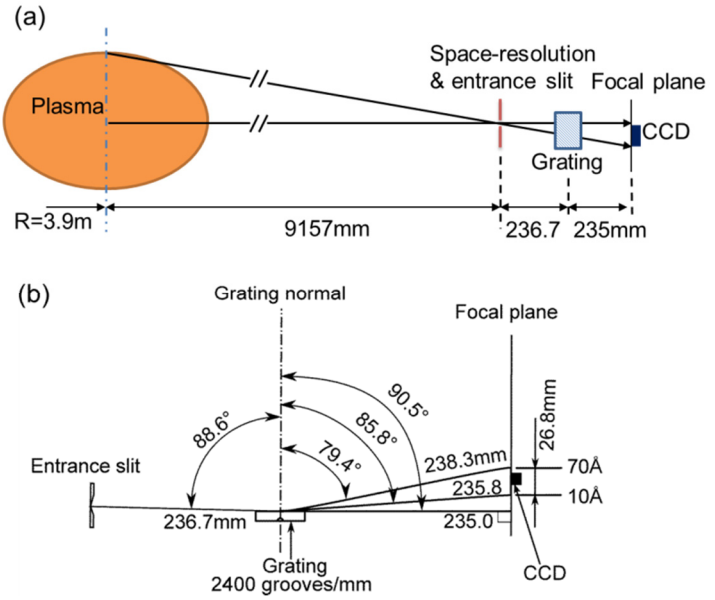

FIG. 1. Schematics of (a) EUV system and (b) optical layout of the spectrometer.

Iron spectrum with n = 3-2 Lα transitions between 10 and 20 Å has been measured by injecting an iron impurity pellet[7]. A typical result is shown in Fig. 2. A lot of Lα transitions from highly ionized iron ions are observed in the spectrum. Since many iron lines are blended, the spectrum appears with structure like pseudo-continuum. The line-integrated vertical profile of the Fe Lα transition from FeXVII to FeXXIV is analyzed by carefully choosing the wavelength interval at each ionization stage. The result is shown in Fig. 3(a). The electron density and temperature profiles are also shown in Fig. 3(b) of which the coordinate is converted into the vertical position at horizontally elongated plasma cross section by taking into account the elliptical magnetic surface. The vertical profile is normalized at each peak position. The peak position of each profile moves inside with increase in the ionization stage, reflecting the centrally peaked electron temperature profile.

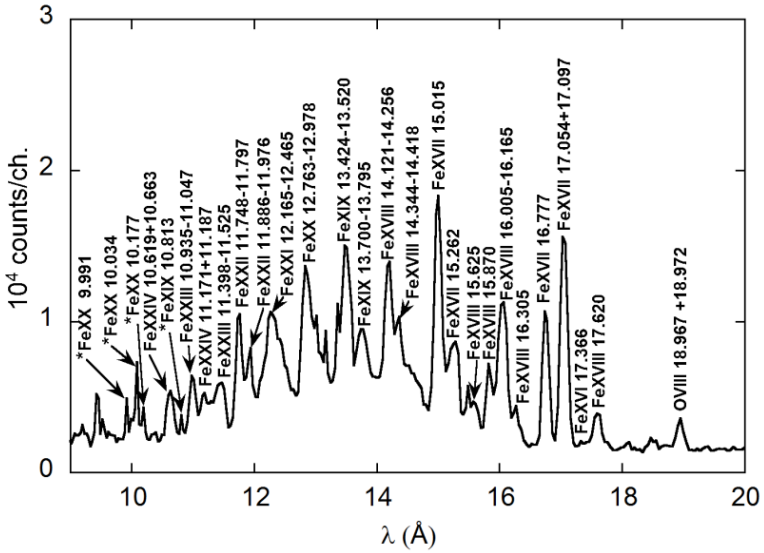

FIG. 2. Fe n = 3–2 Lα spectrum below 20 Å measured after iron impurity pellet injection in NBI discharge with central electron temperature of 3keV. The asterisks (*) before wavelengths denote that two or more lines are blended into the same wavelength position.

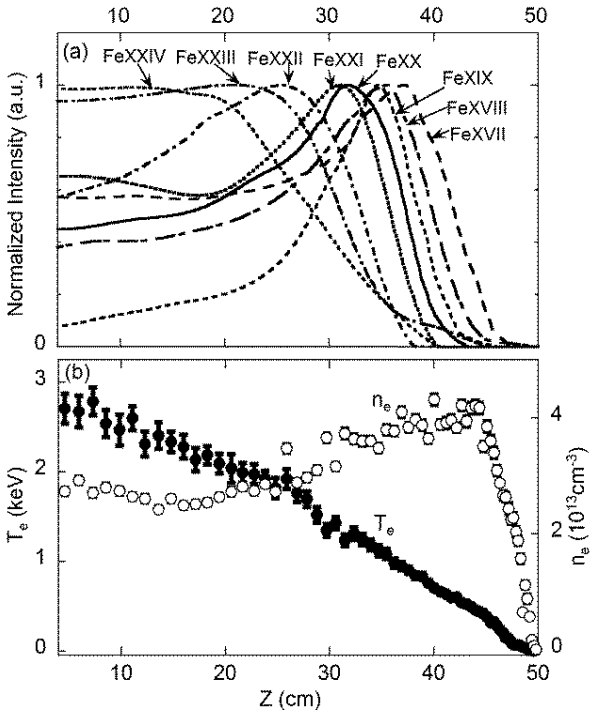

FIG. 3. (a) Line-integrated vertical intensity profiles of FeXVII (17.054 Å + 17.097 Å), FeXVIII (14.121–14.256 Å), FeXIX (13.424–13.520 Å), FeXX (12.763–12.978 Å), FeXXI (12.165–12.465 Å), FeXXII (11.748–11.797 Å), FeXXIII (10.935–11.047 Å), and FeXXIV (10.619 Å + 10.663 Å) and (b) electron temperature (closed circles) and density (open circles) profiles.

Experimental emissivity profiles can be derived from the vertical profile in Fig.3 (a) based on an Abel inversion technique. The magnetic surface structure in LHD plasmas is calculated with variation moment equilibrium code (VMEC)[8,9]. Then, the chord length between adjacent magnetic surfaces along the observation chord of the spectrometer is evaluated at all magnetic surfaces taking into account the finite-β effect. Here, it should be pointed out that the magnetic flux surface is also assumed outside the last close flux surface (LCFS) by extrapolating the magnetic surface contour. Although the assumption may cause certain uncertainty, it does not strongly affect the emissivity peak inside the LCFS because the emissivity outside the LCFS is usually weak.

III. Transport simulation

A one-dimensional impurity transport code is employed to determine the transport coefficient[10,11]. It is assumed that the impurity transport satisfies the following equation:

$$\Gamma_q = -D_q(r)\frac{\partial n_q}{\partial r} + V_q(r)n_q, \quad (1)$$

where Γ_q, n_q, D_q, V_q are the particle flux, the ion density, the diffusion coefficient and the convective velocity of impurity ions in the qth charge state, respectively. Positive and negative velocities stand for outward and inward convection, respectively.

With given transport coefficients and radial profiles of plasma parameters, the code calculates the impurity ion density in all charge states as a function of time. The impurity source is assumed to originate in the sputtering at the first wall of vacuum vessel. In this study, the iron ion density profile in a steady state is used for analysis. The ergodic layer of LHD plasma is not considered in the present work. Consequently, a slight error may occur near the last close flux surface (LCFS) in the simulated result. Nevertheless, the error is usually negligibly small.

The transport coefficient near the emissivity peak can be determined by comparing the emissivity profile obtained from experiment and simulation. In order to determine the transport coefficient at the whole plasma volume, the iron emission is simultaneously analyzed at several charge states. The emissivity profile is calculated from the simulated ion density profile based on intensity coefficients obtained with the HULLAC code[12] and compared with the experimental emissivity profile, which is calculated from the measured line-integrated profile as mentioned in Section II.

IV. Transport analysis at low- and high-density discharges

Impurity accumulation has been observed with a centrally peaked density profile after hydrogen multi-pellet injection in the LHD5. Here, the radial structure of the transport coefficient is analyzed using emissions of FeXVII at 15.02Å and FeXVIII at 14.20Å. The waveform of a high-density discharge with multiple H_2 pellets is shown in Fig. 4 for the line-averaged electron density (n_e), central electron temperature ($T_e(0)$), total radiation power (P_{rad}) and plasma stored energy (W_p) together with NBI port-through power (P_{NBI}). The emission profile is measured at the time frame denoted with hatched area (t=4.6-4.8s) in Fig. 4, at which the plasma stays in a quasi-steady state. The experimental and simulated emissivity profiles are plotted in Figs. 5(a) and (b), respectively. The coefficients determined from the comparison of two emissivity profiles are shown in Fig. 5(c). Figure 5(d) displays corresponding electron temperature and density profiles measured by Thomson scattering system. The simulated emissivity profile is basically in a good agreement with experimental one. The diffusion coefficient, D, is constant along the minor radius, while the convective velocity, V, increases as an inward convection toward plasma outer region and then keeps constant in the plasma periphery ($0.75 \leq \rho \leq 1$). When comparing Fig. 5(c) with (d), the structure of V seems to change with the density profile. The shape of V roughly agrees with conventionally assumed shape, e.g. V is proportional to the normalized minor radius.

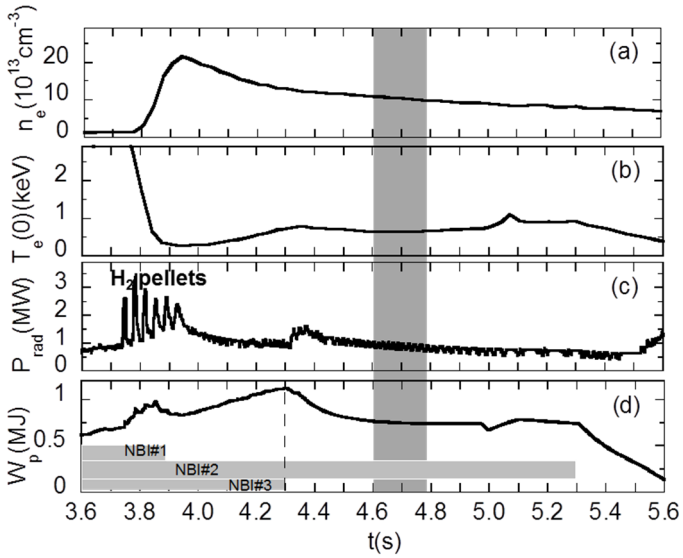

FIG. 4. Time evolution of (a) line-averaged electron density, (b) central electron temperature, (c) radiation power, and (d) plasma stored energy together with NBI port-through power. The vertical hatched region denotes the time frame when the emission profile is measured.

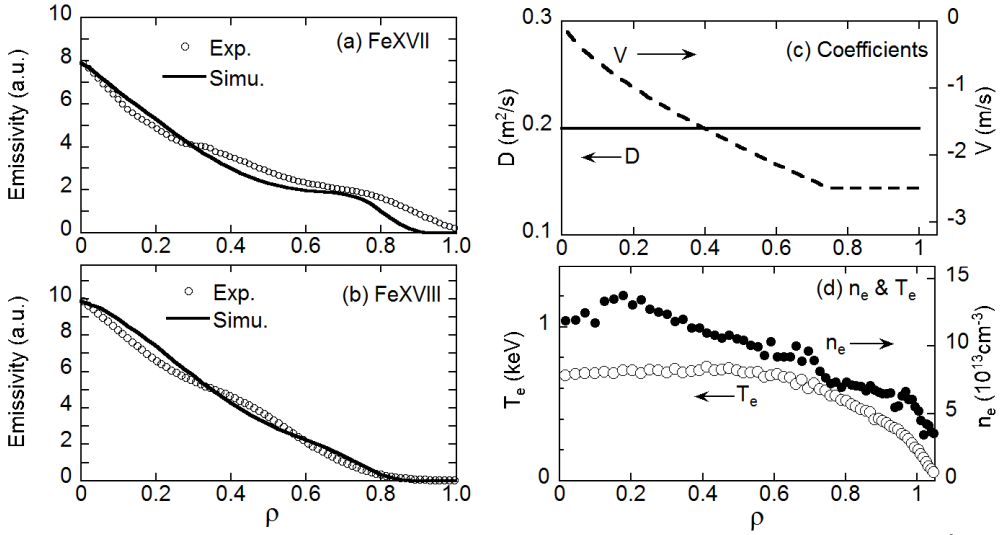

FIG. 5. Experimental (open circles) and simulated (solid line) profiles of (a) FeXVII at 15.02Å and (b) Fe XVIII at 14.20Å, (c) profiles of diffusion coefficient (solid line) and convective velocity (dashed line) and (d) profiles of electron temperature (open circles) and density (solid circles) .

Figure 6 shows the waveform of P_{NBI}, n_e, $T_e(0)$, P_{rad}, W_p and the intensity of the Fe Lα array in the wavelength range of 10-18Å. The emission profile is measured in the time frame denoted with hatched region in Fig. 6. The discharge is maintained at a relatively low density, $n_e < 5\times10^{13}cm^{-3}$. An iron pellet is injected at t = 3.8s for enhancing the iron emission. The intensity of Fe Lα emissions begins to decay just after the pellet injection, as seen in Fig. 6 (f). However, the intensity starts to increases at t = 4.2s after certain impurity confinement time. It strongly indicates iron ions accumulate into the plasma core.

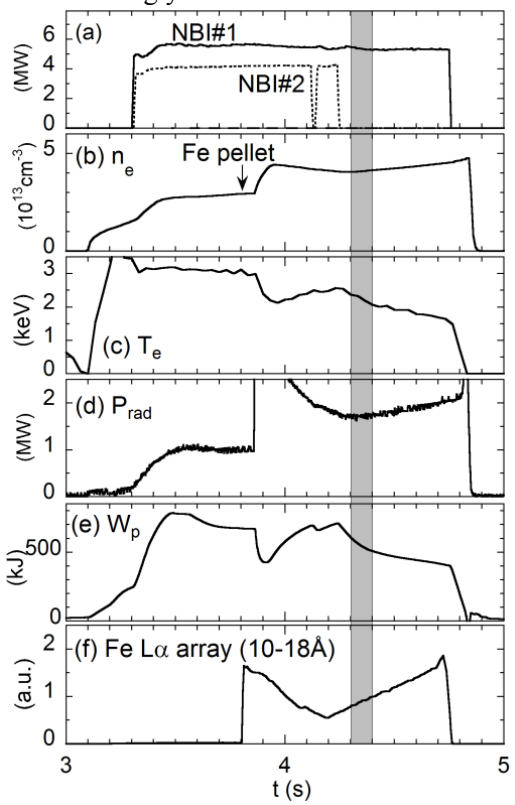

FIG. 6. Time evolution of (a) NBI port-through power, (b) line-averaged electron density, (c) central electron temperature, (d) plasma stored energy together, (e) radiation power and (f) total intensity of Fe Lα array located in the wavelength range 10-18Å.

Electron temperature and density profiles are shown in Fig. 7 (e). In contrast with high density case, the density profile exhibits a slightly hollow one with a central density of $4\times10^{13}cm^{-3}$. On the other hand, the electron temperature is much higher compared with the T_e profile in Fig. 5(e) and its profile shows a centrally peaked one. The emission profile of FeXVII at 15.02Å, Fe XX at 12.80-12.90Å and Fe XXIV at 10.62-10.66Å is plotted for both the measurement and simulation in Figs. 7 (a), (b) and (c), respectively. Reflecting the different ionization energy among three iron ions, each profile has its peak at different radial location. The transport code can well reproduce the profile if the transport coefficient has a radial structure shown in Fig. 7(d). Because of the uncertainty in the measurement and simulation, it is difficult to completely eliminate the deviation between the measurement and simulation in the profile fitting. Nevertheless, the radial structure of transport coefficients determined in the present study can give a valid information on the impurity transport in LHD. A weak outward convection, V = 0.5 m/s, is observed near the plasma center of $0.12 \le \rho \le 0.36$. This may be due to the positive gradient in the density profile. In the outer region of $0.36 \le \rho \le 1.0$, the convection is inversely changed and becomes inward. A detailed analysis on the radial structure of the convection velocity may require the information on the radial electric field, which sometimes plays an important role in the formation of impurity convection[13,14]. As for the diffusion coefficient, the D value of 0.06 m^2/s in the periphery region of $0.6 \le \rho \le 1.0$ is significantly lower than the value of 0.2 m^2/s seen in the plasma core. If the diffusion coefficient is assumed to be constant along the minor radius, the experimental profile cannot be entirely reproduced by the simulation code even if any combination is considered between the V and D. Therefore, the low D value appeared in the edge is justified by the present method using Lα transitions. Considering the collisionality of impurity ions[15], the reduction of D may be attributed to an increase in the collisionality because the iron ion stays in the 1/ν or the plateau regime at the edge region.

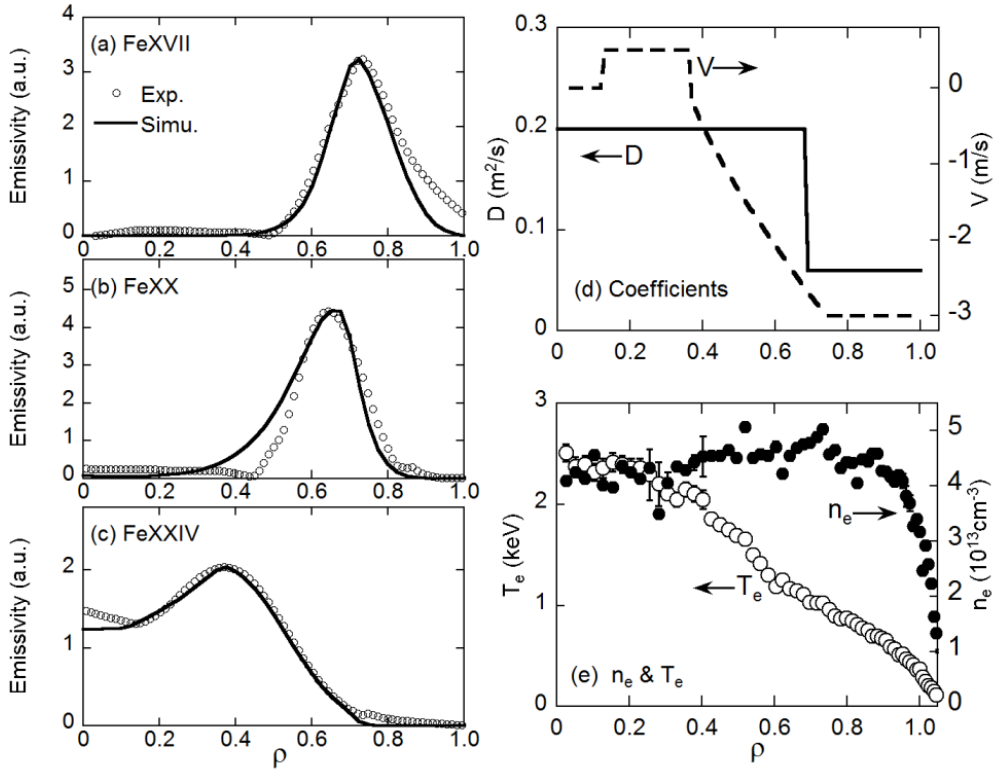

FIG. 7. Measured (open circles) and simulated (solid line) profiles of (a) FeXVII at 15.02Å, (b) FeXX at 12.80-12.90Å and (c) FeXXIV at 10.62-10.66Å, (d) profiles of diffusion coefficient (solid line) and convective velocity (dashed line) and (e) profiles of electron temperature (open circles) and density (solid circles) .

The convective velocity near ρ = 0.8 has been analyzed against the density gradient in low-density (n_e<5×10^{13}cm^{-3}) discharges using above-mentioned method. The result is plotted in Fig. 8. The convective velocity is proportional to the density gradient, which is similar to the conclusion of a previous study on C, Al and Ti[16]. In spite of this, more data are necessary to clarify the dependence of V on density gradient because the analyzed density range is limited in the present study.

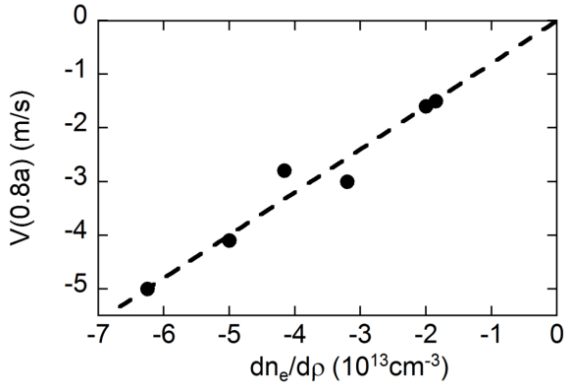

FIG. 8. Convective velocities as a function of density gradient near ρ=0.8 in low-density discharges (n_e<5×10^{13}cm^{-3}). Dashed line stands for linear fitting.

V. Summary

Using space-resolved EUV spectroscopy, we have studied the iron impurity transport under different conditions, such as n_e, R_{ax} and so on. With the help of one-dimensional impurity transport code, the transport coefficients of V and D are successfully obtained by analyzing the Fe Lα emission profile. Several discharges at low and high densities have been analyzed with the profile. One of the present results indicates that the inward convection determined at the plasma edge is proportional to the density gradient.

Acknowledgements

The authors thank all the members of the LHD experiment group for their cooperation including technical supports. This work was partly supported by the JSPS-NRF-NSFC A3 Foresight Program in the field of Plasma Physics (NSFC: No.11261140328, NRF : No. 2012K2A2A6000443).

References

[1]S. Morita, *et al.*, Plasma Sci. Technol. **8**, **5**5 (2006).
[2]M. Yoshinuma, *et al.*, Nucl. Fusion **49**, 062002 (2009).
[3]Y. Nakamura, *et al.*, Nucl. Fusion **43**, 219 (2003).
[4]Y. Igitkhanov, *et al.*, Plasma and Fusion Research **2**, S1131 (2007).
[5]C. F. Dong, *et al.*, Plasma Sci. Technol. **15**, 230 (2013).
[6]X. L. Huang, S. Morita, T. Oishi, M. Goto, and C. F. Dong, Rev. Sci. Instrum. **85**, 043511 (2014).
[7]R. Katai, S. Morita, M. Goto, H. Nishimura, K. Nagai, and S. Fujioka, Jpn. J. Appl. Phys. **46**, 3667 (2007).
[8]K. Yamazaki and L.E. Group, J. Plasma Fusion Res. **79**, 739 (2003).
[9]S. P. Hirshman, W.I. van RIJ, and P. Merkel, Computer Physics Communications **43**, 143 (1986).
[10]T. Amano, J. Mizuno, and J. Kako, Simulation of impurity transport in tokamak, Int. Rep. IPPJ-616, Institute of Plasma Physics, Nagoya University (1982).
[11]S. Morita, *et al.*, Plasma Sci. Technol. **8**, 55 (2006).
[12]A. Bar-Shalom, M. Klapisch, and J. Oreg, J. Quant. Spectrosc. Radiat. Trans., **71**, 169 (2001).
[13]K. Ida, *et al.*, Nucl. Fusion **45**, 391 (2005).
[14]Y. Igitkhanov, *et al.*, Plasma and Fusion Research **2**, S1131 (2007).
[15]S. Murakami, *et al.*, Nucl. Fusion **42**, L19 (2002).
[16]H. Nozato, *et al.*, Phys. Plasmas **13**, 092502 (2006).

Study of runaway electron current during disruptions in KSTAR

C. S. Kang[1], S. G. Lee[1, 2], and H. S. Kim[2]

[1]Department of Plasma Physics and Nuclear Fusion, Korea University of Science and Technology, Daejeon, 305-350, Korea
[2]National Fusion Research Institute, Daejeon, 305-806, Korea

Email : kcs1984@nfri.re.kr

The behavior of runaway electron currents during disruptions is investigated in the Korea Superconducting Advanced Tokamak Research (KSTAR) device. Runaway electron currents are observed only when $B_T \geq 1.8$ T. It is inconsistent with that of other tokamaks, $B_T \geq 2.0 \sim 2.2$ T. Runaway electron suppression has been observed at magnetic fluctuation level larger than a certain threshold. These results help to understand the well-known toroidal field threshold for RE current generation.

1. Introduction

Runaway electrons (REs) generated during the ramp-up phase or during a disruption may cause severe damage by colliding with the plasma facing components of the fusion devices. REs are mainly studied to prevent or mitigate their generation during disruptions where they can be considered to be a potential threat to the operation of large tokamaks, such as the International Thermonuclear Experimental Reactor (ITER) [1]. The conversion of up to 70 % of the pre-disruption current into the RE current is predicted to occur following a spontaneous disruption, an intended disruption or vertical displacement event (VDE) [2]. Since the RE energy will be deposited within the small strike areas, they can cause local damage enough to melt or ablate the ITER wall materials [2]. Therefore, it is important to understand the dynamics of this RE current since it could help in developing methods for suppressing their formation.

The generation of RE currents during the disruption depends on various factors. In present tokamaks, a threshold for the toroidal magnetic field, $B_T \geq 2.0 \sim 2.2$ T, has been reported on JET [3], JT-60U [4], Tore Supra [5], and TEXTOR [6]. There are two proposals for explaining this interesting phenomenon. The first one is the whistler wave instability (WWI) [7]. The WWI can suppress avalanche multiplication by causing a fast pitch angle scattering of the REs. Another possible explanation is magnetic fluctuations [8]. Magnetic fluctuations have been believed to be the dominating transport mechanism of the REs due to their low collisionality and very high parallel velocity. Many analytical and numerical researches show that magnetic fluctuation can suppress the RE avalanche during disruptions. [9-12].

Since the KSTAR device is fully superconducting medium-sized tokamak, KSTAR can play a key role in achieving the ITER project. In this paper, we will illustrate the effort made to identify the dynamics of RE currents during the disruptions and the toroidal magnetic field threshold in KSTAR.

2. A preliminarily study on the dynamics of RE currents during disruptions

The experiments described in this paper were performed in the 2013 campaign. The disruption shots have been collected only when the disruption occurred at the plasma current flat-top phase to reduce other side effects.
Figure 1 shows a typical disruption without RE currents (shot # 9220). The pre-disruption plasma current was 400 kA and the toroidal magnetic field was 2.0 T. The plasma parameters such as the electron temperature (b), the loop voltage (c), the magnetic fluctuation (d), and the soft x-ray (SXR) emission (e) were shown in Fig. 1. The thermal quench occurs at about 2.75 seconds and the current quench is followed.

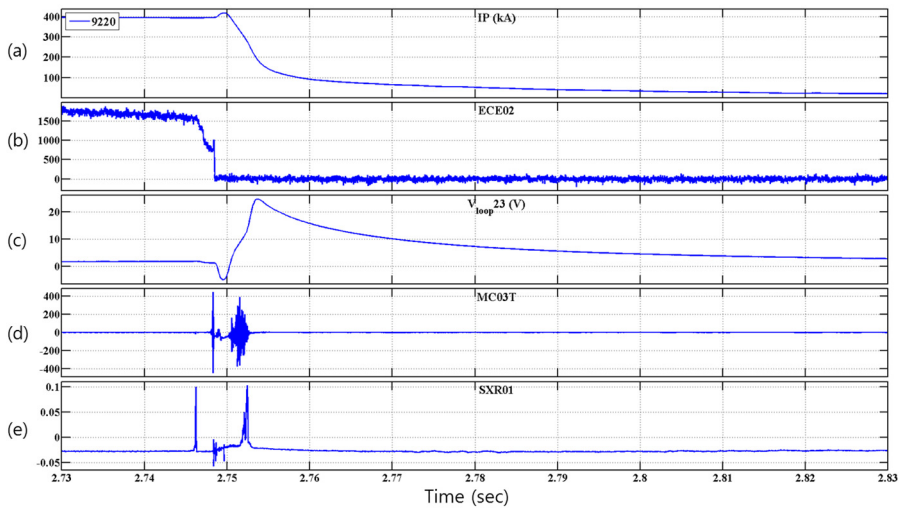

Figure 1 Time traces of plasma current (a), electron temperature (b), loop voltage (c), magnetic fluctuation (d), and SXR (Shot # 9220).

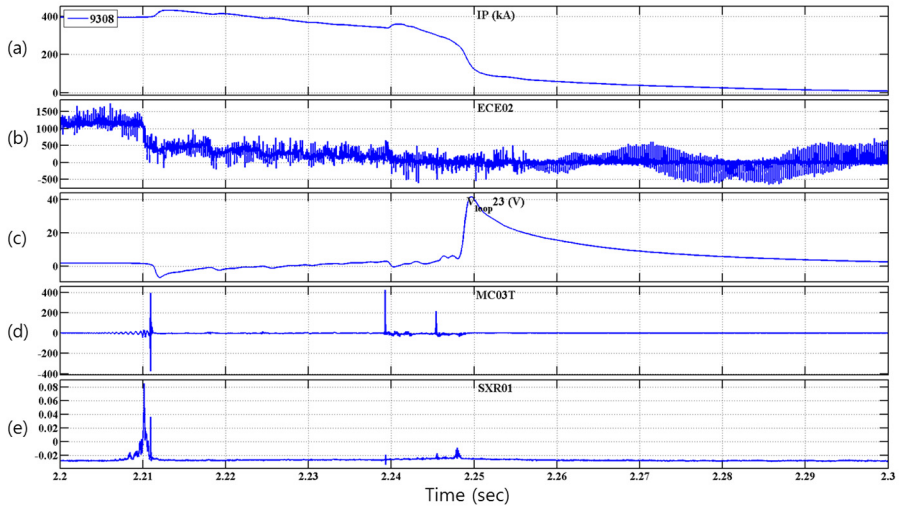

Figure 2 Time traces of plasma current (a), electron temperature (b), loop voltage (c), magnetic fluctuation (d), and SXR (Shot # 9308).

Figure 2 shows a different disruption discharge (shot # 9308). In case of Fig. 2, RE currents would be generated. The pre-disruption current and the toroidal magnetic field are same with shot # 9220. After about 2.21 seconds, the thermal quench occurs. During the following current quench, a RE current plateau has been found to last up to 40 milliseconds.

In general, RE currents can be diagnosed with a Hard x-ray (HXR) monitor system which is specialized to detect thick-target bremsstrahlung emission when REs strike the plasma facing components (PFCs) such as a limiter. Unfortunately, it cannot be utilized to detect RE current during the disruption phase in KSTAR, unlike most present tokamaks. In the 2013 experimental campaign, the HXR signal nearly always remains at zero level after disruptions even when RE currents would be generated. Due to the absence of the HXR signal during the RE current phase, it is difficult to study on the behavior of RE currents during disruptions in KSTAR. Therefore, other methods should be developed to investigate the RE dynamics in KSTAR, such as infrared and SXR camera.

To find the toroidal magnetic field threshold for the generation of RE currents in KSTAR, we have defined an area under the current curve (AUC) of the RE current plateau as shown in Fig. 3. If this AUC is large enough, it can be considered that RE currents are generated during the disruptions.

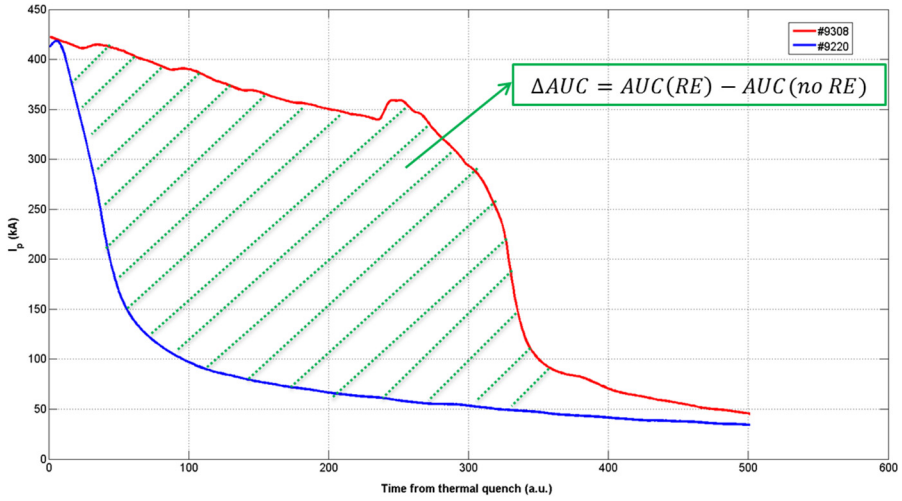

Figure 3 AUCs of Shot # 9220 and 9308.

In Fig. 4, a preliminarily survey of several discharges shows that REs occur after a disruption when the value of the toroidal magnetic field exceeds about 1.8 T.

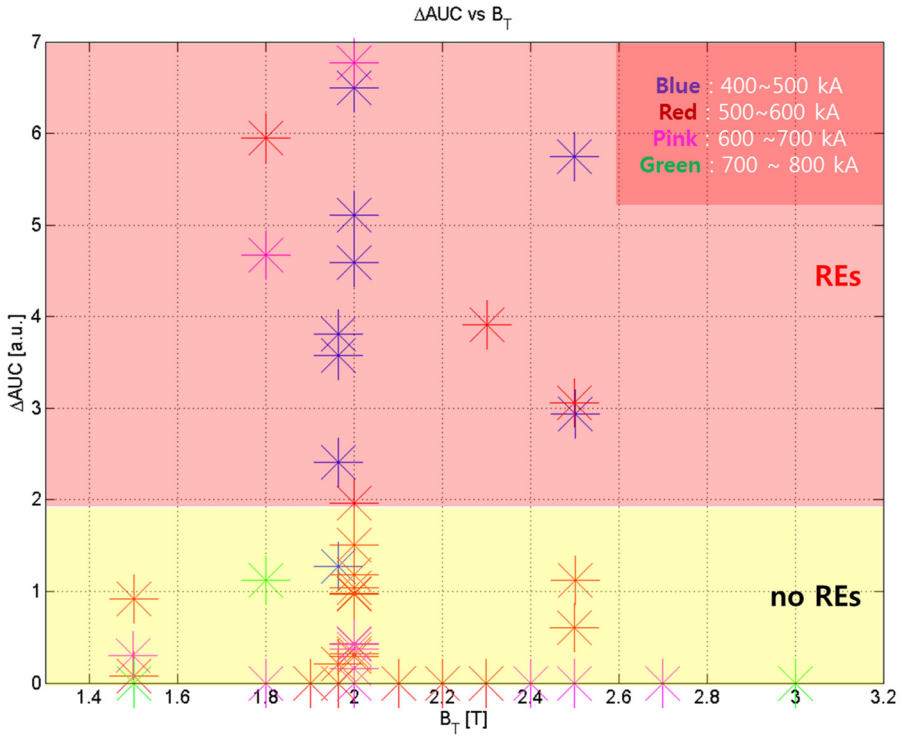

Figure 4 Collected disruptions at different plasma currents and at different toroidal magnetic fields in the 2013 campaign.

This result is inconsistent with that of other tokamaks, $B_T \geq 2.0 \sim 2.2$ T. Figure 5 shows a disruption with RE currents at 1.8 T.

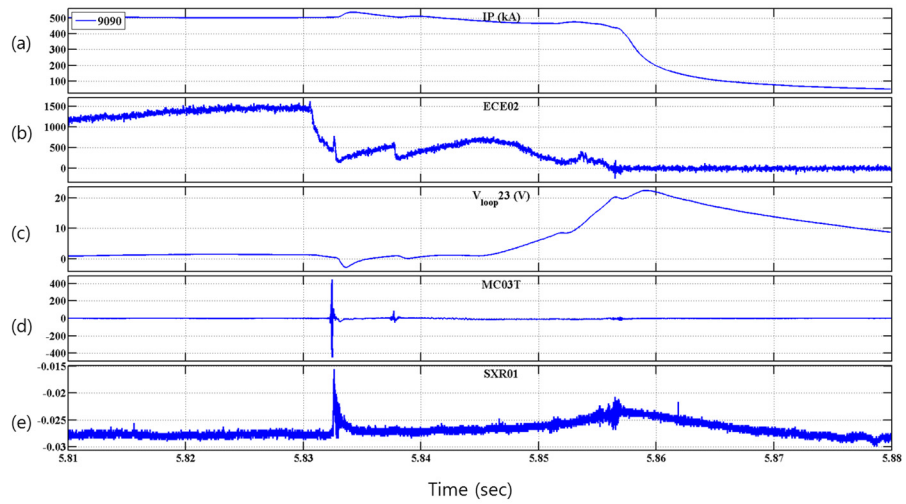

Figure 5 Time traces of plasma current (a), electron temperature (b), loop voltage (c), magnetic fluctuation (d), and SXR (Shot # 9090).

However, the number of the collected data is too small to provide a reliable value of the toroidal magnetic field threshold. In addition, the plasma conditions of the discharges included in Fig. 4 were not exactly same. Hence, we should keep our efforts to find the threshold in KSTAR.

One interesting phenomenon is found in typical KSTAR disruptions. The amplitude of magnetic fluctuations is high in the beginning of the current quench phase when the RE current plateau is not observed. On the contrary, the amplitude of magnetic fluctuations is relatively low when the RE current plateau is observed. It can be considered that magnetic fluctuations play a key role in the generation of RE currents in the disruption phase.

Acknowledgement

This research was supported by Ministry of Science, ICT, and Future Planning under KSTAR project and was partly supported by the JSPS-NRF-NSFC A3 Foresight Program in field of Plasma Physics (NSFC: No. 11261140328, NRF: No. 2012K2A2A6000443).

References

[1] M.N. Rosenbluth, et al., *Nuclear Fusion,* **37** (1997) 1355
[2] T.C. Hender, et al., *Nuclear Fusion,* **47** (2007) S128
[3] R.D. Gill, et al., *Nuclear Fusion*, **42** (2002) 1039
[4] R. Yoshino, et al., *Nuclear Fusion,* **39** (1999) 151
[5] G. Martin*, in Proceedings of the 25th EPS,* (1998), Vol. 22C, P.3.006.
[6] M. Lehnen, et al., *Journal of Nuclear Materials,* **390-391** (2009) 740
[7] T. Fulop, et al., *Physics of Plasmas,* **16** (2009) 022502
[8] L. Zeng, et al., *Physical Review Letters,* **110** (2013) 235003
[9] P. Helander, et al., *Physics of Plasmas,* **7** (2000) 4106
[10] R.W. Harvey, et al., *Physics of Plasmas,* **7** (2000) 4590
[11] J.R. Martin-Solis, et al., *Physics of Plasmas,* **7** (2000) 3369
[12] T. Feher, et al., *Plasma Physics and Controlled Fusion,* **53** (2011) 035014

Performance improvement of two-dimensional EUV spectroscopy based on high frame rate CCD and signal normalization method

H.M.Zhang[1], S.Morita[1, 2], T.Ohishi[1, 2], M.Goto[1, 2] and X.L.Huang[1]

[1]Graduate University for Advanced Studies, Toki 509-5292, Gifu, Japan

[2]National Institute for Fusion Science, Toki 509-5292, Gifu, Japan

Abstract

In the Large Helical Device (LHD), the performance of two-dimensional (2-D) extreme ultraviolet (EUV) spectroscopy with wavelength range of 30–650Å has been improved by installing a high frame rate CCD and applying a signal intensity normalization method. With upgraded 2-D space-resolved EUV spectrometer, measurement of 2-D impurity emission profiles with high horizontal resolution is possible in high-density NBI discharges. The variation in intensities of EUV emission among a few discharges is significantly reduced by normalizing the signal to the spectral intensity from EUV_Long spectrometer which works as an impurity monitor with high-time resolution. As a result, high resolution 2-D intensity distribution has been obtained from CIV (384.174Å), CV (2×40.27Å), CVI (2×33.73Å) and HeII (303.78Å).

1. Introduction

In LHD, the core plasma is surrounded by ergodic layer, which is formed by the presence of higher-order Fourier components in the magnetic fields created by the helical coils. Since the ergodic layer has 3-D structure, 2-D measurement is at least necessary for the impurity transport study in the ergodic layer [1]. A 2-D space-resolved EUV spectrometer has been developed to measure the 2-D distribution of impurity emissions from the ergodic layer. The 2-D profile from several impurity species, i.e. carbon, helium and iron, has been measured and analyzed [1-3]. In LHD two positive-ion-source-based NBIs (p-NBI) and three negative-ion-source-based NBIs (n-NBI) are operated at energies of 40 and 180 keV for plasma heating, respectively. The ECH with injection power up to 4 MW and two perpendicularly injected p-NBIs with total input power up to 10 MW are used for electron and ion heating, respectively. High-density discharges in ranges of 10^{13}-10^{15} cm^{-3} are mainly sustained and heated by three tangentially injected n-NBIs with total input power up to 20 MW. As the pulse length of LHD discharges heated by n-NBIs is normally limited to 3-5s, it is necessary to improve the performance of 2-D EUV spectrometer to measure the 2-D distribution of impurity emissions from high-density plasmas heated by the n-NBI. In 2013 LHD campaign, the performance of 2-D EUV spectrometer greatly improves by installing a new high frame rate CCD and applying a signal intensity normalization method in the 2-D distribution analysis. In this report, the EUV spectroscopy in LHD and the principle of 2-D measurement are introduced in section 2. The performance improvement of 2-D spectroscopy on horizontal resolution and time resolution are shown in section 3. The intensity normalization method is also presented in section 3. Typical high-resolution 2-D distributions from impurity carbon are shown in section 4. The report is summarized in section 5.

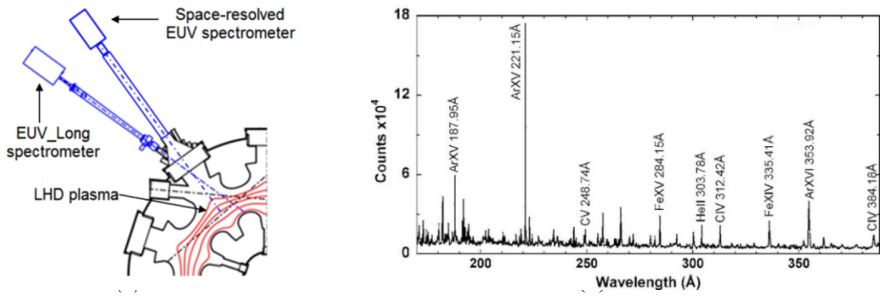

Figure 1. (a) Schedemic view of EUV spectroscopy in LHD with EUV_Long spectrometer and space-resolved EUV spectrometer and (b) typical spectrum measured with EUV_Long spectrometer in range of 170-390Å.

2. EUV spectroscopy in LHD

As shown in Fig. 1(a), two EUV spectrometers working in wide wavelength range of 30 to 650Å, which are named as EUV_Long spectrometer and space-resolved EUV spectrometer, are installed on 10-O port in LHD. The performance of two spectrometers is separately described in papers of [5] and [6] in detail. The EUV_Long spectrometer is developed as an impurity monitor to measure the time behavior of impurity emissions with sampling time of 5ms. A typical spectrum measured by EUV_Long spectrometer is shown in Fig. 1(b), and the time behavior of impurity emissions measured with the EUV_Long spectrometer, which is used for the intensity normalization method, is shown in Fig. 7 (d). As shown in Fig. 2, the space resolved EUV spectrometer observes s vertical profile of impurity emissions at horizontally elongated plasma cross section when the observation chord is fixed at the center of LHD port (θ=0°). The vertical observation range is about 550mm. The full vertical profile form Z=-550mm to 550mm can be observed by changing the vertical angle of space resolved EUV spectrometer with a vertical stepping motor two or three times. The elliptical shape of the LHD plasma rapidly rotates in the poloidal direction as the toroidal angle θ is changed. The change in the poloidal cross section of the LHD plasma is also shown for different toroidal angles of ϕ =+ 2◦, ϕ = 0◦ and ϕ = −2◦ in Fig. 2. The vertical profiles of impurity emissions as a function of toroidal angle θ, which results in the 2-D distribution measurement, can be measured by horizontally scanning the observation chord with a horizontal stepping motor. A good separation in the impurity emission location between inboard and outboard X-points can be easily obtained when the 2-D distribution is measured [2].

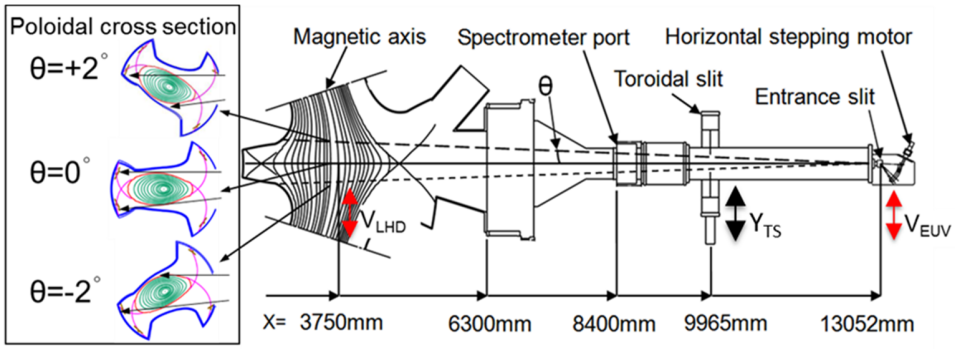

Figure 2. Schematic view of space-resolved EUV spectrometer. Horizontal scanning of space-resolved EUV spectrometer is carried out with a horizontal stepping motor. V_{EUV} is horizontal scanning speed of space-resolved spectrometer and V_{LHD} is horizontal scanning speed of observation chord at magnetic axis of R=3.75m. Y_{TS} is the horizontal distance between toroidal slit and central optical axis. The poloidal cross section of LHD plasma at toroidal angle of θ= +2°, θ = 0° and θ = -2° is shown at rectangular frame.

3. Improvements of 2-D data performance

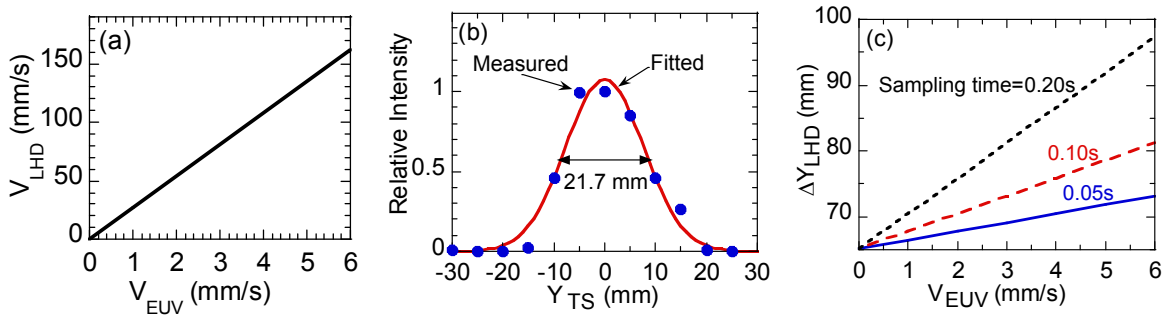

Figure 3. (a) V_{LHD} as a function of V_{EUV}, (b) relative spectral intensity as a function of Y_{TS} and (c) horizontal resolution (ΔY_{LHD}) against V_{EUV} as a parameter of sampling time

A back-illuminated CCD (Andor DO420-BN) with 1024 × 256 pixels was used in the space-resolved EUV spectrometer to detect the impurity emission until 2012 LHD experimental campaign. The active area of the CCD is 26.7 × 6.7 mm^2 with a pixel size of 26 × 26 μm^2. The CCD is usually operated at -20°C, where the thermal noise can be sufficiently reduced. 51×204 subimage mode is usually used for profile measurement with readout time of 63ms and sampling time of 200ms [2]. In 2013 LHD experimental campaign, the CCD was replaced by a new CCD (Andor DO920P-BN). The pixel size and active pixel number of the new CCD is the same as that of the old one. But the readout time of the new one is improved to 16.8ms under the same 51×204 subimage mode. Therefore, the new CCD can be operated with sampling time of 50ms or 100ms [2].

The toroidal resolution of space-resolved EUV spectrometer at $V_{EUV} = 0$, which is basically a function of the angle of incidence and the grating size and curvature, is experimentally determined using a toroidal slit (TS). As shown in Fig. 2, the toroidal slit, which can be horizontally moved, is installed between the LHD plasma and the space resolved EUV spectrometer. Distance between the toroidal slit and the LHD plasma is about 2 times longer than the distance between the toroidal slit and entrance slit of space resolved EUV spectrometer. The spectral intensity changes when the toroidal slit is horizontally scanned. Figure 3 (b) shows a relative spectral intensity as a function of the horizontal position of toroidal slit, Y_{TS}, which means the horizontal distance between toroidal slit and central optical axis. The relative spectral intensity profile is fitted with Gaussian function and the full width at half maximum of the Gaussian curve is determined to be 21.7mm. Since the distance between the entrance slit and the LHD plasma is about 3 times longer than the distance between the entrance slit and the toroidal slit, the horizontal resolution can be estimated to be 65mm at the position of R=3.75m [6].

As shown in Fig. 3(a), the horizontal scanning speed of observation chord at the position of magnetic axis (V_{LHD}) is approximately linear against the horizontal scanning speed of space-resolved spectrometer (V_{EUV}). The horizontal resolution in 2-D measurement shown in Fig. 3 (c) is a function of sampling time and scanning speed. Under the same scanning speed, the horizontal resolution is improved as the CCD sampling time decreases. Fig. 4 (a) and (b) show comparison of the 2-D distribution measured by old CCD with sampling time of 200ms and new CCD with 50ms, respectively. It clearly shows the horizontal resolution is significantly improved.

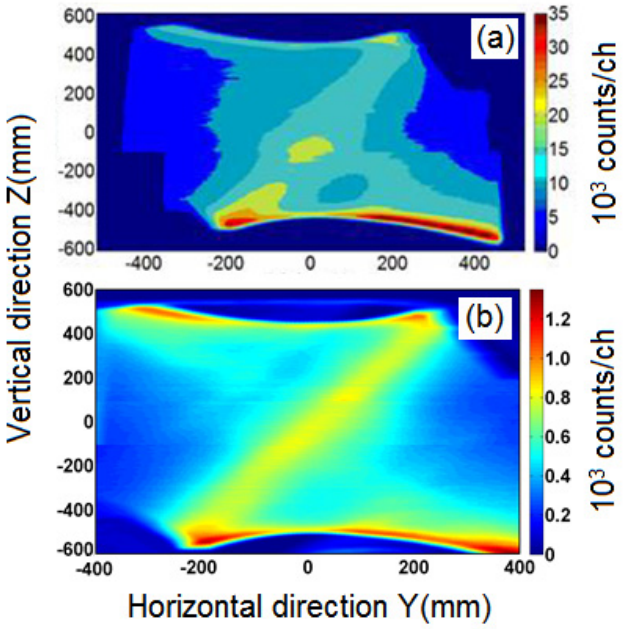

Figure 4 2-D profiles of HeII (303.78 Å) measured by (a) old CCD with V_{LHD} = 135mm/s and sampling time = 200ms and (b) new CCD with V_{LHD} = 162mm/s and sampling time = 50ms

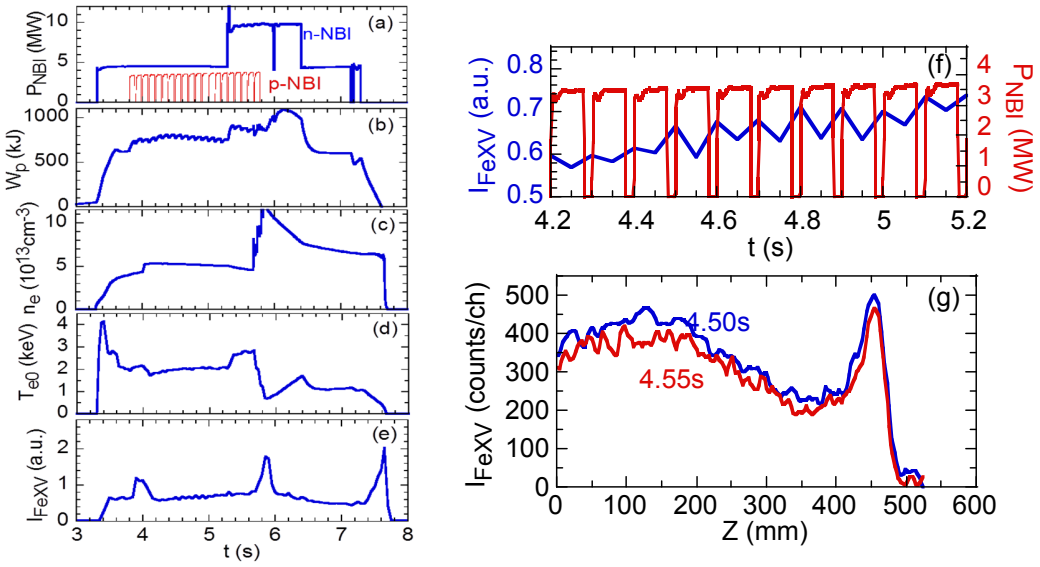

Figure 5 Time behaviors of (a) n-NBI (tangential injection) and p-NBI (perpendicular injection) port-through power, (b) plasma stored energy, (c) line-integrated electron density, (d) central electron temperature and (e) intensity of Fe XV (284.147Å) measured by space-resolved EUV spectrometer, (f) enlarged time behavior of Fe XV (284.147Å) with modulated p-NBI port-through power and (g) vertical profiles of FeXV (284.147Å) at t=4.50s (blue) and 4.55s (red).

For examining the time resolution in the upgraded system, time behavior and vertical profiles of FeXV (284.147Å) are measured during the NBI modulation phase. The interval of NBI modulation is 100ms and the sampling time of CCD is 50ms. As shown in Fig. 5 (f), a good correlation between the emission intensity of FeXV (284.147Å) and the p-NBI port-through power can be clearly observed. Figure 5 (g) shows the vertical profile of FeXV at t=4.50s and 4.55s. The two vertical profiles can be clearly distinguished each other indicating a good time resolution.

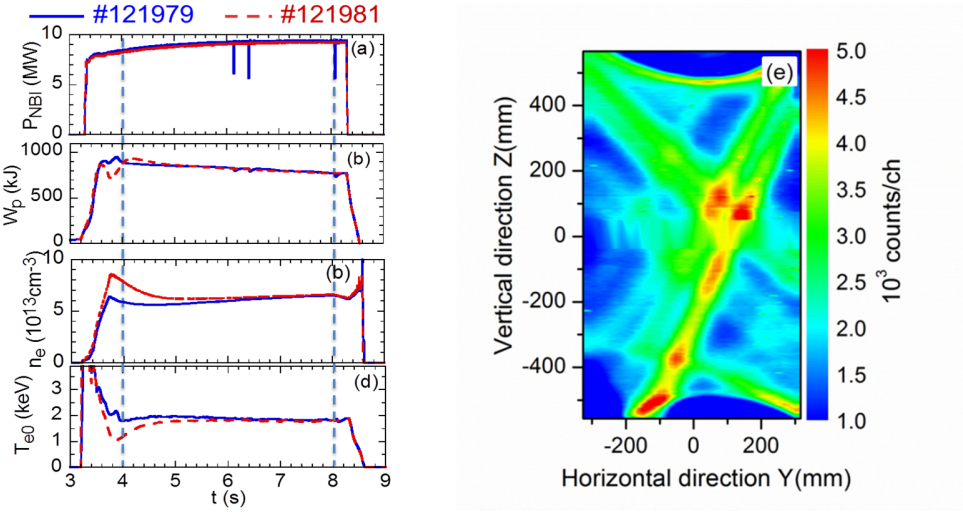

Figure 6. Time behaviors of (a) n-NBI port-through power, (b) plasma stored energy, (c) line-averaged electron density, (d) central electron temperature and (e) 2-D distribution of CIV (384.174Å) from short pulse NBI discharge. The 2-D profile is obtained through horizontal scanning during 4s oft=4s to 8s.

With the new CCD, it is possible to obtain the high-resolution 2-D distribution from high-density discharges. As mentioned above, the pulse length of high-density discharges heated by n-NBI is limited to several seconds. High horizontal scanning speed is required to complete the 2-D measurement during n-NBI pulse. The 2-D distribution of CIV (384.174Å) shown in Fig. 6 (e) is obtained from high-density NBI discharges with scanning speed of V_{LHD}= 162mm/s and sampling time of 100ms. The horizontal resolution is sufficiently good because two X-point diagonal traceries can be clearly observed.

A new method of normalizing the 2-D signal intensity by the spectral intensity from EUV_Long spectrometer is used for the 2-D data analysis to reduce the effect of shot-to-shot variation in the EUV emission during horizontal scan of the space-resolved EUV spectrometer. A steady discharge longer than 4s is required to complete the 2-D measurement. However, EUV emissions during the scanning often temporally change at each discharge. A typical example is shown in Fig. 7. Figure 7 (e) shows CIV 2-D distribution analyzed without intensity normalization using three discharges (#122454: upper trace, #122455: middle trace and #122456: lower trace). The new method is attempted using the time behavior of CIV measured with EUV_Long spectrometer, as shown in Fig. 7(d). The 2-D distribution is analyzed from 2s to 10s. A temporal variation is clearly seen in the emission intensity. The signal level is also changes among three discharges. All these variations in the emission intensity can give a clear influence to the quality of analyzed 2-D distribution. The 2-D distribution after intensity normalization is shown in Fig. 7 (f). When Fig.7(f) is compared with Fig.7(e), we clearly see the effect of intensity variations is almost invisible.

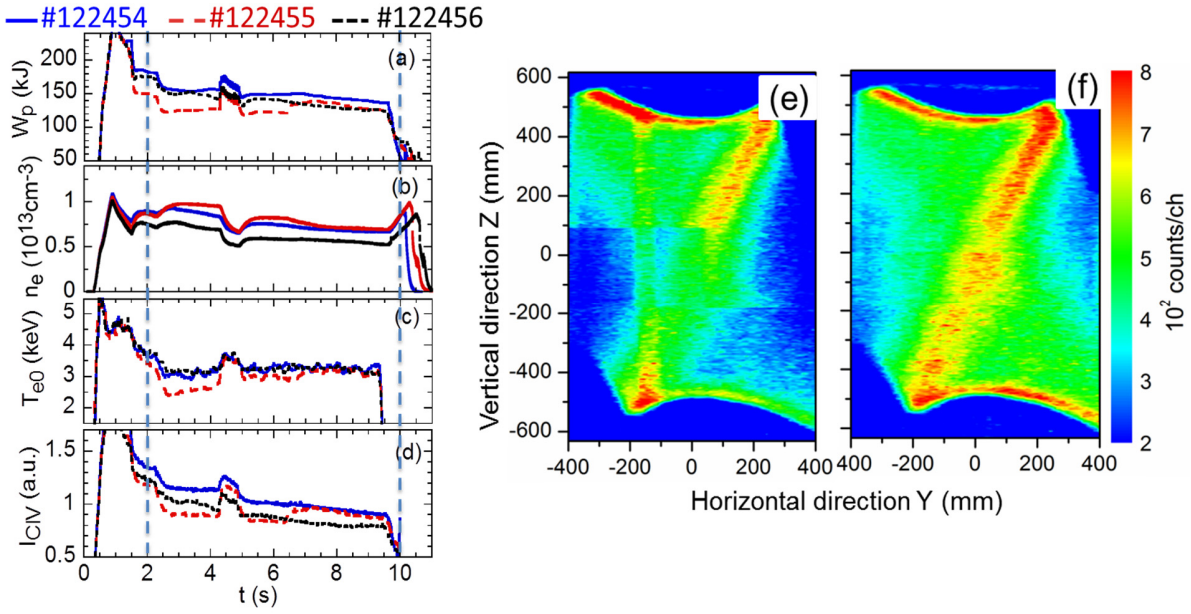

Figure 7. Time behaviors of (a) plasma stored energy, (b) line-averaged electron density, (c) central electron temperature, (d) CIV (312.4 Å) intensity measured from EUV_Long spectrometer, (e) 2-D distribution without intensity normalization and (f) 2-D distribution with intensity normalization.

4. Typical result of 2-D impurity emission distribution

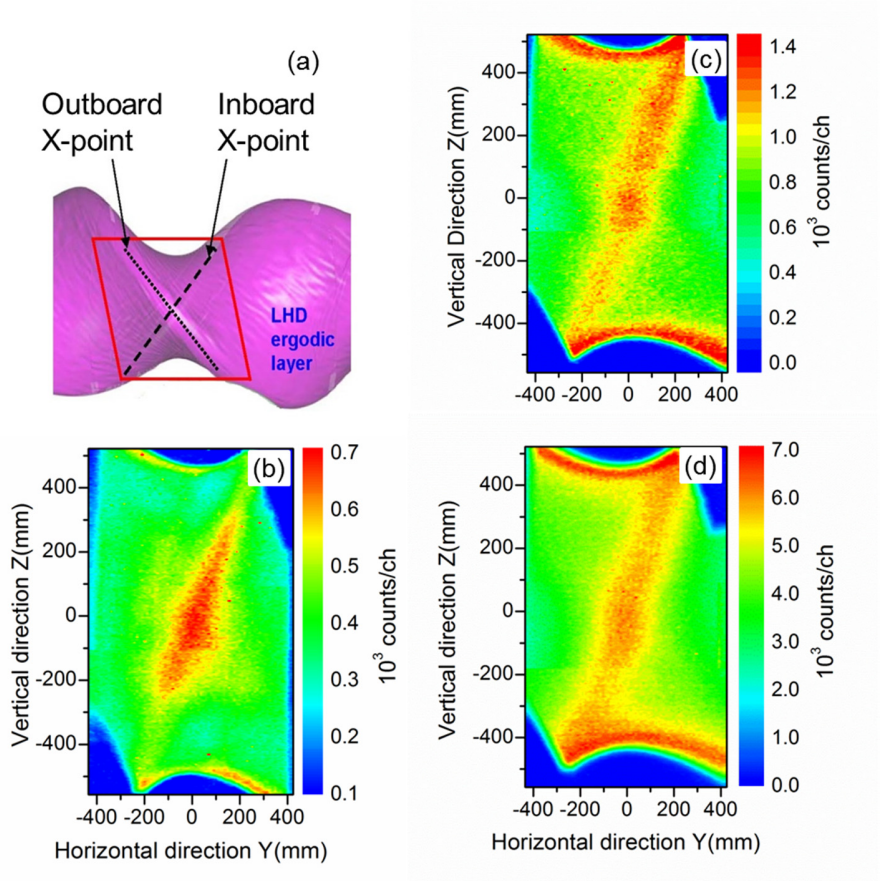

Figure 8. (a) Schematic view of LHD ergodic layer and 2-D distributions of (a) CIV (384.174Å), (c) CV (2×40.27Å) and (d) CVI (2×33.73Å). Observation range of space-resolved EUV spectrometer is denoted with a diamond-shape solid line in Fig.8(a) in addition to diagonal trajectory of inboard (dashed line) and outboard (dotted line) X-points.

The 2-D distribution of CIV (384.174Å), CV (2×40.27Å) and CVI (2×33.73Å) is observed from ICRF discharges at line-averaged density of $n_e = 1\times10^{13}$ cm^{-3}. Data are taken with sampling time of 0.1s and horizontal scanning speed of V_{LHD}=162mm/s. The figures indicate that the carbon emissions are localized in two parts, i.e. the top and bottom edges and the vicinity of inboard X-point. The line-integrated impurity line intensity is usually enhanced in the plasma edge as seen at the top and bottom emissions in the figures because the observation chord length passing through an impurity emission contour reflecting magnetic surface structure is considerably long at the plasma edge. The carbon emission is also enhanced along inboard X-point. It indicates a 3-D structure of the impurity distribution in the ergodic layer, reflecting a specific impurity transport in the ergodic layer.

5. Summary

The performance of 2-D space-resolved EUV spectrometer has been successfully improved without reduction of signal-to-noise ratio by installing a high frame rate CCD. It becomes possible to measure the 2-D distribution of impurity emissions from high-density short-pulse NBI discharges. Shot-to-shot intensity variation during horizontal scan can be significantly reduced by normalizing the 2-D impurity signal to the

spectral intensity from EUV_Long spectrometer. As future work, 2-D distribution will be analyzed against different density ranges.

Acknowledgements

The authors thank all members of LHD experimental group for their technical supports. This work was partially carried out under the LHD project financial support (NIFS13ULPP010). This work was also partly supported by the JSPS-NRF-NSFC A3 Foresight Program in the field of Plasma Physics (NSFC: No.11261140328, NRF: No. 2012K2A2A6000443).

References

[1] S.Morita et al., Nucl. Fusion **53** (2013) 093017.

[2] E.H.Wang et al., Rev. Sci. Instrum. **83** (2012) 043503.

[3] E.H.Wang et al., Plasma Sci. Technol. **15** (2013) 106.

[4] C.F.Dong et al., Rev. Sci. Instrum. **83** (2012) 10D509.

[5] M.B.Chowdhuri et al., Rev. Sci. Instrum. **78** (2007) 023501.

[6] C.F.Donget al., Rev. Sci. Instrum. **81** (2010) 033107.

Program of A3 Seminar
(23-26 June 2014)

22 June 2014 (Sunday)			
Registration: 15:00-21:00			

23 June (Monday)			
Session 1 (Opening & Category I-1) Chair: L.Q.Hu	08:30	**Shigeru MORITA** (NIFS)	**Welcome speech**
	08:40	**Hoon Kyun NA** (NFRI)	**Welcome speech**
	08:50	**Jiangang LI** (ASIPP)	**Opening talk** "EAST Five Year Plan"
	09:20	**Yeong-Kook OH** (NFRI)	Operation and engineering research plan in KSTAR
	09:45	**Zhijiang WANG** (HUST)	Recent progress on the J-TEXT
Coffee Break 10:10-10:25			
Session 2 (Category I-2) Chair: Y.K.Oh	10:25	**Liqun HU** (ASIPP)	Commissioning of EAST new diagnostics and preliminary experimental results
	10:50	**Xinjun ZHANG** (ASIPP)	Recent Progress with ICRF Heating on EAST
	11:15	**Katsuyoshi TSUMORI** (NIFS)	Ionic plasmas in cesium seeded negative ion source for NBI
	11:40	**Sang-hee HAHN** (NFRI)	Status and plan of plasma control system for steady-state operations
	12:05	**Chang Hwan KIM** (NFRI)	Status of the MG installation and the result of the dummy coil commissioning
Lunch Break12:30-13:40			
Session 3 (Category IIa-1) Chair: J.G.Bak	13:40	**Naoko ASHIKAWA** (NIFS)	Characterizations of deposited layers and hydrogen isotope retentions in fusion devices
	14:05	**Suk-Ho HONG** (NFRI)	A3 collaboration activity in PSI, Div/SOL research
	14:30	**Junling CHEN** (ASIPP)	PWI and edge plasma physics study on EAST
	14:55	**Shigeru MORITA** (NIFS)	Effect of neutrals and friction force on edge impurity transport in stochastic magnetic field layer of LHD
Coffee Break 15:20-15:35			
Session 4 (Category IIa-2) Chair: S.Morita	15:35	**Tetsutarou OISHI** (NIFS)	VUV spectroscopy in wavelength range of 500-2200Å for line spectrum and ion temperature measurements of tungsten ions at low ionization stages in Large Helical Device
	16:00	**Izumi MURAKAMI** (NIFS)	Spectroscopic modeling for tungsten EUV spectra
	16:25	**Daiji KATO** (NIFS)	Evaluation of ionization and recombination rate coefficients of tungsten ions in LHD plasmas by using UV-visible M1 lines
	16:50	**Nobuyuki NAKAMURA** (UEC)	Spectroscopic data of highly charged tungsten ions obtained with an electron beam ion trap
Group photos 17:15-17:30			

24 June (Tuesday)			
Session 5 (Category III-1) Chair: B.J. XIAO	08:30	**Mitsutaka ISOBE** (NIFS)	Consideration and discussion about fast-ion loss detector project in EAST (25min)
	08:55	**Junghee KIM** (NFRI)	Experimental observations of fast-ion loss in KSTAR (25 min)
	09:20	**Young-soon BAE** (NFRI)	Operational status in KSTAR NBI and plan of off-axis neutral beam line development (25 min)
	09:45	**Kazuo TOI** (NIFS)	Recent Progress in Experimental Studies of Energetic Ion Driven Global Modes on LHD (25 min)
	10:10	**Yongkyoon IN** (NFRI)	Error Field and its Correction Strategy in Tokamaks (25 min)
Coffee Break 10:35– 10:55			
Session 6 (Category IV) Chair: M.Isobe	10:55	**Nong XIANG** (ASIPP)	Particle-in-cell simulations of interactions between radio frequency waves and plasmas (25 min)
	11:20	**Yasushi TODO** (NIFS)	Multi-phase simulation of fast ion profile flattening due to Alfvén eigenmodes in a DIII-D experiment (25min)
	11:45	**Hao WANG** (NIFS)	Simulation study of a new kind of energetic particle driven geodesic acoustic mode in LHD (25 min)
	12:10	**Jian LIU** (USTC)	Simulation Study on Dynamics of Runaways in Tokamaks (25 min)
Lunch 12:35-14:00			
Session 7 Discussions on A3 program Chair: S.Morita L.Q.Hu Y.K.Oh	14:00-17:00 Education of young scientists Discussion on coordinator meeting Discussion on budget and administrative works Discussion on annual report of A3 collaboration Discussion on web site of A3 collaboration Discussions on next seminar and workshop plans Discussion on machine operation schedules		

25 June (Wednesday)			
Session 8 (Category IIb-1) Chair: N.Xiang	08:30	**Satoshi OHDACHI** (NIFS)	MHD instabilities studied by imaging diagnostics in the Large Helical Device (25 min)
	08:55	**YoungMu JEON** (NFRI)	Features and applications of resonant magnetic perturbations in KSTAR (25 min)
	09:20	**Yuan HUANG** (SWIP)	Experimental studies on pedestal structure and ELM instability on HL-2A tokamak (25 min)
	09:45	**Yong LIU** (ASIPP)	In-situ absolute intensity calibration for ECE measurements on EAST (25 min)
Coffee Break 10:10 - 10:30			
Session 9 (Category I-3) Chair: Y.M.Jeon	10:30	**Jayhyun KIM** (NFRI)	Integrated disruption avoidance and mitigation in KSTAR (25 min)
	10:55	**Satoru SAKAKIBARA** (NIFS)	MHD instabilities determining beta value in LHD (25min)
	11:20	**Bingjia XIAO** (ASIPP)	Quick plasma equilibrium reconstruction using GPU for real-time control (25min)
	11:45	**Ohjin KWON** (Daegu Univ.)	Effect of Local Modification of Equilibrium on the Stability of MHD Modes (25min)
Lunch Break 12:10 - 13:30			
Session 10 (Category IIa-3) Chair: S.Ohdachi	13:30	**Yunbo DONG** (SWIP)	Disruption mitigation with SMBI and MGI on HL-2A and J-TEXT (25 min)
	13:55	**Siwoo YOON** (NFRI)	Recent status of pedestal physics activities in KSTAR (25 min)
	14:20	**Tomohiro MORISAKI** (NIFS)	Estimation of Heat and Particle Transport by means of Transient Phenomena (25min)
	14:45	**Jun-Gyo BAK** (NFRI)	Investigation of divertor particle flux from electric probe measurements during ELMy H-modes in KSTAR (25 min)
Coffee Break 15:10-15:30			
Session 11 (PHD students & closing) Chair: S.Sakakibara	15:30	**Hyun-Seok KIM** (SNU)	Feasibility study of advanced operation scenario in KSTAR using CRONOS (20 min)
	15:55	**Xianli HUANG** (NIFS)	Initial result on iron transport analysis using radial profiles measured by space-resolved EUV spectrometer in LHD (20 min)
	16:20	**Chan-Soo KANG** (UST)	Study of runaway current during disruptions in KSTAR (20 min)
	16:45	**Hongming ZHANG** (NIFS)	Performance improvement of two-dimensional EUV spectroscopy based on high readout time CCD and signal normalization method (20min)
	17:10	**S.Morita Y.K.Oh L.Q.Hu**	Summary reports & Closing

26 June (Thursday)	
Session 12 Discussions on A3 collaboration Chair: S.Morita L.Q.Hu Y.K.Oh	09:00-12:00 Plenary meeting on future collaboration at each category for A3 Foresight Program on Critical Physics Issues Specific to Steady State Sustainment of High-Performance Plasmas **Category I:** Steady state sustainment of magnetic configurations (Current drive and profile control) **Category II:** Edge and divertor plasma control Category IIa: Transport of edge and divertor plasmas Category IIb: Stability of edge plasma **Category III:** Confinement of alpha particles (Interaction of energetic particle and bulk plasma) **Category IV:** Theory and simulation 13:30-17:00 Individual discussion on personnel exchange Individual discussion on hardware construction and operation of diagnostics and heating devices Individual discussion on wall cleaning and its effect Discussion on future study related to A3 collaboration Discussions with young scientists and PHD students

(END)

List of participants

Name	Affiliation
ASHIKAWA Naoko	NIFS
BAE Young-soon	NFRI
BAK Jun-Gyo	NFRI
CHEN Junling	ASIPP
DONG Yunbo	SWIP
HAHN Sang-hee	NFRI
HONG Suk-Ho	NFRI
HU Liqun	ASIPP
HUANG Xianli	NIFS/SOKENDAI
HUANG Yuan	SWIP
IN Yongkyoon	NFRI
ISOBE Mitsutaka	NIFS
JEON YoungMu	NFRI
KANG Chan-Soo	UST
KATO Daiji	NIFS
KIM Chang Hwan	NFRI
KIM Hyun-Seok	SNU
KIM Jayhyun	NFRI
KIM Junghee	NFRI
KWON Ohjin	Daegu University
LI Jiangang	ASIPP
LIU Jian	USTC
LIU Yong	ASIPP
MORISAKI Tomohiro	NIFS
MORITA Shigeru	NIFS
MURAKAMI Izumi	NIFS
NAKAMURA Nobuyuki	UEC
OH Noh-Yeong	NFRI
OH Yeong-Kook	NFRI
OHDACHI Satoshi	NIFS
OISHI Tetsutaro	NIFS

SAKAKIBARA Satoru	NIFS
TODO Yasushi	NIFS
TOI Kazuo	NIFS
TSUMORI Katsuyoshi	NIFS
WANG Hao	NIFS
WANG Zhijiang	HUST
XIANG Nong	ASIPP
XIAO Bingjia	ASIPP
YOON Siwoo	NFRI
ZHANG Hongming	NIFS/SOKENDAI
ZHANG Xinjun	ASIPP